An integrated geological characterisation of the Lower Triassic Main Buntsandstein Subgroup for geothermal applications in the southern Netherlands

Cecchetti, E.

DOI
10.4233/uuid:c0d6907c-d894-4040-953a-a3b68d5c3f3b

Publication date
2025

Document Version
Final published version

Citation (APA)
Cecchetti, E. (2025). *An integrated geological characterisation of the Lower Triassic Main Buntsandstein Subgroup for geothermal applications in the southern Netherlands*. [Dissertation (TU Delft), Delft University of Technology]. https://doi.org/10.4233/uuid:c0d6907c-d894-4040-953a-a3b68d5c3f3b

An integrated geological characterisation of the Lower Triassic Main Buntsandstein Subgroup for geothermal applications in the southern Netherlands

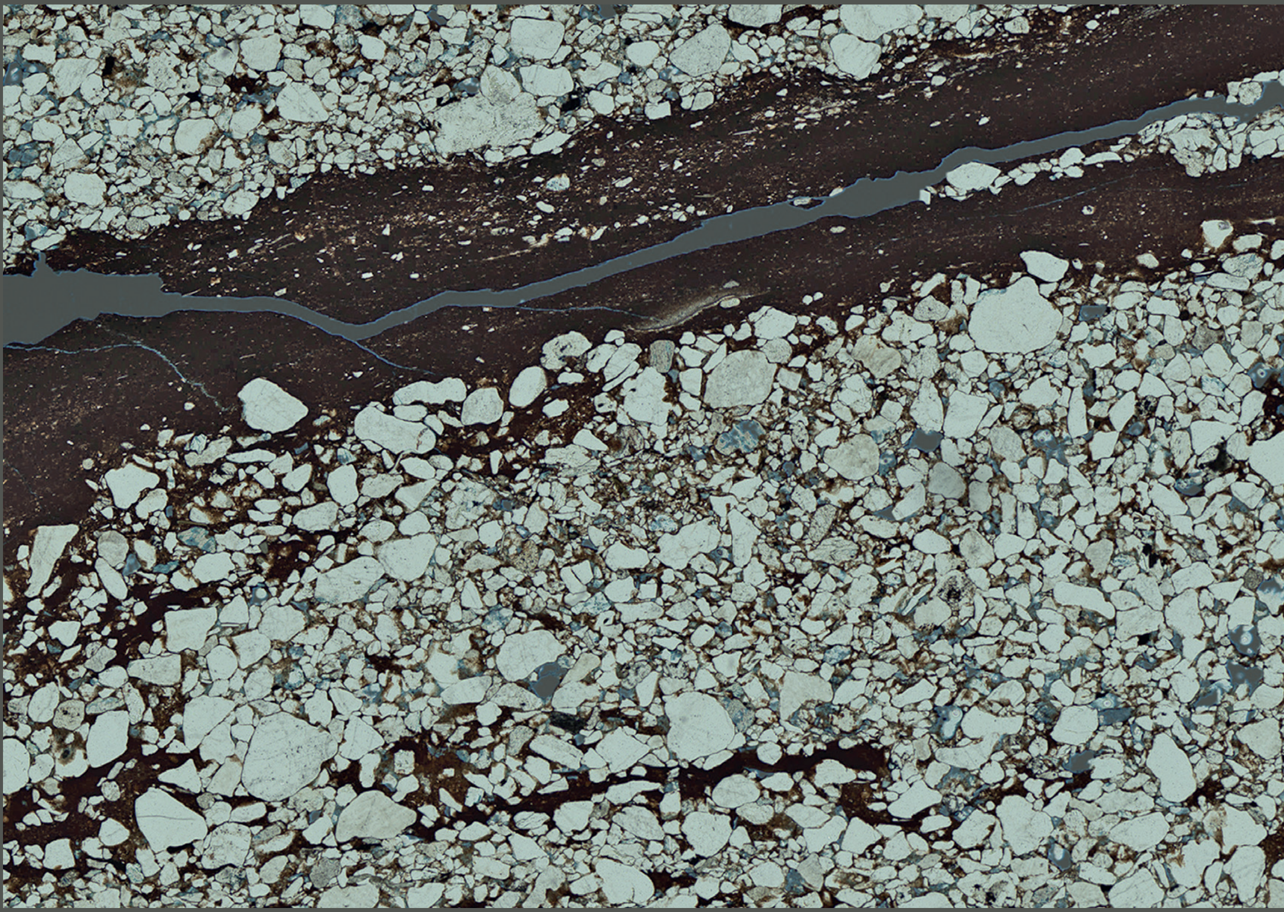

Emilio Cecchetti

An integrated geological characterisation of the Lower Triassic Main Buntsandstein Subgroup for geothermal applications in the southern Netherlands

Dissertation

For the purpose of obtaining the degree of doctor at Delft University of Technology
by the authority of the Rector Magnificus Prof. Dr. ir. E.C. Slob.,
chair of the Board for Doctorates,
to be defended publicly on
Wednesday 11 June 2025 at 12:30

by

Emilio Cecchetti
Master of Science in Earth Science, Utrecht University
born in Firenze, Italy

The dissertation has been approved by the promotors.

Composition of the doctoral committee:

Rector Magnificus	Chairperson
Prof. dr. A. W. Martinius	Delft University of Technology – *Promotor*
Dr. H. A. Abels	Delft University of Technology – *Promotor*

Independent members:

Prof. dr. S. Geiger	Delft University of Technology
Prof. dr. P. J. Vardon	Delft University of Technology
Dr. J. H. Ten Veen	TNO Earth, Environmental and Life Sciences
Prof. dr. S. Bourquin	University of Rennes, France
Prof. dr. A. J. Hartley	University of Aberdeen, United Kingdom
Dr. J. E. A. Storms.	Delft University of Technology – *Reserve member*

This study was supported by Rijksdienst voor Ondernemend Nederland (RVO), with additional support from Aardyn B.V. and PanTerra Geoconsultants B.V.

The author can be reached at: cecchetti.em@gmail.com

Printed by: ProefschriftMaken — www.proefschriftmaken.nl

Contents

Summary

Sandstones from the Triassic Main Buntsandstein Subgroup represent a promising deep geothermal target in the subsurface of the Netherlands. These sands have a widespread distribution and temperatures that locally reach up to 140-150°C at depths of ~ 4 to 5 km. The Main Buntsandstein Subgroup is a sand-prone interval, but the reservoir quality of these sandstones is known to be heterogeneous as a result of the interplay between depositional and diagenetic processes. Recent drilling campaigns at depths greater than 4 km have confirmed the poor reservoir quality in certain areas. Nonetheless, successful geothermal projects have been realized in the southern Netherlands at shallower depths of 2 to 3 km, where temperatures of 70 to 90°C can meet local heating demands for greenhouses and district heating. To facilitate further geothermal exploration, it is important to understand the geological conditions that control reservoir quality and identify areas with favourable subsurface conditions. The Main Buntsandstein sediments have been extensively studied at a regional scale in the Netherlands. The factors controlling reservoir quality remain however poorly understood in the southern Netherlands, particularly in the southeastern region where data are scarce.

This thesis aims to improve the geological understanding of the Main Buntsandstein sediments by conducting an integrated geological study leveraging an extensive hydrocarbon dataset and newly acquired data from geothermal exploration in the southeastern part of the Netherlands. The study characterizes the structural, sedimentological, and diagenetic heterogeneities of the Main Buntsandstein Subgroup and evaluates their control on porosity, permeability, and, ultimately, geothermal potential.

The first part of the thesis (Chapter 2) assesses the structural evolution of the Roer Valley Graben and the distribution of the Main Buntsandstein sediments through detailed seismic and well-data interpretation. A 2D palinspastic restoration was performed to evaluate the burial history and basin geometry during the Early to Middle Triassic. The analysis reveals that the central and southern parts of the Roer Valley Graben were active depocenters during the Early to Middle Triassic, while the northern part was a more marginal area where predominantly fine-grained sediments were deposited. After deposition, the sediments were significantly impacted by faulting, with burial depths reaching 4-5 km in the central graben, while the flanks experienced shallower burial of 2-3 km, making them promising targets for future geothermal investigations given the higher likelihood of preserved primary reservoir properties.

Next, in Chapter 3, the sedimentology and lithostratigraphy of the Main Buntsandstein are examined using a subsurface dataset of well cores, gamma-ray logs, and thin sections. The study identifies six lithofacies associations deposited through different fluvial processes with minor aeolian reworking. Overall, the different depositional processes are linked to tectonic and climate changes and led to the development of three distinct types of reservoir architectures, each with its own set of heterogeneities at different spatial scales. At the scale of the study area the heterolithic sediments deposited as result of playa-lake expansions can hamper the vertical connectivity of sandstone units given their continuity at km scale. Within the sandstone units, cemented zones or mud drapes are the most common fluid baffles.

Furthermore, most of the sandstone types do not preserve a primary relationship with reservoir properties because of post-depositional diagenetic processes.
The diagenetic processes that control porosity and permeability in the Main Buntsandstein Subgroup were analyzed through detailed petrographic studies of available and a series of new thin sections (Chapter 4). The results show that illite, quartz, and dolomite are the dominant cements in these sandstones, with their influence on reservoir quality varying according to the sedimentary facies. In areas such as the Roer Valley Graben flanks, where the maximum burial history during Triassic and Early to Mid-Jurassic was largely shallower than 2 km, lower compaction and cementation rates favour the preservation of primary reservoir properties.

A structural study was conducted to analyse the distribution and characteristics of natural fractures and to investigate the mechanical stratigraphy of the Main Buntsandstein Subgroup (Chapter 5). This study used a dataset from the West Netherlands Basin as the Roer Valley Graben lacks the needed datasets. It revealed that natural fractures are favourably oriented with respect to the present-day in-situ stress, increasing the likelihood that these fractures are open. Fracture density was found to be higher in the heterolithic sedimentary successions, suggesting a link to the depositional environment and Main Buntsandstein Subgroup stratigraphy.

The geological insights gained from these studies were then employed to assess the geothermal potential of the Main Buntsandstein Subgroup in the Roer Valley Graben (Chapter 6). Porosity and permeability were evaluated, and calculations for Heat Initially in Place (HIIP) and Geothermal Power (GP) were made at well scale. A sensitivity analysis identified reservoir thickness and permeability as the parameters that most influence these calculations. The results are contextualized within the broader geological knowledge developed throughout the thesis, and three case studies corresponding to three types of potential geothermal plays are presented and discussed.

A conclusive synthesis is presented in Chapter 7, aimed at summarizing the main findings of this thesis and discussing how these results should be used in the future to reduce uncertainties and mitigate risks in geothermal exploration within the Main Buntsandstein of the southern Netherlands. To keep pace with the growing heat demand and the transition away from hydrocarbons as a primary energy source, the geothermal industry must make fast progresses. The Main Buntsandstein Subgroup has the potential to serve as a promising reservoir, particularly in regions like the northwestern Roer Valley Graben, where geological conditions suggest more favorable reservoir properties. Future exploration and production in these areas could play a crucial role in meeting the Netherlands sustainable energy targets.

Chapter 1: Introduction

1.1 Low enthalpy geothermal energy

The quest for sustainable and renewable energy sources has become increasingly urgent in the face of global climate change and the necessity of moving away from fossil fuels. In this context, low-enthalpy geothermal energy is a feasible alternative offering potential for clean and reliable energy production. These resources are stored in sedimentary rocks and can be found in areas with low subsurface temperature gradients where implementation of high-enthalpy geothermal systems is not possible. In these areas, geothermal reservoirs at 2-3 km depths have often temperatures between 60 and 100 C° given the average geothermal gradient of 30-31 C°/km. These temperatures are then employed for heat production as electricity production requires minimum temperatures of 110-120 C° (DiPippo, 2012). Low enthalpy geothermal systems, nonetheless, still represent an essential energy source since heating can constitute over half the total energy consumption in countries with moderate to cold climates. In the Netherlands, heating represents about 45% of the total energy consumption (Ministry of Economic Affairs and Climate Policy, 2023). This heating demand that is now primarily satisfied by burning fossil fuels could be largely satisfied by geothermal heat (IRENA, 2017), which, in turn, would significantly contribute to reducing the country's CO_2 emissions.

Suitable geothermal sedimentary reservoirs are often explored in provinces with a hydrocarbon exploration and production history. Examples include the Molasse Basin in Germany (Bachmann and Müller, 1991), the West Netherlands Basin in the Netherlands (De Jager et al., 1996) and the Perth Basin in Australia (Crostella and Backhouse, 2000). The extensive heritage of hydrocarbon data and expertise is a valuable resource for the geothermal industry. Data such as regional geological models, seismic surveys, and well logs can be transferred from hydrocarbon to geothermal applications, supporting the identification of potential geothermal reservoirs and the assessment of the feasibility of geothermal operations. Furthermore, both industries drill deep and often deviated wells to access subsurface reservoirs. The similarities between drilling processes allow the transfer of knowledge related to drilling technologies, equipment, and best practices for subsurface operations.

However, many challenges and knowledge gaps still hamper the development of low-enthalpy geothermal implementation projects. For example, the capital required to fully develop a geothermal project, with costs that usually scale exponentially with depth and relatively low profits when compared to the hydrocarbon industry (Lukawski et al., 2016). Furthermore, most wells and geological knowledge available in hydrocarbon regions are from structural highs where hydrocarbon accumulations are more likely to be found. In geothermal systems, the deeper subsurface layers located in the structural lows are instead more of interest given the higher temperatures expected. However, the different burial history experienced in the structural lows when compared to that experienced in the structural highs can result in very diverse reservoir properties such as permeability and porosity. Deeper burial can enhance processes such as cementation and compaction, deteriorating the porosity and permeability in the structural lows thereby increasing the uncertainties in geothermal operations.

1.2 Geothermal energy in the Netherlands

The Netherlands has experienced rapid growth in geothermal activities since the first successful geothermal doublet system installation in 2007. As of the 1st of January 2023, 26 doublets have been installed (Ministry of Economic Affairs and Climate Policy, 2023). Of these doublet systems, 21 produce heat from Permian and Upper Jurassic/Lower Cretaceous reservoirs at depths of around 2000 m with temperatures mostly ranging between 70 and 80 C° (Mijnlieff, 2020)

Despite the rapid expansion of geothermal activities, the Triassic reservoirs have seen minimal development, with only two doublet systems extracting heat from Triassic clastic reservoirs (Ministry of Economic Affairs and Climate Policy, 2023). However, the Triassic reservoirs host a geothermal potential up to 1 GJ/m^2 in the southeastern part of the country (Fig. 1.1 from *www.ThermoGis.nl*). The sandstones from the Main Buntsandstein Subgroup represent the main target within the Triassic sedimentary succession. They have a large distribution onshore and a long history of prolific hydrocarbon production (e.g., the Waalwijk gas field in Noord Brabant). The depth of the Main Buntsandstein Subgroup ranges from 1 to 4-5 km in the southern part of the Netherlands, where these sediments reach temperatures of 120-140 °C and the Subgroup may have thicknesses of 200-250 m (IF Technology, 2012). Furthermore, the Röt Fringe Sandstone Member and the Nederweert Formation where present might add to the entire reservoir thickness (Mijnlieff, 2020).

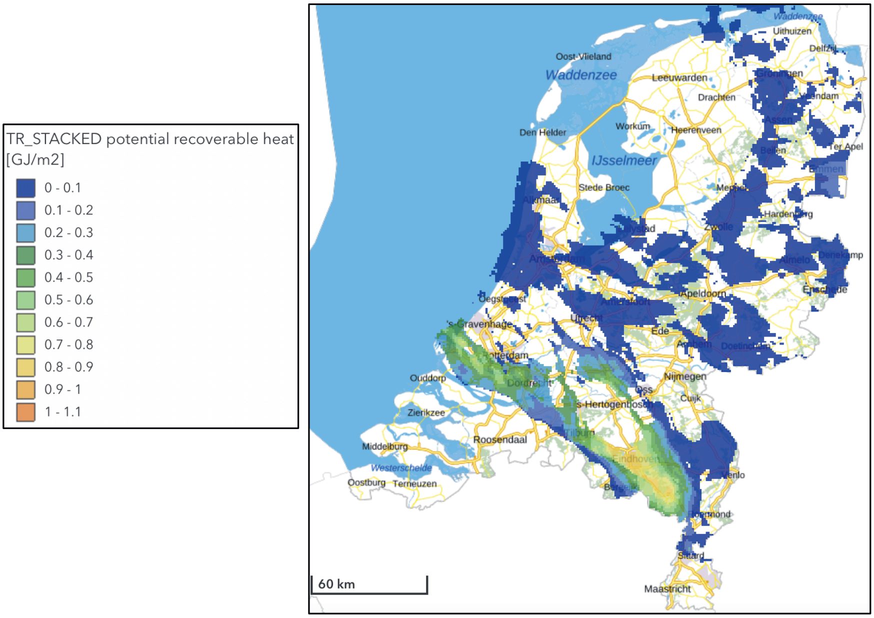

Figure 1.1: Map of the Netherlands displaying the potential recoverable heat from the Triassic reservoirs (source: www.ThermoGis.nl).

However, the quality of Triassic reservoirs is highly heterogeneous as a result of an interplay between depositional and diagenetic processes (Purvis and Okkerman, 1996; Mijnlieff, 2020; Boersma et al., 2021; Cecchetti et al., *this thesis*), which makes geothermal operations in the

Triassic play challenging. In 2017, an exploration well (NLW-GT-01) targeting the lower Triassic Main Buntsandstein sandstones at ~4 km depth revealed extremely poor reservoir quality due to diagenesis with values of porosity in the order of 3-4% and permeability below 0.01 mD (Felder and Fernandez, 2018). This well exemplified the risks associated with the Triassic play and indicated the need for a more comprehensive geological understanding of these sediments, especially when deeply buried.

1.3 Main Buntsandstein geology and uncertainties

The lower Triassic Main Buntsandstein Subgroup is a fluvial-aeolian sedimentary interval deposited under arid to semi-arid conditions across the Germanic Basin, a large endorheic basin that developed during the Late Permian to Early Triassic at the western margin of the Tethys domain (Scheck and Bayer, 1999; Ziegler et al., 2004; Geluk, 2005; Bourquin et al., 2011). The Main Buntsandstein sediments were deposited at the Induan-Olenkian transition in an extensional tectonic regime that led to thick sediment deposition in the southern part of the Netherlands (Zijerveld et al., 1992; NITG, 2004; Geluk et al., 2005).

The interplay between depositional and post-depositional processes resulted in the development of heterogeneities of various character, such as structural, sedimentary, and diagenetic. The origin of these heterogeneities and their role in controlling reservoir quality remain poorly understood. The geological uncertainties are even further amplified in the southeastern part of the Netherlands, where data are more scarce compared to the southwestern part and offshore area. The southwestern part of the country, in the Brabant province mostly, is covered by 2D seismic surveys of different ages and qualities, with wells penetrating the Main Buntsandstein Subgroup in focused areas of hydrocarbon exploration (SCAN, 2019).

The limited character of the geological dataset increases the uncertainties in an area where several tectonic pulses resulted in a network of faults with different orientations and character, resulting in complex structural geometries and architectures (Geluk et al., 1994; Deckers et al., 2023). From the Mid-Jurassic until the Early Cretaceous, fault movements caused the erosion of the Main Buntsandstein sediments in some regions of the Roer Valley Graben and resulted in the development of a regional angular unconformity. These fault movements affected the Main Buntsandstein thickness, lateral extent, and more in general, reservoir properties, due to differential burial, thus diagenesis across the basin. These parameters are key factors controlling the level of heat production and lifetime of a potential geothermal system (Willems et al., 2020).

The Main Buntsandstein Subgroup sediments in the Roer Valley Graben and more in general in the Netherlands, have been investigated in a general context during previous geo-energy campaigns (i.e., IF Technology, 2012), and different depositional models have been made that provide helpful information about sedimentary structures and depositional processes (i.e., Geluk, 2005). However, some of these models differ from each other. For example, Carter et al. (1990) suggest deposition on fluvial fan systems with a northeast average paleoflow direction originating from a source located to the southwest of the Roer Valley Graben. On the other hand, Geluk (2005) proposes a model with deposition by axial river systems flowing to the northwest. The existence of different depositional models creates additional uncertainties as each model produces different types of sedimentary architectures each with distinct geometries and connectivity of the sandstone bodies.

The Main Buntsandstein Subgroup in the Netherlands is formed by three Formations, namely (oldest to youngest): Volpriehausen, Detfurth, and Hardegsen. The Volpriehausen and Detfurth Formations comprise a lower fluvial/aeolian sandstone and an upper playa-lake silt/claystone, while the Hardegsen Formation is formed by an alternation of fluvial sandstones and claystones at meter to tens of meter scale (Van Adrichem Boogaert and Kouwe 1994; Geluk and Röhling, 1997). In this context, the playa-lake claystones at the top of the Volpriehausen and Detfurth Formations are considered stratigraphic markers that can be correlated regionally (Geluk and Röhling, 1997). However, in the southern Netherlands, the spatial extent of these claystone layers is uncertain, and locally, the Main Buntsandstein Subgroup is formed entirely by sandstones (Geluk, 2005). It remains crucial to assess the extent of these claystone units, and more in general, the stratigraphy of the Buntsandstein, to predict the arrangement and extent of the sandstone bodies.

The origin and arrangement of these sandstone bodies can influence primary porosity and permeability distributions and subsequent secondary processes such as diagenesis (Hartmann and Beaumont, 1999; Morad et al., 2000). Compaction and cementation are diagenetic processes that play a crucial role in controlling the reservoir quality of the Buntsandstein sediments (Purvis and Okkerman, 1996; Beyer et al., 2014; Olivarius et al., 2015; Busch et al., 2022). Compaction can significantly reduce the intergranular volume, thus reducing the pore spaces (Busch et al., 2022). Cementation can have a different impact on porosity and permeability depending on the nature of the sediments. For example, offshore in the Netherlands, Purvis and Okkerman (1996) showed how dolomite cement reduces the Buntsandstein intergranular porosity in sandstones. On the other hand, Busch et al. (2022) showed how dolomite cement can help prevent sediment compaction and may help preserve reservoir quality in Buntsandstein sandstones in the Upper Rhine Graben. In summary, it is crucial to understand the different diagenetic processes that the Buntsandstein Subgroup sediments experienced and what the impact of these processes has been on porosity and permeability.

When average matrix permeability is low, natural fractures can play a key role in enhancing the permeability system and unlocking the deep Triassic sandstone's geothermal potential (Boersma et al., 2021). The presence of open natural fractures in the Main Buntsandstein sandstones has been reported in numerous studies (for example, Kourta and Jocker, 2018; Vinci, 2018; Boersma et al., 2021). However, discrepancies exist when results obtained by different interpreters using the same dataset are compared. For example, the total number of interpreted natural open fractures from the image log in NLW-GT-01 ranges from more than 300 (Kourta and Jocker, 2018) to 58 (Boersma et al., 2021). The coexistence of such different interpretations creates added uncertainty when assessing the potential impact of natural fractures on the permeability of the Main Buntsandstein reservoir units. Therefore, a detailed analysis of fracture types and their genesis is necessary to evaluate the potential effect of fractures on geothermal production.

1.4 Thesis objectives and layout

This thesis aims to characterize the Main Buntsandstein Subgroup in the southern Netherlands, to enhance the geological knowledge of the Lower Triassic reservoirs and facilitate future geomodelling of this reservoir. The feasibility of the study is enhanced by leveraging an extensive hydrocarbon dataset, along with recently acquired data from deeper subsurface layers in the Roer Valley Graben gathered during geothermal exploration and production campaigns. Different types of data and methods are integrated to characterize the geological complexities of this geothermal play, focusing on the various types of structural, sedimentological, and diagenetic heterogeneities present in the Main Buntsandstein Subgroup sediments and their control on porosity and permeability, thus geothermal potential.

First, the Roer Valley Graben's structural evolution and the distribution of the Main Buntsandstein sediments are assessed through a detailed seismic and well data interpretation. The results are then used to perform a 2D palinspastic restoration with the scope of assessing the burial history and the basin geometry during the Early Triassic. The study reveals that the central and southern parts of the Roer Valley Graben were active depocenters during the Early to Middle Triassic. In contrast, the northern part was a more marginal area where mostly fine-grained sediments were deposited. After deposition, the Main Buntsandstein sediments were strongly affected by fautling. Sediments were buried to a depth of 4-5 km in the central part of the Roer Valley Graben. The flanks of the graben were instead subjected to less burial (2-3 km), thus representing promising areas for further investigation, given the higher likelihood of having preserved better reservoir properties.

Once the Roer Valley Graben tectonic history and basin geometry were defined, the sedimentology and lithostratigraphy of the Buntsandstein in the Roer Valley Graben have been assessed using a subsurface dataset composed of well cores, gamma-ray logs, and thin section data. This study reveals that different fluvial processes, with minor aeolian reworking, dominate the deposition of the Main Buntsandstein sediments. These different depositional processes resulted in the development of six lithofacies associations, developing three different types of reservoir architectures with their own set of heterogeneities at different spatial scales.

Following the diagenesis and its role on controlling porosity and permeability of the Main Buntsandstein Subgroup have been assessed through a detail petrographic analysis. This work reveles that illite, quartz, and dolomite represent the most dominant types of cement in the sandstones from the Main Buntsandstein in the Roer Valley Graben. The influence of these cements on reservoir quality changes depending on the sedimentary facies. Furthermore, the burial paths, particularly the extent of burial during the Triassic and Early to Mid-Jurassic, strongly impact reservoir properties due to different cementation and compaction rates.

A structural study is then conducted to to document the drivers and characteristics of natural fracture distribution and investigate the Main Buntsandstein Subgroup fracture and mechanical stratigraphy. The study exployes a dataset from the West Netherlands Basin, as no appropriate data (e.g., borehole image logs) are available in the Roer Valley Graben. The study reveals that natural fractures are oriented such that the likelihood of the fractures to be open is significant given their orientation in respect to the present-day in-situ stress orientation.

The fractures are associated with large-scale tectonic events and have a higher density in the heterolithic sedimentary succession, thus appearing to be linked to the depositional environment.

The geological knowledge developed is then employed to analytically asses the geothermal potential of the Main Buntsandstein Subgroup in the Roer Valley Graben. This is done by evaluating the porosity and permeability of the Main Buntsandstein sediments and calculating the Heat initially in place (HIIP) and Geothermal Power (GP) at well scale. A sensitivity analysis is performed to determine the parameters that mostly affect the equation results. The results are discussed in the context of the geological knowledge developed in the previous chapters of this thesis, and three case studies are presented.

All knowledge developed within this thesis is then summarized in a synthesis, where recommendations are provided for further research to de-risk the Buntsandstein geothermal play in the southern part of the Netherlands.

Chapter 2: Structural controls on the Triassic Main Buntsandstein sediment distribution in the Roer Valley Graben, the Netherlands

Chapter 2 is based upon: Cecchetti, E., Martinius, A. W., Bruna, P. O., Bender, A., Abels, H. A., 2024. Structural controls on the Triassic Main Buntsandstein sediment distribution in the Roer Valley Graben, the Netherlands. *Netherlands Journal of Geosciences*, *103*, e23.

Abstract

The lower Triassic Main Buntsandstein Subgroup represents a promising, but high-risk geothermal play in the Netherlands. Although the gross thickness in boreholes locally exceeds 250 m, the spatial distribution, geometries and preservation of these sedimentary units remained uncertain due to the lack of seismic data with sufficient resolution and the sparse borehole network. This creates uncertainty in the quantification of the reservoir dimensions that is essential for the planning of geothermal operations.

In this study, seismic interpretation and 2D palinspastic restoration of new and reprocessed seismic data were conducted and combined with borehole data to assess the tectonic evolution of the Roer Valley Graben in the southeastern Netherlands and its control on the spatial distribution of the Main Buntsandstein Subgroup sediments. Our results show that the central and southern parts of the Roer Valley Graben were active depocenters in the Early to Middle Triassic times dominated by fluvial sandstone deposition, providing important play elements for prospective leads on geothermal exploration. The northern part of the basin was a more marginal area where mostly fine-grained sediments were deposited. To the northwest, differential subsidence resulted in the development of areas where the Buntsandstein thickness is reduced to ~150 m.

After deposition, the Main Buntsandstein sediments were compartmentalized by faulting related to post-depositional tectonic activity, locally reducing the lateral extent of the geothermal target areas down to 1-2 km in a ~NE-SW direction. On the platform areas adjacent to the Roer Valley Graben and to the southeast, Jurassic sediments are largely absent and the Main Buntsandstein sediments are present at depths shallower than 2 km. These platforms are promising targets for further investigation, as the relatively shallow burial depths, compared to the central part of the graben, may have contributed to the preservation of more favorable reservoir properties.

2.1 Introduction

The lower Triassic Main Buntsandstein Subgroup is considered to be a promising geothermal play in the subsurface of the Netherlands (Kramers et al., 2012; Mijnlieff, 2020). In the Roer Valley Graben in the southeastern Netherlands, the Main Buntsandstein Subgroup is composed of stacked sandstones locally reaching total thicknesses of over 200 m and temperatures of 80-130 °C at depths of 2 to 4 km (IF Technology, 2012; Kramers et al., 2012; Mijnlieff, 2020). This makes the Main Buntsandstein sediments an attractive deep geothermal play that could contribute to open-up the geothermal potential in an area where geothermal energy is rather underdeveloped (Ministry of Economic Affairs and Climate Policy, 2023).

The Roer Valley Graben area is a geologically under-explored area compared to the adjacent West Netherlands Basin or the offshore sector (Van Lochem et al., 2019). It is mostly covered by 2D seismic surveys of different ages and qualities, with a series of wells penetrating the lower Triassic Main Buntsandstein Subgroup in focused, tectonically-high areas. The relatively poor quality of the geological dataset increases uncertainties for geothermal operations in an area where several tectonic phases resulted in a network of faults with different orientations and characters, creating complex geometries and architectures during and after deposition (Geluk et al., 1994; Deckers et al., 2023). These complexities can affect the Buntsandstein thickness, lateral extent, and properties, which are key parameters controlling the level of injectivity and lifetime of a geothermal system (Willems et al., 2020).

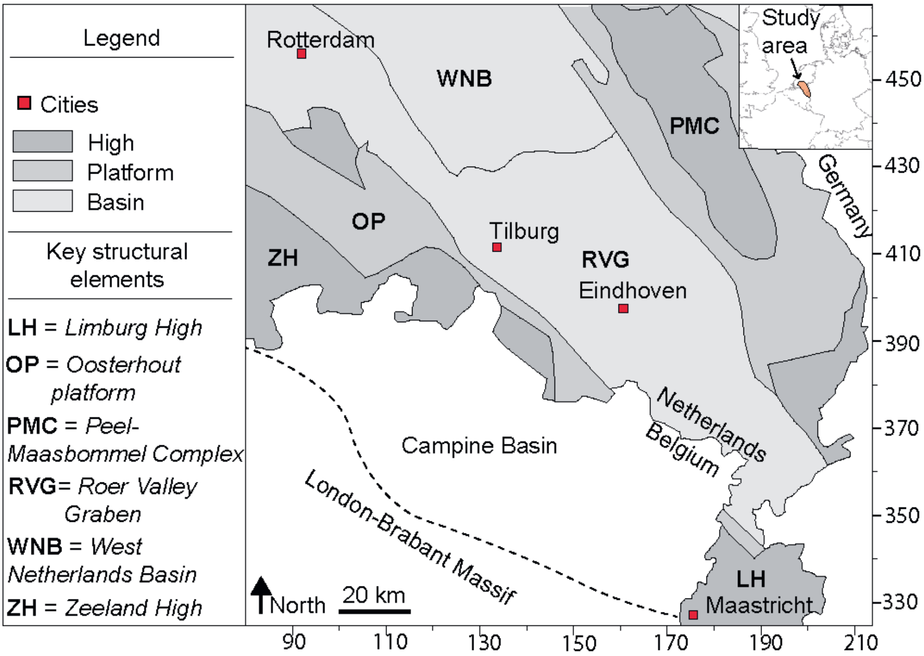

Figure 2.1. Main structural elements at present-day in the southern part of the Netherlands (after Kombrink et al., 2012). The Main Buntsandstein sediments are present in the basin and the platforms, while they are not encountered on the highs.

In this study, we evaluate the impact of the structural evolution on the distribution, character, and preservation of the Main Buntsandstein sediments in the Roer Valley Graben. The sediment depth and thickness variations are outlined by seismic mapping, as are the faults. These parameters, combined with well data, are essential to determine the extent, lithology, and geometry of the Main Buntsandstein sedimentary units. Then, 2D restoration analysis is performed on a network of transects up to the base of the Main Buntsandstein to assess the structural evolution of the basin, the burial history of the lower Triassic sediments and reconstruct the basin geometry at the time of deposition of the Main Buntsandstein units. Finally, the results of this evaluation and its intrinsic uncertainties are discussed, and recommendations for future geothermal exploration in the southeastern part of the Netherlands are proposed.

2.2 Regional geological setting

2.2.1 The Roer Valley Graben

The subsurface in the southeastern part of the Netherlands is characterized by the presence of several structural elements, with the Roer Valley Graben being the most prominent (Fig. 2.1). The Roer Valley Graben is a NW-SE oriented graben forming the propagation of the most western branch of the Rhine Graben rift system, a Cenozoic rift system that extends from the Alps to the North Sea area (Ziegler, 1992).

In its present-day form, the Roer Valley Graben is ~20-45 km wide and 130 km long, bounded to its NE flank by the Peel-Maasbommel Complex (Fig. 2.1). To the southwest, the Oosterhout Platform and the Zeeland High separate the Roer Valley Graben from the Campine Basin and the London Brabant Massif further to the south (Kombrink et al., 2012; Deckers et al., 2023). To the northwest, the Roer Valley Graben continues into the West Netherlands Basin, where the fault direction changes from overall NW-SE to more WNW-ESE striking (Geluk et al., 1994; NITG, 2004; Worum et al., 2005).

2.2.2 Structural evolution

The structural evolution of the study area began during the Caledonian Orogeny in the Devonian, when the London-Brabant Massif was uplifted and the Campine basin formed a large depression to the north (Geluk et al., 1994; NITG, 2004). However, it was only during Late Carboniferous times that as a result of the Variscan Orogeny the precursor structure of the Roer Valley Graben and Peel-Maasbommel Complex started developing (NITG, 2004).

During Late Permian to Late Triassic times, a regime of extensional tectonics led to basin subsidence, allowing the accommodation of a thick sequence of sediments in the Roer Valley Graben area (Zijerveld et al., 1992; Geluk, 2005; NITG, 2004). The Roer Valley Graben formed a ~NW-SE oriented half-graben as result of fault activity along the northern margin of the London-Brabant Massif (Winstanley, 1993; Geluk, 2005). To the north of the Roer Valley Graben, the Central Netherlands Swell was a positive topographic element where only minor sedimentation occurred (Geluk and Röhling, 1997).

From the Late Jurassic to the Early Cretaceous, the Mid- and Late-Kimmerian tectonic phases marked a further structural reorganization. The Mid-Kimmerian tectonic phase led to the uplift of block terrains adjacent to the Roer Valley Graben, such as the Peel Maasbommel Complex and the Zeeland High. Then, differential fault movements during the Late-Kimmerian resulted in further uplift of the block terrains and the development of sub-graben systems within the Roer Valley Graben. These tectonic phases locally caused deep truncation and erosion of Mesozoic deposits across the Roer Valley Graben area (Winstanley, 1993; Geluk et al., 1994; NITG, 2004; Kombrink et al., 2012).

During the Middle to Late Cretaceous, regional subsidence accompanied by sea-level rise resulted in the deposition of the Chalk Group (Herngreen and Wong, 2007). The deposition of the Chalk Group on top of older sediments of Early Cretaceous (Berriasian) to Carboniferous age resulted in the development of an unconformity, which is referred to in this article as the base Chalk Group unconformity.

During and after the deposition of the Chalk Group, the Roer Valley Graben was inverted as result of the convergence between Africa and Europe (De Jager, 2003). This caused deep erosion in the graben area, while the flanks continued to subside (Winstanley, 1993). The faults in the Roer Valley Graben were then reactivated as part of the Rhine Graben rift system during the Late Oligocene (Geluk et al., 1994; Deckers et al., 2023).

2.2.3 The Main Buntsandstein Subgroup

During the Early to Middle Triassic, the Roer Valley Graben was part of the Germanic Basin, a large endorheic basin located at the western margin of the Tethys domain (Geluk, 2005; Bachmann et al., 2010; Bourquin et al., 2011). The Germanic Basin extended from England in the west to the eastern border of Poland in the east, resulting in the widespread sedimentation of the Main Buntsandstein sediments across northern Europe (Geluk, 2005).

In the Dutch lithostratigraphic nomenclature, the Main Buntsandstein Subgroup is subdivided into three formations: the Volpriehausen, Detfurth, and Hardegsen Formations (Van Adrichem Boogaert and Kouwe, 1993). The Volpriehausen and Detfurth Formations represent each a sequence of sediments in which a basal fluvial/aeolian sandstone unit is overlain by a playa-lake claystone unit (Geluk and Röhling, 1997). In the Roer Valley Graben, these playa-lake claystone units are largely absent, and locally substituted by their time-equivalent basin-fringe sandstones (Van Adrichem Boogaert and Kouwe, 1993; Kortekaas et al., 2018). The Hardegsen Formation is instead characterized by an alternation of fluvial sandstone and claystone at the meter to tens-of-meter scales (Fig. 2.1b) (Van Adrichem Boogaert and Kouwe, 1993; Geluk and Röhling, 1997). Across northern European basins, the top of the Main Buntsandstein is often associated with the Hardegsen unconformity that locally truncates and erodes the Lower Triassic sediments (Linol et al., 2009; Pharaoh et al., 2010; Bourquin et al., 2011). However, this unconformity has not been observed in the Roer Valley Graben, where the Main Buntsandstein stratigraphy is reported to be entirely preserved (Geluk, 2005).

In the Roer Valley Graben, the sedimentation of the Main Buntsandstein Subgroup occurred through fluvial systems grading northwards into playa-lake deposits (Geluk, 2005). Sediments were supplied by source terrains over distances of 50-150 km from adjacent basin flanks (Mckie and Willems, 2009) and via major river systems over 200-400 km from remote catchment areas, which suggests substantial precipitation in the distant catchments (Audley-Charles, 1970; Mckie and Willems, 2009). Based on heavy mineral analysis, the London Brabant Massif located to the southwest represents an important source for the Main Buntsandstein sediments during the Early to Middle Triassic in the Germanic Basin (Olivarius et al., 2017). In parallel, the Armorican Massif in northeastern France and the Rhenish Massif in northwestern Germany are considered more distant sediment sources (Bourquin et al., 2009; Bachmann et al., 2010).

2.3 Data and Methods

2.3.1 The dataset

To conduct this study, thirty-five 2D seismic profiles, two 3D seismic surveys (L3CLY1992A_1 and L3NAM1988A-2), and data from 33 wells have been collected and analyzed (Fig. 2.2). In addition, other 2D vintage seismic profiles have been consulted when interpretation was uncertain or lateral variability needed to be assessed beyond the study area. 2D seismic lines make up a regional grid of the study area, while the 3D seismic volumes provide additional data in the area around Tilburg. Most of the data can be publicly downloaded through NLOG (www.nlog.nl), including the eleven regional 2D seismic lines acquired within the framework of the SCAN project (www.scanaardwarmte.nl). Eighteen reprocessed and six recently acquired 2D seismic lines have been made available for the study by Aardyn B.V.

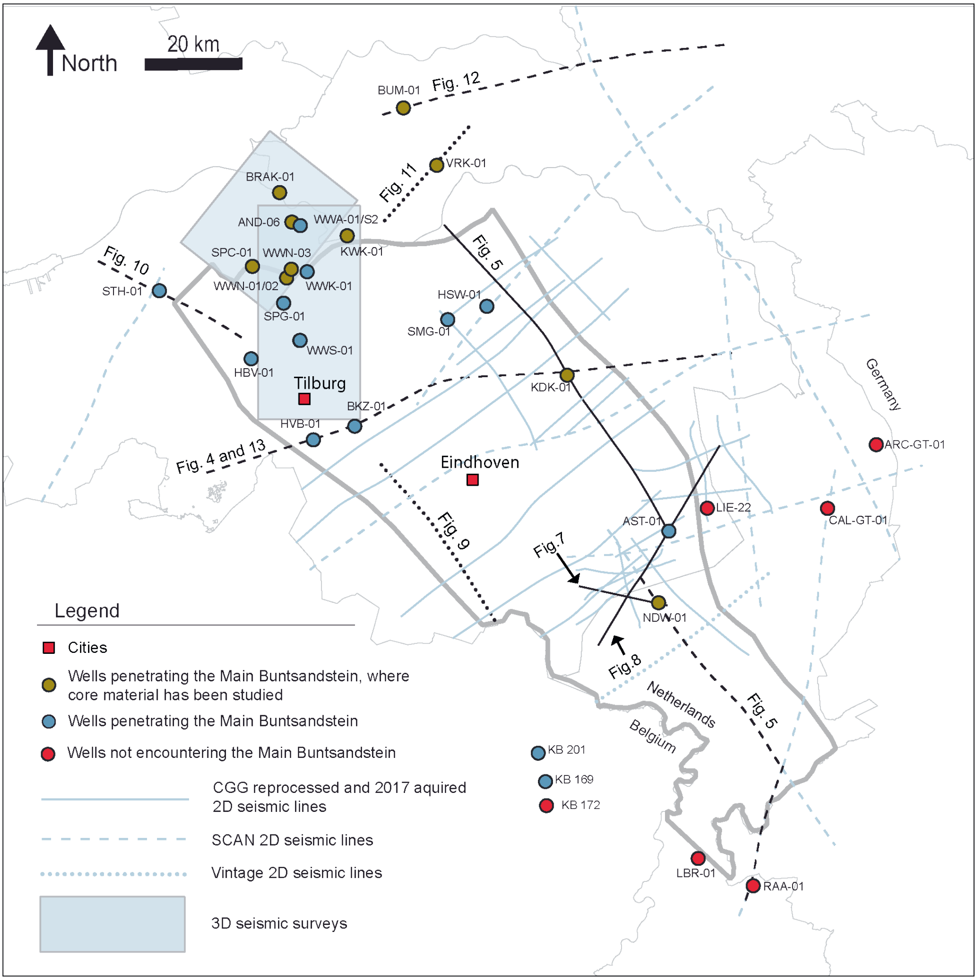

Figure 2.2. Overview of the data used for this study. The 2D seismic transects displayed are composed by SCAN lines, CGG reprocessed and 2D lines acquired in 2017. The lines in black correspond to the seismic lines interpreted and shown in this paper. The thick grey line represents the outline of the Roer Valley Graben (after Kombrink et al., 2012).

The seismic dataset was acquired through several campaigns by different operators, thus corrections in datum and seismic polarity convention were applied. Well data includes gamma-ray, density and sonic logs, checkshot data, mudlogs, cuttings, and core photos, which were mainly used to: i) determine the seismic response of the different horizons at well scale; ii) calculate time-to-depth relationships; iii) analyze lithologies. The well dataset also includes 3 wells from the Belgian side of the Roer Valley Graben (courtesy of VITO). The regional velocity model "VELMOD-2" was employed to convert the interpretations from time to depth domain. Input parameters for the VELMOD-2 include velocity data from the main lithostratigraphic units in the subsurface of the Netherlands. For more information on the velocity model see https://www.nlog.nl/en/velmod-2.

2.3.2 Wireline interpretation

Wireline logs were used to mark the boundary between the major lithological units present in the subsurface, allowing the identification of the principal horizons of interest for the study such as the top and the base of the Main Buntsandstein. First, the true stratigraphic thickness was determined at borehole scale by integrating well path surveys and structural dip obtained through seismic interpretation. To assess lithological changes within the Main Buntsandstein sequence, a gamma-ray cut-off was applied to separate shales from sands. The cut-off was chosen according to the grain sizes obtained through the analysis of core material from different wells in the study area (Fig. 2.2). By plotting the gamma-ray distribution of the cored interval, a clear bimodal distribution revealed the most appropriate value for the cut-off being 90 API. The cut-off application produces the first net sand thickness at well scale**.** The net sand thickness value was subsequently divided by the true stratigraphic gross thickness to estimate an average N/G ratio for the stratigraphic interval.

2.3.3 Seismic interpretation

The seismic interpretation was carried out in the Petrel software (www.software.slb.com). The SEG seismic polarity convention (Veeken and Moerkerken, 2013) was adopted to harmonize seismic input data, and a mis-tie analysis between seismic datasets was performed by applying a constant correction through cross-cutting seismic lines without changing the initial structure of the seismic data. Misfits were resolved manually by matching the Triassic reflectors at the expense of the shallower counterparts. Checkshot data were used where available to calibrate the sonic log and increase the accuracy in the seismic-to-well tie process. As part of the seismic-to-well tie, a synthetic seismogram was calculated to tie the horizons of interest to the seismic reflectors (Fig. 2.3).

Seismic interpretation was conducted by mapping horizons and faults to reveal the main stratigraphic architecture of the study area and the controls on the Main Buntsandstein depth and thickness. Horizons were interpreted based on ties with borehole data (Fig. 2.3). Once horizons were picked on the seismic line along the boreholes, the interpretation was extended to surrounding seismic lines. Fault timing was inferred from the identification of syn-sedimentary sequences, and the main deformation phases in the study area were reconstructed. Faults interpreted in multiple 2D lines and considered part of the same fault plane were grouped together in the same fault set and used for the computation of the geological surfaces. Fault planes and lithostratigraphic horizons from the Digital Geological Model (DGM-deep V5) were locally used as proxy to laterally extend the faults and horizons interpreted within this study. The DGM data are publicly available and can be downloaded from www.nlog.nl. The horizons mapped as the top and the base of the Main Buntsandstein were then used to build structural depth maps deploying Petrel’s convergent interpolation algorithm. This algorithm estimates values at locations within the data point neighbourhood based on the known values at the data points until convergence is reached. These maps were subsequently used as a trend map in combination with well data to construct maps of the Main Buntsandstein total thickness, sandstone thickness, and N/G.

The geological complexity of the subsurface and the presence of strong reflectors like those associated with the Posidonia Shale and the Chalk Group overlying the Lower Triassic sediments locally absorb, backscatter and reduce the amount of energy transmitted to deeper layers. Thus, a study of the reflection geometries, such as the amplitude, configuration, continuity, and terminations of the Main Buntsandstein reflectors was conducted near well locations by extrapolating information of the rock units from the wellbore. This was done to assess the spatial variation in lithologies and large-scale sedimentary structures.

2.3.4 2D palinspastic restoration

A 2D palinspastic restoration study was performed for 6 seismic transects in the Roer Valley Graben using the software MOVE (www.petex.com) in order to: i) investigate the deformation and burial history of the Main Buntsandstein; ii) reconstruct the basin geometry during the Early to Middle Triassic. Before restoring, each section was prepared by manually smoothing all the interpreted seismic horizons and removing faults without visible offset to avoid artifact occurrences during the restoration. Additionally, a line-length balancing method was performed to validate the quality of the seismic interpretation. The approach assumes that horizon lengths do not change between deformed (present-day) and restored horizon lengths (Suppe, 1985; Lingrey and Vidal-Royo, 2016).

No effect of the Hardegsen unconformity on the lower Triassic sediments was observed in the seismic data. Therefore, seismic facies representing sediments of the Main Buntsandstein were grouped with seismic facies representing sediments of the Upper Germanic Trias Group (Solling, Röt, Muschelkalk and Keuper Formations). Furthermore, for simplicity, we assumed that the erosion related to the Mid- to Late Kimmerian tectonic phases occurred once the Schieland Group was deposited, as detailed reconstructions of the tectonostratigraphic history of the Altena and Schieland Groups go beyond the scope of this paper.

During the restoration, horizon reconstructions were performed for the lithostratigraphic units eroded during Mesozoic tectonic events. The lithostratigraphic units that were reconstructed are: Chalk Group, Schieland Group, Altena Group, Germanic Trias Group, and the Permian units. The thickness of the individual lithostratigraphic units mapped in the area and available erosion maps (Nelskamp and Verweij, 2012) were used as a proxy for horizon reconstructions.

The first step of the restoration process consists in removing the youngest sedimentary layer and decompact the units underneath. Decompaction in MOVE accounts for isostatic changes and uses a compaction curve that assumes constant values of porosity and lithology assigned to each sedimentary layer. Lithologies for each lithostratigraphic unit were chosen following Van Adrichem Boogaert and Kouwe (1993). Average porosity values were taken from www.ThermoGIS.nl. Once the youngest layer was removed, the effect of faults was removed and the top of the model was unfolded to a reference datum. The datum depends on the topography/bathymetry at the time of deposition of each sedimentary unit (Van Adrichem Boogaert and Kouwe, 1993; Nelskamp and Verweij, 2012). The restored horizons were finally used to create a map of the restored base of the Main Buntsandstein Subgroup, which helped assess the Early to Middle Triassic basin geometry.

2.4 Results

2.4.1 Interpreted horizons

In total, 10 horizons corresponding to stratigraphic group and formation boundaries were interpreted in seismic data across the Roer Valley Graben (Fig. 2.3). The horizons were named after the stratigraphic nomenclature used in the Netherlands (TNO-GDN, 2023) and the corresponding codes were selected to logically represent the full names of the horizons interpreted. For the Triassic horizons, the adjective “near” was added to the horizon names when their interpretation was uncertain. The uncertainties were caused by the low impedance contrast between reflectors and poor resolution of the seismic profiles at depths starting from below 2 km.

The shallowest interpreted horizons represent the bases of the Upper North Sea Group (BUNS) and Lower North Sea Group (BLNS). The boundary between the North Sea Supergroup and the underlying Chalk Group is generally sharp as a result of a change in lithology from the sandstones of the Lower North Sea Group to the carbonates of the Chalk Group. This produces a strong acoustic impedance contrast between the two units.

The carbonate rocks from the Chalk Group unconformably overly sediments ranging from Early Cretaceous (Berriasian) to Carboniferous in age. This regional angular unconformity is referred to in this study as the base Chalk Group unconformity (BCGU). In the southeastern part of the Netherlands, the base Chalk Group corresponds to the base of the Oploo or younger formations as the Texel Formation is largely absent (TNO-GDN, 2023).

Below the base Chalk Group unconformity, a sequence of high amplitude reflectors corresponds to the clastic deposits of the Schieland Group of which the base is separately mapped as the base Schieland Group (BS). The Schieland Group is only present in the northwest part of the Roer Valley Graben. The next high amplitude reflector is interpreted as the organic-rich Posidonia Shale (PS) showing a sharp density and velocity contrast with the overlying units. This horizon is present only in the central parts of the Roer Valley Graben, where it is used as reference to locate the underlying Triassic units.

The upper part of the Triassic units is characterized by a package of high amplitude reflectors, reflecting acoustic impedance contrasts likely associated with anhydrite claystones of the Keuper Formation and argillaceous dolomites and limestones of the Muschelkalk Formation. The top of this package has been labeled as the top Triassic (TT), while the base has been interpreted as the near base Lower Muschelkalk (NBLM). The near top and base of the Main Buntsandstein Subgroup (NTMB and NBMB, respectively) are usually characterized by weak reflections, reflecting the lack of a sharp density and velocity contrast with the overlying and underlying units. A detailed analysis of the Main Buntsandstein reflections is provided later in the text.

Below the Triassic horizons, a prominent angular unconformity is interpreted to represent the base Permian unconformity (BPU), separating Permian from Carboniferous sediments. In the southeastern termination of the Roer Valley Graben (e.g. well RAA-01 in Fig. 2.2), Permian deposits are absent, and consequently, the Triassic succession directly overlies Carboniferous deposits.

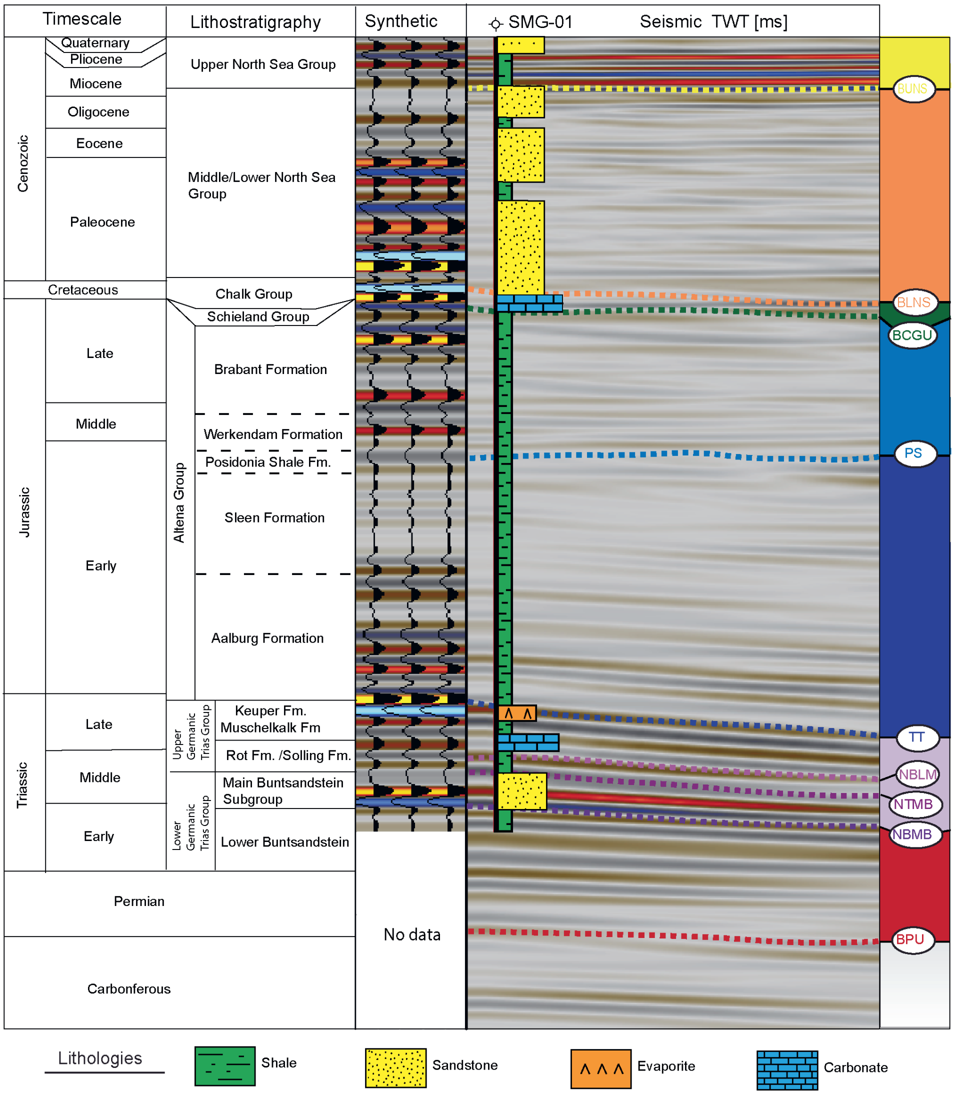

Figure 2.3. Seismic stratigraphy of the Roer Valley Graben. Lithological column after Van Adrichem Boogaert et al. (1993). The synthetic seismogram has been generated for well SMG-01 using a zero phase Ricker 25 Hz wavelet with length of 128 ms. The synthetic is tied to the reprocessed seismic line 81-08. See location of the well in Figure 2.2.

2.4.2 Seismic mapping

Two transects are shown to illustrate the architecture of the Roer Valley Graben and the Main Buntsandstein Subgroup distribution across the area. The first is oriented WSW-ENE (Fig. 2.4) and roughly perpendicular to the main trend of faults in the Roer Valley Graben; the second one is oriented SE-NW (Fig. 2.5) and semi-parallel to the Roer Valley Graben axis. Both transects will be described in more detail below.

2.4.2.1 Semi-perpendicular to the graben axis section

The preservation of the Main Buntsandstein sediments in the Roer Valley Graben is delimited by a series of normal faults separating the Roer Valley Graben from the adjacent highs, the Zeeland High and the Peel-Maasbommel Complex (e.g. F14 and F2 in Fig. 2.4). Beyond these faults, the Main Buntsandstein sediments are truncated at the base Chalk Group unconformity (Fig 2.4b). The Main Buntsandstein reflector package displays a sheet-like external shape, with reflector configuration changing from parallel/sub-parallel to chaotic from WSW to ENE (Fig. 2.4c).

The Main Buntsandstein is encountered at its greatest depths in the central part of the Roer Valley Graben. Here, depths of 4 km are locally exceeded and reflectors appear semi-horizontal (Fig. 2.4b and c). Towards the flanks, the Main Buntsandstein sediments are shallowing up to just below 1 km (Fig. 2.4a) and dip basinwards as a result of faulting and tilting (Fig. 2.4c). Along both flanks of the Roer Valley Graben, two sub-basin structures are present (Fig. 2.4c). These two structures are bounded by normal faults labeled F2 and F6 for sub-basin 1 and F12 and F13 for sub-basin 2. These sub-basins define areas where the Main Buntsandstein Subgroup is present around 100 to 500 m deeper than in the adjacent blocks (Fig. 2.4c).

Several faults are recognized along the WSW-ENE seismic section, mostly with a normal slip character. The faults bounding the Roer Valley Graben have the largest vertical offset, displacing the Main Buntsandstein sediments by ~700-800 m (e.g. F2 and F13 in Fig. 2.4) and laterally juxtapose Triassic to Jurassic and Carboniferous units. These faults affect the lateral continuity of the Triassic units, reducing the lateral extent of the Main Buntsandstein sediments locally to less than 2 km in certain areas along the section strike (Fig. 2.4c). These large boundary faults separate the Roer Valley Graben from the adjacent platform areas, where the Main Buntsandstein sediments are found at depths of 1000-1500 m and are locally truncated at the base Chalk Group unconformity (Fig. 2.4c).

Overall, the Main Buntsandstein Subgroup thickens southwestwards, where the wells BKZ-01 and HVB-01 record thicknesses of 250 m. This thickening is locally enhanced by the presence of syn-sedimentary fault activity (e.g. F7 in Fig. 2.4b). In the central part of the Roer Valley Graben, four more syn-sedimentary faults have been interpreted where the Buntsandstein sediments display a change in thickness in the order of tens of meters across the fault plane (Fig. 2.4c).

Small reverse faults occur within the two sub-basin structures displacing the overlying Jurassic horizons of ~30-40 m (e.g. F5, F7 and F9 in Fig. 2.4b). Further to the north, reverse faults are instead cross-cutting the Triassic units and reducing their lateral extent (Fig. 2.11). No faults have been mapped below the Base Permian unconformity due to the low seismic resolution of these deeper strata. As a consequence, the continuation of faults at depths greater than 2 to 3 km is uncertain and marked with a dashed line in the figures.

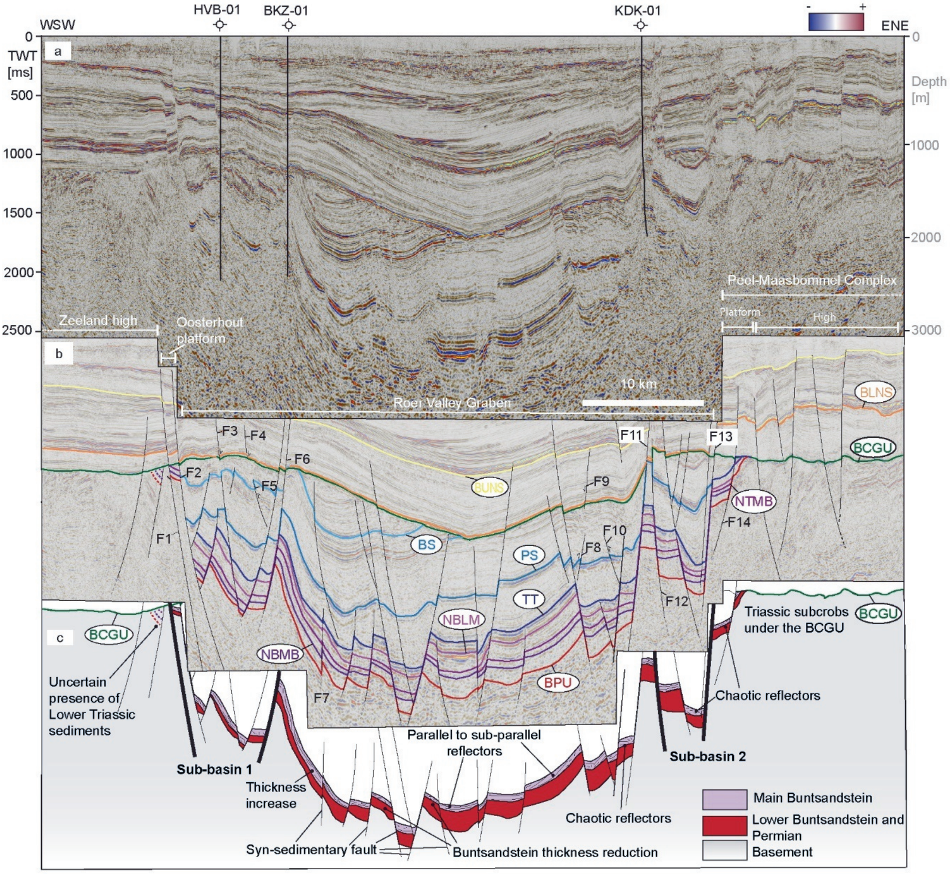

Figure 2.4. Un-interpreted (a) and interpreted (b–c) seismic section EBN017-EBN018. The horizon colours refer to specific stratigraphic units (see Fig. 3). Only the main faults are interpreted in the section. Some of these faults have been numbered to refer to in the text. See Fig. 2.2 to see location of the seismic section.

2.4.2.2 Semi-parallel to the graben axis section

In the southeastern part of the Roer Valley Graben, the Main Buntsandstein reflectors are mostly continuous at km-scale, with a dominant parallel/sub-parallel configuration. Nevertheless, reflectors lose continuity in an area where the configuration changes from parallel/sub-parallel to chaotic and Mesozoic deposits could not be mapped (Fig. 2.5c). An absence of wells in that area prevent to discern whether that is a structural high, where Mesozoic sediments have not been deposited or preserved, or it is a large fault shadow that creates these seemingly chaotic reflections (Fig. 2.5c).

To the northwest, detailed mapping of the Main Buntsandstein was not possible due to a low resolution of the seismic data below 1500 m and a larger number of faults compared to the southern part of the seismic section (Fig. 2.5c). Nonetheless, the configuration of reflectors below the top Triassic in the northwestern area appears to be more chaotic and their overall continuity being reduced by faulting with respect to the southeastern part of the Roer Valley Graben.

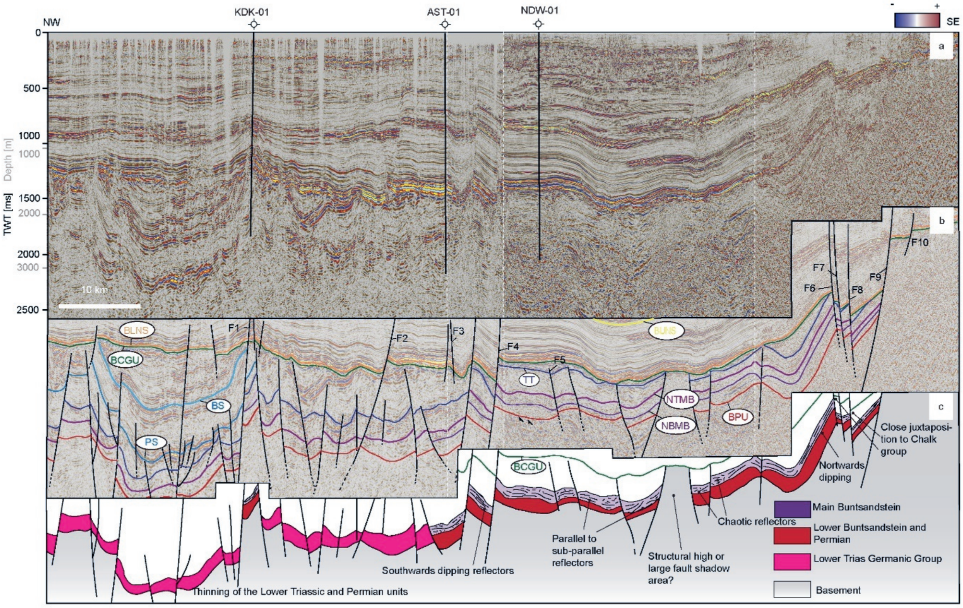

Figure 2.5. Un-interpreted (a) and interpreted (b–c) composite line partially along the basin axis realized merging together the following transects: EBN031, EBN030, 80-3 and 81-17. Colours refer to specific stratigraphic units (see Fig. 3). The seismic imaging in the left part of the transect is of poor quality, thus the interpretation of the Main Buntsandstein was not always possible. For the location of the composite line see Fig. 2.2.

Overall, the Main Buntsandstein Subgroup sediments are present at depths below 2 km in the southeastern part of the Roer Valley Graben, while they reach 3.5-4 km near the graben axis (Fig 2.5c). In the southeastern part of the Roer Valley Graben, a 50-100 m succession of Jurassic units separates the Triassic sediments from the overlying base Chalk Group unconformity (Fig. 2.5b and c). Locally, normal faulting juxtaposes the Main Buntsandstein to the upper Triassic, Jurassic and Carboniferous units, as exemplified by F4, F5, and F7 in Figure 2.5c. To the southeast, a series of normal faults displace sediments up to Cenozoic in age (e.g. F4 and F8 in Fig. 2.5b). These faults represent the furthest southeastern margin of the Roer Valley Graben and yield normal displacements of up to 200-300 m.

2.4.3 Main Buntsandstein depth and gross thickness maps

The depth map of the near base Main Buntsandstein is caonstructed by integrating data from all wells and interpreted seismic profiles. The map shows that the base of the Main Buntsandstein deepens from the flanks to the center of the Roer Valley Graben (Fig. 2.6a). To the northeast of Tilburg, the base of the Buntsandstein locally reaches depths of ~4 km (Fig. 2.6a). In the southeastern part of Roer Valley Graben, the base of the Main Buntsandstein shallows up to 2-3 km. In the platform areas that separate the Roer Valley Graben from the adjacent highs where the Buntsandstein is absent, the depth of the Main Buntsandstein is generally found between 1 and 2 km (Fig. 2.6a). These areas have a width from ~1 to 15 km

(Fig. 2.6a). To the southeast, the Roer Valley Graben is narrower (~ 27 km) compared to the northern part (~ 45 km), which reflects a reduction of the area where the Main Buntsandstein sediments are preserved (Fig. 2.6b; see also Appendix Fig.S2).

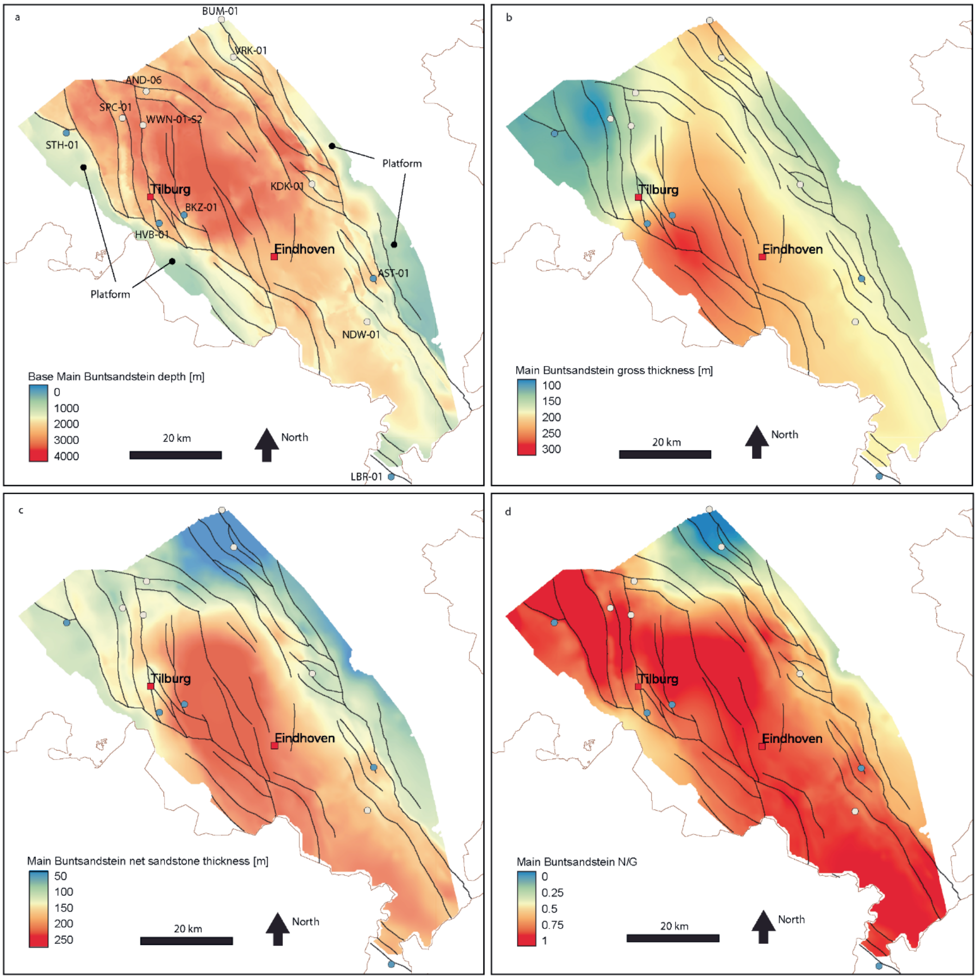

Figure 2.6. a) Structural depth in meters of the near base Main Buntsandstein. b) Gross thickness in meters of the Main Buntsandstein. c) Net sandstone thickness in meters for the Main Buntsandstein. d) Net to gross ratio. Black continuous lines represent faults mapped after TNO Digital Geological Model (https://www.dinoloket.nl/en/the-digital-geological-model-dgm).

The thickest preserved Main Buntsandstein succession, called Main Buntsandstein gross thickness in Figure 2.6b, is located between the cities of Tilburg and Eindhoven, where the thickness locally reaches values up to 300 m (Fig. 2.6b). In this area, thickness variations across fault planes indicate syn-sedimentary fault activity (e.g. F7 in Fig. 2.4). The thickness decreases to the northwest, where well STH-01 records a thickness of ~125 m for the whole Main

Buntsandstein. This well is located in the Oosterhout Platform, where the Main Buntsandstein occurs shallower at depths of ~ 1000-1500 m (Fig. 2.6a). The Main Buntsandstein overall thins towards the northern flank of the Roer Valley Graben where thicknesses of 100-150 m are recorded. In the southeastern part of the Roer Valley Graben, the Main Buntsandstein Subgroup thickness reaches values over 200 m. However, the presence of only two wells penetrating the Main Buntsandstein in this part of the study area makes the thickness quantification more uncertain.

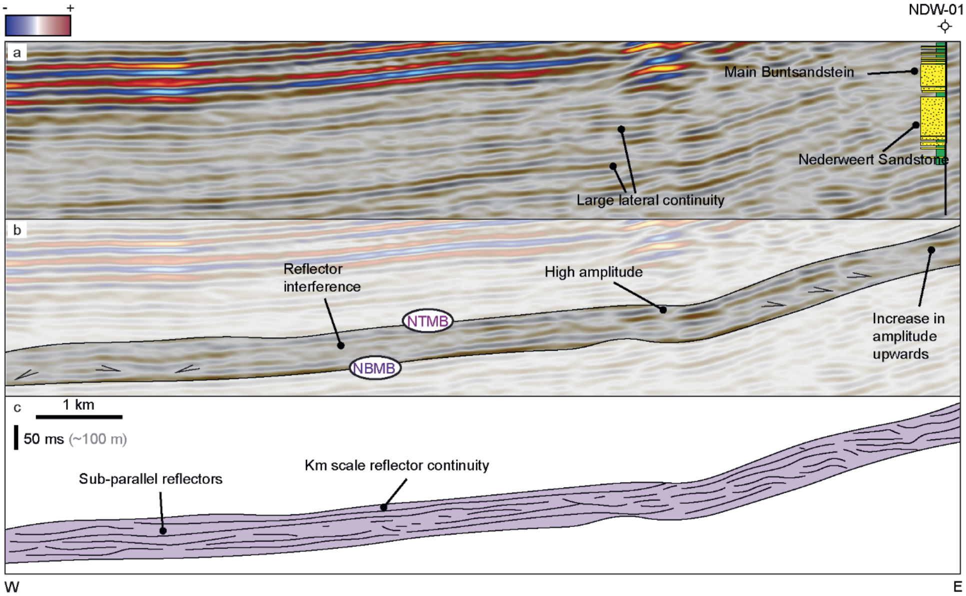

Figure 2.7. Uninterpreted (a) and interpreted (b–c) 2D seismic profile 82-11 (see location on Fig. 2.2) showing the main geometries in the Main Buntsandstein observed around NDW-01. A schematic lithological log is displayed along the well track of NDW-01, where sandstone intervals are coloured in yellow and claystone intervals in green. The sandstone units below the Main Buntsandstein are classified as the Nederweert Sandstone

2.4.4 Main Buntsandstein reflector characterization

From south to north, the Main Buntsandstein Subgroup reflectors show variations in amplitude, frequency, and wavelet geometries. The change in reflector character is illustrated through six seismic profiles, three located south of the city of Eindhoven (Fig. 2.7, 2.8 and 2.9) and three located in the area north of Eindhoven (Fig. 2.10, 2.11, and 2.12).

2.4.4.1 Southern area

In the southeastern part of the study area, the top and base of the Main Buntsandstein are laterally continuous, marked by low amplitude reflectors that can be correlated for over 5 km (Fig. 2.7a). Such continuity results in a sheet-like external shape without major lateral variation in thickness. Around NDW-01, top and base Main Buntsandstein continuity is interrupted by faults (e.g. F5 in Fig. 2.5). Internally, reflectors display a parallel to subparallel configuration with overall low amplitudes and minor frequency variation (Fig. 2.7b and c). Reflectors are mostly parallel; nonetheless, downlap terminations have been mapped (Fig. 2.7b). Local increases in reflector amplitudes at the top of the Main Buntsandstein units seem to represent velocity contrasts as a result of changes in lithology and bed thickness from the lower to the upper part of the Main Buntsandstein, as exemplified by the lithological log in NDW-01 (Fig. 2.7a and b).

Moving towards the northern flank of the Roer Valley Graben, the geometry of the reflectors becomes more heterogeneous, with configurations alternating between parallel to sub-parallel and chaotic, toplap terminations and variable amplitudes (Fig. 2.8c and 2.5). The reflector at the base of the Main Buntsandstein sequence remains continuous over 5-6 km, while the reflector at the top becomes more discontinuous with higher amplitudes and frequencies.

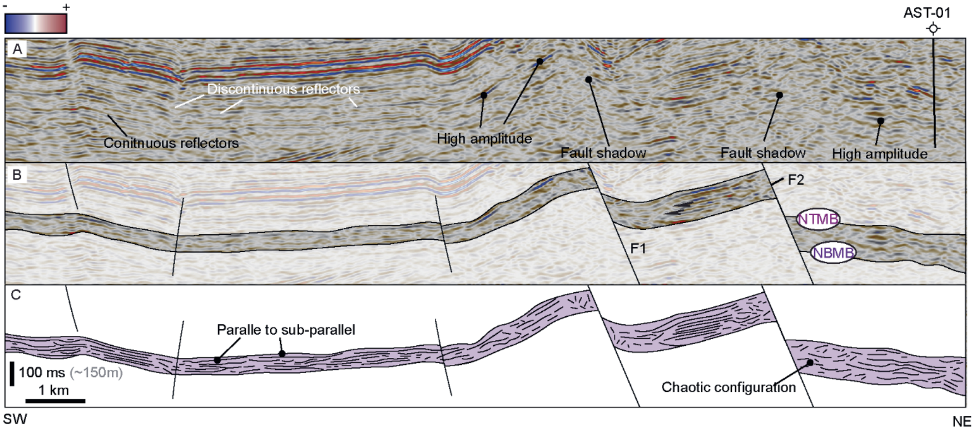

Figure 2.8. Un-interpreted (a) and interpreted (b–c) 2D seismic profile 80-03 (see location on Fig. 2.2) showing the main geometries in the Main Buntsandstein observed around AST-01. See text for detail description of the seismic profile.

Along the southwestern flank of the Roer Valley Graben, the top of the Main Buntsandstein is marked by a high amplitude reflector that is continuous at km scale and locally disrupted by the presence of small normal faults (Fig. 2.9 a and b). The base of the Main Buntsandstein has lower amplitude reflectors that are continuous at km scale. Internally, the Main Buntsandstein reflector geometry changes from prograding downlapping reflections to chaotic and parallel/sub-parallel (Fig. 2.9c). The prograding reflectors form a package approximately 100 m thick and about 1 km wide before pinching out to the northwest (Fig. 2.9c). To the southeast, chaotic reflectors are observed as infilling on a slope-like geometry. Internal, parallel to sub-parallel reflectors are aggrading, losing continuity over 1-2 km.

2.4.4.2 Northern area

In the northwestern part of the Roer Valley Graben, the top and base of the Main Buntsandstein are marked by discontinuous low-amplitude reflectors (Fig. 2.10a). In the Oosterhout Platform, high-amplitude reflectors at the base and the top of the Main Buntsandstein seem to reflect a decrease in N/G, as exemplified by the lithological log of well STH-01. Overall, the lateral continuity of the Main Buntsandstein reflectors is reduced to less than 1 km. These reflectors display parallel to sub-parallel configurations and less frequently more chaotic configurations (Fig. 2.10c). To the northwest, the Main Buntsandstein reflectors subcrop beneath the base Chalk unconformity, where upper Triassic and Jurassic sediments are not preserved.

Towards the north, the area around well VRK-01 is dominated by chaotic reflections with low to medium amplitudes (Fig. 2.11c). Combining the lithological information from VRK-01 with the geometry of the observed reflectors, chaotic reflections are likely to be the product of fine-grained clastic sediments with occasional conglomeratic deposits as observed in the core pictures of VRK-01 (www.nlog.nl).

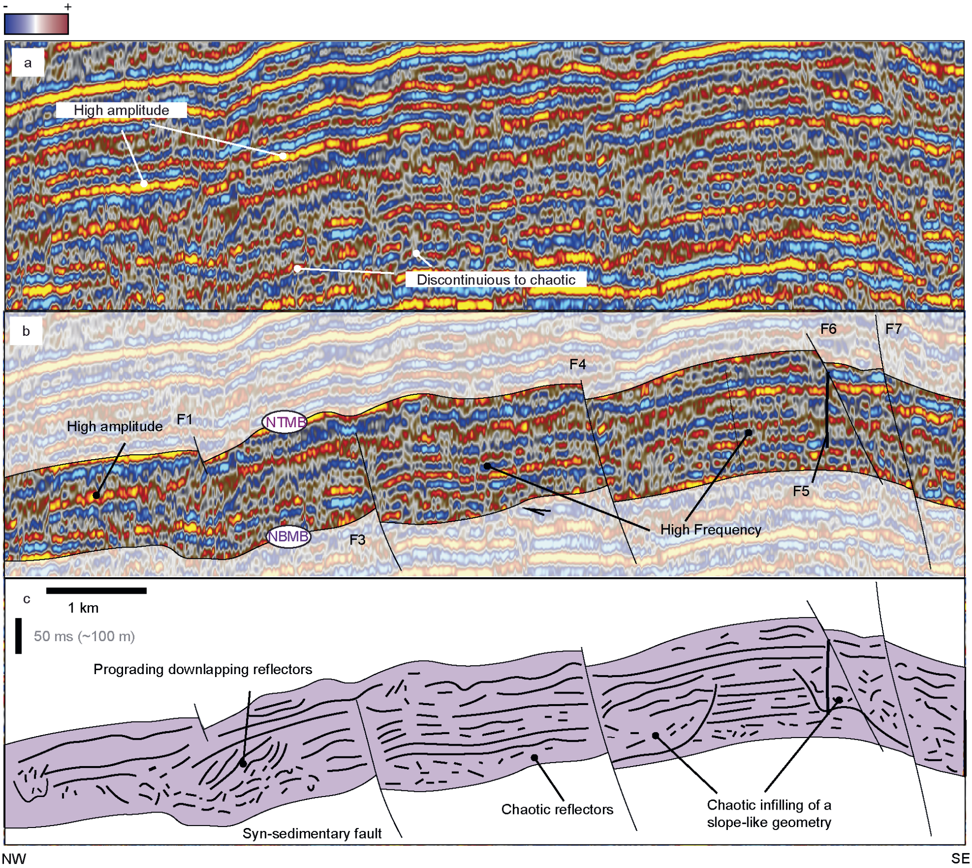

Figure 2. 9. Un-interpreted (a) and interpreted (b–c) 2D seismic profile 81-12 (see location on Fig. 2.2) showing the main geometries in the Main Buntsandstein along the southwestern margin of the study area. See text for detail description of the seismic profile.

Further to the north, reflections near well BUM-01 are characterized by overall high frequencies and amplitudes, likely reflecting the alteration of sandstones and claystones in the lithological log (Fig. 2.12a). Unfortunately, the presence of a fault shadow zone in the footwall of F2 does not allow a direct tie between the seismic reflectors and the well (Fig. 2.12a and b). In the hanging wall, the top of the Main Buntsandstein is marked by a high amplitude reflector of which the continuity is laterally interrupted by the presence of faulting (F1 and F2 in Fig. 2.12b). Conversely, the base is marked by a chaotic reflection configuration.

2.4.5 Net sandstone thickness and N/G maps

Net sandstone thickness and net-to-gross (N/G) maps display the distribution of the Main Buntsandstein across the Roer Valley Graben and its immediate surroundings. The thickest sandstone sequences have been deposited in the central and southeastern part of the study area, with local maxima up to 250 m in between the cities of Tilburg and Eindhoven (Fig. 2.6c). In this area, reflectors are mostly continuous at km-scale, with an overall low amplitude indicating rather homogeneous lithologies. The northern part of the study area is dominated instead by the deposition of fine-grained sediments and displays a net sandstone thickness of locally less than 50 m. This trend is best displayed by a decrease in N/G from south to north, where the area around wells BUM-01 and VRK-01 show the highest percentages of fine materials (Fig. 2.6d). Along with this fining trend, the seismic reflection character shows a decrease in reflector continuity and increase in amplitudes northwards while also chaotic configurations become more dominant compared to parallel or subparallel configurations. To the northwest, the net sandstone thickness decreases to 100 m around well STH-01, while the N/G is still above 0.75.

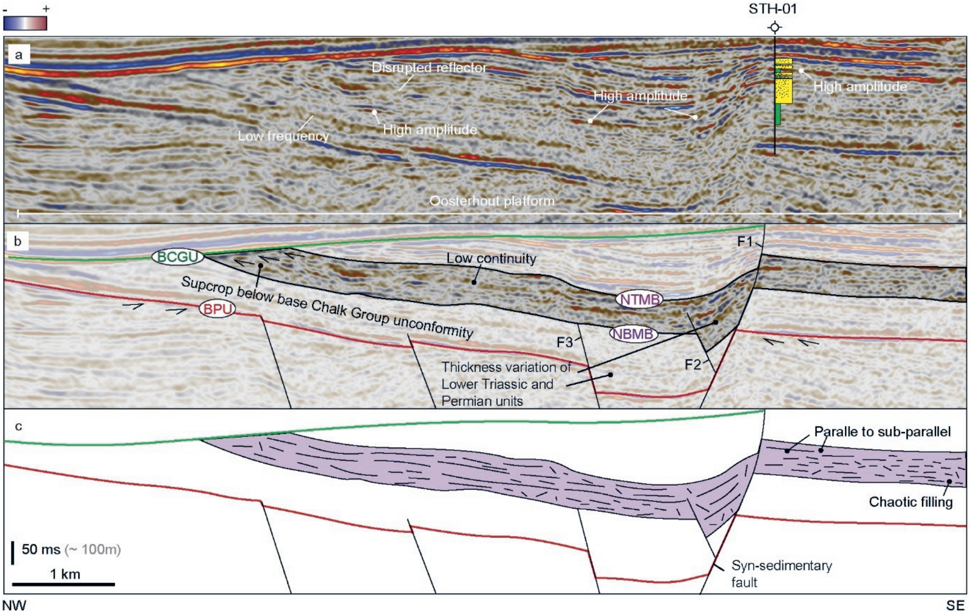

Figure 2.10. Un-interpreted (a) and interpreted (b–c) 2D seismic profile EBN033 (see location on Fig. 2.2) showing the main geometries in the Main Buntsandstein around STH-01. A schematic lithological log is displayed along the well track of STH-01, where sandstone intervals are coloured in yellow and claystone intervals in green

2.4.6 Sequential restoration

The deformation and burial history of the Main Buntsandstein Subgroup in the Roer Valley Graben and adjacent areas can be split into four main stages: i) Main Buntsandstein deposition and initial burial during an extensional regime characterized by the normal faulting throughout the Triassic and the Middle Jurassic (Fig. 2.13 g and f); ii) a Late Jurassic to Early Cretaceous local uplift, truncation and erosion responsible for the absence of the Main Buntsandstein on the Roer Valley Graben flanks (Fig. 2.13 e); iii) uplift of the central parts of the Roer Valley Graben and subsidence of its flanks during the Late Cretaceous basin inversion (Fig. 2.13d and e); iv) a second phase of extension and sedimentation of Cenozoic sediments in the Roer Valley Graben and to limited extent on its flanks (Fig. 2.13a, b and c).

The restored section indicates that there is a thickening of the middle to upper Triassic units to the southwest (Fig. 2.13g). This is caused by syn-sedimentary faulting in this part of the Roer Valley Graben (Fig. 2.4c). After deposition, the Main Buntsandstein sediments were continuously buried until Jurassic times. Once the marine Altena and terrestrial Schieland Groups were deposited, the base of the Main Buntsandstein Subgroup was buried down to ~3-3.5 km in the central parts of the Roer Valley Graben (Fig. 2.13g). This burial depth decreased down to ~2.5 km towards the southern flank of the Roer Valley Graben (Fig. 2.13g), where a thinner Jurassic sequence with a thickness of ~ 2 km was likely being deposited.

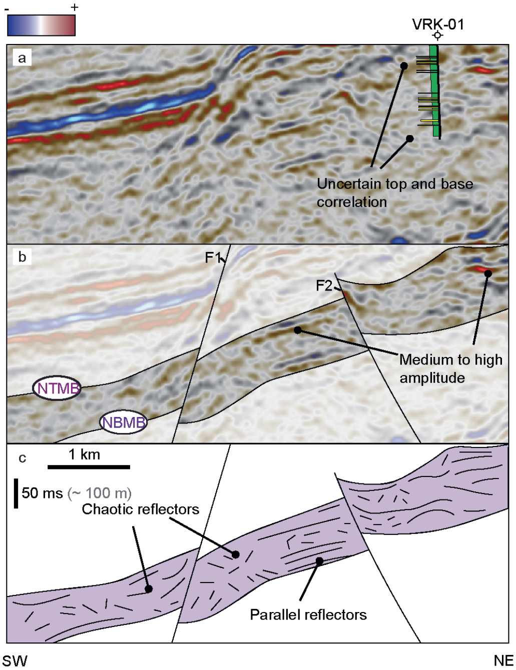

Figure 2.11. Un-interpreted (a) and interpreted (b–c) 2D seismic profile 872104 (see location on Fig. 2.2) showing the main geometries in the Main Buntsandstein around VRK-01. A schematic lithological log is displayed along the well track of VRK-01, where sandstone intervals are coloured in yellow and claystone intervals in green.

During Late Jurassic to Early Cretaceous times, the Roer Valley Graben flanks were affected by widespread uplift and erosion, which largely removed the Jurassic, Triassic, and Permian units, especially in the Peel Complex, Zeeland High, and Oosterhout Platform (Fig. 2.13 f). The uplift and erosion were likely driven by the activity of the large faults that bound the Roer Valley Graben (e.g. F2 and F13 in Fig. 2.4b). In parallel, fault movements within the Roer Valley Graben produced a horst and graben geometry, with the development of sub-basin structures (e.g. sub-basins 1 and 2 in Fig. 2.4). At this stage, the Main Buntsandstein sediments were buried at depths ranging between ~2 and 3.5 km in the central part of the Roer Valley Graben (Fig. 2.13e). The burial depths gently decreased across the areas adjacent to the Roer Valley Graben, where the Main Buntsandstein sediments were encountered closer to the surface as result of uplift and erosion of the overlying Jurassic and Cretaceous units (Fig. 2.13 e and Fig. S4d in the Appendix).

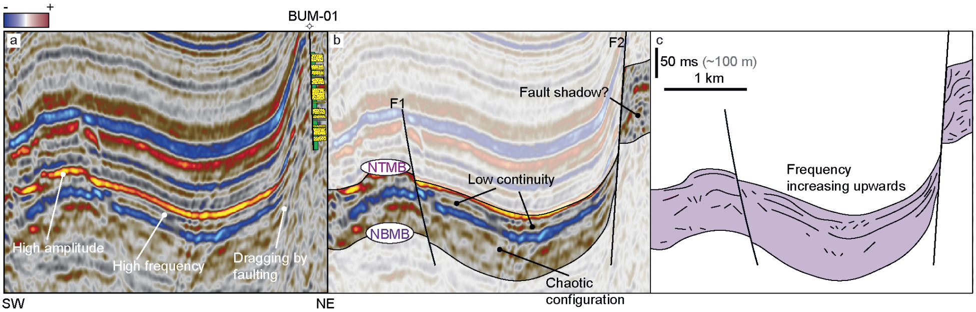

Figure 2.12. Un-interpreted (a) and interpreted (b–c) 2D seismic profile EBN003 (see location on Fig. 2.2) showing the main geometries in the Main Buntsandstein around BUM-01. A schematic lithological log is displayed along the well track of BUM-01, where sandstone intervals are coloured in yellow and claystone intervals in green

Subsequently, a sequence of Chalk was deposited across the Roer Valley Graben area on top of Lower Cretaceous or older sediments, developing an angular unconformity that is referred to in this work as the base Chalk Group unconformity (Fig. 2.3). Sediments from the Chalk Group are thinner in the Roer Valley Graben compared to the adjacent platforms and highs. This is caused by the inversion of some of the faults along the flanks of the Roer Valley Graben during and after the deposition of the Chalk Group. The inversion of these faults resulted in the uplift and the widespread erosion of Chalk sediments in the graben area. In contrast, the Chalk sediments were preserved along the flanks, which continued to subside at this time. The inverted faults display normal offset in the lowermost tracts, while they show reverse displacement in the upper portion of the fault, a diagnostic feature of fault inversion (Williams et al., 1989). The inversion seems also to propagate across the Lower North Sea Group (Fig. 2.13 c).

The last burial phase lasts until present-day, and the sediment infill causes the base of the Main Buntsandstein to be buried locally below 4 km (Fig. 2.13 a and b). During this phase, the Roer Valley Graben represents the main subsiding area where ~ 1500 m of North Sea Supergroup sediments have been deposited, while a thinner sequence (500-1000 m) of North Sea Supergroup sediments is present in the blocks adjacent to the Roer Valley Graben.

2.5 Discussion

2.5.1 Structural evolution of the Roer Valley Graben

The presence of syn-sedimentary faults producing thickness variation in the Main Buntsandstein sediments (e.g. F1 and F2 Fig. 2.10b) indicates that the Roer Valley Graben was tectonically active during Early to Middle Triassic times. These faults have a normal component and oriented ~NW-SE, producing depocenters for sedimentation on their hanging walls. The Main Buntsandstein Subgroup is thus interpreted to represent a syn-rift sequence, where the thickness of the syn-rift infill increases in the area around Eindhoven and southeast of Tilburg. The syn-sedimentary faults observed in the Roer Valley Graben could be related to larger NW-SE fault complexes along the northern margin of the London-Brabant Massif that were active during Early to Middle Triassic times (Geluk, 2005). This rift developed contemporaneous with the Permo-Triassic rifting stage affecting the North Sea area (Fossen et al., 2021). The lack of internal unconformities within the Triassic sediments in the seismic interpretations supports the absence of the Hardegsen unconformity in graben systems such as the Roer Valley Graben (Mckie, 2011).

During Jurassic to Early Cretaceous times, our palinspastic restoration shows that the Main Buntsandstein sediments have been buried up to 3.5 km depth in the central part of the Roer Valley Graben in response to regional extensional tectonics (Ziegler, 1992; Geluk et al., 2007). The present-day occurrence of the Altena and Schieland Group sediments in the central part of the basin and their partial absence in the adjacent platforms and highs indicate that these blocks were subjected to different degrees of subsidence. During Jurassic times, the Main Buntsandstein experienced a shallower burial depth (~ 2-2.5 km) in the southern platform areas compared to the deeper burial depths experienced by the Main Buntsandstein sediments in the blocks located in the central graben areas (e.g. Fig. 2.13f; see also Appendix Fig. S4e).

Carter et al. (1990) indicate the Main Buntsandstein reached maximum burial depths of ~ 2.5 km during the Jurassic, in the wells located in the northern part of the Roer Valley Graben. In this work, we assume that the Altena and Schieland Groups were largely deposited across the Roer Valley Graben and on the adjacent platforms and highs. However, our horizon reconstruction was performed based on the thicknesses observed in the central parts of Roer Valley Graben, where Jurassic sediments are preserved and thickest. This assumption may have resulted in an overestimation of the burial depths of the Triassic in areas where, instead, a thinner Jurassic sedimentary sequence was deposited (Fig. 2.13 f).

The sediments in the Roer Valley Graben were subsequently eroded during the Middle to Late Jurassic in response to the Mid- to Late-Kimmerian tectonic phases that caused the formation of a series of faults responsible for the creation of sub-graben systems within the Roer Valley Graben (e.g. sub basins 1 and 2 in Fig. 2.4) and the uplift of the adjacent block terrains (Vercouter and Van de Haute, 1993; NITG, 2004; Deckers et al., 2023). This uplift resulted in the deep truncation and erosion of Mesozoic sediments across the Roer Valley Graben flanks and the development of areas where Triassic sediments are now truncated at the base Chalk Group unconformity (Fig 2.4 and 5).

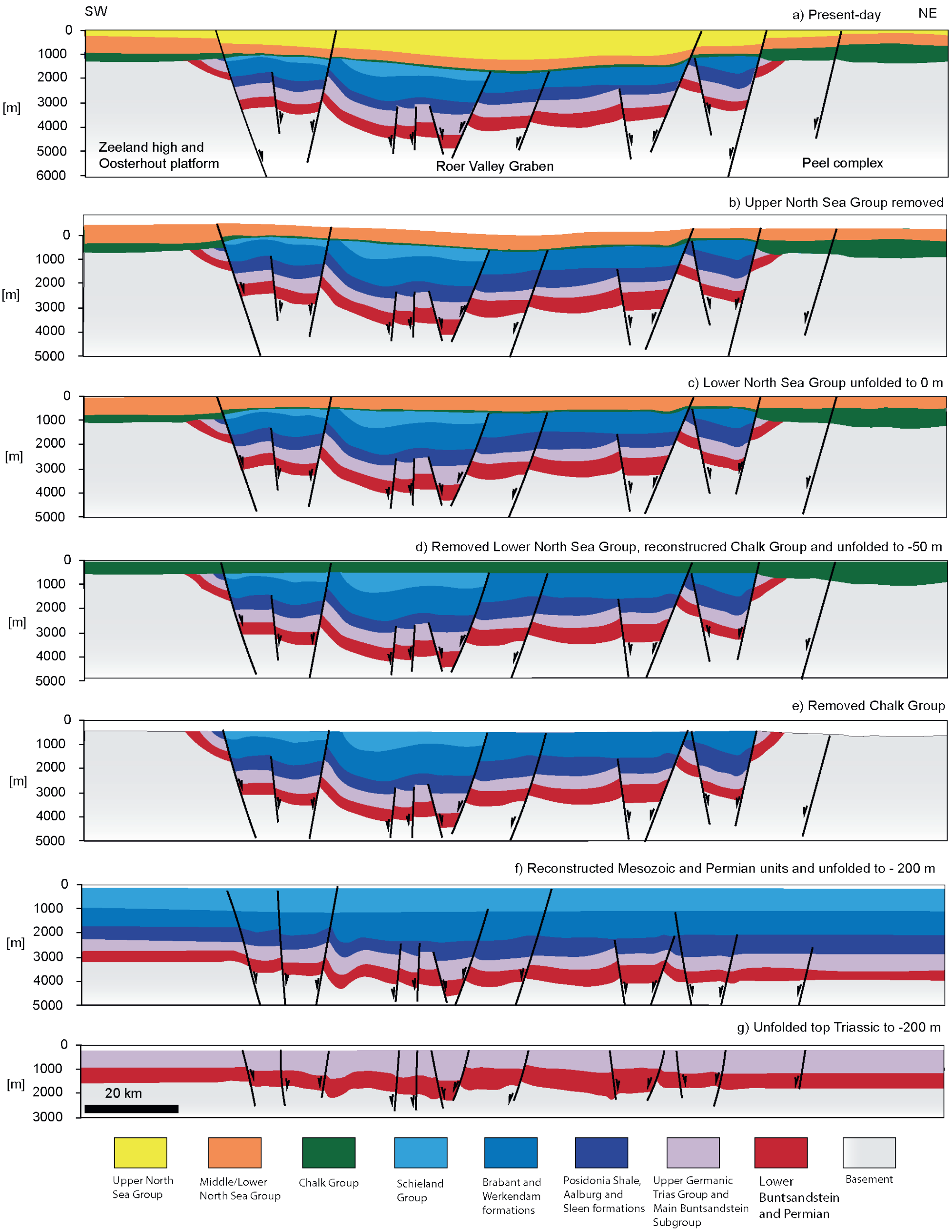

Figure 2.13. Main steps taken to restore transect EBN018 (see Fig. 2.4 for the un-interpreted and interpreted seismic line). Some of the interpreted faults in Fig. 2.4 were removed to simplify the restoration process. Colours refer to specific stratigraphic units (see Fig. 2.3). Horizon reconstruction is displayed in f) and d).

The platforms are the areas along the Roer Valley Graben flanks where the Main Buntsandstein sediments are usually present at depths shallower than 1500-2000 m and locally subcrop at the base Chalk Group unconformity and (e.g. Fig. 2.4). These platforms are narrowest on the southeast termination of the Roer Valley Graben, where the Main Buntsandstein is mostly absent on the blocks adjacent to the Roer Valley Graben (Fig. S2c Appendix). The base Chalk Group unconformity represents an angular unconformity that developed as the result of fault inversion along the flanks of the Roer Valley Graben. Palinspastic restoration analysis displayed how the thicker deposition of the Chalk Group on the platforms and highs is associated with fault inversion, reflected by faults displaying normal offset in their lower tracts and reverse displacement in their upper portion. In this context, sediments were mostly deposited on the fault footwalls, while the hanging walls were mostly affected by erosion. This is aligned with previous studies on the tectonic history of the Roer Valley Graben area (Geluk et al., 1994; Deckers et al., 2023). The reactivation of normal faults as reverse faults indicates the control exerted by pre-existing faults on the Roer Valley Graben deformation history (Deckers et al., 2021). This event is mostly evident in the northern part of the Roer Valley Graben as exemplified by the decrease in reverse fault occurrences further to the south (Fig. S3 in the Appendix).

After the Late Cretaceous inversion, the Roer Valley Graben was affected by an extensional regime that continues today (Geluk et al., 1994; Deckers et al., 2023). This is indicated by the presence of border faults that cut through the North Sea Supergroup sediments. These faults are well developed across the central and southern parts of the Roer Valley Graben, creating accommodation space filled with a thick coverage of Cenozoic sediments. This event buried the Main Buntsandstein sediments down to 4-4.5 km in the central part of the Roer Valley Graben, where they reach maximum burial depths confirming the results of previous burial history studies (Zijerveld et al., 1992; Nelskamp and Verweij, 2012).

2.5.2 Controls on the Early to Middle Triassic depocenter activity

The restored 2D transects allow to reconstruct the basin geometry and to evaluate the presence of depocenters at the time of deposition of the Main Buntsandstein (Fig 2.14). By integrating these data with the reflector characteristics, sandstone thickness and N/G maps, the characteristics of the Main Buntsandstein fluvial sedimentary system in the Roer Valley Graben can be discussed.

During the Early to Middle Triassic the central and southern parts of the Roer Valley Graben that extends from wells BKZ-01 to and beyond NDW-01 appeared to be a preferred sandstone depocenter considering the sandstone thicknesses recorded (Fig. 2.6c). These depocenters were likely produced by faults that were interpreted as active during the Early to Middle Triassic times (e.g. F7 in Fig. 2.4b). This is aligned with sediment dispersal patterns in a half-graben system associated with fluvial sedimentation, where the coarse-grained facies are likely to be located close to active faults or along the basin axis (Gawthorpe and Leeder, 2000). In the central and southeastern parts of the Roer Valley Graben, the Main Buntsandstein reflectors show high continuity, locally over 5-7 km, and low amplitudes (e.g. Fig. 2.7, 2.8, and 2.10). The average high continuity and low amplitude suggest a great lateral extent of the same sedimentation conditions and rather homogeneous lithologies (Veeken and Van Moerkerken, 2013; Zeng, 2018). This is further supported by the average high N/G values in these parts of the Roer Valley Graben.

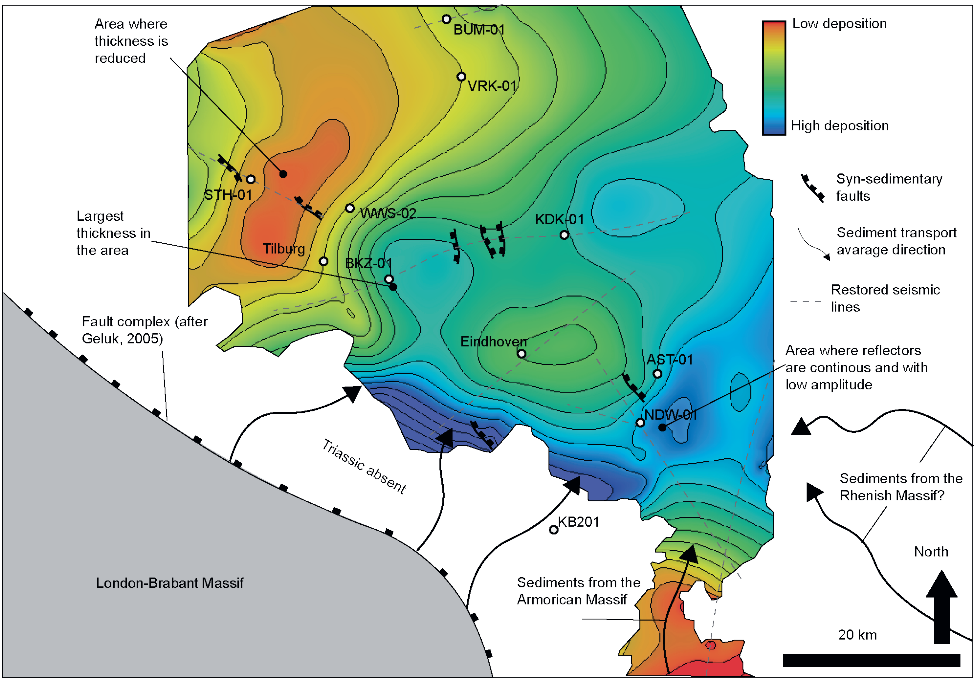

Figure 2.14. Basin geometry reconstruction derived through merging of the restored seismic transects (displayed as dashed black lines). Colour gives an estimation of the presence of depocenters for the Main Buntsandstein sedimentation. The sedimentation of the Main Buntsandstein Subgroup occurred in a continental setting, with no marine influence.

To the northwest, the overall decrease in the Main Buntsandstein gross and net sandstone thickness (Fig. 2.6b and c) and the presence of syn-sedimentary faults (Fig. 2.10) suggest the presence of an area where a lower subsidence rate in the footwall of active faults may have resulted in the deposition of a thinner Main Buntsandstein sequence (~ 125 m) as recorded in well STH-01. On the other hand, southeast of STH-01, a depocenter is displayed in the reconstructed basin geometry and confirmed by a Main Buntsandstein thickness of 250 m in well BKZ-01, where a higher subsidence rate may have enhanced the deposition of a thicker Main Buntsandstein sequence (Fig. 2.14).

To the northern edge of the study area, an increase in reflector amplitudes exemplifies the frequent lithological contrasts between sandstones and claystones observed in the available wells (e.g. Fig. 2.13a). In the Roer Valley Graben, fluvial sandstones pinch out northwards into playa-lake claystones (Geluk, 2005). The change in reflector characteristics in the northern part of the Roer Valley Graben and the lower N/G values in BUM-01 and VRK-01 suggest that these wells are in a more marginal area close to the southern edge of the Central Netherlands swell where mostly fine particles were delivered (Geluk and Röhling, 1997).

At the time of the deposition of the Main Buntsandstein, the London Brabant Massif was cropping out with an elevation of 2-3 km feeding sediments to the Roer Valley Graben (Carter et al., 1990; Köppen and Carter, 2000; Olivarius et al., 2017). Unfortunately, the widespread erosion of the Triassic layers on the Zeeland High does not allow to define the southern limit of the Main Buntsandstein deposition. However, the presence of a depocenter along the southern margin of the area may reflect the presence of fault activity along the northern margin of the London-Brabant Massif during the Early to Middle Triassic, where the Main Buntsandstein sediments from the London-Brabant Massif may have been deposited before being eroded during later tectonic events (Geluk et al., 1994; NITG, 2004; Kombrink et al., 2012).

The Roer Valley Graben represents the fareway for sediments from the Armorican Massif to enter the Germanic Basin (Geluk, 2005; Geluk, 2007; Palermo et al., 2008; Bourquin et al., 2009). A major river system transported sediments for over 400 km from the Armorican Massif to the north, fed by the substantial precipitation in the remnants of the Variscan orogeny (Mckie and Williams, 2009). The restored base of the Main Buntsandstein and the thickness maps suggest that the area around the Nederweert well (NDW-01) was potentially a locus of deposition for these sediments. During the Early to Middle Triassic times, the Rhenish Massif was also exposed to the southeast of the study area. However, its role as a sediment source during the Main Buntsandstein deposition in the Roer Valley Graben remains unclear (Köppen and Carter, 2000; IF Technology, 2012; Augustson et al., 2019).

2.5.3 Implications for geothermal exploration

The Main Buntsandstein Subgroup may represent a promising geothermal play in the Roer Valley Graben considering its widespread distribution and expected in-situ temperatures between ~60 and ~140°C given the depth ranging from 2 to and 4.5 km and the average geothermal gradient of the area of ~31°C/km (Bonté et al., 2012; Békési et al., 2020). This is in line with borehole temperature measurements across the area, where temperatures of ~ 120°C are encountered at depths of ~ 3000 m (IF Technology, 2012).

This study shows that the Main Buntsandstein Subgroup in the Roer Valley Graben is a sand-prone sedimentary succession with sandstone thickness largely above 150 m and N/G on average higher than 50% (Fig. 2.6c and d). The net sandstone thickness and N/G maps presented in this study are derived from large-scale well interpolation, thus they become more uncertain when moving away from the wells. However, combining these maps with reflector characteristics provides an overview of sandstone distribution across the Roer Valley Graben. A more in-depth study is needed to define these properties locally and to analyse the lithological heterogeneities therein.

The reconstruction of the basin geometry and the sandstone thickness map indicate that the central and the southeast parts of the Roer Valley Graben were active depocenters during the Early Triassic rifting phase, where normal faults create the accommodation space for the deposition of thick sandstone sequences (~150-200 m). In this area, the reflector continuity indicates that these units may be continuous at 4-5 km scale. The lateral continuity of these sandstone units in the southeastern part of the Roer Valley Graben is further supported by their overall low amplitudes, suggesting the occurrence of similar lithologies (Zeng, 2018). Sandbodies are usually well-connected in systems with a N/G higher than 30% (Larue and Hovadik, 2006). Although connectivity may be less of an issue in sand-prone reservoirs, internal sandbody heterogeneities such as permeability barriers and baffles may affect the dynamic behavior of these types of reservoirs (Mckie, 2011).

In addition, the ~200 m thick Nederweert Sandstone is largely present below the Buntsandstein in the southeastern part of the Roer Valley Graben (IF Technology, 2012). This formation may further enlarge the recovery volume if connected with the Buntsandstein above. However, more research needs to be done to evaluate the distribution and reservoir quality of the Nederweert Sandstone.

IF Technology (2012) suggested that the northern flank of the Roer Valley Graben represents an area where geothermal systems are feasible in the Triassic sediments. Based on the current study, the Buntsandstein has average lower N/G along the northern flank compared to the rest of the Roer Valley Graben. Such a reduction in N/G suggests the connectivity of the sandbodies is more uncertain compared to the southern part of the Roer Valley Graben, where sandstones are thicker and likely better connected. However, the presence of less conductive lithologies such as claystone can produce a thermal blanket effect and increase the temperature of the underlying sandstone units, producing thermal anomalies important to consider when exploring geothermal resources (Hamm and Lopez, 2012).

The Main Buntsandstein in the central part of the Roer Valley Graben has experienced deep burial. With burial, formation water experiences an increase in temperature and pressure that may trigger physical and chemical processes affecting the primary composition and texture of sediments (Milliken, 2003) and, consequently, reservoir properties. The Main Buntsandstein Subgroup sediments experienced burial depths deeper up to ~ 3-4 km in the central part of the Roer Valley Graben. This is the area where diagenesis may have deteriorated reservoir quality the most making geothermal operations more challenging. This challenge has been exemplified by data from the well NLW-GT-01 in the West Netherlands Basin, which encountered very poor reservoir quality (porosity < 5% and permeability < 0.1 mD) in the Main Buntsandstein Subgroup at depths of ~ 4 km as result of diagenesis (Felder and Fernandez, 2018).

The shallower burial depths (~1.5-2.5 km) experienced by the Main Buntsandstein in the platform areas may have instead enhanced the preservation of reservoir quality. Overall, borehole STH-01 shows the best reservoir properties in the basin with an average porosity of ~20% and permeability exceeding 1 Darcy (www.nlog.nl). The well is located on the Oosterhout Platform, where the Main Buntsandstein experienced average shallower maximum burial depths compared to the central parts of the graben, which could have helped in the preservation of the primary porosity. In addition, the Main Buntsandstein sediments were located at surface conditions before the deposition of the Chalk Group, which may have resulted in leaching of the sediments enhancing reservoir properties (Mijnlieff, 2020). This would suggest a higher chance of encountering the best reservoir properties along the southern flank and to the southeast of Eindhoven, where the Triassic is often present at shallow depths below the Chalk Group. However, a more detailed study on diagenesis and its relationship with reservoir properties is needed to confirm this hypothesis.

The Roer Valley Graben is an area affected by faults that largely control the present-day extent of the Main Buntsandstein sediments. Many faults are concentrated along the Roer Valley Graben flanks where the Main Buntsandstein may offer a promising geothermal target due to the shallower burial depths and the higher likelihood to have preserved reservoir quality. Faults create a structural configuration dominated by roughly SE-NW oriented blocks. These faults compartmentalize the Buntsandstein sediments, reducing their extent along the ~SW-NE direction. However, these blocks are continuous over tens of kilometers along the ~SE-NW direction, thus it is likely that a potential doublet could be oriented parallel to the orientation of the faults.

2.6 Conclusions

Subsurface mapping integrated with 2D palinspastic restoration of seismic section reveals a heterogeneous nature and distribution of the Main Buntsandstein sediments as a result of an interplay between tectonic activity and depositional processes. Tectonic activity during the Early to Middle Triassic resulted in depocenter development and a larger thickness of the Main Buntsandstein in the central and southeastern parts of the Roer Valley Graben. After deposition, the Main Buntsandstein sediments were buried down to 3-4 km across the Roer Valley Graben in response to extensional tectonics and the deposition of the Jurassic units above. The Roer Valley Graben flanks were instead subjected to shallower burials and locally the Main Buntsandstein was present at surface conditions during the Middle to Late Jurassic. During Cretaceous times, the Chalk Group was deposited unconformably over an area affected by faulting and tilting. This led to the development of the base Chalk Group unconformity. This unconformity is well visible along the Roer Valley Graben flanks, where the Triassic is often observed to be truncated at the base of the Chalk Group. Subsequently, the Roer Valley Graben was inverted during the Late Cretaceous before subsidence could resume during the Cenozoic, burying the Main Buntsandstein sediments down to maximum burial depths of ~4-4.5 km in the center of the Roer Valley Graben.

Overall, the present-day architecture of the Main Buntsandstein sediments is largely controlled by faults. Faults create juxtapositions to Carboniferous, Jurassic, and Chalk deposits, and limit the lateral extent of the sediments by post-depositional compartmentalization of the lower Triassic units. The largest thicknesses attained in the central and southern parts of the Roer Valley Graben are explained by the presence of fault-induced depocenters during the Early to Middle Triassic. In these areas, sandstone sequence thicknesses are larger, up to 300m thick, and reflectors exhibit low amplitude and high lateral continuity. To the north, a change in lithology is indicated by the N/G map and stronger amplitude reflectors. Such a change in lithology is also visible upwards in the stratigraphy across the Roer Valley Graben, where an increase in reflector amplitude contrasts seems to reflect a decrease in N/G. The area around STH-01 represented an area where a lower subsidence rate resulted in a reduced thickness of the Main Buntsandstein gross thickness. In terms of extra-basinal sediment sources, the London-Brabant Massif to the southwest, the Armorican Massif to the south and the Rhenish Massif to the east were the major sediment suppliers.

The central part of the Roer Valley Graben appears to be the most promising geothermal target considering the sandstone thicknesses of over 200 m and the lateral reflector continuity over 4-5 km. However, while the deep burial depths may favor high in-situ temperatures, the temperatures and pressures experienced at deeper levels may also have enhanced diagenetic processes that deteriorate reservoir properties suggesting the center of the Roer Valley Graben to be a high-risk target. The adjacent platform areas and the southeastern part of the Roer Valley Graben may instead represent better targets for further investigation, where shallower burial depths may have helped preserve reservoir quality.

Chapter 3: Sedimentology, stratigraphy and reservoir architecture of the Lower Triassic Main Buntsandstein in the Roer Valley Graben, the Netherlands

Chapter 3 has been submitted to the Journal of Marine and Petroleum Geology: Cecchetti, E., Martinius, A. W., Felder, M., Donselaar, M.E., Abels, H.A., 2025. Sedimentology, stratigraphy and reservoir architecture of the Lower Triassic Main Buntsandstein Subgroup in the Roer Valley Graben, the Netherlands.

Abstract

The Main Buntsandstein Subgroup in the Roer Valley Graben is a sand-prone sedimentary interval deposited in a fluvial-aeolian environment and is currently investigated for its suitability as target for geothermal exploration. The current depositional models in the Roer Valley Graben do not fully address the facies heterogeneities within and between Buntsandstein sedimentary units and their impact on the prediction of reservoir architecture. It is therefore crucial to detailly analyse the Main Buntsandstein sedimentary facies heterogeneities to de-risk future sustainable energy operations. In the present study, the sedimentology and lithostratigraphy of the Buntsandstein in the Roer Valley Graben are assessed in a multidisciplinary analysis by use of a subsurface dataset composed of well cores, gamma-ray logs, and thin section data.

The deposition of the Main Buntsandstein sediments is dominated by different fluvial processes, with minor aeolian reworking. River planform style evolved through geological time from highly mobile and ephemeral to more perennial. The change in river style seems to be dictated by climatic variations in aridity and by a decrease in tectonic activity.

These different depositional processes resulted in the development of six lithofacies associations, developing three different types of reservoir architectures with their own set of heterogeneities at different spatial scales. Amalgamated stacked sandstones have the highest net-to-gross (N/G) with a high degree of lateral and vertical connectivity, and the highest average porosity and permeability. Compensational stacked sandstone reservoirs have a lower N/G and are the most heterogeneous due to the frequent occurrence of cemented intervals and mud drapes in the sandstone bodies. Marginal isolated sandstones show a preserved relationship between reservoir properties and depositional facies, while more data are needed to limit the uncertainties related to the spatial connectivity and lateral continuity of the sandstone bodies.

The results of this study enhance the understanding of Lower Triassic reservoir architecture and sedimentary heterogeneities and provide a solid basis for future investigation of the relationship between sedimentary facies, diagenesis, and reservoir quality.

Keywords: Main Buntsandstein Subgroup; Sedimentology and Stratigraphy; Reservoir architecture; Heterogeneities.

3.1 Introduction

The Lower Triassic Main Buntsandstein Subgroup stands as a well-established clastic hydrocarbon reservoir and reservoir unit in the North Sea Basin and beyond. In the Netherlands, valuable hydrocarbon accumulations occur in the fluvial-aeolian sandstone reservoirs of the Main Buntsandstein Subgroup onshore and offshore (Bachmann, 2010). Sandstones from the Main Buntsandstein Subgroup have also attracted attention for their potential application in geothermal energy, leveraging their widespread distribution and favorable in-situ temperatures (Kramers et al., 2012; Hjuler et al., 2019; Mijnlieff, 2020). In the Roer Valley Graben in the southeastern Netherlands, sandstones with a total thickness up to ~200-250 m (Cecchetti et al., in press), and in-situ temperatures up to 120-130 °C at depths of 2-3 km could provide energy for different applications such as district and greenhouse heating, and direct electricity use (Kramers et al., 2012; www.ThermoGIS.nl).

Several models provide insight into the depositional processes and resulting sedimentary structures in the Early to Middle Triassic in the Roer Valley Graben (Carter et al., 1990; Van Adrichem Boogaert and Kouwe, 1993; Geluk et al., 1997; Geluk 2005; Palermo et al., 2008; IF Technology, 2012). However, most of the depositional models available for the Main Buntsandstein seem to be incomplete and somehow in contradiction with each other. For example, Carter et al. (1990) suggest deposition via fluvial fan systems with a northeast average paleoflow direction originating from a terrain source located to the southwest. Geluk (2005) proposes a model with deposition via axial river systems flowing to the northwest. More recently, a model by IF Technology (2012) suggests that the Main Buntsandstein Subgroup was deposited as result of an interplay between fluvial fan systems sourcing from two different terrains located along the Roer Valley Graben margins and an axial river system with an average northwest paleoflow direction. The existence of different depositional models creates uncertainties as each model results in different sedimentary architectures with distinct geometries and spatial distribution of the sandstone bodies.

The origin and arrangement of these bodies introduce sedimentary heterogeneities at various scales from centimeter to kilometer that can influence primary porosity, permeability, and subsequent secondary processes such as diagenesis (Hartmann and Beaumont, 1999; Morad et al., 2000; Ringrose et al., 2008). Busch et al., 2022 have documented the positive relationship between grain size and porosity and permeability in the Buntsandstein of the Upper Rhine Graben. More specifically, the variation in grain size and sorting between the foreset and bottomset within channel bar elements can result in fluid-flow anisotropy (Hartkamp-Bakker and Donselaar, 1993; McKinley et al., 2011). Furthermore, the presence of chemically reactive intraclasts, such as detrital dolomite clasts, can lead to early cement precipitation creating flow baffles (Molenaar and Felder, 2019; Bertier et al., 2022; Busch et al., 2022). These examples of heterogeneities can create flow anisotropies at different levels; thus, it is crucial to evaluate the presence of such heterogeneities and integrate them into reservoir architecture models (Ringrose et al., 2008; Larue and Hovadik, 2015).

The present study of the Main Buntsandstein Subgroup focuses on its development in the Roer Valley Graben (Fig. 3.1a). We perform a comprehensive sedimentological, petrographical and petrophysical analysis to understand the depositional origin, reservoir architecture, and sedimentary heterogeneities of the Main Buntsandstein Subgroup. This was possible by leveraging a publicly available data set (www.nlog.nl), alongside a rediscovered 20 m core from the southeastern region, and newly acquired thin section data from multiple wells. We conducted a sedimentological analysis of all well cores available to analyze the sedimentary facies and provide a better understanding of their genesis and distribution. These results integrated with petrophysical data allowed to study the architecture, heterogeneities, and quality of the potential reservoir units. This study contributes to the understanding of the Main Buntsandstein Subgroup reservoir architecture and heterogeneities in the Roer Valley Graben, and more in general it contributes to the understanding of Lower Triassic systems in northwestern Europe basins.

3.2Geological setting

3.2.1 Tectonics and paleogeography

The Roer Valley Graben is 30-40 km wide and about 130 km long (Fig. 3.1a) and is bounded by a NW-SE oriented fault system that developed in the Carboniferous and was subsequently reactivated during later Mesozoic and Cenozoic tectonic events (NITG, 2004; Kombrink et al., 2012; Cecchetti et al., *2024*). During the Early to Middle Triassic, the Roer Valley Graben was a half-graben system and an active depocenter for the Main Buntsandstein Subgroup. The accommodation space was created as a result of a series of short-lived tectonic pulses intermitted with regional thermal subsidence resulting in a NW-SE oriented half-graben structure with normal faulting and local depocenter development across the Roer Valley Graben where thickness changes up to 100 m occurr (Geluk, 2005; Cecchetti et al., 2024). Tectonic activity decreases throughout the deposition of the Buntsandstein. Eventually, the Roer Valley Graben became a tectonically stable region where only a thin sequence (10-25 m) of Solling sediments were deposited (Geluk and Röhling, 1997).

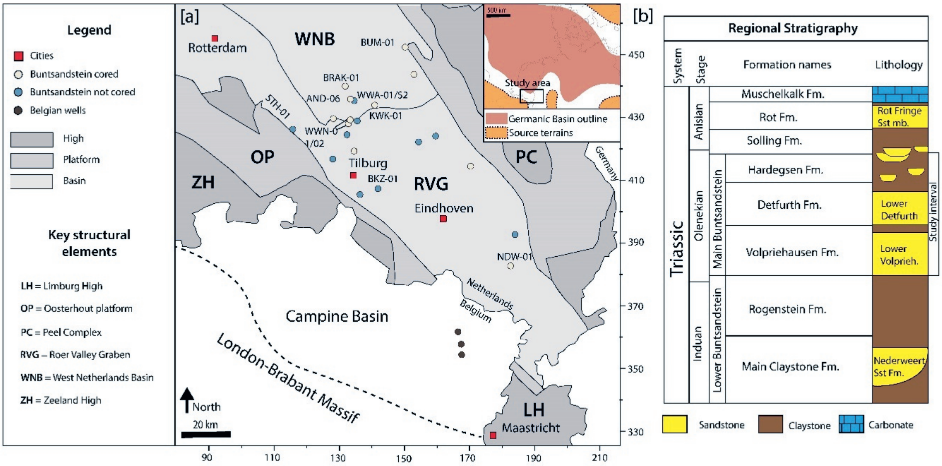

Figure 3.1: a) The location of the study area with the main structural elements after Kombrink et al., 2012. Note that most of the cored wells are located in the northern part of the area, while in the southern part only one well (NDW-01) has part of the Buntsandstein stratigraphy cored. b) Triassic regional stratigraphy with over- and underburden after Van Adrichem Boogaert & Kouwe (1994).

During the Early to Middle Triassic, the Roer Valley Graben was located on the southwestern margin of the Germanic Basin (Fig. 3.1a), a large endorheic basin that developed during the Late Permian to Early Triassic and was located at the western margin of the Tethys domain (Scheck and Bayer, 1999; Ziegler et al., 2004; Geluk, 2005; Bourquin et al., 2011). The Germanic Basin was bounded by the relicts of the Hercynian orogeny to the south that fed sediments to the Roer Valley Graben (Geluk, 2005; Bourquin et al., 2011). To the north of the Roer Valley Graben, the Netherlands swell was a topographic high where little deposition occurred as confirmed by the thinner Buntsandstein sequence (~50 m) compared to the Roer Valley Graben (Geluk and Röhling, 1997; Bachmann et al., 2010).

The Main Buntsandstein Subgroup was deposited via river systems in the southwestern part of the Germanic Basin under arid climatic conditions as indicated by the widespread occurrence of aeolian facies and lack of diffuse paleosol development in many Triassic basins across Europe (Geluk, 2005; Bourquin et al., 2011). Water and sediments were supplied from the adjacent reliefs to the south, largely controlled by the amount of precipitation in the catchment areas as suggested by recent paleoclimatic simulations (Peron et al., 2005).

3.2.2 The Main Buntsandstein Subgroup

The sedimentation of the Main Buntsandstein Subgroup commenced at the Induan to Olenekian transition (Szurlies, 2004). In the Netherlands, the Main Buntsandstein Subgroup is divided into three formations: Volpriehausen, Detfurth, and Hardegsen (Fig. 3.1b). The Volpriehausen and Detfurth Formations are usually formed by a lower fluvial/aeolian sandstone and an upper playa-lake silt/claystone (Van Adrichem Boogaert and Kouwe 1994; Geluk and Röhling, 1997). The playa-lake silt/claystone units are thicker and better developed to the north (Kortekaas et al., 2018), while they can be absent close to the basin margin (Geluk, 2005).

The playa-lake sediments represent an important stratigraphic marker across the Netherlands and adjacent basins, generally considered to be deposited as a result of water table rise across the Germanic Basin (Geluk and Röhling, 1997; Bourquin et al., 2006). Such variation is interpreted to reflect sediment supply and water discharge fluctuation in response to climate changes upstream (Peron et al., 2005). The Hardegsen Formation is instead characterized by an alternation of fluvial sandstone and claystone at meter to tens of meter scale (Fig. 3.1b) (Van Adrichem Boogaert and Kouwe 1994; Geluk and Röhling, 1997).

The Main Buntsandstein Subgroup is ~200 to 250 m thick in the Roer Valley Graben and it is considerably thinner (~150 m) or locally absent due to erosion on the adjacent platforms/highs (Cecchetti et al., 2024). It overlies the Rogenstein Formation, a ~ 100 m succession of claystone and oolitic beds deposited in a near-shore, shallow water environment (Fig. 3.1b) (Palermo et al., 2000). The boundary between the Rogenstein and the Main Buntsandstein Subgroup is taken at the base of the first sandstone bed (Van Adrichem Boogaert and Kouwe 1994).

Above the Main Buntsandstein Subgroup, the Solling Formation consists of sandstone and claystone units deposited in a fluvial-lacustrine environment (Geluk, 2005). This boundary between the Hardegsen and Solling Formations is easily discernible when associated with the Hardegsen Unconformity, an angular unconformity induced by tectonics that is responsible for the erosion of Lower Triassic sediments in part of the Germanic Basin (Geluk, 2005). However, in the Roer Valley Graben, the Hardegsen Unconformity is not present and the sandstones of the Solling Formation are stacked conformably on top of the sandstones of the Hardegsen, making the boundary between the Hardegsen and Solling Formations difficult to discern (Fig. 3.1b).

3.3 Material and Methods

The present study is based on the analysis of core, rock samples and petrophysical data from 24 wells in the Roer Valley Graben (Fig. 3.1a). Lithofacies, sedimentary structures, sediment composition, and texture were evaluated from slabbed cores, cuttings, and thin sections. A well-log correlation was conducted across the study area to determine the Buntsandstein lithostratigraphy in the area and assess reservoir architecture. Porosity and permeability data from publicly available dataset (www.nlog.nl) were integrated to assess the reservoir quality of the different lithofacies types, and to assess the characteristics and scale of heterogeneities such as permeability baffles, and barriers.

3.3.1 Core and cutting analysis

Approximately 382 m of core material from the Main Buntsandstein Subgroup was described from 9 wells across the Roer Valley Graben (Fig. 3.1a and Table 1). In the Waalwijk-North (WWN-01-S2) well, approximately 72% of the Main Buntsandstein Subgroup stratigraphy is covered by core material, providing a relatively continuous record to analyze the changes in sedimentary structures and heterogeneities through the stratigraphy (Table 1). The well inclination was taken into account to establish the true stratigraphic thickness (TST) of the lithofacies types. Grain size for the core samples was determined with a grain-size chart under a hand lens.

The analyzed sediments were subdivided in lithofacies types defined by macroscopic characteristics. The lithofacies types were clustered into lithofacies associations representing assemblages of spatially and genetically related lithofacies deposited in a particular sub-environment. For the wells where core samples were not available, rotary and PDC (Polycrystalline Diamond Compact) cuttings were used in combination with mud logs to determine sediment characteristics such as colour, grain size, and composition.

Table 1: Summary of the rock samples data available to the study. Note that only well WWN-01-S2 has an appropriate core recovery that allowed to study vertical changes in sedimentary facies throughout the Buntsandstein stratigraphy. Thin sections from different studies have been integrated with the data produced within this work. Different authors are represented by the following symbols: * GAPS well reports; **This study; *** Carter et al. (1990). The works by GAPS and Carter et al. (1990) can be downloaded from www.nlog.nl.

Well name	Top Buntsandstein (MD)	Bottom Buntsandstein (MD)	Top Cored interval (MD)	Bottom Cored interval (MD)	Cored interval(MD)	Core recovery	Thin Sections studied	Author	Plugs measured
Andel-06 (AND-06)	2867.12	3136	2894	2910.65	16.65	6.19%	4*	GAPS	33
Brakel-01 (BRAK-01)	2446	2637	2452	2477	25	13.09%	6*	GAPS	85
Buurmalsen-01 (BUM-01)	1368.74	1576	1498	1531	33	15.92%	29**	This study	91
Keerwijk-01 (KWK-01)	2547	2754	2548	2601.63	53.63	25.91%	20**	This study	160
Keldonk-01 (KDK-01)	2076	2287.93	2258	2275.1	17.1	8.07%	4*	GAPS	79
Nederweert-01 (NDW-01)	2030	2237.12	2120.5	2135	14.5	7.00%	12**	This study	23
Sprang Capelle-01 (SPC-01)	2607.62	2756.5	2647	2675	28	18.81%	9**	This study	80
Varik-01 (VRK-01)	1623	1810.57	1656.5	1660.73	4.23	2.26%	7**	This study	12
Waalwijk North-01-S2 (WWN-01-S2)	3166.23	3355	3169	3305.5	136.5	72.31%	22***	Carter et al., 1990 (BP)	536

Preserved dune-scale cross-set thickness (Sm) was used to estimate the mean bedform height (*Hm*) through the following empirical equation following Bridge and Tye (2000) and Leclair and Bridge(2001):

$$Hm = 2.9 * (\mp 0.7) * Sm \tag{1}$$

The resulting bedform height (*Hm*) measurements were used to estimate the formative bankfull depth (Bd) using Eq. 2 after Bradley and Venditti(2017):

$$Bd = 6.7 * Hm \tag{2}$$

Due to the absence of borehole images, the foreset laminae dip angle was interpreted relative to truncation surfaces and to sedimentary structures estimated to be deposited horizontally (e.g. claystone lamination).

3.3.2 Thin section study

Sediment texture and composition of 63 thin sections from 6 wells were studied with an optical microscope. In addition, petrographic legacy data of 32 thin sections from 3 wells available via www.nlog.nl were integrated into the study (Table 1). The thin sections were representative of most of the studied core material, giving the average sampling rate ranging from 0.5 to 6.5 m. The diameters of 100 grains per sample were measured to determine grain-size distribution and sorting following Folk and Ward (1957). Sediment composition was studied through the Gazzi-Dickinson point-counting method (200 points per thin section). Point-count results were grouped following Pettijohn (1975) and plotted in a ternary diagram (QFL).

3.3.3 Well log correlation

The gamma-ray log was used to correlate the Main Buntsandstein lithostratigraphy between wells. The aims were to assess the spatial variation of the different lithofacies associations and to explore the 2D potential reservoir architecture. In the absence of chronostratigraphic markers (e.g. biozones) lateral correlation at the scale of the study area is highly uncertain. For this reason, a lithostratigraphic correlation of the individual sandstone bodies was only attempted between wells at distances shorter than 1.5 km.

First, in the cored wells, a core-to-log shift was applied to correct for potential depth misfit between the sedimentological log created from the core study and the gamma-ray log. Secondly, a characteristic GR log profile was determined for each lithofacies association in the cored wells. Subsequently, these GR log patterns were extrapolated to non-cored wells and depth intervals were assigned to particular lithofacies associations. This was done with the help of cuttings where available. Thereafter, variations in the thickness of the lithofacies associations between wells were identified and a lithostratigraphic framework was tentatively established.

3.4.Results

3.4.1 Sedimentology of the Buntsandstein in the Roer Valley Graben

Twelve lithofacies types were identified based on grain-size distribution, lithology, texture, and sedimentary structures in full cores and core slabs (Fig. 3.2 and Table 3.2). There are two gravel lithofacies named: homogenous to crudely-stratified gravel (G) and stratified gravel (Gs); six sandy lithofacies: pebbly sandstone (Slx), cross-stratified sandstones (Sx), horizontally-stratified sandstones (Sh), ripple cross-laminated sandstone (Sl), bioturbated ripple cross-laminated sandstones (Slb) and homogeneous sandstones (Sm); and four silty/muddy lithofacies: laminated to homogeneous claystone (F), bioturbated claystone (Fb), bioturbated heterolithic mud, silt, to sand (Fib), pedogenetic claystone/siltstone (Fp). The twelve lithofacies were grouped into six lithofacies associations based on vertical successions and geometrical arrangement; four gravelly to sandy lithofacies associations (LA-1 to LA-4) and two muddy lithofacies associations (LA-5 and LA-6).

Table 2: Description and interpretation of the lithofacies types.es in the Main Buntsandstein Subgroup.

Lithofacies name	**Description**	**Statistics**	**Interpretation**
Massive to crudely stratified gravel (G)	Pebble- to cobble-size gravel with an undefined structure to crude horizontal stratification. This lithofacies is composed by granules- to cobble-size intraclasts that are moderately to poorly sorted. The intraclast lithology ranges from mudstone, silt/sandstone, and dolomite. Locally, a bimodal texture may occur with fine to medium-grained angular to sub-rounded sandstone as matrix. Rarely, clay, silt, or cross-stratified sandstone lenses may be interbedded with gravels.	**Unit thickness** mean = 0.13 m std = 0.1 m	Reworking of intrabasinal clasts of floodplain mudstones, silt/sandstones, or dolomite, transported and redeposited quickly by high-energy, turbulent unidirectional flows. The unsorting, massive- to crudely-stratified character may indicate channel-lag deposition through debris flow (Miall, 1977). The frequent superimposition of stratified gravel (Gs) suggests sediment organization into bedforms (Nichols , 2009).
Stratified gravel (Gs)	Stratified gravel makes up beds of granules- to cobble-size intraclasts. The intraclast lithology ranges from mudstone, silt/sandstone to dolomite. Bimodal texture may occur with fine to medium-grained angular to sub-rounded sandstone as matrix. This facies is usually organized in normally-graded cross-stratified sets, where clasts lay on the foreset slopes. Reactivation surfaces may be present. Individual sets are usually separated by inclined surfaces with an angle larger than 5° . Usually, the sorting within each set increases upwards. Planar to trough strata cannot be distinguished due to the bidimensionality of the core samples and poor spatial resolution. Dolomite cement may be pervasive and alter the primary sedimentary structure.	**Set thickness** mean = 0.12 m std =0.07 m **Coeset thickness** mean = 0.26 m std = 0.25 m	Eroded mud and carbonate clasts transported and redeposited by high energy, turbulent unidirectional flows during plane bed migration, associated with channel lags. The presence of cross-stratification indicates the individual strata were produced by avalanching movements of clasts on downward or lateral flanks (Miall, 1981; Yagishita, 1997; Steel and Thompson, 1983).
Pebbly sandstone (Slx)	Fine- to coarse-grained, commonly bearing granule-size intraclasts, cross-stratified sandstones. The intraclast lithology varies from mudstone, silt/sandstone to dolomite. This facies can be either found as a solitary set or organized coesets. Contact between foresets laminae and lower bounding surface is usually tangential. Periodic, thick, coarse cross-strata may occur within singular sets. Overall, the foresets differ in grain size and are locally cut by reactivation surface. Convex set boundaries can occur. This facies overlies scour surfaces at the base of channels and may occur at the base of macroforms within channel sandstones.	**Set thickness** mean = 0.15 m std =0.05 m **Coeset thickness** mean = 0.63 m std = 0.45 m	Migration of (3D) sinuous subaqueous dunes under upper to lower flow regime. The presence of intraclasts and unsorted basal deposits suggests erosion and transportation of antecedent deposits and incorporation into bottomset architecture (Herbert et al., 2018).

Cross-stratified sandstone (Sx)	Fine to medium-grained, well-rounded, and moderate- to well-sorted planar cross-stratified sandstone. Locally, bimodal grain-size distribution is observed. Set boundaries are flat and sharp. Usually, set thickness decreases upward. However, it depends on the preservation potential. Foresets represent avalanching slopes. Occasionally showing bimodal grain size distribution in the foresets, with coarser foresets that may have been cemented by later diagenesis. Finer laminae in the foresets can be micaceous. Bottomsets can show horizontal laminations or ripples. Contact between foresets laminae and lower bounding surface is usually abrupt.	**Set thickness** mean = 0.11 m std =0.06 m **Coeset thickness** mean = 0.94 m std = 0.89 m	Subaqueous (2D) dune migration under lower-flow regime unidirectional flows, associated with the channelized flow. The evidence of flow brief pauses in sand transport (mud drapes) indicate periodic emersion/very shallow water level (Herbert et al., 2018). In NDW-01, these dunes can be subaerial and shaped by the action of wind with suspension and saltation lamina pairs (Fig. 3.4) (Henares et al., 2014).
Horizontally-stratified sandstone (Sh)	Very fine- to coarse-grained sandstone, well-rounded, moderately to well-sorted, occasionally bearing pebble-granule size clasts. The units of this lithofacies are represented by isolated sets or coesets of parallel to low-angle cross strata that range in thickness from 0.045 to 1.7 m. The distinction between horizontal and low-angle cross-stratified could not, or only seldom, always be done due to well path deviation and small spatial resolution of the core samples. Strata sets may be separated by slightly inclined (<5°) truncation surfaces in coesets.	**Set thickness** mean = 0.12 m std =0.04 m **Coeset thickness** mean = 0.47 m std = 0.36 m	This facies is formed by a transition from lower to upper flow regime. Horizontal stratification forms at low flow velocity for medium to coarse grain sizes, with dune bedforms start developing as flow speed increases (Nichols, 2009).
Ripple cross-laminated sandstone (Sh)	Very fine- to medium-grained sandstone, with the rare occurrence of medium- to coarse-sand. The base is often gradational. The top is sharp or erosive. Asymmetrical to symmetrical wave ripple lamination commonly develop, including mud-draped bidirectional bedforms. Flaser to wavy beddings may occur, bounded by mud and silt. This facies can be organized in solitary sets or coesets of ripple-scale cross laminae.	**Unit thickness** mean = 0.17 m std = 0.15 m	Sediment transport occurs under a lower flow regime(Miall, 1977; Nichols, 2009). Deposition may have occurred within fluvial channels or pond/lake, with water oscillation induced by wind.
Bioturbated ripple cross-laminated sandstone (Slb)	Very fine to fine cross-laminated sandstone. Burrows (Palaeophycus and maybe Planolites), mud cracks and rootlets that may obscure primary sedimentary structures. Asymmetrical to symmetrical wave ripple lamination frequently occurs, with mud drapes and clay chips. This facies forms units with an average thickness of 31 cm, however, they can stack up to a meter.	**Unit thickness** mean = 0.31 m std = 0.26 m	Sediment transport occurs under a lower flow regime (Miall, 1977; Nichols, 2009). Deposition may have occurred within fluvial channels or pond/lake, with water oscillation induced by wind. The presence of desiccation and bioturbation suggests periodical emersion and an environment favorable for subaqueous life (Buatois et al., 1998).
Homogeneous sandstone (Sm)	Fine to medium grain size sandstone, moderately to well sorted. It may bear pebbles size clasts. Usually, top and bottom boundaries are sharp or erosive. Sandstone is mostly structureless, however, orientated pebble size clasts and faint lamination are visible. Burrows rarely occur.	**Unit thickness** mean = 0.34 m std = 0.2 m	High rate of deposition during high discharge periods or sediment reworking from biological activities.
Bioturbated heterolithic mud, silt to sand (Fib)	This facies is formed by mm to cm (< 5 cm) alternation of mudstone/siltstone with fine to coarser sandstone. Beds can be lenticular to wavy. Sandstone can be homogenous to laminated. Current ripples can occur together with abundant mud drapes. Mud cracks, rootlets, and burrows (Palaeophycus and maybe Planolites) are frequent that may overprint primary sedimentary structures. The color of the mud changes from brownish (7.5YR 2.5/3) to red (10R 4/8) and/or greyish (GLEY 1 6/5G). Desiccation cracks can reach lengths up to 5 cm. This facies is organized in units reaching up to meter scale, with a mean of around 25 cm.	**Unit thickness** mean = 0.27 m std = 0.24 m	Low flow regime, deposition from suspension alternated with periodical inputs of sand transported by current. The environment of deposition was favorable for subaqueous life, periodically drying up (Buatois et al., 1998). Deposits of waning floods, overbank deposits, lakes, or ponds (Miall, 1977; Mckie, 2011; Coronel et al., 2020).
Laminated to homogeneous claystone/siltstone (F)	Clay to siltstone with laminated to homogeneous structure. The lithofacies is reddish (2.5YR 4/2), brownish (7.5YR 2.5/3) and/or greenish (GLEY 2 6/10G), occurring in isolated units ranging from 2 to 40 cm in thickness. The top boundary is generally erosional. The bottom can either is often sharp, but can also be gradational.	**Unit thickness** mean = 0.11 m std = 0.11 m	Deposition from suspension during waning flows within a channel, or in a floodplain under a temporary water level (Miall, 1977).
Pedogenic mudstone/siltstone (Fp)	Mudstone to siltstone with laminated to homogeneous structure. Structureless to faint laminated very fine sand intervals can also be interbedded. The lithofacies is reddish (5YR 4/4) or	**Unit thickness**	

	greyish (GLEY 1 5/N). It usually exhibits a mottled aspect and paleosol development. The frequent presence of dolomite nodules and bioturbation often overprint primary structures. Top boundaries are erosional, while the bases are often gradational. This facies is organized in isolated units reaching up to 1.2 m in thickness.	mean = 0.7 m std = 0.33 m	Deposition from suspension. Soil formation may occur with chemical precipitation developed on overbank fines. (Kraus, 1999; Pimentel et al., 1996).
Bioturbated claystone (Fb)	Bioturbated mudstone to siltstone. Primary structures are overprinted, however, locally this lithofacies can have laminated to homogeneous structures. Rootlets and burrows (Palaeophycus and maybe Planolites) are frequent. Mud cracks can occur. Structureless to faint laminated very fine sand can be interbedded. The color of lithofacies from brownish (7.5YR 2.5/3) to red (10R 4/8) and/or greyish (GLEY 1 6/5G). It is organized in isolated units ranging from 5 to 70 cm in thickness, with a mean of 20 cm.	**Unit thickness** mean = 0.19 m std = 0.19 m	Deposition from suspension during waning flows within a channel, or in a floodplain under a temporary water level favorable for subaquatic life (Buatois et al., 1998). Periodically emersion led to mud crack formation.

3.4.1.1 Stacked stratified sandstone (LA-1)

Lithofacies association 1 (LA-1) is composed of very-fine to coarse-grained sandstones with conglomerate (G and Gs) occasionally found at the base (Fig. 3.3a and b). Sandstones are usually greyish (GLEY 1 8/N). However, in the eastern part of the basin, these can be orange to red (5YR 6/4), oxidized with presence of hematite coating (Fig. 3.3a). LA-1 is usually multistoried forming stacked complexes over of tens of meters in thickness, where each storey has an average thickness of 3.7 m and a standard deviation of 1.4 (Fig. 3.9b). Within each storey, coarse to medium-grained pebbly sandstones (Slx) can be found at the base, bearing intrabasinal fragments, such as mud chips, silt-sandstone grains, and dolomite grains (Fig. 3.3a and d). Mud chips are usually angular and elongated, reaching 2-3 cm in diameter. Silt-sandstone and dolomite grains are subrounded, which diameter can reach up to 1-2 cm in length. Unfrequently, pebbly sandstone (Slx) can be found superimposing thin (< 0.5 m) gravel lithofacies (G and/or Gs) developing a sharp contact with the underlying sediments. The core of each storey is composed of moderately- to well-sorted cross-stratified sandstones (Sx) and horizontally- stratified sandstones (Sh) together accounting for ~ 75% of the total lithofacies assemblage in LA-1 (Fig. 3.9a). Cross-stratified sets (Sx) can reach thickness of ~ 45 cm and can be organized in coesets reaching thicknesses up to 5 m. Within each set, foresets can bear elongated mud chips of few cm in size at the base. Bottomsets can reach thickness of 3-4 cm and they are usually formed by very fine to fine-grained sandstones. Bottomset sandstones can be horizontally-laminated or cross-laminated with ripple structures (Fig. 3.3c).

Cross- and horizontally-stratified sandstone (Sx and Sh) can be characterized by a bimodal grain-size distribution organized in pairs of laminae with a thickness of 0.2 to 1 cm (Fig. 3.4a and c). When this occurs, usually grains are coated with hematite. Each pair of laminae has a sharp flat base, while the boundary between the laminae is gradational. The lower laminae is usually moderately to well-sorted, rounded to well-rounded, medium to coarse-grained. The upper laminae consists of moderately sorted, subrounded to rounded, very fine to fine-grained sand.

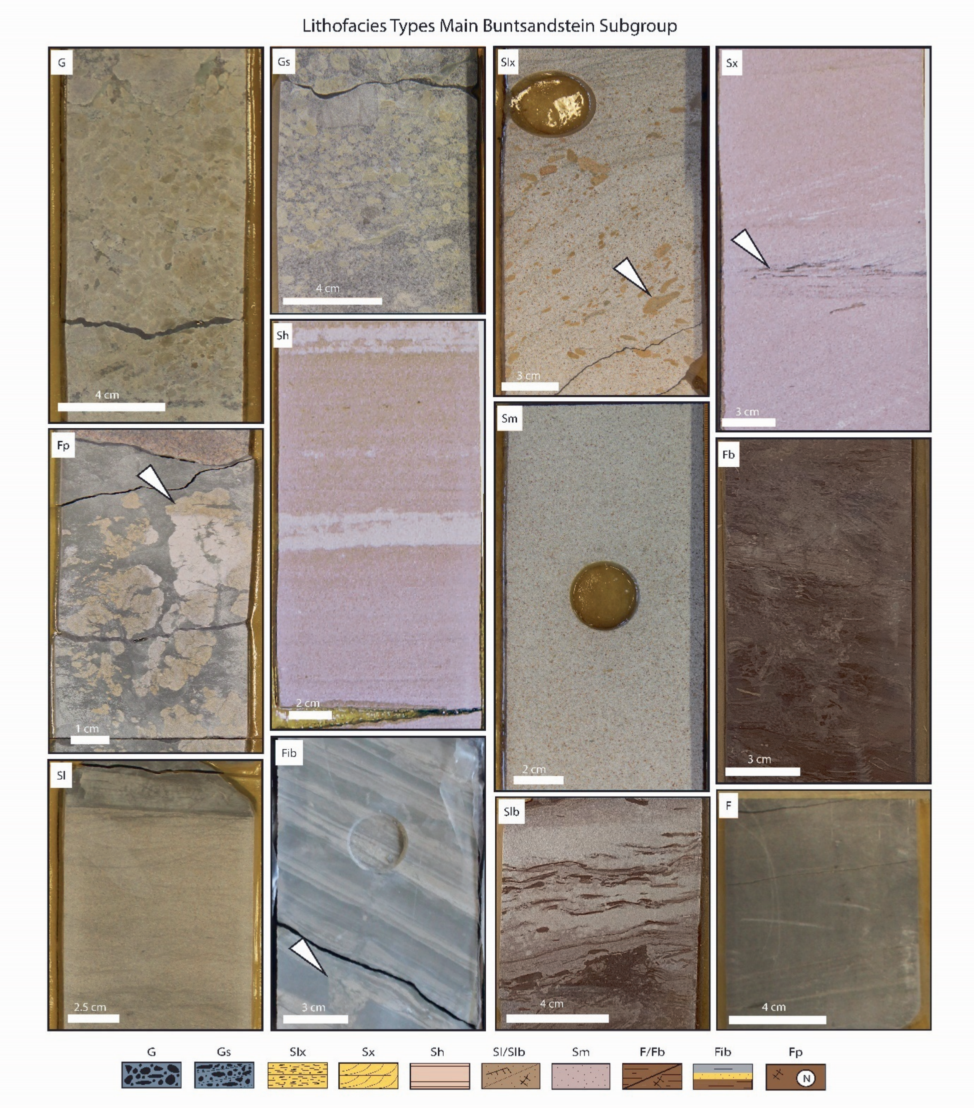

Figure 3.2: Lithofacies types recognized in the study area. (G) Massive to crudely- stratified gravel. (Gs) Stratified gravel. (Slx) Pebbly sandstone. The arrow indicates a dolomite detrital grain. (Sx) Cross-stratified sandstone. The arrow indicates the set boundary with small mud chips aligned along the foreset direction. (Sh) Horizontally-stratified sandstone. (Sl) Ripple cross-laminated sandstone. (Slb) Bioturbated ripple cross-laminated sandstone. (Sm) Homogeneous sandstone. (F) Laminated to homogeneous claystone. (Fb) Bioturbated claystone. (Fib) Alternated bioturbated clay, silt, and sandstone. The arrow indicates a mud crack. (Fp) Pedogenic mud/siltstone. The arrow indicates pedogenic dolomite nodules.

At the top of each story, ripple cross-laminated sandstones (Sl) are found, which may be overlain by very thin, usually thinner than 10 cm, beds of homogenous to laminated claystone (F). Ripple cross-laminated sandstones can show distinctive ripples (Fig. 3.3a). On the gamma-ray, LA-1 is characterized by a rather blocky shape, with values that rarely exceed 90 API (Fig. 3.3e).

Petrographic analysis on 35 samples from LA-1 reveals that sandstones are mostly sublitharenites, with few samples that can be classified as litharenites and subarkoses (Fig. 3.8b). Lithic fragments range from 5 to 50% of the total detrital composition, where silt/sandstone and dolomite detrital grains represent the most dominant clasts. 134 measurements of preserved cross-set (Sx) thickness allow the reconstruction of bankfull flow depth of ~ 2.2 ±1.283 m (df. Bridge &and Tye, 2000; Bradley and Venditti, 2017).

Interpretation: The abundance of cross-stratified sandstones in LA-1, the presence of intraclasts, and moderate sorting in a continental setting suggest deposition via fluvial processes. The different sedimentary structures encountered in LA-1 indicate these rivers had variable discharge velocities. Cross- stratified sets and co-sets (Sx and Sxl) compose channel floor elements suggesting deposition under a lower flow regime. Horizontal-stratified (Sh) and ripple cross laminated sandstones (Sl and Slb) usually compose the top of subaqueous bedforms and indicate deposition under lower flow regime (Fielding, 2006). The presence of fine-grained ripple cross-laminated (Sl) sandstones on top of cross- stratified sandstone (Sx) might represent bars that fine upwards into supra-platform deposits with periodical emergence (Steel and Thompson, 1983). Laminated claystone draping upper bar topography records deposition under very low energy discharge via suspension settling (Bridge, 2006).

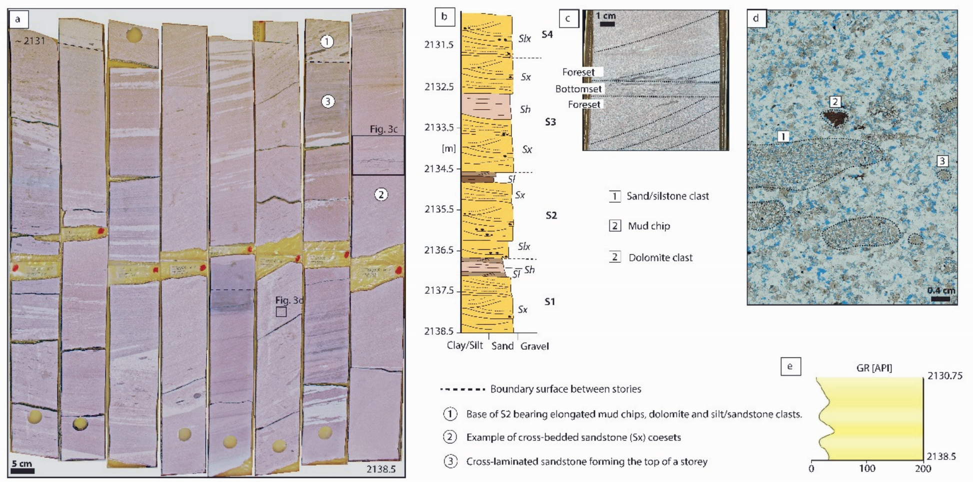

Figure 3.3: Stacked stratified sandstone (LA-1). a) Example of LA-1 from well NDW-01 where dashed black lines represent the limit between storeys. b) Simplified sedimentary log displaying the succession of 3 storeys stacked on top of each other. Abbreviations are listed in Fig. 3.2. c) Bottomset foreset transition. See Fig.3.3a for location. d) Example of texture and intraclasts from a pebbly sandstone (Slx). See Fig. 3.3a for location. e) Gamma ray profile of the core slabs displayed in Fig. 3.3a.

In well NDW-01, to the southeast, the occurrence of oxidized sandstones with pairs of laminae that show normal grading and bimodal grain size distribution suggests subaerial exposure with aeolian sediment transport by saltation and suspension (Henares et al., 2020). This would indicate that sediments were periodically reworked and deposited through aeolian process, possibly in an interfluvial environment as recorded in many dryland settings (Mountney and Thompson, 2002; Bourquin et al., 2009; Cain and Mountney, 2009; Henares et al., 2014).

The dominance of medium to coarse-grained bedload material, the absence of fining-upward profile, the cm- to dm-scale thickness preservation of the cross-stratified sets, the near absence of preserved mudstone and the high degree of amalgamation indicate that LA1 was deposited by rivers that were shallow and highly mobile (Steel and Thompson, 1993; Gibling, 2006; Sambrook et al., 2006; Bourquin et al., 2009; Limaye, 2020). This may be related to: i) a high energy braided fluvial system and the presence of non-cohesive erodible banks (North and Taylor, 1996); ii) high rate of deposition as result of ephemeral flows and low accommodation rate that forced the rivers to frequently shifting thereby eroding the floodplain (Mackey and Bridge, 1995; Bryant et al., 1995; Postma, 2014).

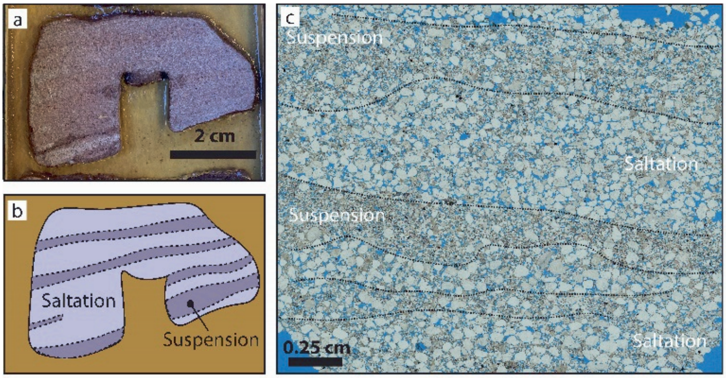

Figure 3.4: Example of saltation and suspension deposited laminae from well NDW-01. a,b) Raw and interpreted core sample. c) Thin section from the sample in Fig. 3.4a. Pair of laminae where a lower well sorted laminae is deposited via saltation and an upper moderately sorted laminae is developed via suspension.

3.4.1.2 Fining-upward sandstone (LA-2)

Lithofacies association 2 (LA-2) is composed of very-fine to medium-grained sandstones organized in fining-upward successions with gravel lithofacies (G and Gs) observed at the base (Fig. 3.5a and b). LA-2 occurs either as single units of 2-3 m in thickness (Fig. 3.9b) vertically enclosed between floodplain deposits or stacked on top of each other composing multi-storey intervals of up to 6-7 m thickness. The lower part of each storey is formed by sharp-based gravel lithofacies (G and/or Gs) or pebbly cross-stratified medium to fine-grained sandstones (Slx). These lithofacies types usually contain poorly sorted, subangular to subrounded mud chips, silt/sandstone and dolomite clasts with diameters that can reach up to 3-4 cm (Fig. 3.5c and d). Locally, large (4-5 cm) mud clasts are present within the gravel lithofacies. The central part of the lithofacies association is characterized by an internal arrangement of stacked sets of medium to very fine-grained, moderately to well-sorted cross-stratified sandstones (Sx). The cross-bed sets can form coesets reaching ~ 2 m in thickness. These sandstones may occasionally bear dolomite clasts, micas and mud chips (Fig 3.5a). These are usually subrounded to subangular and below cm-scale, oriented with their longest axis parallel to the foresets. Foresets are either angular or tangential at their bases, lying over bottomsets that can be horizontally or cross-laminated with ripple structures. Cross-stratified sandstones (Sx) may be interbedded at dm to m scale with horizontally-stratified sandstones (Sh) and structureless sandstones (Sm). The upper part of this lithofacies association is dominated by fine-grained ripple cross-laminated sandstones (Sl) grading up into muddy lithofacies. This fine-grained upper section can be bioturbated by insect burrows and rootlets. Locally, claystone can be found directly superimposing the lower part of this lithofacies association. On the gamma-ray, LA-2 typically has a bell shape bounded by high gamma-ray readings at the top (Fig. 3.5e).

Thin section analysis reveals that samples are mostly litharenites to sublitharenites (Fig 3.8b). Rock fragments can make up to 40-50% of the total detrital components, with dolomite and silt/mudstone clasts representing the most abundant classes. An average dune-scale bedform thickness of ~ 0.6 (± 0.7) m based on 58 set thickness measurements suggests a bankfull depth in the order of ~ 4.3 m ±3.692 m (cf. Bridge & Tye, 2000; Bradley & Venditti, 2017).

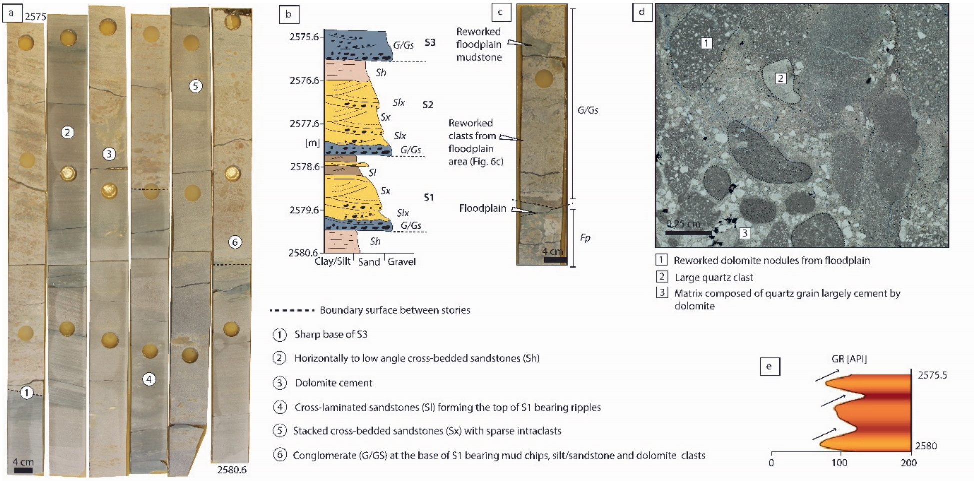

Figure 3.5: Fining-upward sandstone (LA-2). a) Example of LA-2 from KWK-01 where dashed black lines represent the limit between storeys. b) Simplified sedimentary log displaying the succession of 3 storeys stacked on top of each other. Abbreviations are listed in Fig. 3.2. c) Example of gravel facies (G/Gs) overlying floodplain deposits showing soil development (Fp). d) Thin section from a gravel facies (G) from well KWK-01 at the depth of 2552.55 m. Note that most of the intraclasts are composed of dolomite. e) Gamma ray profile of the core slabs displayed in Fig. 3.5a.

Interpretation: The vertical assemblage of lithofacies suggests that these sediments have been deposited by fluvial processes. This lithofacies association is dominated by lithofacies (G, Gs, Slx and Sx) deposited mostly via bedload transport under medium to high-flow discharge (Bridge, 2006). The muddy upper sections of the fining-upward cycles were periodically exposed and locally vegetated, as shown by the presence of rootlets and vertical burrows produced by insects. The fining-upward trends of grain sizes, reconstructed bankfull depth of average ~4 m, presence of bioturbation and preservation of overbank deposits with paleosols suggest a rather perennial nature of these rivers potentially induced by the higher stability of the banks and a less ephemeral discharge.

The presence of poorly-sorted gravel lithofacies (G and Gs) with intraclasts at the base of the sandstone bodies indicates the fill of erosional scours in response to channel incision into adjacent floodplain areas (Gómez-Gras and Alonso-Zarza, 2003). The abundance of argillaceous and dolomite clasts suggests erosion of muddy-dominated floodplains with indurated dolocrete nodules. Locally, the superposition of overbank facies over gravel (G and Gs) and cross-stratified sandstones (Slx and Sx) indicates channel migration or abrupt loss of stream power and infilling of abandoned channels (Toonen et al., 2012).

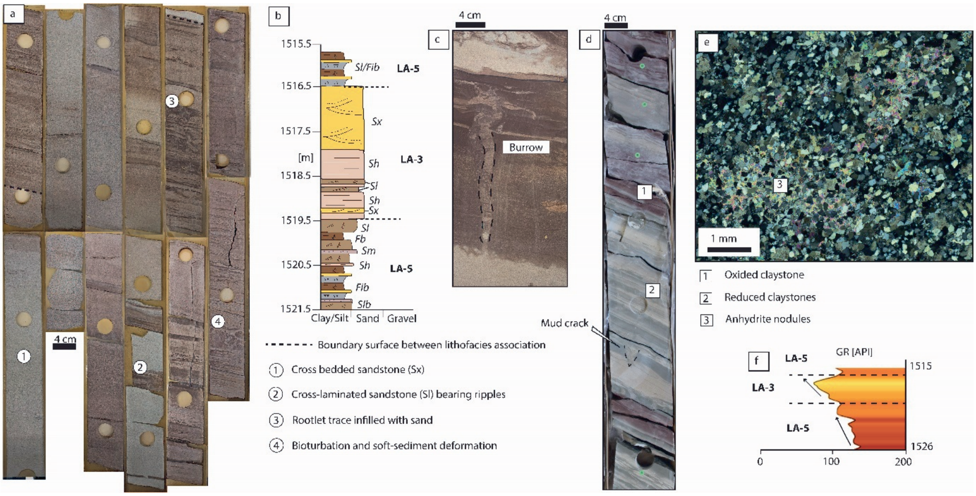

Figure 3.2: Coarsening-upward sandstone (LA-3) and heterolithics (LA-5). a) Example of LA-3 and LA-5 from BUM-01 where dashed black lines represent the limit between the two lithofacies associations. b) Simplified sedimentary log displaying the succession of the two lithofacies associations. Abbreviations are listed in Fig. 3.2. c) Example of a bioturbated claystone (Fb) with a burrow (palaeophycus or planolites). d) Heterolithic interval from well WWN-01-S2. Note the presence of both grey (GLEY 16/5G) and red (2.5YR 4/2) indicating reduced and oxidized conditions respectively. e) Thin section from well BUM-01 at the depth 1502.2 m. The thin section shows the presence of anhydrite nodules. f) Gamma ray profile of the core slabs displayed in Fig.3.6a.

3.4.1.3 Coarsening-up sandstone (LA-3)

Lithofacies association 3 (LA-3) consists of very-fine to fine-grained, moderately to well-sorted sandstones organized into coarsening-upward successions (Fig. 3.6a, b). This lithofacies association occurs only in the BUM-01 well in the northern section of the study area (Fig. 3.1a). The lower part of LA-3 is characterized by an alternation of fine to very-fine ripple cross-laminated sandstones (Sl and Slb), intercalated at cm to dm scale within horizontally-stratified sandstones (Sh), structureless sandstones (Sm), and bioturbated heterolithic deposits (Fib). The heterolithic sediments bear mud cracks and show evidence of soft sediment deformation

(Fig. 3.6a). The upper part of this lithofacies association is characterized by an alternation at m scale of fine to very-fine, cross-stratified sandstones (Sx) and horizontally-stratified sandstones (Sh), which respectively account for 52 and 25% of LA-3 (Fig. 3.9a). These stratified sandstones are usually fine to medium grained and can present a bimodal grain-size distribution organized in pairs of laminae, where the coarser laminae are usually better sorted than the finer ones. The cross-stratified sandstone individual sets are on average 10 cm thick, while the entire sandstone unit can reach up to 3-4 m in thickness (Fig 3.9b). LA-3 is characterized by a funnel wireline profile, with values below 90 API generally found at the top where the cross-stratified sandstones (Sx) occur (Fig. 3.6f).

The analysis of 11 thin sections indicates that sandstones of LA-3 are litharenites (Fig. 3.8d) They are composed of mono- and polycrystalline quartz, and mudstone, dolomite, and silt/sandstone fragments usually smaller than 0.5 cm in diameter. Small anhydrite and/or gypsum nodules (< 1 cm) are often present in the cross-stratified sandstones (Sx) of this lithofacies association (Fig 3.4d). The detrital grains are mostly coated with hematite, which gives them a red/brown colour (Fig. 3.6 and c).

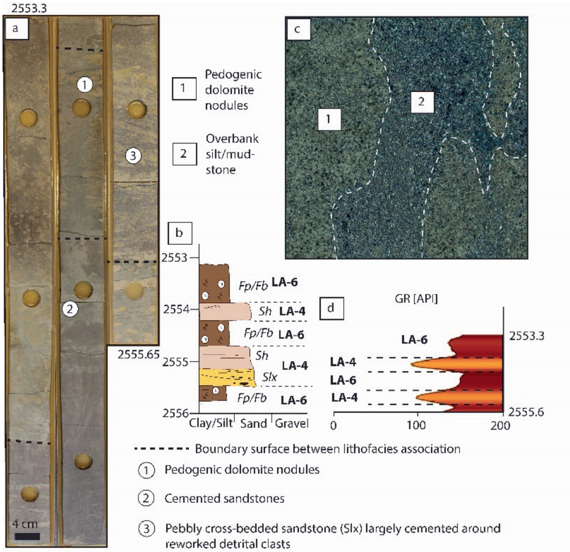

Figure 3.3: Thin-bedded sandstone (LA-4) and bioturbated and pedogenic mudstone (LA-6). A) Example of LA-4 and LA-6 from KWK-01 where dashed black lines represent the limit between the two lithofacies associations. Abbreviations are listed in Fig. 3.2. B) Simplified sedimentary log displaying the succession of the two lithofacies associations. c) Thin section from well KWK-01 at the depth of 2581.55. The thin section shows pedogenic dolomite nodules in a pedogenic mudstone (Fp). D) Gamma ray profile of the core slabs displayed in Fig.3.7a.

Interpretation: Ripple cross-laminated bioturbated sandstones (Slb) and horizontally-stratified sandstones (Sh) are interpreted to have formed from shallow, unconfined flow. The occurrence of Slb and Sh above muddy units (Fib and Fb mainly) indicates a low energy environment, with periodic input of sand transported by traction current. In this context, the mud cracks and hematite coatings suggest periodical subaerial exposure (Walker, 1979). The coarsening upward nature of LA-3 and the presence of heterolithic sediments above and below this facies association are interpreted to be the result of the progradation of the fluvial system into a floodplain area.

Considering the northern position in the basin, the widespread hematite coating, the fine grain size, and the relatively low thickness of the sandstone units, LA-3 is interpreted to be part of terminal-splay complex coalescing into a large arid plain. Similar deposits are as described in ancient and present-day analogues (Parkash et al., 1983; Nichols and Fisher, 2007; Fisher et al., 2008; Cain and Mountney, 2009; McKie, 2011; Voigt, 2017; Donselaar et al., 2022).

3.4.1.4 Thin-bedded sandstone (LA-4)

Lithofacies association 4 is characterized by thin-bedded (~ 0.6 m ± 0.5), very-fine to medium-grained sandstones (Fig. 3.7a and Fig. 3.9b). This lithofacies association is usually embedded in overbank facies (e.g. LA-6). It has a sharp lower boundary, while the upper boundary can be gradational into a sandstone from LA-1 or LA-2. The lower part of LA-4 is usually composed of pebbly (Slx) and structureless sandstones (Sm) (Fig. 3.7a). These lithofacies can contain angular to subrounded intraclasts that range in diameter from few mm up to 3 cm. The sediments where dolomite clasts are abundant are usually cemented (Fig. 3.7a). Cross-stratified and structureless sandstones are overlain by horizontally-stratified (Sh) and ripple cross-laminated (Sl and Slb) sandstones. LA-4 shows gamma-ray values around 100 API (Fig. 3.7c). The 4 thin sections studied for LA-4 reveal a detrital composition where quartz grains account on average for 76 %, silt/mudstone clasts for ~14 % and feldspars for ~ 8% (Fig. 3.8d).
Interpretation: This lithofacies association is interpreted to be formed as a consequence of unconfined flow conditions on the floodplain associated with erosion of the channel levée (Fisher et al., 2007; 2008). In the Roer Valley Graben, this element is usually found in association with channel complexes, suggesting an origin as lateral or terminal splay of the channel (Tooth, 2005). Their sharp basal contact is an indication of high flow energy, supported by the occurrence of rip-up mud clasts and dolocrete clasts in the lower part of LA-4 transported as bedload material.

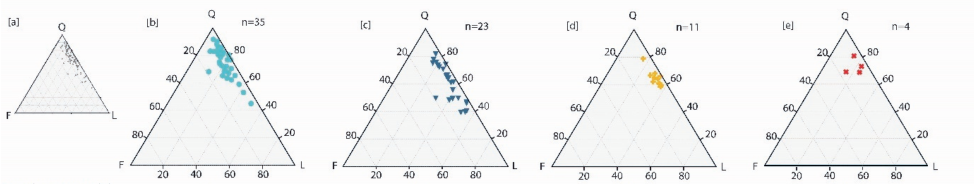

Detrital components (%)	LA-1	LA-2	LA-3	LA-4
Quartz	74.7	63.9	76.7	76.0
Feldspars	5.3	6.2	5.3	8.1
Silt/mudstone	10.3	19.2	16.4	13.8
Volcanic	< 0.1	0.5	< 0.1	< 0.1
Metamorphic	< 0.1	0.60	< 0.1	< 0.1
Dolomite	7	6	< 0.1	< 0.1
Chert	1.07	1.3	1.4	< 0.1
Mica	1.8	2.2	<0.1	2.1

Figure 3.4: Detrital composition data of the sandy lithofacies associations. a) All thin section data. b) Detrital composition data of stacked stratified sandstone (LA-1). c) Detrital composition data of fining-upward sandstone (LA-2). d) Detrital composition data for coarsening-upward sandstone (LA-3). e) Detrital composition data for thin-bedded sandstone (LA-4).

3.4.1.5 Heterolithics (LA-5)

This lithofacies association is characterized by mm to cm scale alternations of bioturbated claystones and sandstones (Fib, Fb), (bioturbated) ripple cross-laminated sandstones (Slb) (Fig. 3.6a and b). Horizontally-stratified sandstones (Sh) and homogeneous sandstones (Sm) rarely occur. Lamination can be lenticular to wavy. Claystone can be reddish (5YR 4/4), brownish (7.5YR 2.5/3) to greyish (GLEY 1 6/5G) in colour (Fig. 3.6a, c and d). Injection structures and mud cracks are encountered (Fig 3.6d) and are usually few cm in vertical length and diameter. These structures are infilled with sand or silt. Burrows and rootlets are occasionally encountered (Fig. 3.6a and c). Burrows are usually 3-4 cm in length, while rootlets can reach 10-15 cm. LA5 is characterized by an alternation of high (> 125 API) and intermediate (100> API >125) readings (Fig. 3.6f). This lithofacies association can be up to 10 m thick when composed of multiple beds. Fib and Slb represent the most dominant lithofacies, accounting for 49% and 28% of the lithofacies assemblage (Fig. 3.9a).

Interpretation: The heterolithic sediments of LA-5 record episodic density currents formed in a low-energy environment. Mud is deposited through waning flow, whereas sand is periodically transported and deposited by traction currents. Occasionally, the environment of deposition was favorable for life, as indicated by the presence of burrowing and partially vegetated as indicated by the rootlets. The presence of mud cracks and extensive oxidized intervals suggest subaerial exposure (Walker, 1979).

The sharp, or undulating, bases and repeated alternation of sandstones and mudstones indicate high discharge flows entering a shallow-water environment, such as a small pond or playa-lake (Rogers and Astin, 1991; Clemmensen et al., 1998; Zhang et al., 1998). In well WWN-01, mudstones are mostly blue to grey suggesting mostly reducing, thus subaqueous conditions. In well BUM-01, the presence of hematite coatings around the sandstone grains, mud-crack structures, and gypsum/anhydrite nodules in the sandstones (Fig. 3.6e) indicates subaerial exposure, likely on arid mudflats (Zhang et al., 1998).

3.4.1.6 Bioturbated and pedogenic mudstone (LA-6)

This lithofacies association is characterized by a cm to m alternation of bioturbated and pedogenic claystone, siltstones, and sandy siltstone beds (Fig. 3.7a and b). Primary sedimentary structures are obscured, overprinted by the intense bioturbation and pedogenesis. Colour mottling is frequent with matrix colour ranging between reddish (5YR 4/4) to greyish (GLEY 1 5/N). Burrows and rootlets represent the main type of bioturbation activity. Often, dolomite pedogenic nodules are present reaching 5-6 cm in size (Fig. 3.7a and c). On the gamma-ray, LA6 shows values above 120-130 API (Fig. 3.7d).

Interpretation: The lithofacies assemblage, fine grain size, and intercalation with LA-2 and LA-4 suggest deposition via suspension in a floodplain area. The absence of primary depositional structures, and the presence of bioturbation, colour mottling, and pedogenic nodules indicate soil-forming processes (Bourquin et al., 2009; Henares et al., 2020). The presence of dolomite nodules in the paleosol is likely related to precipitation under phreatic diagenetic conditions, with the incorporation of Mg into soil carbonate cement (Casado et al., 2014). These processes are enhanced in alkaline conditions in arid to semi-arid settings (Spötl and Wright, 2003). The presence of this lithofacies association on top of medium-grained cross-stratified sandstones (Sx) indicates that LA-6 could also form as mud plugs as a result of channel abandonment.

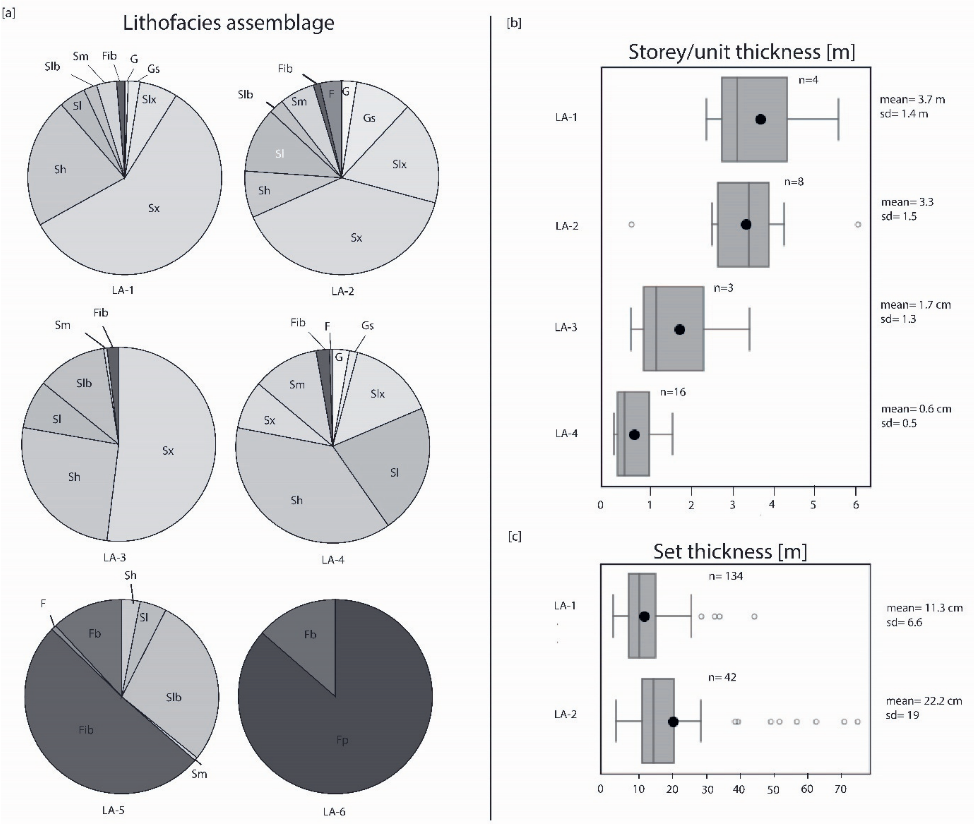

Figure 3.9: a) Relative abundance of different lithofacies in each lithofacies association. Abbreviations are listed in Fig. 3.2. B) Sandstone thickness for the sandy lithofacies association. For LA-1 and LA-2 these values refer to each singular storey. For LA-3 and LA-4, these values refer to the thickness of the entire sandstone unit. c) Individual set thickness for LA-1 and LA-2.

3.4.2 Main Buntsandstein Lithostratigraphy in the Roer Valley Graben

A lithostratigraphic correlation between wells is conducted to assess how lithofacies associations are distributed across the Roer Valley Graben and throughout the Main Buntsandstein Subgroup stratigraphy. First, the Main Buntsandstein Subgroup top and base boundaries have been identified in all the wells adopting the scheme proposed by Van Adrichem Boogaert and Kouwe (1993). The wells L02-01 and BUM-01 have been used as proxies (Fig. 3.10), as they record a typical Main Buntsandstein sedimentary section (Van Adrichem Boogaert and Kouwe, 1993). Following the same logic, the Main Buntsandstein Subgroup internal stratigraphic subdivision has been evaluated, and the lithofacies association distribution assessed.

3.4.2.1 Top and Base Main Buntsandstein Subgroup

The Main Buntsandstein Subgroup is enclosed between the Lower Triassic Rogenstein Formation and the Upper Triassic Solling Formation (Van Adrichem Boogaert and Kouwe, 1993). In the Roer Valley Graben, the boundary with the Rogenstein Formation is marked by a sharp decrease in gamma-ray values from the claystones with oolite intercalations of the Rogenstein Formation (Palermo et al., 2000) with API values above ~120-130, to the sandstones of the Volpriehausen Formation with API values below ~70-80 (Fig. 3.10). This boundary is less pronounced in the southeastern part of the Roer Valley Graben (i.e. NDW-01 in Fig. 3.10) where the Rogenstein formation becomes more sandy (Palermo et al., 2000) and display lower average gamma ray values.

The upper boundary of the Main Buntsandstein is generally associated with the Hardegsen Unconformity in many basins across Europe (Bourquin et al., 2011). In the Roer Valley Graben, this unconformity has not been observed (Cecchetti et al., in press) and the Hardegsen Formation appears to be conformably overlain by the Solling Formation. The Solling Formation in the Roer Valley Graben is composed of a 2-3 m thick lower sandy member (Basal Solling Sandstone Member) overlain by a ~10-20 m unit composed of silt/claystones interpreted as the Solling Claystone Member (Van Adrichem Boogaert and Kouwe, 1993). The sandstones from the Basal Solling Sandstone Member are stacked on top of the sandstones of the Hardegsen Formation, making the boundary between the Solling and Hardegsen Formations uncertain to define in the Roer Valley Graben. Thus, we decided to group the Basal Solling sandstones with the Hardegsen Formation (H+BSS in Fig. 3.10). This allows to take the top of the highest sandstone below the Solling Claystone Member as the marker of the top of the Main Buntsandstein Subgroup.

3.4.2.2 Main Buntsandstein Subgroup Lithostratigraphy

The Volpriehausen and Detfurth Formations are each typically formed by a basal sandstone member and an upper claystone member (e.g. L02-01 in Fig. 3.10). In the proximal, southwestern part of the Roer Valley Graben, the Volpriehausen and Detfurth Formations form a continuous sandstone unit, composed of fluvial sandstones (LA-1) with gamma-ray values below ~70-80 API that reaches a maximum thickness of ~ 200 m in BKZ-01 (Fig. 3.10). Locally, silt-clay intercalations at dm to m scale cause gamma-ray values to increase up to ~ 100-110 API. The blocky profile on the gamma ray and the absence of significant claystone lithologies indicate that the claystone members are substituted by their lateral equivalent sandy basin-fringe unit (Van Adrichem Boogaert and Kouwe, 1993). In this context, it is difficult to define formation boundaries given the prevalence of sandy lithologies. Thus, we have group the Volpriehausen and Detfurth Formations in the most proximal part of the Roer Valley Graben (VS+DS in Fig. 3.10).

In the distal sector of the Roer Valley Graben, a ~10-15 m interval of playa-lake (LA-5) sediments (VC2 in Fig. 3.10) seems to separate the Volpriehausen Formation from the Detfurth Formation and allows a tentative lithostratigraphic subdivision. In this area, the Volpriehausen Formation ranges in total thickness between ~60 to ~75 m and is argued to be composed of two sandstone units (VS1 and VS2) with a generally blocky gamma ray profile and API values lower than ~90. These two sandstone units are largely composed of stacked stratified sandstones (LA-1) and show average thicknesses of ~25 m per unit across the distal area. In the northern part of the distal sector, the lithofacies association composition of the Volpriehausen Sandstone units changes. VS1 shows a bell profile on the gamma-ray suggesting fining-upward sandstones (LA-2), while VS2 shows a funnel-shape gamma ray profile indicating coarsening-upward sandstones (LA-3).

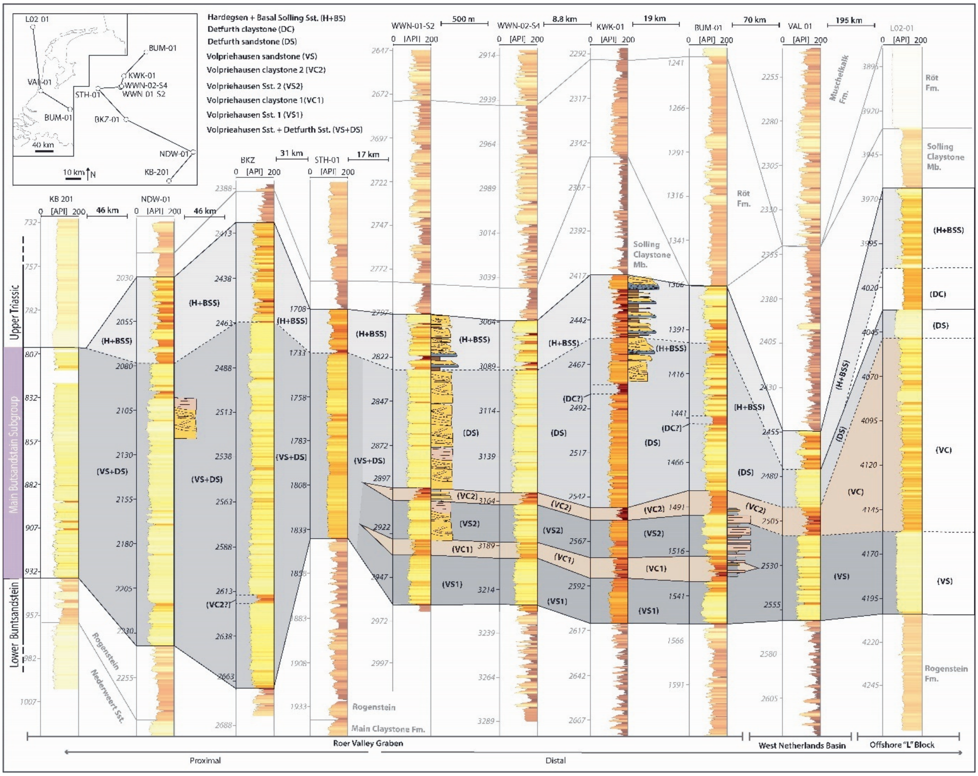

Figure 3.10: Panel displaying the Buntsandstein lithostratigraphy across the study area. Well VAL-01 from the West Netherlands Basin and well L02-01 from offshore "L" block are included for regional correlation. The sedimentary logs are displayed next to the gamma-ray where core samples have been interpreted. See the text for full description.

In the Roer Valley Graben, VS1 and VS2 are respectively overlain by a claystone interval that is defined here as the Volpriehausen Claystone unit (VC1 and VC2 in Fig. 3.10). The gamma-ray profile of the Volpriehausen Claystone units is formed by an alternation of peaks (> 125 API) and troughs (100> API >125) readings. These peaks and troughs display similar profiles and values over a distance of ~500 m (e.g. WWN-01-S2 and WWN-02-S4 in Fig. 3.10). The two Volpriehausen Claystone units range from 10 to 15 m in thickness and display a general thickening from south to north. The transition from the Volpriehausen Claystone (VC1) to the Volpriehausen Sandstone (VS2) is generally gradual.

The character of the Volpriehausen Formation changes in the adjacent West Netherlands Basin and offshore the Netherlands (Fig. 3.10). In these areas, the Volpriehausen Formation is instead formed by the characteristic Main Buntsandstein Subgroup profile of a single basal sandstone of ~50 m in thickness and an upper claystone that reaches about 100 m offshore the Netherlands.

The Detfurth Formation has a blocky gamma-ray profile in the Roer Valley Graben and is largely composed of stacked fluvial sandstones (LA-1) with a total thickness that ranges from

~60 to 75 m (DS in Fig. 3.10). The dominance of sandy lithologies in the Roer Valley Graben seems to indicate that the Detfurth Claystone observed offshore the Netherlands is absent in this area and in the adjacent West Netherlands Basin (Fig. 3.10). To the north of the Roer Valley Graben, the average N/G of the Detfurth Formation decreases, and low gamma-ray readings (~70-80 API) are locally alternated with high gamma-ray (~140-150 API) intervals. These high gamma-ray intervals are on average 1-2 m thick, but they can reach 7-8 m (e.g. KWK-01 and BUM-01 in Fig. 3.10). Although it may be tentative to correlate these high gamma ray intervals with the Detfurth Claystone observed offshore the Netherlands, the absence of core data makes such correlation speculative.

The lower boundary between the the Volpriehausen Claystone unit 2 (VC2) and the Detfurth Sandstone unit (DS) is generally characterized by a sharp decrease in gamma-ray readings from 160-170 API for the VC2 to ~60-70 API for the DS. This likely represents the fluvial system building out while the playa-lake system retreats. To the north, the transition from VC2 to DS becomes gradual. The boundary between the Detfurth Formation and the overlying Hardegsen Formation is characterized by an increase in average gamma-ray of 40-50 API. This reflects the increase in claystone lithologies in the Hardegsen.

The Hardegsen Formation (H+BSS) is composed of an alternation of fluvial sandstones (LA-2), crevasse splays (LA-4), and paleosols (LA-6). The formation thickness ranges from ~25 to over 50 m in certain wells located in the proximal area (e.g. BKZ-01 in Fig. 3.10). It is distinguished from the underlying Detfurth Sandstone due to the lower N/G and the presence of paleosols. Fluvial sandstone units have on average values below ~80-90 API and can be stacked forming complexes up to ~9-10 m. These are embedded in claystone units with gamma-ray readings larger than ~110-120 API and thickness up to ~4-5 m.

3.5. Discussion

3.5.1 Regional depositional model

Three conceptual depositional models are proposed to explain the processes responsible for the deposition of the different lithofacies associations observed in the Main Buntsandstein Subgroup in the Roer Valley Graben (Fig. 3.11). The first two models represent depositional environments for the Volpriehausen and Detfurth Sandstone and Claystone units respectively, while the third represents depositional environment for the Hardegsen Formation.

3.5.1.2 Deposition of the Volpriehausen and Detfurth Sandstone units

The Volpriehausen and Detfurth Sandstone units are dominated by vertically-stacked fluvial sandstones representing deposition through high-energy, shallow rivers (Fig. 3.11a). The multistorey character, high degree of vertical amalgamation, lack of grain size trends, and high mobility of these channels suggest that these river systems were likely to be braided, as exemplified in many other adjacent Triassic basins (Ames and Farfan, 1996; Bourquin et al., 2007). The mobilization was likely enhanced by the presence of poorly consolidated banks due to the absence of vegetation and the sandy character of the interfluve environment (Steel and Thompson, 1983; Hassan, 2005; Gibling, 2006; Bourquin et al., 2009). The sandy interfluve environment was the locus for the formation of dolocrete, which subsequently was reworked and deposited within the channel sequences. This process is commonly observed in dryland systems (Molenaar and Felder, 2019) and, more particularly, in Triassic systems across northern European basins (Spotl and Wright, 1992; Schmid et al., 2006; Bertier et al., 2022).

Sediments in the Roer Valley Graben were sourced from the Variscan relicts as suggested by a general decrease in N/G from south to north. This is in agreement with previous regional palaeogeoraphic reconstruction at Germanic Basin scale (McKie and Williams, 2009; Bourquin et al., 2011; Olvarius et al., 2017). To the southeast, the Roer Valley Graben represented the gateway for the sediments from the Armorican and Rhenish Massifs to enter the Germanic basin. Once entered the Roer Valley Graben, rivers were likely flowing on average to NW, semi-parallel to the main fault trend (Cecchetti et al., 2024), like also suggested by the models of Geluk (2005) and IF Technology (2012). These long-drainage systems (~300-400 km) resulted in an overall high maturity of the sediments with a high level of sorting, roundness, and high percentage of quartz grains.

The London-Brabant Massif was also a prominent structure during the Middle Triassic (Geluk et al., 2005; McKie and Williams, 2009). Considering its position and the half-graben setting, the London-Brabant Massif may have contributed to feeding sediments to the Roer Valley Graben. Sediments were likely transported northwards by fluvial fan systems as suggested by Carter et al. (1990). However, these fan systems did not represent the major transport system in the Roer Valley Graben, Instead, they only represent a transverse zone located in the part proximal to the London-Brabant Massif feeding sediments to the major axial rivers flowing semi-parallel to major fault lineaments, with greater sediment accumulation occurring in the more subsided hanging wall blocks, a process commonly observed in half-graben settings (Gawthorpe and Leeder, 2000). Unfortunately, the erosion of Buntsandstein sediments along the northern margin of the London-Brabant Massif does not allow us to further investigate this observation.

The Early to Middle Triassic was a period characterized by widespread arid to semi-arid conditions across the Germanic basin (Peron et al., 2005), with seasonal wetness enhanced by summer monsoons (Van der Zwan and Spaak, 1992). The very scarce presence of vegetation, absence of soil formation and sparse occurrence of aeolian sediments in the Volpriehausen and Detfurth Formations would support the rather arid climatic conditions. In the Roer Valley Graben, evidence of aeolian sedimentation has been found only in the southeastern part (Fig. 3.11a). The absence of aeolian sediments in the central part of the Roer Valley Graben may be related to the presence of basement massifs such as the London-Brabant Massif, acting as windshield and partly deflecting wind directions (Mader and Yardley, 1985) or simply the strong dominance of fluvial processes in the area given the proximity to the London-Brabant Massif source. Furthermore, the reductive colours of the fluvial sandstone in the north-west suggest more prolonged subaqueous conditions, thus less exposure to subaerial conditions and wind action. This could be the result of i) higher water discharge from the hinterland in relation to frequent precipitations during monsoon season (van der Zwan and Spaak, 1992); ii) shallower groundwater level considering the proximity to the recharge area; iii) the presence of faults located along the southern margin of the Roer Valley Graben (Cecchetti et al., in press) potentially inducing upward water flow from the deeper reservoirs (Verweij, 1993).

Along the northern flank of the Roer Valley Graben, the average low N/G indicates that the northern sector was an area subjected to sedimentation of fine-grained sediments (Cecchetti et al., 2024). The presence of terminal splays and fining-upward sandstones in BUM-01 suggests the northern sector to be more distal and tectonically less active side of the basin, as supported by the absence of syn-sedimentary faults in this area. The occurrence of mud cracks and hematite-coated sediments indicates more frequent subaerial conditions than to the south where sandstones and claystones show reducing colours. The exposure to subaerial conditions can be related to a higher topographic position of the northern area of the Roer Valley Graben given the vicinity to the Central Netherlands Swell, a high topographic element during the Early to Middle Triassic times where only minor Buntsandstein sedimentation occurred (Geluk and Röhling, 1997). Unfortunately, the erosion of Lower Triassic sediments across the Roer Valley Graben flanks does not allow to further investigate this observation.

3.5.1.2 Deposition of the Volpriehausen Claystone unit

This model is representative for the deposition of ~ 10-15 m of playa-lake sediments in the central and northern part of the study area (Fig. 3.11b). The establishment of playa-lake conditions in the Roer Valley Graben is likely the product of repeated flash floods as a result of higher precipitation rates in the hinterland (Peron et al., 2005). The occurrence of oxidized and reduced mudstones indicates that sediments were exposed to both subaerial and subaqueous conditions. The presence of burrows and rootlets indicates that the environment was favourable for the formation of life. On average, the playa-lake claystones in the central part of the Roer Valley Graben show more reducing colours than in the northern part where sediments are largely oxidized. Thus, the water level was likely higher and more long-lasting in the central part of the Roer Valley Graben, while the northern sector was subjected to more frequent drainage (Fig. 3.11b). This can be a consequence of: i) shallower groundwater level closer to the London-Brabant Massif; ii) low topographic elevation induced by higher subsidence rates in the central part of the Roer Valley Graben creating a depression area where water accumulated

Sands were periodically fed to the playa-lake through low-relief deltas as suggested by the coarsening-upward sandstone successions alternating with playa-lake sediments observed in the northern sector of the study area. The playa-lake sediments of the Volpriehausen Claystone units thin out and then disappear to the south (Fig. 3.10). The absence of playa-lake sediments along the southern margin of the Roer Valley Graben is likely dictated by the more proximal position in the basin, where sedimentation via fluvial processes was dominant. No clear evidence of the occurrence of Detfurth Claystone has been observed in the Roer Valley Graben, while this unit is present in the offshore sector of the Netherlands. This suggests that during the deposition of the Detfurth Formation, the Roer Valley Graben was an area subjected to fluvial activity, while playa-lake sedimentation was more restricted to the northern distal area of the Netherlands (i.e. well L02-01 in Fig. 3.10).

The presence of similar playa-lake sedimentary structures and gamma-ray patterns in many wells across the Roer Valley Graben, the West Netherlands Basin, and other onshore and offshore basins in the Netherlands (Ames and Farfan, 1996; Kortekaas et al., 2018), indicates a large lateral extent of the same sedimentation conditions. The thickening of these sediments to the north (e.g. L02-01 in Fig. 3.10) suggests that playa-lake sedimentation was more pervasive and likely prolonged in the northern part of the Netherlands, while the Roer Valley Graben was more frequently interrupted by fluvial deposition. This is further supported by the presence of oolite and Avicula beds offshore in the Netherlands indicating the establishment of more perennial lacustrine conditions (Van Adrichem Boogaert and Kouwe, 1993).

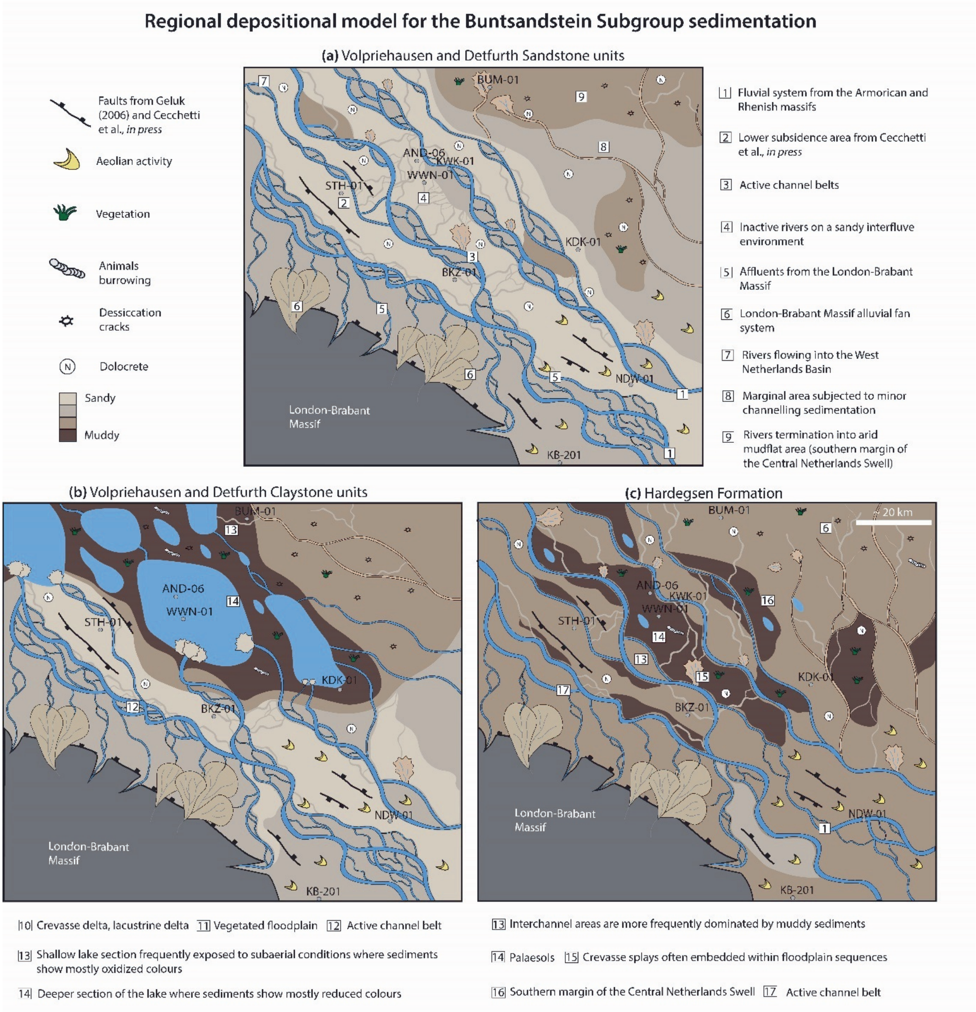

Figure 3.11: Conceptual depositional model for the Main Buntsandstein in the study area. a) Depositional model for the deposition of the Volpriehausen and Detfurth Sandstone units in the study area. b) Depositional model for the deposition of the Volpriehausen and Detfurth claystone units. c) Depositional model for the deposition of the Hardegsen Formation.

3.5.1.3 Deposition of the Hardegsen Formation

This depositional model is representative for the upper part of the Buntsandstein stratigraphy, where the fining-upward nature of the fluvial sandstones, the preservation of overbank sediments and the development of paleosols indicate deposition via rivers that were more perennial and laterally stable than the rivers responsible for the deposition of the Volpriehausen and Detfurth Formations (Fig. 3.11c). The formation of soils with fine sediments and rootlets enhances the cohesivity of the banks, limiting channel breaching and frequent shifting across the river plain.

Nonetheless, the paleosols were frequently affected by periods of river erosion. This is indicated by the presence of scour deposits at the base of the sandstone bodies with large intraclasts reworked from the surrounding overbank areas. Frequent interbedded crevasse splays suggest water escaping the main channel, which subsequently may act as an avulsion site for the channel to migrate giving rise to a new active branch of the river system (Field, 2001).

The Hardegsen Formation may represent a period in time during which a less arid climate (Bourquin et al., 2011) and reduced tectonic activity (Geluk, 2005) enhanced the development of a more stable fluvial system in the Roer Valley Graben. A change in climatic conditions and fluvial style during the deposition of the Hardegsen has been reported in many Triassic basins (Bourquin et al., 2011 and references therein). Bourquin et al. (2009) observed paleosol development in the northern part of France at the top of the Buntsandstein, suggesting a decrease in aridity upwards through the Buntsandstein stratigraphy in northern France. Such a change in climate seems also to be reflected in a different fluvial style, with channels more laterally stable and with higher average sinuosity (Mader, 1982).

3.5.2 Reservoir architecture and sedimentary heterogeneities

The Buntsandstein Subgroup experienced significant burial up to 3-4 km (Cecchetti et al., 2024) that has partially deteriorated reservoir quality. An interplay of compaction and cementation processes resulted in an overall reduction of porosity and permeability (Zijerveld et al., 1992; Purvis and Okkerman, 1996; Mijnlieff, 2020; Bertier et al., 2022). Nonetheless, sandstones from the Main Buntsandstein Subgroup in certain wells across the southern part of the Netherlands (e.g. SPC-01) show porosities up to 20% and permeability values over 250-300 mD (www.nlog.nl).

In the Roer Valley Graben, the main reservoirs in the Buntsandstein Subgroup occur in fluvial sandstones (LA-1 and LA-2). However, terminal splay deposits in BUM-01 (LA-3) may represent additional reservoirs where these elements form stacked complexes. Fluvial sandstones yield the largest scatter in values with porosity ranging between 2.6% and 19.2% and permeability between 0.02 and 752 mD (Fig. 3.12). Overall LA-1 shows higher porosity and permeability values (av. 13% and 109 mD) than LA-2 (av. 8.1% and 2 mD). The porosity and permeability of terminal splay sandstones average with 15% and 60 mD. We acknowledge that diagenesis has a large impact on the Buntsandstein reservoir quality (Purvis et al., 1996; Geluk, 2005; Mijnlieff, 2020). However, its effect on present-day reservoir quality is beyond the scope of this work that focuses on the reservoir architecture and the primary heterogeneities.Each sandstone type developed its own reservoir architecture with its set of heterogeneities (Fig. 3.13, 14 and 15) that will subsequently be discussed.

3.5.2.1 Reservoir architecture style: stacked amalgamated sandstones

This type of reservoir architecture is formed by stacked stratified fluvial sandstone bodies (LA-1) and mostly occurs in the Volpriehausen and Detfurth Formations. In the proximal area of the Roer Valley Graben, where the Volpriehausen and Detfurth Formations form a single sandstone unit (VS+DS in Fig. 3.10), the architecture of the reservoir interval is mainly represented by a single continuous sandstone unit of ~ 200 m in thickness. In the wells located across the distal part, this continuous sandstone unit splits into thinner (~30 to 60 m) sandstone units separated by the 10-15 m thick playa-lake units (LA-5) (Fig. 3.13a). These fine-grained playa-lake sediments seem to be laterally present over distances of ~20-30 km

(Fig.3.10) and are usually characterized by low permeability values (av. ~4 mD). Therefore, these playa-lake sediments, if continuous, can form an important heterogeneity at km scale, by compartmentalizing the reservoir units and hamper vertical fluid flow.

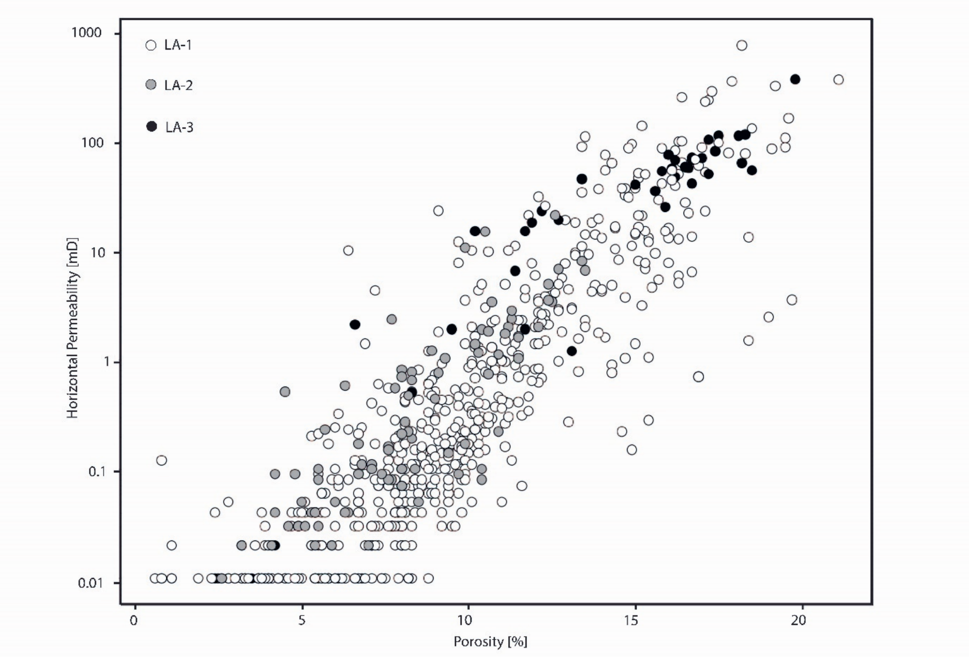

Figure 3.12: Conceptual model representing architecture and sedimentary heterogeneities of stacked amalgamated sandstone reservoirs. a) Field-scale architecture with main reservoir bodies composed of stacked stratified sandstone bodies. The panel is semi-perpendicular to the average paleoflow direction. b) This figure represents the internal lithofacies assemblage and heterogeneities within LA-1. c) Boxplots displaying permeability and porosity of the main lithofacies occurring in this lithofacies association. The black dot represents the mean and the line within each box is the median. d) Typical example of sorting and grain size variation in the cross-stratified sandstones (Sx) that may result in preferential fluid pathways. Thin section from well NDW-01 at the depth of 2120.75 m. e) An example of vertical barrier where a mud drape overlies a fine-grained ripple cross-laminated sandstone. The thin section is from well NDW-01 at the depth of 2137.20 m.

The lateral extent of the reservoir units could not be quantified based solely on the available data. The analysis dune-scale bedforms suggests a width in the order of ~1375 ±1022.4 m for the active channel belts based on empirical relations (Bridge and Tye, 2000). This would be in agreement with the dimensions of ancient and present-day channel-belt dimensions in such arid to semi-arid endorheic basins (Gibling, 2006). Furthermore, Cecchetti et al. (in press) show how the Buntsandstein reflectors are laterally continuous over 5 to 10 km, which would support the presence of similar sedimentation conditions over such a scale. The connectivity of the sandstone bodies is also a function of N/G, where connectivity is usually greater than 90% if N/G is above 30% for randomly distributed sandstone objects (Larue and Hovadik, 2006). In the Roer Valley Graben, the Volpriehausen and Detfurth Formations show N/G largely above 30%, especially in the proximal area where these two form a continuous sandstone unit (Cecchetti et al., *in press*). Therefore, considering the high mobility of these channels, reflector continuity, and the N/G across the Roer Valley Graben, sandstone bodies are likely to be connected horizontally at km scale.

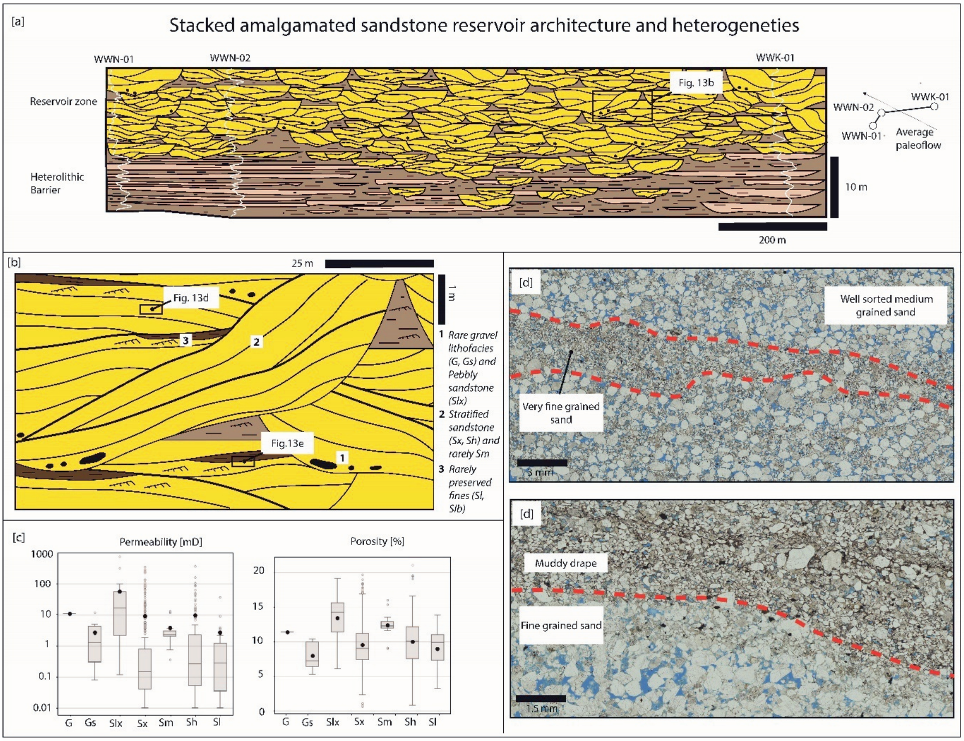

Figure 3.13: Conceptual model representing architecture and sedimentary heterogeneities of stacked amalgamated sandstone reservoirs. a) Field-scale architecture with main reservoir bodies composed of stacked stratified sandstone bodies. The panel is semi-perpendicular to the average paleoflow direction. b) This figure represents the internal lithofacies assemblage and heterogeneities within LA-1. c) Boxplots displaying permeability and porosity of the main lithofacies occurring in this lithofacies association. The black dot represents the mean and the line within each box is the median. d) Typical example of sorting and grain size variation in the cross-stratified sandstones (Sx) that may result in preferential fluid pathways. Thin section from well NDW-01 at the depth of 2120.75 m. e) An example of vertical barrier where a mud drape overlies a fine-grained ripple cross-laminated sandstone. The thin section is from well NDW-01 at the depth of 2137.20 m.

The permeability structure of stacked amalgamated sandstone reservoirs is partially driven by the lithofacies and grain size dependency of the sandstone bodies, with the average permeability value decreasing from coarse to finer lithofacies. Pebbly sandstones (Slx) have the highest average permeability and porosity, with means of ~ 56 mD and 13.4% respectively (Fig. 3.13c). Cross-stratified (Sx) and horizontally- stratified sandstones (Sh) are the most abundant lithofacies in stacked amalgamated sandstones, thus they compose the core of the reservoir units. These two lithofacies have permeability means of ~90.5 and ~10 mD respectively, with standard deviations of ~30 and ~37 (Fig. 3.13b and c). Such a scatter of permeability values could be related to: i) rhythmic variation in grain size and sorting between foresets cross-laminae and bottomsets producing interstitial fluid-flow anisotropy (Fig. 3.13d) (McKinley et al., 2011); ii) different burial history in the basin resulting in diverse diagenesis-related heterogeneities. The rest of the lithofacies that compose the lower and middle part of the reservoir body have mean permeability values ranging between 0.1 and 10 mD and porosities between 7 and 12.5%. At the scale of the individual sandstone bodies (Fig. 3.13b), fine-grained deposits that drape bar elements, or channel plugs represent the main heterogeneities that can behave as baffles. These elements are generally formed by an assemblage of bioturbated ripple cross-laminated sandstones (Sl) and homogeneous laminated claystone (F), which yield values of permeability below 0.1 mD (Fig. 3.13e).

3.5.2.2 Reservoir architecture style: compensational stacked sandstones

This reservoir architecture is mainly composed of fining-upward sandstones (LA-2) and mainly occurs in the Hardegsen Formation. However, this type of architecture can also be found in the Volpriehausen and Detfurth Formations along the northern margin of the Roer Valley Graben (e.g. BUM-01 in Fig. 3.10). The architecture is characterized by sandstone units that can reach vertical thicknesses of ~ 9-10 m and can be embedded in overbank sequences bearing paleosols up to 2-3 m thick that may lower the vertical connectivity of the reservoir units (Fig. 3.14a).

The common preservation of floodplain sediments results in N/G values generally below ~0.6/0.7 for the Hardegsen Formation. A more heterogenous lithology is also supported by the presence of disrupted reflectors over distances below 1 km and frequent amplitude contrasts (Cecchetti et al., in press). This indicates a more uncertain sandstone connectivity over spacings of a few hundred meters and that preserved remnants of floodplain deposits may represent major boundaries to vertical fluid flow if these are laterally continuous. Nonetheless, when sufficiently permeable, crevasse sandstones (LA-5) can enlarge the recovery volume and help increase sandstone connectivity (Fig. 3.14b) (Larue and Hovadik, 2006; Colombera et al., 2021).

Internally, the permeability structure of the sandstone units is less depositional fabric dependent compared to the stacked amalgamated sandstones (Fig. 3.14c). The coarser part of these sandstone bodies that is largely composed by gravel (G and Gs) and sandy lithofacies (Slx, Sx and Sm) have average permeability below 2.5 The average low values of porosity and permeability of these gravel elements is likely related to the abundant presence of dolomite cement in these sandstones. The cement is sourced from the detrital dolomite reworked as intraclasts from the adjacent floodplain (Fig. 3.14e), a process widely recognized in dryland systems (Henares et al., 2016; Molenaar and Felder, 2019). At the scale of the individual sandstone bodies, these dolomite-cemented units represent a heterogeneous layer that may act as baffle.

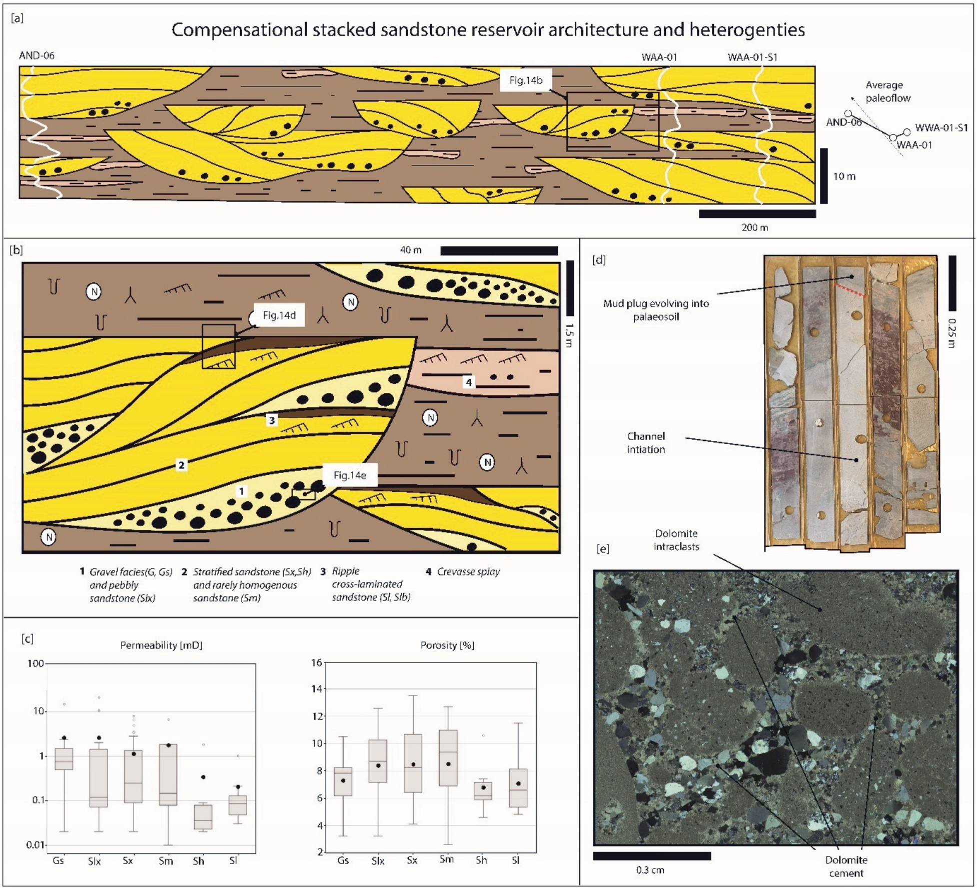

Figure 3.14: Conceptual model representing architecture and sedimentary heterogeneities of stacked compensational sandstone reservoir. a) Field-scale architecture with main reservoir bodies composed of fining-upward sandstone bodies. Crevasse splays (LA-4) can locally help increasing overall connectivity and enlarge recovery volume. The panel is semi-parallel to the average paleoflow direction. b) This figure represents the internal lithofacies assemblage within LA-2. c) Boxplots displaying permeability and porosity of the main lithofacies occurring in this lithofacies association. The black dot represents the mean and the line within each box is the median. d) Sequence of sediments from well AND-06 displaying channel deposits subsequently plugged by bioturbated ripple cross-laminated sandstones evolving into paleosol above. e) Example of dolomite cemented gravel (G) where the dolomite intraclasts are sourced from the surrounding floodplains. The thin section is from well KWK-01 at the depth of 2552.55 m.

The rest of the sandy lithofacies assemblage that usually composes the upper part of the reservoir units has permeability means below 1 mD, with ripple cross-laminated sandstones (Sl) yielding the lowest average permeability of 0.2 mD (Fig. 3.14c). This may be associated with the alternation of finer and coarser grain size laminae, sorting and presence of small-scale micaceous laminae and rip-up clasts (Henares et al., 2020). Locally, as a result of channel abandonment, channel plugs can develop with bioturbated ripple cross-laminated sandstones and mudstones that may exhibit bioturbation (Fb) (Fig. 3.14d). The permeability of these elements is usually below 1 mD, thus they represent heterogeneities that can hamper flow.

3.5.2.3 Reservoir architecture style: marginal isolated sandstones

These reservoirs are composed of coarsening-up sandstones that can be stacked on top of each other reaching a total thickness of ~4/5 meters (Fig. 3.15a). This type of reservoir has only been observed in the Volpriehausen Formation, but it is not excluded that it could be found in the other Buntsandstein formations along the northern margin of the Roer Valley Graben (Fig. 3.11) The architecture is characterized by sandstone units that are vertically separated by 5 to 15 m intervals of playa-lake sediments (LA-5) (Fig 3.15a). Given the km-scale lateral extent of these playa-lake units, sandstone units are likely to be stratigraphically compartmentalized. However, cm-scale mud cracks and injection structures may form a network of vertical sandy pathways that can connect the main reservoir units to the sandy layers present in the playa-lake sediments and potentially enlarge the reservoir volume (Fig. 3.15c).

The lateral extent and connectivity of this lithofacies could not be determined due to its identification in only a single well. This limited occurrence may suggest deposition within a restricted environment. However, similar facies in both modern and ancient analogues have been shown to extend from hundreds of meters to several kilometers (Tooth, 2000; McKie and Audretsch, 2005; Fisher et al., 2008; Coronel et al., 2020). Therefore, its absence in other wells may be attributed to sampling limitations rather than true absence.

The porosity and permeability of these sandstone bodies appear to be depositional facies controlled given the general decrease of the average values from the coarser to the finer grain size fraction (Fig. 3.15e). The best reservoir quality is found in the coarser upper part of the coarsening-up sandstones composed by very fine to medium cross- stratified sandstones with an average permeability and porosity of ~75.8 mD and ~16.1% and standard deviation of ~75. And 2.6 respectively. In the foresets, the coarser-grained laminae are usually better sorted and represent the more porous and permeable layers, while the finer laminae have a worse sorting and higher clay content (Fig. 3.15e). Such structure will likely establish preferential flow pathways across the dip of the inclined laminae (Weber 1982). The lower part of the complex where very fine to fine-grained, horizontally-stratified and ripple cross-laminated sandstones are dominant is characterized by a lower average permeability and porosity compared to the upper section, with minimum values of permeability and porosity that can reach 0.01 mD and 6% respectively (Fig. 3.15e).

3.6. Conclusions

A comprehensive study of sedimentology and lithostratigraphy has shown that the Main Buntsandstein Subgroup in the Roer Valley Graben has been deposited through different fluvial processes with minor aeolian influence.

The Volpriehausen and Detfurth Formations are characterized by an alternation of amalgamated fluvial channel sediments, deposited through highly mobile ephemeral rivers, and playa-lake sediments. The fluvial deposits are thicker and better developed in the southern part of the basin, in the hanging wall blocks of syn-sedimentary faults. In fact, the playa-lake sediments are not present along the southern margin of the Roer Valley Graben, where sandstones are stacked to form a continuous sandstone unit reaching thicknesses of ~ 200 m.

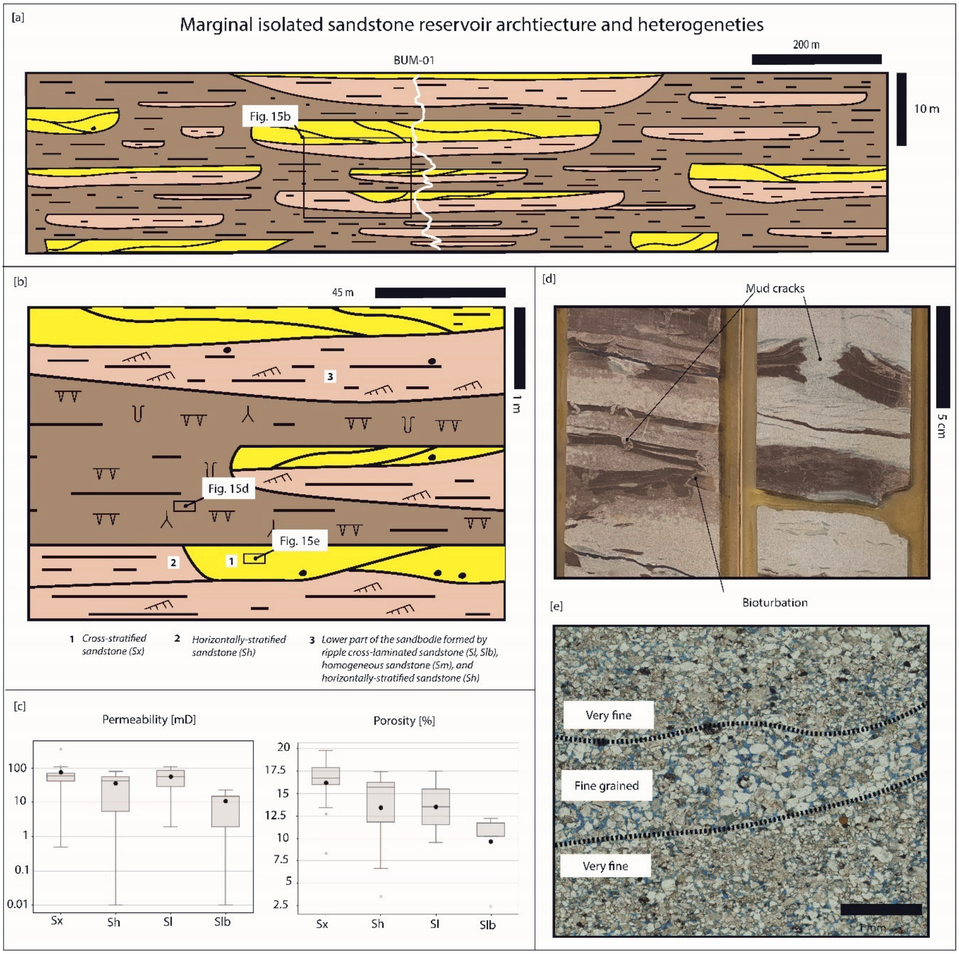

Figure 3.15: Conceptual model representing architecture and heterogeneities of marginal isolated sandstone reservoir. a) Field-scale architecture, with main reservoirs composed of LA-3. b) This figure represents the internal lithofacies assemblage within LA-3. c) Boxplots displaying permeability and porosity of the main lithofacies occurring in this lithofacies association. The black dot represents the mean and the line within each box is the median. d) Core examples from well BUM-01 displaying extensive mud cracks and bioturbation that can connect the thin sandstone layers. e) Example of porosity and permeability variation between laminae with different grain size. The thin section is from well BUM-01 at the depth of 1502.2 m.

The Hardegsen Formation, which forms the upper part of the Buntsandstein Stratigraphy, is instead characterized by an alternation of fluvial channel sediments, deposited by less mobile and more perennial-like rivers, and overbank facies that show paleosol development.

We believe that such a change in sedimentary facies association across the Buntsandstein stratigraphy is related to a decrease of aridity in time and a decrease in tectonic activity upwards in the Buntsandstein stratigraphy, as observed in adjacent Triassic basins. Despite the presence of many common depositional features between our model and the models already available in the literature for the Roer Valley Graben area, the change in fluvial style across the Buntsandstein stratigraphy had not been documented before. This is a fundamental aspect as different depositional processes produce different types of reservoir architectures with their own set of heterogeneities.

In the Buntsandstein, we identified three main types of reservoir architecture. Stacked amalgamated sandstones are the product of highly mobile rivers and are composed of interconnected sandstones. These sandstone bodies show the highest average permeabilities and porosities. However, the distribution in grain size and sorting within the sandstones may result in uneven fluid flow. Compensational stacked sandstones form a reservoir architecture where sandstone bodies are less interconnected and a primary relationship with permeability and porosity seemed to have been altered by later diagenetic events. Within this architecture type, dolomite cemented intervals and mud plugs are important heterogeneities that may hamper fluid flow. The reservoir architecture composed of marginal isolated sandstone shows apparent preserved relationship between primary reservoir properties and depositional facies. The vertical connectivity of these sandstone bodies largely depends on the lateral extent of the heterolithic barriers.

Chapter 4: Diagenetic controls on sandstone properties of the Main Buntsandstein Subgroup in the Roer Valley Graben, the Netherlands

Abstract

The Lower Triassic Main Buntsandstein sandstones exhibit heterogeneous reservoir quality. Deep burial often results in these sandstones to become extremely tight due to diagenetic processes. Understanding the factors influencing the quality of these sandstones is crucial for predicting regions where reservoir properties may be favourable for geo-energy applications such as geothermal energy. We here present results of a detailed petrographic analysis of thin sections from different wells penetrating the Buntsandstein in the Roer Valley Graben, the Netherlands, at depths between 1500 and 2500 m. The results are compared against permeability and porosity and the controls on the quality of the sandstones in the Roer Valley Graben are discussed.

This study shows that the diagenetic history of the Buntsandstein sediments can be summarized in four main phases: i) eogenesis, ii) 1st mesogenesis, iii) telogenesis, and iv) 2nd mesogenesis. Each of these phases occurs as a result of a particular tectonic regime the Roer Valey Graben was subjected to. Overall, illite, quartz, and dolomite represent the most dominant cements in the sandstones from the Main Buntsandstein in the Roer Valley Graben. Grain coating by tangential illite is among the earliest cementation phase to develop. It can help preserve sediment porosity as it inhibits quartz cementation. However, it may enhance grain compaction and reduce the intergranular volume. Furthermore, when developing a radial meshwork, illite can reduce the pore throat and decrease the permeability of the sandstones. Dolomite cement occurs in different habits, which formed during eogenesis and the two mesogenetic phases. Quartz cement mostly developed during the two mesogenetic phases. Quartz and dolomite cements have a positive effect on porosity in very fine-grained sandstones as they stabilize the grain frame and prevent the sediment from much compaction. In coarser sandstones, these two types of cement tend to reduce porosity. However, a strong statistical relationship between quartz and dolomite cements and porosity and permeability could not be established. Dissolution is an important process that occurred during telogenesis as result of exhumation and contributed to the creation of secondary porosity. Secondary porosity can constitute up to 65% of the total optical porosity in certain samples in the southeast part of the Roer Valley Graben.

Overall, the flanks of the Roer Valley Graben represent areas where shallower maximum burial depths have helped to preserve more favourable reservoir properties. However, the burial paths, particularly the extent of burial during Triassic and Early to Mid-Jurassic, have a strong impact on reservoir properties due to different cementation and compaction rates. This suggests that favourable reservoir properties may still be found in certain areas in the centre of the graben where the Main Buntsandstein sediments are located at depths over 2500 m at present-day. This study contributes to the understanding of diagenesis and its control on the quality of Lower Triassic sandstones in the Roer Valley Graben. The results of this study can be used to facilitate future geothermal energy applications.

4.1 Introduction

Sandstones from the Main Buntsandstein Subgroup represent an important deep geothermal play in the subsurface of the Netherlands, given their widespread distribution and high in-situ temperatures reaching 120-130 °C at depths of ~ 3-3.5 km (IF Technology, 2012; Mijnlieff, 2020; Cecchetti et al., 2024). However, the reservoir quality of the sandstones is highly heterogeneous as result of an interplay between depositional and diagenetic processes (Mijnlieff, 2020; Boersma et al., 2021; Cecchetti et al., in press b). In 2017, an attempt to install a geothermal system in a Triassic layer at ~4 km depth in the West Netherlands Basin revealed extremely poor reservoir quality due to diagenesis with values of porosity in the order of 3-4% and permeability below 0.01 mD (www.nlog.nl). The diagenesis of the Lower Triassic sediments is complex understood given the multi-stage burial history the sediments have experienced. With burial, formation water is subjected to an increase in temperature and pressure that can trigger physical and chemical processes that may alter the primary sediment properties and the quality of the reservoir units (Worden and Burley, 2003).

The reservoir quality of the Buntsandstein sediments is known to be largely affected by diagenetic processes such as compaction and cementation (Purvis and Okkerman, 1996; Beyer et al., 2014; Olivarius et al., 2015; Busch et al., 2022). Compaction can significantly reduce the intergranular volume, thus reducing pore spaces (Busch et al., 2022). Cementation can have a different impact on porosity and permeability depending on the nature of the sediments. For example, offshore the Netherlands, Purvis and Okkerman (1996) showed how dolomite cement reduces the Buntsandstein intergranular porosity in fine grained sandstones. On the other hand, in the Upper Rhine Graben, Busch et al. (2022) indicated how dolomite cement can help prevent sediment compaction and may help preserve reservoir quality. Anhydrite is also reported to be an important pore-filling cement in the Buntsandstein in the North Sea area, which can strongly reduce the permeability of the sandstone units (Purvis and Okkerman, 1996; Olivarius et al., 2015). However, this cement is not reported in the Buntsandstein in the Belgian side of the Roer Valley Graben (Bertier et al., 2022).

Dissolution is commonly known as a diagenetic process that can create secondary porosity, thus contribute to enhancing the sediment total porosity. In the Netherlands, dissolution is considered to occur in the sandstones from the Buntsandstein as result of meteoric water influx when the Buntsandstein is truncated at the base Cretaceous unconformity (Mijnlieff, 2020). However, no petrographic studies have documented this process and its potential effect on reservoir quality. In fact, dissolution may also result in the formation of non-connected pore networks and can weaken the rock matrix, leading to compaction or collapse of the pore spaces.

This work aims to investigate the post-depositional history of the Lower Triassic Main Buntsandstein in the Roer Valley Graben in the southeastern Netherlands. In its present-day form, the Roer Valley Graben is about 130 km long and 20-45 km wide (Fig. 4.1a). During the Early to Middle Triassic, the Roer Valley Graben was an active depocenter for the Main Buntsandstein Subgroup, resulting in the deposition of up to ~ 300 m of Main Buntsandstein sediments (Geluk, 2005; Cecchetti et al., *in press a*). The Main Buntsandstein Subgroup in the Roer Valley Graben consists of three formations, namely Volpriehausen, Detfurth, and Hardegsen. Sediments were sourced from the Variscan relicts to the south and deposited in a fluvial/lacustrine environment influenced by aeolian processes (Cecchetti et al., *in press b*). A decrease in aridity and tectonic activity is generally perceived upwards in the Buntsandstein stratigraphy. This is reflected in a lower N/G of the Hardegsen compared to the Volpriehausen and Detfurth formations (Fig. 4.1b). By integrating geological knowledge of the Main Buntsandstein Subgroup in the area with available petrophysical and new petrological data, the diagenesis of the Buntsandstein and its impact on reservoir quality can be analyzed to identify areas where reservoir properties may be favorable for geothermal energy in the Roer Valley Graben.

4.2 Tectonics and Burial History

The Main Buntsandstein sediments have been subjected to 4 main tectonic phases that resulted in a complex burial history for the sediments across the basin. The burial history curves for each well were reconstructed based on the available knowledge of the burial history of the Roer Valley Graben (i.e. Zijerveld et al. (1992); Nelskamp and Verweij, 2012; Cecchetti et al. 2024) and well legacy data from Carter et al., 1990, Green et al., 1992a, 1992b.

After deposition, the Main Buntsandstein sediments were buried as result of the extensional tectonic regime that lasted through Late Triassic until the Mid-Jurassic (Zijerveld et al., 1992; Geluk et al., 1994; Cecchetti et al., in press a). Across the central part of the Roer Valley Graben, sediments from the Main Buntsandstein were deeply buried below 2-2.5 km as result of the overlying sedimentary infill (Fig. 4.2). Locally temperatures up to 150-160 °C were likely experienced. Along the flanks of the Roer Valley Graben, slower and shallower burials of 1-1.5 km were recorded related to a thinner Jurassic infill. Temperatures in these areas were likely below 130-140 °C. Overall, the sediments in the central part were buried more rapidly and deeper than the sediments closer to the flanks of the Roer Valley Graben.

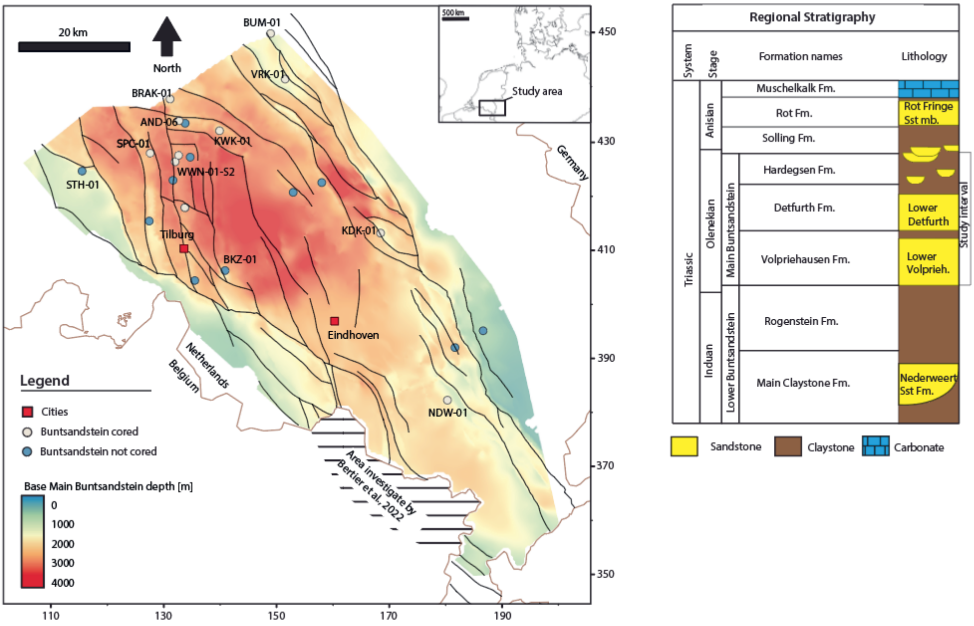

Figure 4.1: a) depth map of the Main Buntsandstein Subgroup base after Cecchetti et al., 2024. The faults have been traced following the Digital Geological Model (DGM in DinoLoket.nl) as a proxy. b) Stratigraphic column of the Triassic sediments in the Roer Valley Graben region (after Van Adrichem Boogaert and Kouwe, 1993). Note how the N/G ratio decreases in the Hardegsen Formation with respect to the Volpriehausen and Detfurth Formations.

During the Mid to Late Jurassic, local uplift and erosiondue to fault-block tilting in response to a transtensional regime caused widespread erosion of the Mesozoic deposits across the Roer Valley Graben (Geluk et al., 1994; Kombrink et al., 2012; Cecchetti et al., in press a). During this time, the Main Buntsandstein sediments were locally uplifted and burial depths overall decreased (Fig. 4.2). Across the Roer Valley Graben flanks and to the southeast, the Buntsandstein were exhumated up to 0.5-1 km below the surface. In the central part of the Roer Valley Graben, minor exhumation was recorded and the Main Buntsandstein sediments were still located at around 2 km.

During the Early to Mid-Cretaceous, regional subsidence in response to extensional tectonics led to the deposition of the Chalk Group. This caused the Mesozoic sediments in the central part of the Roer Valley Graben to be locally buried down to 2.5 km, where they experienced temperatures of ~120 °C.

The Roer Valley Graben area was then inverted during the Late Cretaceous as result of the Africa and Eurasia collision (Geluk et al., 1995). This led to the uplift of the central part of the Roer Valley Graben and the subsidence of its flanks (Cecchetti et al., 2024). During this time, the Main Buntsandstein Subgroup sediments experienced temperatures below 80 °C (Fig. 4.2).

Subsequently, the Roer Valley Graben entered an extension phase still lasts today (Geluk et al. 1994; Deckers et al., 2023). This phase has led to burial of the Main Buntsandstein sediments that presently reach maximum burial depths up 4-4.5 km in certain parts of the Roer Valley Graben (Cecchetti et al., 2024).

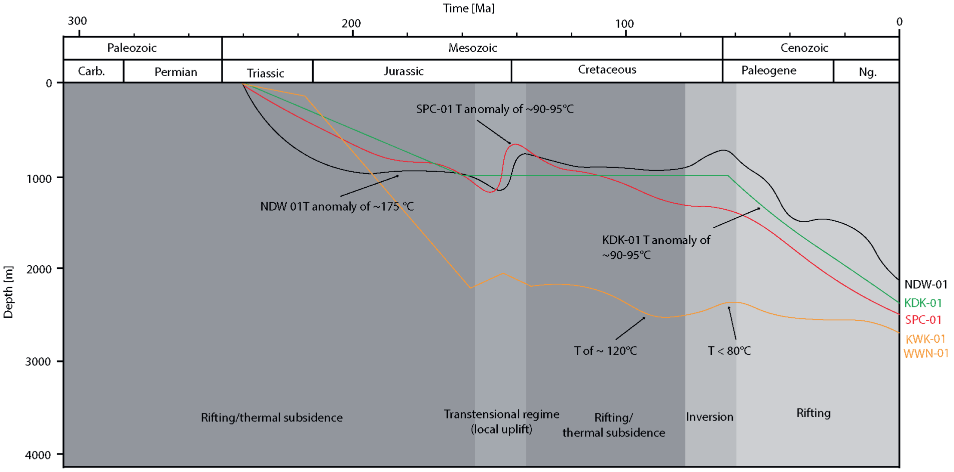

Figure 4.2: Burial history curves of the analysed wells in the Roer Valley Graben. Maximum burial depth corresponds to present-day depth The curves are based on Carter et al. (1990), Green et al., (1992a and 1992b), Zijerveld et al. (1992) and Nelskamp and Verweij (2012).

4.3 Permeability-porosity relationships

The publicly available permeability and porosity plug measurements from the Main Buntsandstein sediments in the Roer Valley Graben have a large spread with permeability ranging from ~0.01 to ~ 750 mD and porosity from ~0.5 to ~21% (Fig. 4.3; data from www.nlog.nl). The permeability and porosity positively correlate with a R^2 of 0.77.

The sediments of the Volpriehausen and Detfurth Formations have higher average permeabilities (av. 13.4% and 18.1 mD) than the sediments of the Hardegsen Formation (av. 1.8 mD) (Fig. 4.3). The permeability in the Volpriehausen and Detfurth Formations reaches maximum values of 752 and 365 mD respectively. The Detfurth Formation has the highest average porosity (av. 11.8 %), while the Hardegsen and Volpriehausen Formations have average porosities of 7.4 and 8.9 % respectively.

The plug measurements have then been plotted against the lithofacies associations developed in Chapter 3 of this thesis. The ephemeral (LA-1) and perennial fluvial (LA-2) sandstones are the most sampled facies (Fig. 4.3). Ephemeral fluvial sandstones have the largest spread in the porosity (0.6 – 21.1 %) and permeability (0.01 – 752 mD) and averages of 10 % and 15 mD. Perennial fluvial sandstones have a lower average permeability of 3 mD. Terminal splay sandstones (LA-3) have the highest average permeability (~ 60 mD). Aeolian sandstones are under-sampled as only 1 measurement for porosity and permeability is available. Crevasse splays (LA-4) have average porosity and permeability of 9.9% and 4.1 mD. Heterolithic sediments (LA-5) have the lowest average values of porosity and permeability (av. 7.5% and 2.6 mD).

Permeability and porosity overall decrease with depth (Fig. 4.3). The samples shallower than 2500 m have average porosity and permeability of 10.3% and 27.5 mD, while deeper samples have lower porosity and permeability averages of 8.2 % and 7.6 mD respectively.

Very-fine grained sandstones have the highest average porosity and permeability (av. 11.3 % and 28.9 mD). Gravels have the lowest average porosity and permeability (av. 7.6% and 2 mD) (Fig. 4.3). Finer grained sandstones have usually smaller pores compared to coarser sandstones. The absence of this trend in the Main Buntsandstein of the Roer Valley Graben suggests the alteration of primary reservoir properties by diagenesis.

4.4 Data and Methods

In total, 56 thin sections from 6 wells were analyzed in this study (Table 4.1 and Fig. 4.1a). The thin sections from wells BUM-01, VRK-01, KDK-01 and KWK-01 were made available by Nederlandse Aardolie Maatschaappij (NAM) and Winthersall Nordzee. The thin sections from wells SPC-01 and NDW-01 were acquired from core samples during this study (courtesy of TNO). All the thin sections are impregnated with a blue-dyed epoxy resin to highlight porosity. Most of the samples are stained with a combination of Alizarin Red S and potassium ferricyanide to help the identification of the different carbonate minerals.

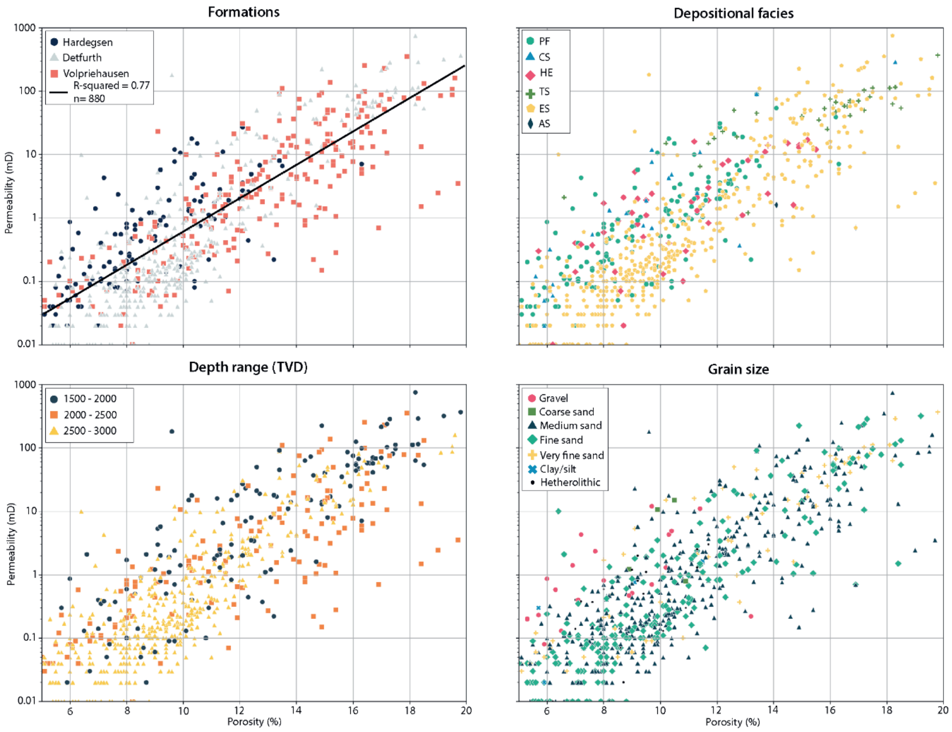

Figure 4.3: Porosity-permeability plots for the Main Buntsandstein subgroup. The dataset is composed of 925 data points each representing a pair of porosity and permeability plug measurements (www.nlog.nl). The same dataset is plotted with different colour and marker codes to highlight how values are distributed across different formations, depositional facies, depth ranges, and grain sizes. Formations, depositional facies, and grain size have been re-assigned after Cecchetti et al. (in press).

Samples are retrieved from different wells penetrating the Main Buntsandstein Subgroup at depths ranging between 1500 and 2500 m. The thin sections sampled ephemeral and perennial channels, aeolian, terminal splay, crevasse splay, and playa-lake sedimentary facies from the Volpriehausen, Detfurth, and Hardegsen Formations. A detailed description and interpretation of these sedimentary facies and their depositional environment can be found in Cecchetti et al., (in press).

Table 1: Summary of the samples available for the study. Note that wells NDW-01 and SPC-01 do not have plug measurements at the location where the thin sections were sampled.

Well name	Depth range (TVD)	Stratigraphic interval	Samples	Av. sampling rate (m)	Petrophysic measurement types	Owner
BUM-01*	1497-1515	Volpriehausen	10	1.81	Plugs/logs/optical	NAM
VRK-01*	1605-1608	Hardegsen	7	0.44	Plugs/logs/optical	NAM
NDW-01*	2120,75-2181,93	Detfurth	10	6.12	tinyperm/optical	TNO
KDK-01*	2134-2147	Volpriehausen	5	3.20	Plugs/logs/optical	Wintershall
KWK-01*	2420-2468	Detfurth/Hardegsen	16	3.17	Plugs/logs/optical	NAM
SPC-01*	2437-2451.5	Detfurth	8	2.25	tinyperm/logs/optical	TNO

Helium porosity and air permeability plug measurements are obtained from publicly available repositories (www.nlog.nl). Plug measurements were not always available at the location where certain thin sections were sampled (Table 1). In this case, the average of the plug measurements above and below the thin section location was used to estimate porosity and permeability. This was done by making sure that plug measurements were derived from sediments with comparable lithology and texture. In addition, a portable hand-held air permeameter device (New England Research TinyPerm) was used to measure permeability on the slabbed core at the locations where thin sections were taken.

Samples were studied with transmitted light microscopes (Leica Microsystems Wetzlar GmbH, model No: 888500) to assess texture, grain size, detrital and authigenic components, and optical porosity. To quantify the mineralogy and optical porosity, an automatic point counter (James Swift, model F) mounted on the microscope was adopted. A minimum of 200 points per thin section was counted, adjusting the step size to the maximum observed grain size.

Detrital compositions were plotted in a ternary diagram after Pettijohn (1975). Diameters from 100 grains per sample were measured to determine grain-size distribution and sorting following and Folk and Ward (1957). Grain size was calculated as following:

$$Grain\ size\ mean = \frac{(\varphi_{16}+\varphi_{50}+\varphi_{84})}{3} \tag{1}$$

where φ_{16} , φ_{50} and φ_{84} represents 16, 50 and 84 grain size percentiles. The sorting was calculated using grain size percentiles according to the following formula:

$$Sorting = \frac{(\varphi_{84}-\varphi_{16})}{4} + \frac{(\varphi_{95}-\varphi_{5})}{6.6} \tag{2}$$

The results were then transformed into grain size and sorting classes following Wentworth (1922).

The intergranular volume (IGV) was used to quantify the effect of compaction on each sample. The intergranular volume is calculated by adding up the intergranular pore space (IPS), intergranular cement (IC), and depositional matrix (DM), as shown in Eq.3 (Paxton et al., 2002).

$$IGV = IPS + IC + DM \tag{3}$$

To assess the effect of compaction and cementation on the loss of porosity, compactional porosity loss (COPL) and cementational porosity loss (CEPL) were calculated according to Lundergard (1992). For these calculations, an initial porosity (Pi) of 45% was used for fluvial sandstones, and the optical porosity (Pmc) and the volume-percent pore-filling cement (C) were calculated from point-counting results (see Lundergard (1992) for details about the method).

$$COPL = Pi - \left\{\frac{[(100-Pi)*(Pmc)]}{100-Pmc}\right\} \tag{4}$$

$$CEPL = (Pi - COPL) * \left(\frac{C}{Pmc}\right) \tag{5}$$

For the calculations mentioned above, the samples with a matrix percentage higher than 10% were discarded as the mechanism of compaction in grain supported sandstones (detrital matrix <10%) is different than in matrix-rick sandstones where detrital matrix is larger than 10% (Paxton et al., 2002; Lundergard, 1992).

4.5 Results

4.5.1 Thin section analysis

4.5.1.1Texture

Grain sizes of the Buntsandstein samples range from 83 µm to 364 µm with an average of 221 µm (fine sand). The samples from the Volpriehausen Formation range in grain size from 90 to 156 µm with an average of 115 µm (very fine sand). They are mostly well-sorted. These samples are representative of the terminal splay complex in the northern part of the study area. The overall coarser and moderately sorted fluvial channel sandstones that occur in the southern and southwestern Roer Valley Graben have not been sampled in the Volpriehausen Formation.

Samples for the Detfurth Formation range in grain size from 120 µm to 364 µm with an average of 261 µm (medium sand). Sorting in the samples from the Detfurth Formation varies from moderately sorted to well sorted across the Roer Valley Graben.

The samples analysed from the Hardegsen Formation range from 92 µm to 310 µm in grain size with an average of 215 µm (fine sand). In the Hardegsen Formation, sorting is usually moderate. These samples are representative for the Hardegsen in the northern part of the Roer Valley Graben.

4.5.1.2 Detrital composition

Quartz grains represent the most dominant detrital component among all the samples analysed, with an average of 45 % and a range from 25 % to 58 %. Quartz is encountered in its monocrystalline and polycrystalline form (Fig 4.4 a, b, and c).

Feldspars occur in minor percentages (av. 2.7%) in the Buntsandstein sediments in the Roer Valley Graben, including both plagioclase and alkaline feldspars. Alkaline feldspars are usually more dominant than plagioclase feldspars, with microcline and orthoclase being the most common grains encountered (Fig 4.4 a and b). The samples with the highest feldspar percentages (max of ~ 12%) belong to the fine-grained crevasses splays and playa-lake heterolithics (Fig. 4.5) in the northern parts of the Roer Valley Graben. However, these facies are under-sampled, thus this observation is not statistically valid.

Rock fragments represent an important detrital constituent considering the average value of 12.7 % and maximum observed of 32.5 %. Rock fragments from the Main Buntsandstein Subgroup in the Roer Valley Graben are mainly of sedimentary origin. However, undifferentiated volcanic and metamorphic rock fragments have also been encountered. These account on average for 0.4 % of the total composition. The average amount of rock fragments increases upwards in the Buntsandstein Stratigraphy, with samples from the Hardegsen Formation showing an average of ~20%, while samples from the Detfurth and Volpriehausen Formations have averages below 12% (Fig. 4.5). Perennial fluvial sandstones have the highest average percentage of rock fragments fragments (av. ~20%).

Shale clasts (Fig. 4.4e) and fragments of silt/sandstones (Fig. 4.6e) are overall the most abundant type of rock fragments (av. 4-5 %). These siliciclastic grains have diameters ranging from 0.1 to 0.5 mm. However, larger clasts up to 1 cm have been observed (Fig. 4.5b). They can be substituted by their metamorphic equivalents, metapelite and metapsammite (Garzanti and Vezzoli, 2003). These clasts show a low metamorphic rank with weak cleavages and amount of mica recrystallization (Fig. 4.6a).

Dolomite grains represent an important constituent of the rock fragment group and occur with an average of 3.7% on the samples from the Buntsandstein. However, in certain samples, detrital dolomite content can reach values of 27% of the entire sediment composition. Dolomite grains occur with an average of 4-5% in the samples from the Detfurth and Hardegsen formation, while the analyzed samples from the Volpriehausen Formation are instead more depleted in dolomite grains (Fig. 4.3). The fluvial sandstones are the most enriched in dolomite grains with averages of 4-5% (Fig. 4.3). Dolomite can occur in three different habits.

One type of grain is formed by aggregates of dolomite crystals that can be encased in a clay matrix and can contain dispersed quartz grains (Fig. 4.4d, 4.4f and 4.6c). The dolomite crystals are usually euhedral when dispersed in the clay matrix, while they can be anhedral when closely packed. These may be dolomite nodules reworked by river channels eroding adjacent floodplain fines. These grains can reach ~2 cm in diameter (Fig. 4.44f). Within each grain, the size of the individual dolomite crystals can reach up to 0.1-0.2 mm. Quartz grains of similar size to the individual dolomite crystals are commonly found (Fig. .4f). The size of the crystals contained by the clasts is usually smaller than the rest of the detrital grains within the sample (Fig. 4.4d).

A second type of dolomite grain is formed by subrounded sand-size singular anhedral crystal clusters (Fig. 4.4e and 4.6b). These grains are usually subrounded and are mostly dispersed through the samples.

A third type of dolomite grain is represented by spheroidal dolomite-coated grains that resemble ooids (Fig. 4.6a and b). The ooid nuclei are often not clearly defined and dissolved. These dolomite grains have a diameter usually below 1 mm.

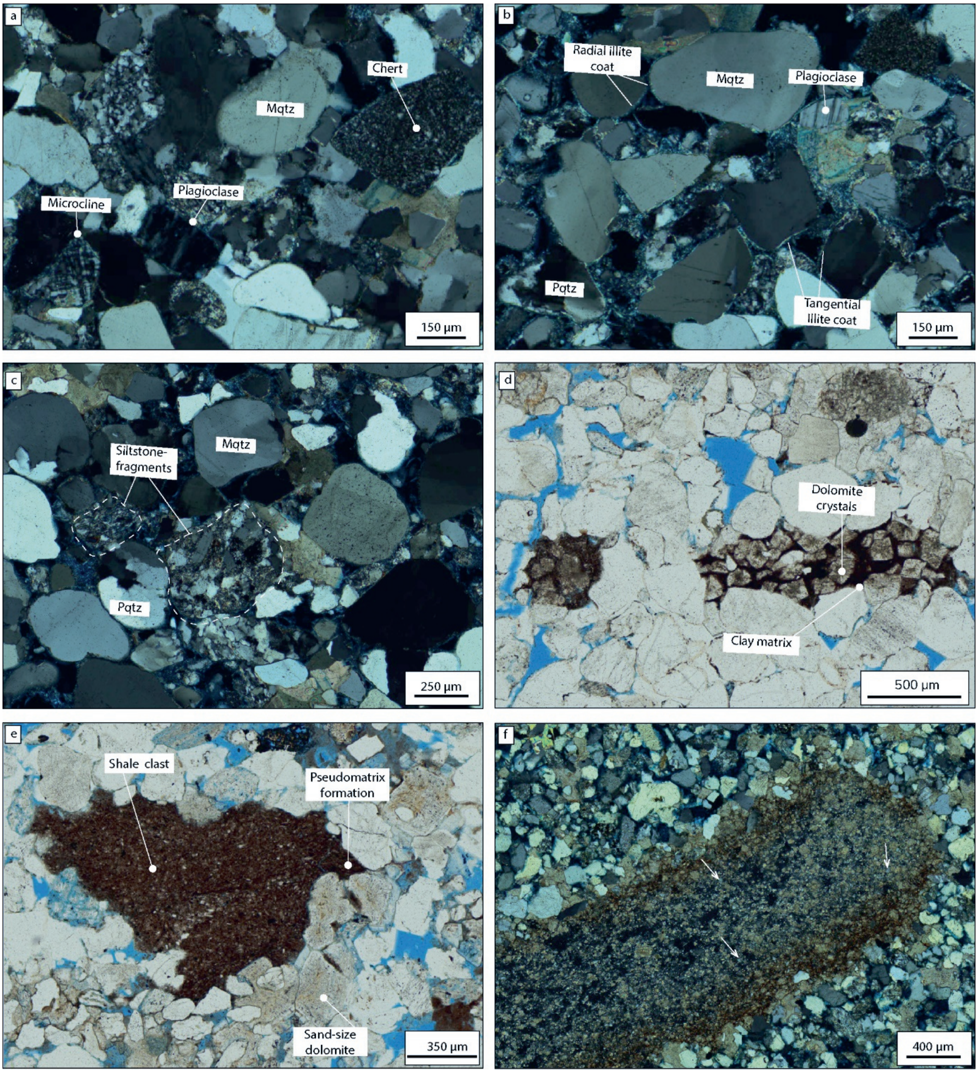

Figure 4.4: Key detrital and authigenic grain types in the Main Buntsandstein Subgroup in the Roer Valley Graben. a) Detrital microcline, plagioclase, monocrystalline quartz (Mqtz) and chert (xpl, Detfurth Fm. in NDW-01, 2126.79 m). b) Detrital monocrystalline (Mqtz) and polycrystalline (Pqtz) quartz grains, and plagioclase. Detrital grains are covered by tangential and radial illite grain coating. Note that the tangential illite grain coating is often present at grain contacts. The radial illite is overgrowing tangential counterpart (xpl, Detfurth Fm. in NDW-01, 2126.79 m). c) Sedimentary fragment formed by silt-size quartz grains in a clay matrix (xpl, NDW-01, 2120.75 m). d) Dolomite crystals encased in a clay matrix (ppl, Detfurth Fm. in NDW-01, 2136.75 m). e) Shale clast deformed by compaction, thus developing pseudomatrix. Different anhedral sand-size dolomite grains with diameters reaching 350 µm in length and ooids (ppl, Detfurth Fm. in NDW-01, 2136.57 m). f) Large dolomite fragment formed by smaller euhedral to anhedral dolomite crystals encased in a clayish matrix where small quartz grains are present (white arrows) (xpl, Volpriehausen Fm. in BUM-01, 1505.5 m).

Chert can occur in minor amount with an average lower of < 1% of the total sediment composition. Chert grains are usually rounded to subrounded and have a diameter that can reach up to 1 mm (Fig. 4.4a). Cherts can be partially dissolved.

The detrital clay matrix can be present with an average of 1.9%. However, this occurs in very fine to fine grained sandstones only, whilst coarser sandstones are largely grain-support. Mica is observed in minor quantities as muscovite and biotite (av. 0.7%). Zircon, iron oxide grains, and other undifferentiated opaque grains are found in traces (<0.1%).

The samples are mostly matrix-free sublitharenites. Few samples are lithic arenites, only one sample is subarkose (Fig. 4.7). Overall, most of the samples enriched in rock fragments belong to the Hardegsen Formation. The low percentage of feldspars in the Buntsandstein sediments may be partly due to their dissolution as evidenced by the presence of partially and completely dissolved feldspar grains (e.g. Fig. 4.6d).

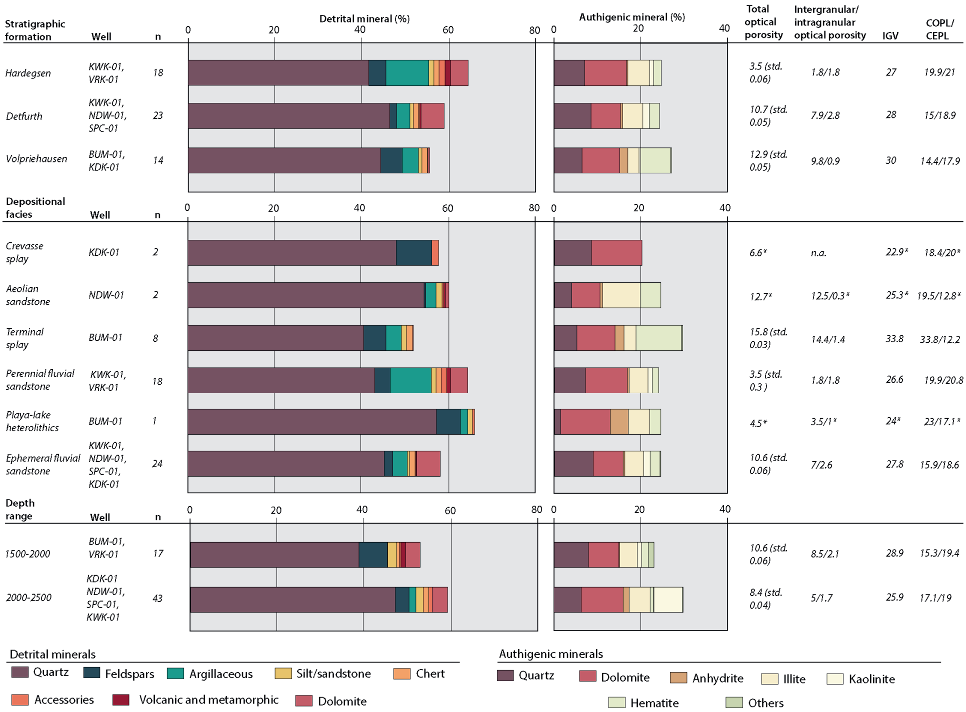

Figure 4.5: Detrital and authigenic mineral contents, total optical porosity, intergranular and intragranular porosity, IGV, COPL, and CEPL for each stratigraphic formation, depositional facies, and depth ranges.

4.5.1.3 Authigenic composition

Dolomite cement represents a frequent authigenic component, with an average of 8 % and a maximum of 25 %. It occurs in largest amount in the Hardegsen Formation. Dolomite cement exists in the Buntsandstein sediments in 3 different habits.

The first habitat is poikilotopic cement encasing detrital grains that can show floating and point contacts (Fig. 4.8a). The encased detrital grains are of the same size as the rest of the detrital grains observed in the sample. This suggests that the dolomite formed in place, thus it is referred to as a dolomite nodule. These nodules in the sandstones can reach up to 0.5-1 cm in size.

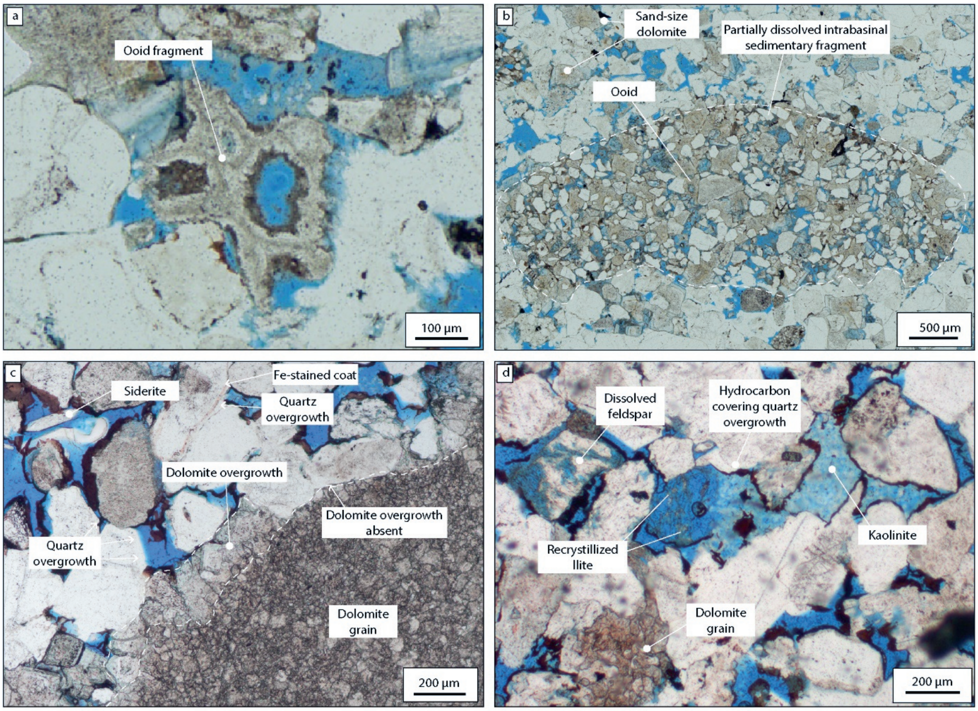

Figure 4.6: Key detrital and authigenic grain types in the Main Buntsandstein Subgroup in the Roer Valley Graben. a) Fragment containing cemented ooids with dissolved nuclei (ppl, Detfurth Fm. in NDW-01, 2136.57 m). b) Partially dissolved intrabasinal fragment containing several dolomite and quartz grains and relict of dissolved grains (ppl, Detfurth Fm. in NDW-01, 2136.57 m). c) Reworked dolomite grain with well-developed dolomite overgrowth on the edge. Note how the overgrowth is not present everywhere. The section contains examples of quartz overgrowth that are clearer when the grain surface is stained with hematite. On the top right part of the section, an elongated siderite crystal is present (ppl, Hardegsen Fm. in VRK-01, 1659.09 m). d) Examples of dissolved feldspar grains, likely k-feldspars, that show illite recrystallization. Hydrocarbon traces are also present around most of the grain surfaces. Kaolinite fills primary and secondary pores (ppl, Hardegsen Fm. in VRK-01, 1659.09 m).

The second habitat is represented by syntaxial dolomite cement growing around the rim of dolomite detrital grains (Fig. 4.6a). This overgrowth can be mono- or polycrystalline depending on the fabric of the original detrital grain. In the case of sand-size monocrystalline dolomite grains, a simple syntaxial overgrowth develops (Fig. 4.8c). This has commonly a euhedral shape if developing in open pore space. Sometimes, this overgrowth is formed by blue-stained ferroan dolomite, usually euhedral structure (Fig. 4.8c). In the case of polycrystalline dolomite grains, the dolomite overgrowth has a more complex, multi-crystal texture, where a preferred orientation of the cement is commonly absent. The cement is not always continuous around the grain rim, but it is locally interrupted when the grain is in direct contact with another grain (Fig. 4.6c). The third habitat represents dolomite cement that precipitates in inter- and intragranular pores, often showing a patchy euhedral or anhedral structure (Fig. 4.6d). Siderite can be found close to dolomite cement (Fig. 4.5c). It occurs only in traces, with values generally below 1 % of the total sediment composition.

Quartz cement is present with an average of 7.5 %, while it can reach up the 27 % of the total sediment authigenic composition in certain samples. Samples of the Detfurth Formation are the most enriched in quartz. It largely manifests as syntaxial overgrowth, and it can be easily identified when overgrowing grain coating around the original detrital grain (Fig. 4.6d). It develops a euhedral structure when growing in open pore space. The sharp edges and the often unweathered aspect allow to distinguish it from the original detrital grain when the coating is not present. When the coating is extensively developed around the grain surface, quartz syntaxial overgrowth is usually absent and poikilotopic outgrowths can form (Fig. 4.8e). Quartz outgrowth can form extensive cement zones that give the sediments a white colour. This is especially visible when the sediments are reddened by hematite coating (Fig. 4.8e). Quartz cement is found both encasing dolomite cement (Fig. 4.8c) and being encased by dolomite cement.

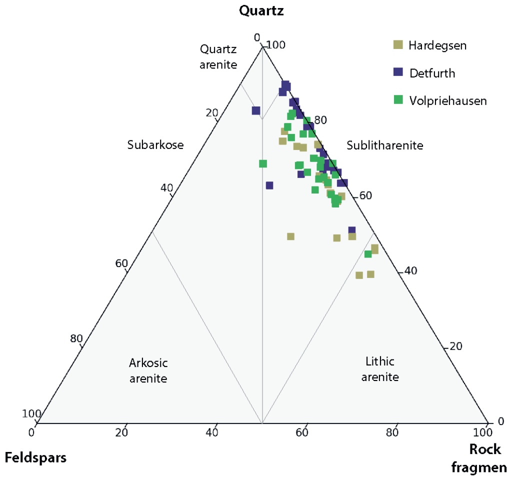

Figure 4.7: QFR diagram of the Main Buntsandstein samples coloured based on the stratigraphic formations. Samples classification is based on Pettijohn (1975).

Kaolinite is present as pore-filling cement in both inter- and intragranular pores. It is characterized by its typical booklet shape (Fig. 4.6d). It occurs with an average of 1 %, ranging from 0% to 6.5%. Kaolinite only occurs in the fluvial sandstones and it mostly occurs in samples deeper than 2000 m (Fig. 4.3).

Illite is present with an average of 9.8 % and it develops mostly as tangential coating around detrital grain rims and as radial grain coatings (Fig. 4.4b). Nonetheless, it has been encountered with fibrous structure within intra- and intergranular pore spaces (Fig. 4.6d).

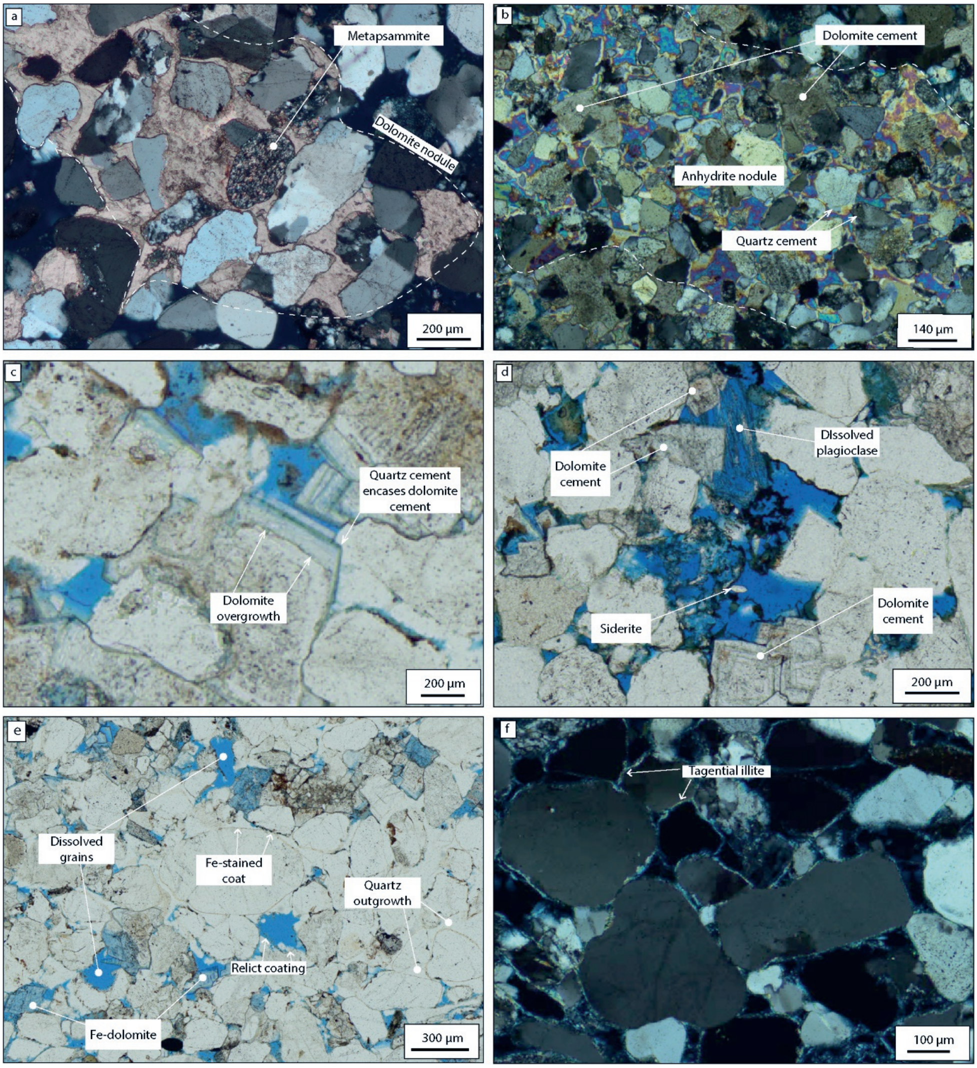

Figure 4.8: Key detrital and authigenic grain types in the Main Buntsandstein Subgroup in the Roer Valley Graben. a) Dolomite cement encasing detrital grains in a nodule. The grains within the nodules are not coated and do not show quartz overgrowth (xpl, Hardegsen Fm. in VRK-01, sample depth not available). b) Anhydrite cement encasing detrital grains in a nodule. Within the nodules, dolomite cement and quartz overgrowth are present (xpl, Volpriehausen Fm. in BUM-01, 1502.5 m). c) Example of quartz cement encasing dolomite overgrowth. The blue stain marked the Fe enrichment (ppl, Detfurth Fm. in NDW-01, 2181.92 m). d) Euhedral dolomite cement growing inside a partially dissolved plagioclase grain (ppl, Hardegsen Fm. in VRK-01, 1659.09 m). d) Example of pervasive quartz outgrow. The sample presence of secondary pores was enhanced by the complete dissolution of detrital grains (ppl, Detfurth fm. in NDW-01, 2181.92 m). f) Example of tangential illite (xpl, Detfurth Fm. in NDW-01, 2126.79 m).

Tangential illite is commonly present at grain contacts (Fig. 4.8f). Illite coating is well developed in the two samples from aeolian sandstones, where it averages with ~8-9%. At locations where illite grain coating is continuous across quartz grain surfaces, the amount of quartz syntaxial overgrowth is reduced and primary porosity is largely preserved (Fig. 4.9). Radial illite has been encountered in one well and it usually grows on top of the tangential illite grain coating.

In some cases, the grains are pigmented with reddish hematite that can be encased by overgrowth cement (Fig. 4.6c and 8e). Hematite coating occurs more frequently in the samples from the Volpriehausen Formation which shows an average of 5-6% of the total mineral composition (Fig. 4.3). Aeolian sandstones and terminal splay sediments are the depositional facies where hematite coating is better developed with a maximum of ~8%. Hematite coating is often observed at grain contacts (Fig. 4.8 e).

Anhydrite is present as patchy pore-filling cement with an average of 1 %, but it can reach up to 6 % in the norther part of the Roer Valley Graben. It can have a poikilotopic habitat, forming nodules that encase detrital grains and reach 0.5 cm in dimension (Fig. 4.8b). Anhydrite is often found encasing dolomite and quartz cements. Anhydrite average amount decreases upward in the Buntsandstein stratigraphy and occurs in larger amounts of 3 to 4% in the terminal splay and playa-lake heterolithic depositional facies (Fig. 4.5)

Hydrocarbon traces (< 0.1 %) are present covering illitic meshwork and quartz syntaxial overgrowth (Fig. 4.6c and d). Hydrocarbon can be found as bitumen in the same samples (Fig. 4.10d).

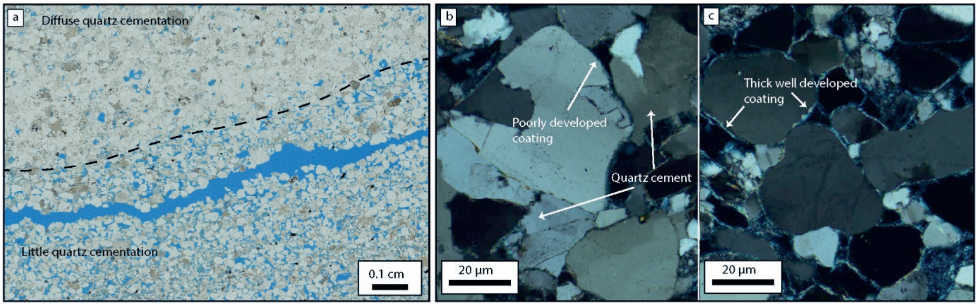

Figure 4.9: a) Diffuse quartz cementation in the upper part of the sample, while the quartz cement is practically absent in the lower part of the sample (ppl, NDW-01, 2126.79). b) The grains on the upper cemented part of the sample displayed in (a) show a poorly developed illite coating. c) Well-developed illite grain coating from the lower part of the sample shown in (a).

4.5.1.4 Dissolved minerals and replacive cements

Partially and completely dissolved feldspars and rock fragments are often encountered in the sediments from the Buntsandstein Subgroup and result in the formation of secondary pores (e.g. Fig. 4.6d and Fig. 4.8d). If the coating textures are present, these are preserved and help identify the presence of the grain relict (Fig. 4.6e). Feldspars can be filled with kaolinite and illite. Where illite is present, it forms ghost structures along the feldspar cleavage (Fig. 4.8d). In NDW-01, ooid fragments are encountered with the nuclei dissolved (Fig. 4.6a). Dolomite and siderite are also encountered as intracrystalline replacement within dissolved grains (Fig. 4.8d). Chert and silt/sandstone fragments are often partially dissolved (Fig. 4.6b).

4.5.1.5 Fractures and stylolites

Open fractures with an aperture of ~ 0.5-1 mm have been encountered in the samples from the Main Buntsandstein (Fig. 4.10a). A network of smaller open subparallel fractures can be present next to the largest fractures (Fig. 4.10b). These smaller fractures are usually continuous over 2-3 mm but have a limited aperture of few µms. Ferroan dolomite crystals can recrystallize within the principal fractures (Fig. 4.10c). The area adjacent to these open fractures can be interested in grain dissolution.

Stylolite-like elements have been encountered where pressure dissolution is enhanced at the grain contacts by the presence of organic matter or clay (Fig. 4.10d). The elements develop subperpendicular to the main compaction direction and can be continuous for 3-4 mm.

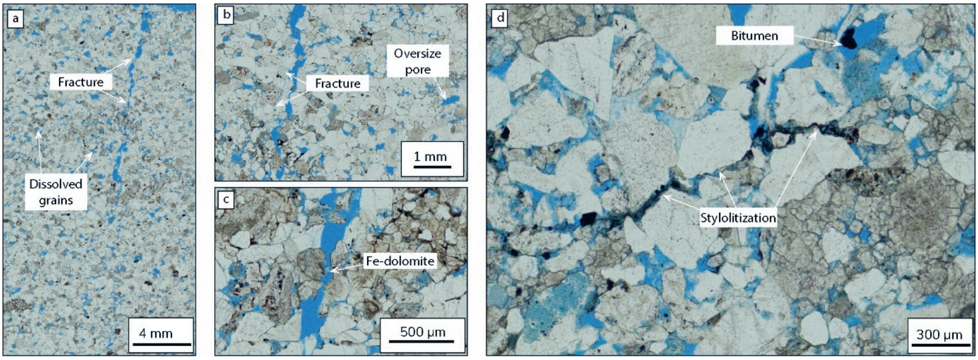

Figure 4.10: Fractures and stylolitizations in the Main Buntsandstein Subgroup in the Roer Valley Graben. a) Example of an open fracture long ~1.5.2 cm (ppl, NDW-01, 2181.92 m). The fracture is surrounded by many secondary pores formed by the dissolution of detrital grains. b,c) Closer look at the same fracture and the network of smaller fractures that are present nearby. Many oversize pores up to 0.5 mm in diameter have been encountered. Fe-dolomite is recrystallized within the fracture. d) Pressure dissolution at grain contacts enhanced by the presence of what is likely to be organic matter in black (ppl, SPC-01, 2651.77 m).

4.5.1.6 Optical porosity

Total optical porosity (inter- and intragranular) for the Main Buntsandstein averages 11.7 %, ranging between 0-1% and 23.5%. Overall, the samples shallower than 2000 m show higher optical porosity (av. ~ 10.6%) than the samples deeper than 2000 m that show an average total optical porosity of 8.4% (Fig. 4.5). In particular, the samples shallower than 2 km have higher average intergranular porosity (av. 8.5%) than deeper samples (av. 5%). Intragranular secondary porosity averages 2.1% in samples shallower than 2000 m and 1.7% in deeper samples (Fig. 4.5). The secondary pores can reach a dimension of 0.3-0.4 mm.

4.5.1.7 IGV, COPL and CEPL

The intergranular volume (IGV) is a quantitative indicator of compaction. In the Main Buntsandstein samples across the Roer Valley Graben, the IGV ranges from 6.6% to 48% with an average of 28.2%.

Overall, IGV decreases with depth. Samples shallower than 2000 m have higher intergranular volume (av. 29.9%) than deeper samples (av. 25.9%). This suggests that the deeper samples are on average more compacted than the shallower samples.

COPL and CEPL measure the loss of porosity through compaction and cementation. COPL and CEPL in the Main Buntsandstein samples average 16.2% and 19.1% respectively (Fig. 4.4). The maximum values observed are 31% for COPL and 42.8% for CEPL. This indicates that cementation has a larger impact on the loss of porosity than compaction. Samples shallower than 2000 m have lower COPL (av. 15.3) than deeper samples (17.1). This indicates that compaction has a larger impact on porosity loss in the deeper samples than in the shallower samples. CEPL averages with 19.4 and 19 in the shallower and deeper samples respectively.

4.5.2 Rock typing

The computation of a correlation matrix for petrographic and petrophysical data allows to assess the relationship between pairs of variables expressed by the Pearson's Product-Moment Correlation (r) (Fig 4.11). To correlate permeability, only 30 of the 56 samples were considered as wells KWK-01 and NDW-01 do not have permeability measurements. Overall, the sample porosities and permeability are positively correlated (r =0.58), while the permeability and optical porosity show a weaker positive correlation (r =0.26). This is likely related to the underestimation of optical porosity, which does not account for microporosity when optically determined.

Plug porosity displays a weak negative correlation with dolomite cement (r = - 0.29). This correlation is weaker when dolomite cement is plotted against permeability (r = - 0.19). However, when separating samples by grain sizes, dolomite correlates positively with porosity and permeability in very fine-grained samples, while it shows a negative correlation with porosity in coarser-grained samples (Fig. 4.12 a and b). This may be related to the fact that dolomite stabilizes the grain frame and prevents the finer grain-size sediments from compaction.

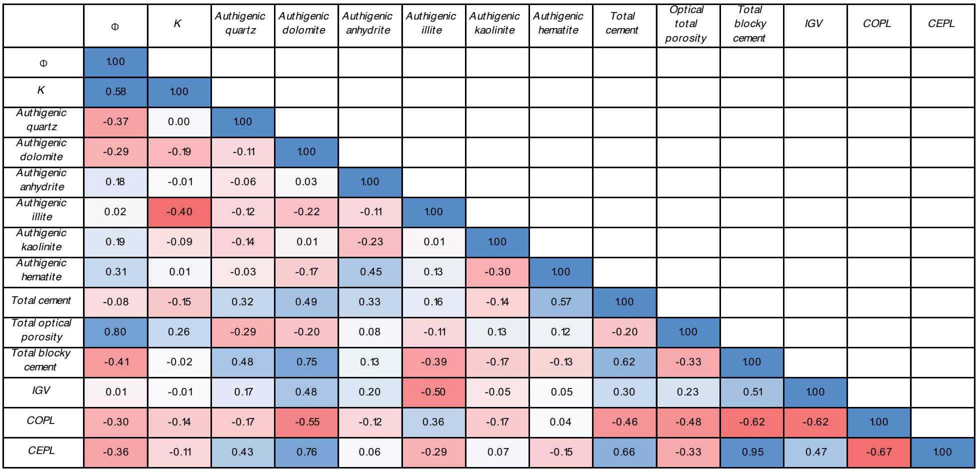

	Φ	K	Authigenic quartz	Authigenic dolomite	Authigenic anhydrite	Authigenic illite	Authigenic kaolinite	Authigenic hematite	Total cement	Optical total porosity	Total blocky cement	IGV	COPL	CEPL
Φ	1.00													
K	0.58	1.00												
Authigenic quartz	-0.37	0.00	1.00											
Authigenic dolomite	-0.29	-0.19	-0.11	1.00										
Authigenic anhydrite	0.18	-0.01	-0.06	0.03	1.00									
Authigenic illite	0.02	-0.40	-0.12	-0.22	-0.11	1.00								
Authigenic kaolinite	0.19	-0.09	-0.14	0.01	-0.23	0.01	1.00							
Authigenic hematite	0.31	0.01	-0.03	-0.17	0.45	0.13	-0.30	1.00						
Total cement	-0.08	-0.15	0.32	0.49	0.33	0.16	-0.14	0.57	1.00					
Total optical porosity	0.80	0.26	-0.29	-0.20	0.08	-0.11	0.13	0.12	-0.20	1.00				
Total blocky cement	-0.41	-0.02	0.48	0.75	0.13	-0.39	-0.17	-0.13	0.62	-0.33	1.00			
IGV	0.01	-0.01	0.17	0.48	0.20	-0.50	-0.05	0.05	0.30	0.23	0.51	1.00		
COPL	-0.30	-0.14	-0.17	-0.55	-0.12	0.36	-0.17	0.04	-0.46	-0.48	-0.62	-0.62	1.00	
CEPL	-0.36	-0.11	0.43	0.76	0.06	-0.29	0.07	-0.15	0.66	-0.33	0.95	0.47	-0.67	1.00

Figure 4.11: Correlation matrix to highlight the relationship between petrophysical and petrographic properties. Φ (porosity) and k (permeability) are derived from plug measurements. The other paramters are calculated from petrographic analysis. Total cement

includes quartz, dolomite, anhydrite, illite, kaolinite, and hematite cements, while total blocky cement accounts only for quartz, dolomite, and anhydrite cements. Total optical porosity includes inter- and intragranular porosities.

Permeability negatively correlates with illite with a correlation coefficient of - 0.4 respectively, whilst no apparent correlation between porosity and illite can be seen when comparing all the samples. Authigenic illite shows a negative correlation with IGV (r = - 0.5), thus it seems that higher illite contents correspond to lower intergranular volume. IGV is also positively correlated (r= 0.51) with total blocky cement, which is calculated by summing the relative abundances of quartz, dolomite, and anhydrite cements. Thus, when cement content increases compaction decreases.

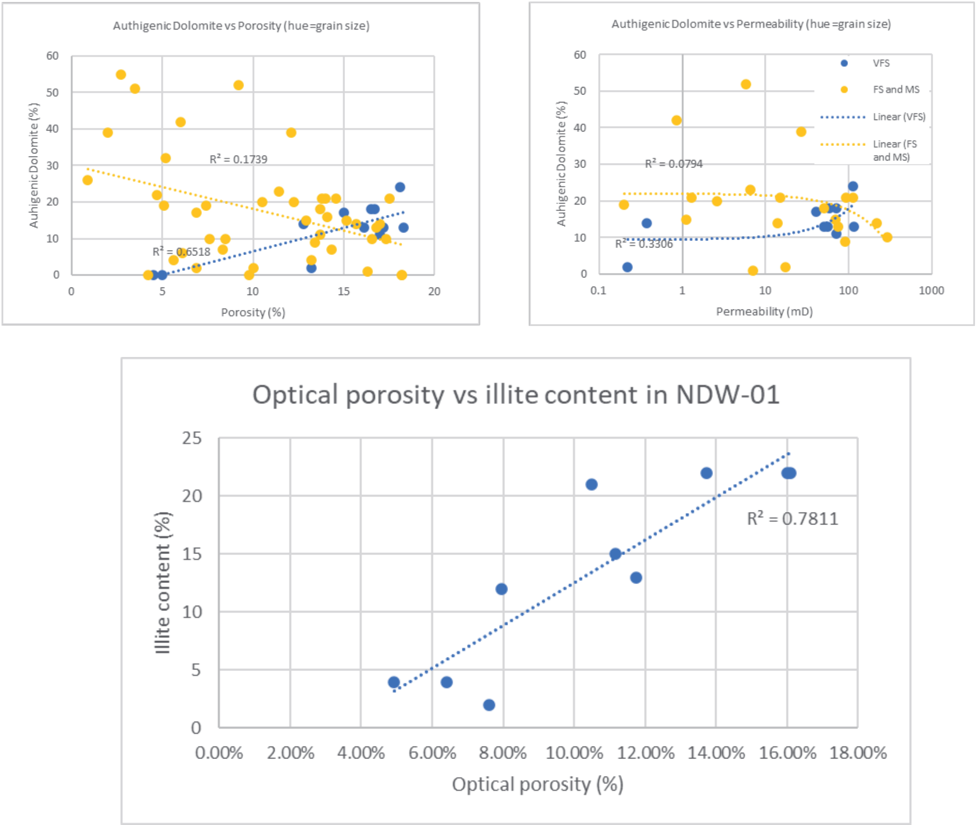

Figure 4.12: Crossplots displaying relationship between reservoir properties and illite and dolomite cement for data subsets. a,b) Relationship between authigenic dolomite cement content (%) and porosity (%) and permeability (mD). Samples from wells KWK-01 and NDW-01 are excluded from Figure 4.11b as they do not have plug permeability measurements at the sample location. The data suggest that porosity and permeability are positively affected in very fine-grained samples, while they are negatively affected in coarser sediments. c) In NDW-01, optical porosity is positively correlated with illite authigenic content.

When comparing illite and total optical porosity a weak negative correlation can be observed (r = -0.39). However, if isolating the samples of well NDW-01, a strong positive correlation (R^2 =0.78) exists between optical porosity and authigenic illite (Fig. 4.11). The samples where illite grain coating is well developed show higher optical porosities than the samples with a lower illite content. This may be related to the absence of quartz syntaxial overgrowth in the samples where a thick illite coating is developed (Fig. 4.13). Quartz shows a weak negative correlation with porosity (r = 0.37).

4.6 Discussion

4.6.1 Paragenesis

4.6.1.1 Eogenesis

Eogenesis refers to the earliest diagenetic changes that take place in or near the environment of deposition where the chemistry of the fluid is still controlled by the depositional environment (Chapelle, 1993). In this regime, the precipitation of dolomite cement as nodules represents one of the earliest diagenetic phases to occur. The dolomite nodules encase under-compacted and uncemented grains indicating that these nodules form relatively early in the diagenetic history prior to major mechanical compaction and grain arrangement (Fig. 4.8 a). The presence of early diagenetic dolomite nodules is frequently reported in Triassic systems (Henares et al., 2014; Busch et al., 2022) and more in general in arid to semi-arid settings (Molenaar et al., 2019). Their formation is related to pedogenic processes and helps to preserve intergranular volume (Aehnelt et al., 2021). Hematite-stained rims can be found at grain contacts (Fig. 4.8e); thus, the emplacement of hematite is also interpreted to occur shortly after the time of deposition. The formation of this type of coating can be related to sediment deposition in arid settings. Iron-rich clay infiltration occurs at shallow burial causing oxidation and reddening (Glennie et al., 1978).

Tangential grain coating by illite is locally present at grain contacts (Fig. 4.8f), thus its emplacement likely commenced before major grain rearrangement by compaction. Furthermore, it is often found encased by quartz cement, so its emplacement must be relatively early in the diagenetic history. The occurrence of illite grain coating is typical in fluvio-aeolian sediments in arid settings (Busch, 2020). The tangential illite may be related to pedogenesis, as observed in fluvio-aeolian Rotliegend samples from the Southern Permian Basin (Molenaar et al., 2019). Illite can also be recrystallized from kaolinite at temperatures higher than 70 °C (Worden and Burley, 2003). However, kaolinite was likely emplaced later in the diagenetic history as a result of feldspar dissolution during telogenesis (Fig. 4.13). Thus, we believe the pedogenic origin of illite to be the most reasonable.

Radial illite is present on top of the tangential illite grain coating, therefore it is interpreted to have formed after the emplacement of tangential illite. This is consistent with a study on radiometric ages of different illite textures on Rotliegend sandstones that indicate how radial illite mostly post-date tangential illite (Liewig and Clauer, 2000). Locally, it is present at grain contacts, thus it is likely that radial illite formed before major grain rearrangement due to mechanical compaction. Radial illite is characteristic of authigenic growth in open pore space (Wilson and Pittman, 1977). This suggests that primary porosity was still present.

The emplacement of syntaxial dolomite overgrowth is also a product of the eogenesis. Dolomite overgrowth usually develops on top of sand-size dolomite detrital clasts or large cm-scale reworked nodules, both in anhedral (Fig. 4.6c) and euhedral habits (Fig. 4.8c). The emplacement of anhedral overgrowth is caused by the presence of other detrital grains in contact with the original dolomite grain. Therefore, this overgrowth likely occurred contemporaneously with mechanical compaction and grain arrangement. However, the presence of overgrowth with euhedral crystal shape and the engulfing by quartz cement (Fig. 4.8c) suggest that this process occurs early in the diagenetic history. The overgrowths are composed of iron-poor and ferroan dolomite, where the dolomite grains likely represent the nucleation sites for the precipitation of the dolomite as observed in the sandstones from the Permian Rotliegend in the North Sea (Molenaar and Felder, 2019).

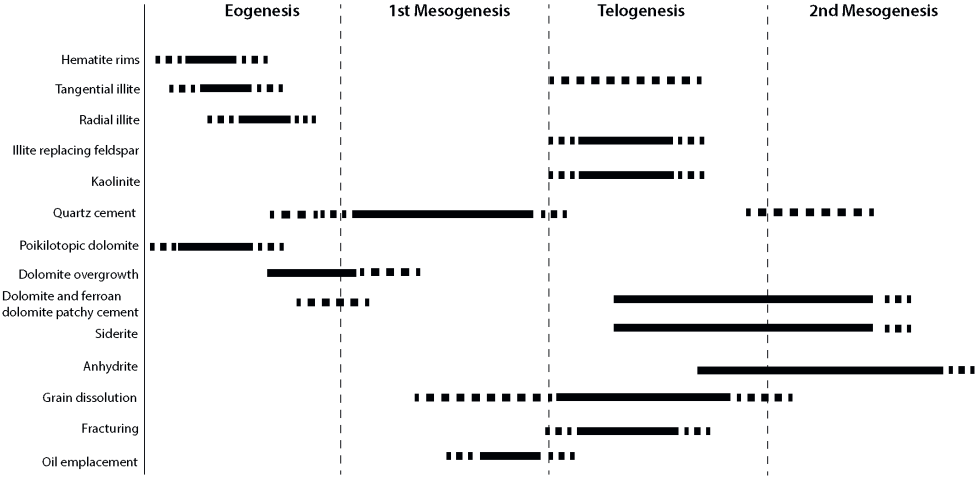

Figure 4.13: Reconstructed paragenetic sequence for the Buntsandstein sediments in the Roer Valley Graben

4.6.1.2. Mesogenesis

The transition between eogenesis and mesogenesis occurs when the sediments pass from being primarily influenced by the depositional environment (eogenesis) to the earliest stages of low-grade metamorphism which result in changes in pressure, temperature and pore water chemistry (Schmidt and Macdonald, 1979; Worden and Burley, 2003). The Buntsandstein sediments experienced mesogenesis during Mesozoic and Cenozoic rifting stages respectively, when sediments were buried at depths over 2-3 km and were subjected temperatures far above 90 °C (Fig. 4.2).

Syntaxial overgrowth (Fig. 4.6c) and poikilotopic quartz (Fig. 4.8c) cements represent the main cement developed during mesognesis. Quartz-dolomite genetic relationship in our samples indicate that the genesis of quartz overgrowth occurred in between an early and a late dolomite cementation phases, thus we interpreted the development of quartz cement as a mesogenetic product. The quartz overgrowth is likely sourced by the quartz pressure dissolution enhanced by the presence of illite at grain contacts (Monsees et al., 2020) and stylolite-like elements (Fig. 4.9d). An additional potential source is related to the (partial) dissolution of feldspars (Ulmer-Scholle et al., 2019), which may have started already during mesogenesis as suggested by Bertier et al. (2022). Bertier et al. (2022) proposed an eogenetic origin for the quartz syntaxial overgrowth as they observed quartz cement encased by carbonate cement, where carbonate cement formed prior to compaction. In well NDW-01 in the southeast of the Roer Valley Graben, we have observed poikilotopic cement encasing sediments that still preserve point-to-long contacts, suggesting a possible relatively early origin of the quartz. This poikilotopic cement may represent early silica nodules with a phreatic origin, which are common in distal sediments deposited in arid climates (Morad et al., 2000). This would explain the preservation nature of less compacted sediments therein.

Kaolinite is present in intergranular and intragranular pores from the Buntsandstein (Fig. 4.6d). Its presence as replacive phase within (partially) dissolved feldspars (Fig. 4.6d) suggests that kaolinite from after the dissolution of feldspars (Gaupp et al., 1993; Ulmer-Scholle et al., 2019). In this context, the frequent preservation of the original feldspar shape suggests that most of the compaction already occurred and the grain frame was already stable.

A second phase of dolomite precipitation in the remaining pores formed during later diagenetic stages, after quartz cementation and dissolution of feldspars (Fig. 4.8d). At this stage, siderite may also precipitate as it is observed to crystallize within dissolve grains. This late dolomite phase and siderite precipitation may have occurred late in diagenetic history, potentially during the second phase of major burial after the Cretaceous-Paleogene inversion.

Anhydrite is one of the latest diagenetic cement to precipitate as it encases both quartz syntaxial overgrowth and late dolomite patchy cement (Fig. 4.8b). Anhydrite can form in response to: i) brine reflux from underlying or overlying sediments through pore network and faults (Jones and Xiao, 2005), where the anhydritic layers in the Muschelkalk and Keuper Formations may be the saline fluid sources. ii) Percolation of saline meteoric water when the sediments were close to surface conditions. Given the quality of the collected data, the sourcing of Anhydrite could not be estabilished.

4.6.1.3 Telogenesis

Telogenesis refers to the phase in diagenetic history that occurs during uplift of the rocks in the subsurface (Worden & Burley, 2003). During the Jurassic, sediments from the Buntsandstein were locally uplifted as result of fault movements and brought to depths shallower than 1000-500 m. At these depths, sediments may have been exposed to the influx of low salinity, highly oxidized, and CO2-charged waters. These waters can enhance chemical changes, such as feldspar and rock fragments dissolution and alteration (Worden & Burley, 2003).

In the Buntsandstein sediments from the Roer Valley Graben, partial and complete dissolution of feldspars (Fig. 4.6d) and rock fragments (Fig. 4.6a and b) have been observed. This particularly observed in samples shallower than 2000 m and located close to the basin margin, and samples where fractures are present. The dissolution of feldspars explain the overall low percentage of feldspars in the Buntsandstein sediments (Fig. 4.7). Since the grain coating is still preserved and was not deformed, dissolution likely occurred once the grain frame was already stable either by cementation or mature stage of compaction. For this reason, we interpreted dissolution not to be an early diagenetic process.

In well NDW-01, dissolution is frequent in samples that are largely cemented by quartz (Fig. 4.10a and b). The emplacement of quartz cement occurred before dissolution took place as quartz cement traces have not been encountered within the dissolved grains. Under these circumstances, it is likely that grains may have dissolved in response to exhumation to near-surface conditions and reflux of water brines, during Late Jurassic to Late Cretaceous times (Cecchetti et al., 2024). Furthermore, the vicinity to fractures seems to have a positive impact on the dissolution. In well NDW-01, the fractured samples show widespread dissolution. Fractures may have enhanced the reflux of acidic water, which consequently induced the dissolution of rock fragments, dolomite mainly (Wennberg et al., 2016).

4.6.2 Diagenetic control on reservoir properties

Based on the data presented above, the controls on the reservoir quality of the studied Buntsandstein sample can be assessed. The effect of diagenesis on porosity and permeability have been addressed separately given the heterogeneity of the petrophysical measurements across the studied samples (see Data and Method).

4.6.2.1 *Porosity controls*

Porosity reduction in the Buntsandstein samples is more induced by cementation than compaction as indicated by the overall higher values of CEPL with respect to COPL. The opposite effect seem to have occurred in NDW-01, where instead compaction seems to be responsible for most of the porosity loss.

The effect that different types of cement have on porosity seems to be conditioned by the sediment heterogeneities. This is exemplified by the effect that dolomite has on the porosity of samples with different grain sizes (Fig. 4.12a). A possible explanation is related to the effect that cement has on grain frame stabilization during the early stages of compaction. Very fine-grained sandstones are usually more subjected to compaction than coarser sandstones (Worden and Burley, 2009). In these sandstones, dolomite cement likely counteracted compaction and preserved the intergranular volume. This is further supported by the positive correlation (r=0.51) between IGV and total blocky cement (quartz, dolomite, and anhydrite) indicating that in general blocky cement can help inhibit compaction. This result is consistent with data from previous studies on the interaction between compaction and cementation (Paxton et al., 2002; Busch et al., 2022).

Quartz cement appears to have a generally negative correlation with helium porosity (r = -0.37) when analysing all samples. This would be in contrast with data published recently by Schmidt et al. (2020) and Busch et al. (2022). However, there are samples with porosities lower than 5% and quartz cements below <5% and samples with porosities higher than 15% and quartz cement higher than 20%. An explanation similar to the one employed for dolomite cement can be used. The samples with low porosities and low quartz cement have high dolomite cement content. The samples that have high porosity and high quartz cement are instead very fine-grained sandstones, where quartz cement may have prevented compaction and deterioration of primary porosity.

Illite content does not correlate with helium porosities when the samples are plotted altogether (Fig. 4.10). However, when only the samples from well NDW-01 are plotted, a positive linear relationship ($R^2 = 0.78$) is observed between illite grain coating and optical porosity (Fig. 4.12 c). The relatively high porosities (10-15%) in samples where illite content is higher than 10% is likely related to the completeness of the illite grain coating that inhibits the quartz cement development (Fig. 4.19). This agrees with recent findings by Busch et al. (2022) and Beyer et al. (2014). However, illite grain coating can be a catalyst to enhance pressure

dissolution processes at grain contacts (Schöner & Gaupp 2005). In fact, illite cement correlates negatively with IGV (r=-0.5), suggesting that higher illite content reduces the intergranular volume.
Secondary porosity development in the Buntsandstein sediments occurs as a result of feldspar, cherts, carbonate, and silt/sandstone fragment dissolution. Mijnlieff (2020) indicates that when the Triassic sub-crop below the base Cretaceous unconformity, cements and grains are leached and reservoir properties are enhanced. In our dataset, we did not analyse samples in such a structural setting. However, the Triassic in well NDW-01 is situated about 200 m below the base Chalk Group unconformity (Cecchetti et al., 2024), where the presence of faults and fractures seem to have enhanced leaching. In medium-grained sandstones from well NDW-01, secondary pores can constitute ~65% of the total optical porosity (e.g. sample 2128.4 m). When considering all the samples from well NDW-01, secondary pores represent about 35% of the total optical porosity. Therefore, it seems that leaching can contribute to enhancing the porosity of the system to different extents without damaging the stability of the reservoir.

Overall, the Volpriehausen and Detfurth Formations have higher helium and optical porosities than the Hardegsen Formation. This may also be related to different fluvial styles. The Hardegsen formation is dominated by perennial like river deposits which are heavily cemented by dolomite. The higher amount of dolomite cement present in the Hardegsen Formation is likely a consequence of the soil formation and abundance of dolomite nodules therein. These nodules were acting as source for the dolomite cement (Cecchetti et al., in press). On the other hand, the Volpriehausen and Detfurth are dominated by more ephemeral river deposits, where dolomite paleosoil swith dolomite nodules are less frequently encountered.

4.6.2.2 Permeability controls

No strong correlation between permeability and the point-counted data is observed when considering all the samples together. This suggests that permeability is likely controlled by an interplay of different processes, rather than a singular dominant one. A negative moderate correlation (r = -0.4) is present between permeability and illite clay grain coating. Illite can have a negative effect on permeability when present in its radial habit, as its stacked meshwork can block pore through and transform macropores into micropores (Molenaar and Felder, 2018). However, radial illite is present in small traces only in the southeast part of the Roer Valley Graben (well NDW-01), thus we could not assess its impact on permeability. The overall negative effect of illite coating on permeability could be then related to the higher compaction in samples where illite coating is present and enhance pressure solution (Busch et al., 2020).

The petrographic study reveals the presence of stylolite-like dissolution horizons (Fig. 4.9 d), which were attributed to the presence of claystone, and micaceous horizons enhancing the dissolution of quartz grains. Similar elements have been reported in the Buntsandstein in the Campine Basin, NE Belgium (Bertier et al., 2022). The presence of insoluble minerals along the stylolite creates a baffle to flow across the stylolite but may enhance the flow along the stylolite (Bruna et al., 2019).

4.6.3 Implications for reservoir quality prospect in the Roer Valley Graben

The Main Buntsandstein sediments have experienced a complex tectonic history that resulted in the occurrence of a wide spectrum of diagenetic processes, which affected the reservoir quality of the sediments across the Roer Valley Graben. The burial history indicates that the Main Buntsandstein sediments are currently at their maximum burial depth (Fig. 4.2). IF Technology (2012) suggests that heat production from the Triassic sandstones in the southeastern part of the Netherlands is feasible where the sediments are located at present-day depths shallower than 2784 m. However, the employment of this proxy alone may result in unrealistic reservoir property prediction. This is exemplified by comparing the reservoir properties of the sediments in wells KWK-01 and SPC-01, which are both located close to the basin axis and have comparable maximum burial depths. Sediments in well KWK-01 display much lower average porosity than the sediments in well SPC-01, where instead the higher reservoir properties may be more favourable for geothermal energy (Table 4.2). The difference in reservoir properties is likely related to different burial paths the sediments in these two wells experienced. The sediments in well KWK-01 experienced a much rapid burial after deposition, which resulted in strong compaction and reduction of primary porosity. This is exemplified by the lower IGV and COPL in well KWK-01 compared to SPC-01 (Table 4.2). Moreover, the sediments in well KWK-01 are on average more cemented than in SPC-01 as indicated by the higher total blocky cement and quartz cement (Table 4.2). This is also likely a consequence of the rapid burial in well KWK-01. The sediments in well KWK-01 may have entered the mesogenic window early when porosity was still high leading to pervasive quartz cementation across the pore space. These data indicate that the maximum burial depth cannot be used as absolute proxy to assess reservoir quality and that the Main Buntsandstein sediments could still have preserved reservoir quality even if deeply buried below 2.5 km if the sediments experienced shallower burials right after deposition.

Table 4.2: Summarize of key petrographic and petrophysic values for the analysed samples. In the well column, the deepest sample depth is displayed in between brackets next to the well name. TBC = Total blocky cement.

Well	Quartz	Dolomite	Illite	Kaolinite	IGV	COPL	CEPL	TBC	Porosity	Permeability
BUM-01 (1515 m)	5.67%	8.69%	3.25%	0.00%	32.80%	13.35%	17.00%	16.57%	19.8	36.72
VRK-01 (1608 m)	7.75%	10.57%	4.39%	1.50%	23.63%	16.92%	21.44%	18.52%	10.11	6.2
NDW-01 (2181.9m)	8.96%	4.33%	6.89%	0.05%	22.45%	19.83%	14.58%	13.75%	12.83	n.a.
KDK-01 (2147m)	7.34%	11.22%	0.00%	1.25%	21.49%	15.38%	19.79%	18.57%	11.76	56.5
SPC-01 (2451)	5.72%	8.88%	2.89%	3.16%	32.44%	10.82%	18.91%	14.66%	14.46	31.15
KWK-01 (2468)	9.90%	11.59%	4.11%	0.35%	24.51%	22.44%	22.39%	21.66%	4.8	n.a.

The flanks of the Roer Valley Graben still represent the areas where the chances to find more favourable reservoir properties are higher. Cecchetti et al., (2024) indicated that the platform areas located across the Roer Valley Graben flanks have experienced less burials compared to the central part of the graben, thus reservoir properties are likely to have been less deteriorate by compaction. However, no thin sections have been analysed across the southern flank of the Roer Valley Graben, as no core data are available for the Main Buntsandstein sediments in that area. Bertier et al., (2023) show the Main Buntsandstein sediments have good reservoir properties (av. porosity 13.7% and permeability 38.7 mD) on the Belgian side of the Roer Valley Graben. However, their samples from the Buntsandstein sediments are representative for depths shallower than 1000 m, so they may not necessarily be an appropriate analogue for the Dutch side.

The wells across the northern flanks of the Roer Valley Graben show average porosity above 11% and permeability above 50 mD as exemplified by well KDK-01. However, Cecchetti et al.,

(*in press*) show that the sandstones along the northern flank are likely to be compartimentalized by mudstone units, thus less connected, which result in a higher number of wells needed to drain the reservoir (Geel and Donselaar, 2007).
The southeast part represents a rather underexplored area, where Triassic sediments may have preserved favourable reservoir properties. This may be related to shallower burials, lower amount of dolomite cement, and presence of quartz-cement free intervals where porosity over 20% are found. This is likely to be related to the different depositional environment, where a combination between aeolian coarser grain sandstones and illite may have helped the preservation of better reservoir quality.

4.7 Conclusion

A comprehensive petrological study on the Main Buntsandstein Subgroup sediments allow to assess the diagenesis and its control on the quality and the distribution of the reservoir properties in the Roer Valley Graben. The study revealed that quartz is the most abundant detrital grain followed by rock fragments. Among rock fragments, siliciclastic grains, and dolomite grains are the most frequently occurring type of grains. Siliciclastic and dolomite grains are intraclasts and are linked to the depositional environment. River deposits, particularly the sediments deposited by perennial rivers present in the Hardegsen Formation are the most enriched in intraclasts.

Illite, dolomite, and quartz represent the most dominant cements. These occurred in different habits at different stages during the diagenetic history. Tangential and radial Illite, and dolomite nodules occur early in the diagenetic history before major mechanical compaction. As the sediments were buried and compacted, quartz cementation became dominant. The sediments were then locally exhumated during the Mid to Late Jurassic. This enhanced the dissolution of feldspars and rock fragments, which then became the locus for illite and dolomite recrystallization during the second burial phase from Cretaceous onwards.

Cementation has on average a larger impact on porosity reduction than compaction. Dolomite and quartz cements have an overall positive impact on the porosity of very fine-grained sandstones, where these cements have helped prevent and preserve the intergranular volume. Conversely, these two cements have a negative impact on coarser samples that are less prone to compact, where these cements have filled pore spaces and decreased the total porosity of the samples. Tangential illite grain coating can inhibit quartz cementation when the coating has a high degree of completeness around the grain. In well NDW-01, a strong positive relationship between illite content and optical porosity is present. This relationship is driven by the capacity of tangential illite to inhibit quartz cementation that would otherwise reduce the porosity. Radial illite can decrease permeability transforming macropores into micropores. However, no statistical relationship between radial illite and permeability could be inferred. Dissolution can create secondary porosity that may constitute up to 65% of the entire optical porosity. It remains unclear whether the secondary pores are interconnected and can really contribute to enhancing the permeability of the system.

Overall, the sediments that experienced a less rapid burial after deposition are more likely to have preserved favourable reservoir properties due to less compaction and cementation rates. This would indicate higher chances to find more favourable reservoir properties along the flanks and on the southeastern part of the Roer Valley Graben where Buntsandstein sediments were subjected to less burial after deposition. Nonetheless, certain areas in the central part of the graben may still represent favourable areas as the relatively shallow burials right after compaction may have helped the preservation of primary reservoir properties.

Chapter 5: Fracture characterization and development in the Main Buntsandstein Subgroup in the West Netherlands Basin

Abstract

The geothermal well NLW-GT-01 in the West Netherlands Basin targeting the Lower Triassic Main Buntsandstein sediments at depths of about 4 km encountered a reservoir with low porosity (≤5.0%) and low matrix permeability (≤ 0.1mD). Natural fractures could serve as secondary flow conduits making geothermal production feasible. Multiple interpretations have however been made of the fractures in the this well making a judgement on whether these can enhance the fluid flow where matrix permeability may not be sufficient. In this study, a full re-evaluation is performed of the well data of the NLW-GT-01 well and the VAL-01 well on the other side of the basin. The analysis compares rock core inspection, wireline and image logs interpretations to document the drivers and characteristics of natural fracture distribution in the WNB and investigate the fracture and mechanical stratigraphy to place these along the geodynamics history of the basin.

The cores of NLW-GT-01 and VAL-01 display five types of discontinuities: veins, joints, Mode II fractures, stylolites and drilling-induced fractures. The natural fractures have a dominant NW-SE strike orientation. The drilling-induced fractures and the borehole breakouts indicate a NE-SW oriented in-situ minimum stress and an NW-SE oriented maximum stress. The natural fractures are favourably oriented to be open based on their orientation compared to the in-situ stress orientation.

The natural fractures are formed during large-scale tectonic events. During the burial of the formation related to the extensional phase of the West Netherlands Basin during the Mesozoic, veins, joints, conjugate fractures, and stylolites could have formed. Later, during the inversion of the basin in the Late Mesozoic-Cenozoic, tectonic stylolites likely formed, and the previously formed conjugate fractures may have been reactivated. Natural fractures are concentrated in more heterolithic intervals of the VAL-01 and NLW-GT-01 wells in both image logs and cores. These heterolithic sections display alternations of medium sandstones with silt- and claystones. The identification of more fractures in VAL-01 compared to NLW-GT-01 can be explained a more central location within the basin of VAL-01 where distal playa environments resulted in the deposition of more fine-grained material alternating with coarser sands. The more proximal NLW-GT-01 is dominated by fluvial sandstones that display less natural fractures. A correlation with density and Young’s modulus was not observed. This suggests fracture distribution is more controlled by changes in lithology in relation to different depositional environments, rather than absolute values of density and Young’s Modulus. The results of this study provide insights about the fracture characteristics and distribution in the Main Buntsandstein Subgroup across the West Netherlands Basin, contributing, more in general, to the understanding of natural fracture systems in clastic reservoir and their impact on porosity and permeability.

5.1 Introduction

Heat extraction from clastic sedimentary reservoirs is a common procedure in tectonically-stable areas where conventional high-enthalpy geothermal systems are not possible. The production potential of these reservoirs largely relies on the porosity and permeability of the sedimentary units. However, when deeply buried, the matrix quality of these reservoirs can be poor as result of physical and chemical processes that alter the primary sediment properties (Worden and Burley, 2003). In this context, natural fractures can play a key role in enhancing reservoir fluid flow (Nelson, 2001). Fractures can form the primary conduits for fluid flow and unlock the geothermal potential of deep and/or tight reservoir units.

This work focuses on the characterization of fractures in the Main Buntsandstein Subgroup in the West Netherlands Basin area. The Main Buntsandstein Subgroup is a siliciclastic succession situated at depths between 2-4 km with in-situ temperatures ranging from 60-120° C. In 2017, a well (NLW-GT-01) was drilled to explore the Main Buntsandstein Subgroup geothermal potential at depths of approximately 4 km. The well data reported low porosities (≤ 5.0%) and matrix permeabilities (≤ 0.1 mD) as result of intense diagenesis (Felder and Fernandez, 2018).

The role of fractures in enhancing fluid flow in the Main Buntsandstein Subgroup was investigated post-mortem by Boersma et al. (2021), who concluded that the assumed-to-be open fractures observed in well NLW-GT-01 could increase the permeability and provide sufficient heat production from the Main Buntsandstein in the area around well NLW-GT-01. The analysis of open fractures in another well (VAL-01) in the northern sector of the West Netherlands Basin support the presence of fracture permeability in the Lower Triassic sediments (Atlas Geoscience, 1998).

However, there is a lack of consensus when comparing all the available studies on fractures in these two wells (Vinci, 2018; Boersma et al., 2021; Kourta and Jocker, 2018). For example, the number of interpreted natural open fractures from the image log in NLW-GT-01 ranges from over 300 interpreted by Kourta and Jocker (2018) to 58 interpreted by Boersma et al. (2021). The discrepancy in these studies is enhanced by the presence of drilling-induced fractures that can mislead the interpretation of natural fractures (Lorenz & Cooper, 2017; Lai et al., 2018; Chatterjee & Mukherjee, 2023). This creates uncertainty in the assessment of the fracture permeability and, consequently, the feasibility of geothermal operations in the Main Buntsandstein units.

This study aims to document the characteristics of natural fractures and their distribution in the West Netherlands Basin and explores the factors that controlled their formation. This is achieved by integrating core data, image and wireline logs from wells NLW-GT-01 and VAL-01, located in different sectors of the West Netherlands Basin (Fig. 5.1). The fractures are studied in parallel with the sedimentology of the cores to study the fracture types and geometries in relation to sediment textures and lithologies. These results were then integrated with image and wireline logs to extrapolate the fracture and sedimentological analysis to the uncored intervals and assess the fracture distribution in the Main Buntsandstein Subgroup sediments. Finally, the fracture origin, drivers and control are discussed. This study contributes to the understanding of fracture network characteristics in the Main Buntsandstein Subgroup in the West Netherlands Basin and identifies aspects that may be applicable to other naturally fractured clastic reservoirs.

5.2 Geological setting

5.2.1 Structural framework

The West Netherlands Basin is a prominent subsurface structure in the southwestern part of the Netherlands (Fig. 5.1). It is bounded by the Central Netherlands Basin to the northeast, and it is connected with the Roer Valley Graben to the southeast. Along its southern margin, a series of normal faults separates the West Netherlands Basin from the Oosterhout platform and Zeeland High. To the northwest, the West Netherlands Basin continues into the Broad Fourteen Basin offshore the Netherlands (Geluk et al., 1996; van Balen et al., 2000; Wong et al., 2007; Kombrink et al., 2012; Willems et al., 2020; Fig. 5.1).

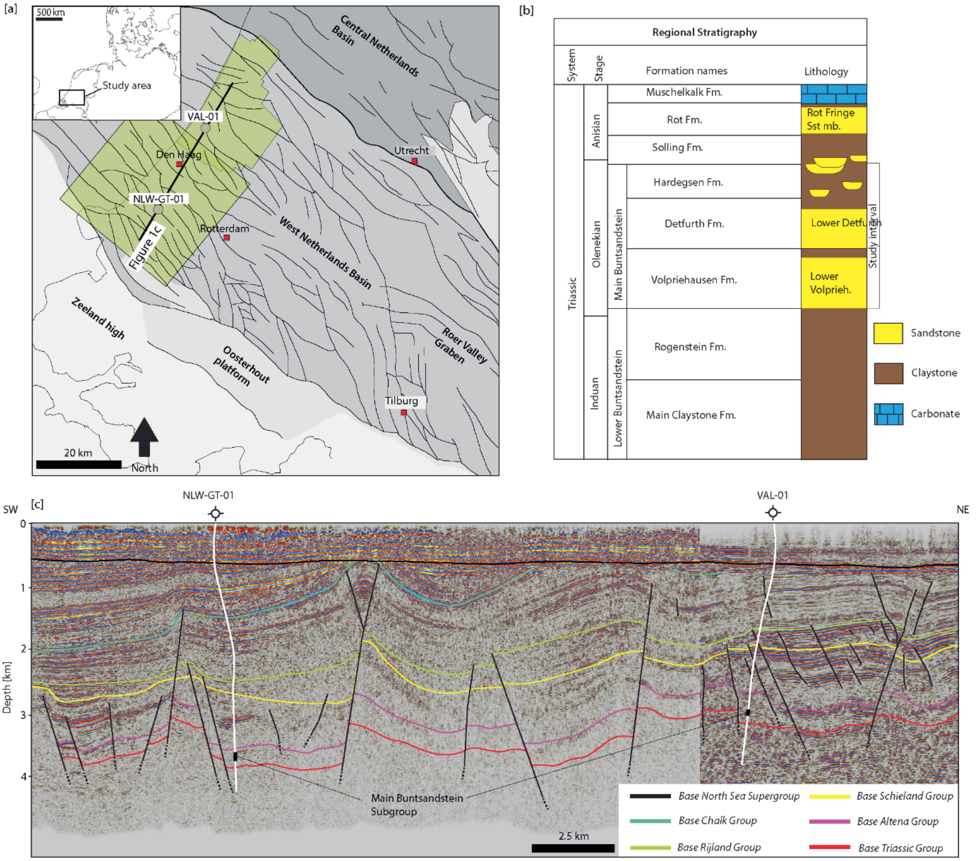

Figure 5.1: a) Study area with wells used in the study and seismic surveys (L3NAM1989J and L3NAM1990C) used to interpret the subsurface structures. b) Simplified stratigraphic column for the lower and upper Triassic sediments (after Cecchetti et al., in press)c) composite seismic section displaying the main structural features and main stratigraphic group horizons.

The West Netherlands Basin started developing as result of the assembly of Pangea in the Paleozoic (Van Wijhe, 1987; Pharaoh et al., 2010). During the Late Carboniferous to Early Permian, wrench faulting led to the reactivation of the Early Paleozoic NW-SE oriented faults and the development of a conjugate set with NE-SW to NNE-SSW strikes (Van Wijhe, 1987; Van Balen et al., 2000; Worum et al., 2005; Wong et al., 2007).

During the Mesozoic, Pangea began to split in response to an E-W-oriented extensional regime (Wong et al., 2007). The rifting commenced in the Triassic and lasted throughout the Jurassic and the Early Cretaceous (Geluk, 1998; De Jager, 2007). This rifting phase created a horst and graben system within the West Netherlands Basin with a dominant N-S to NW-SE fault orientation (Van Wijhe, 1987; Geluk, 1998; Van Balen et al., 2000; Wong et al., 2007).

Crustal extension across the North Sea graben system decreased gradually during the Early Cretaceous and ended during the Aptian to Albian (Van Wijhe, 1987; Van Balen et al., 2000; Pharaoh et al., 2010). During the Late Cretaceous, the West Netherlands Basin was inverted as result of the Alpine Orogeny (Van Balen et al., 2000; Worum et al., 2005; Wong et al., 2007; Kilhams et al., 2018). Compressional and transpressional stresses reactivated pre-existing N-S to NW-SE trending faults formed during the Late Jurassic and the Early Cretaceous (Van Wijhe, 1987; Wong et al., 2007). This period was then followed by a period of regional subsidence (Van Wijhe, 1987; Van Balen et al., 2000; Wong et al., 2007).

5.2.2 The Main Buntsandstein Subgroup

5.2.2.1 Stratigraphy and sedimentology

In the West Netherlands Basin, the Main Buntsandstein Subgroup consists of three Formations, namely: Volpriehausen, Detfurth, and Hardegsen (Van Adrichem Boogaert and Kouwe 1994) (Fig. 5.1b). The Volpriehausen and Detfurth Formations are formed by a lower sandstone unit of fluvial/aeolian origin, and an upper silt/claystone unit deposited in a playa-lake environment. The Hardegsen Formation usually has a lower Net to Gross (N/G) compared to the lower two Formations. It consists of a more frequent alternation between fluvial sandstones and claystones, as revealed by an extensive sedimentological study recently (Cecchetti et al., in press).

The sedimentation of the Main Buntsandstein Subgroup commenced at the Induan to Olenekian transition during the Early to Middle Triassic. Sediments were deposited through fluvial systems in an endorheic basin under arid to semi-arid conditions (Ames and Farfan, 1996; Geluk, 2005). A major fluvial system in the south-eastern Netherlands supplied sediments in the West Netherlands Basin during the Early to Middle Triassic, with additional sediments delivered from the adjacent London Brabant Massif (Cecchetti et al., under review).

5.2.2.2 Diagenesis

The initial permeability and porosity of the Main Buntsandstein sediments were altered by different diagenetic processes like compaction, cementation, and dissolution (Purvis and Okkerman, 1996; Mijnlieff, 2020; Cecchetti et al., in press). Shortly after deposition (eogenesis), the sediment grains were coated with iron and clay, then cemented with dolomite and compacted (Bath et al., 1987; Purvis & Okkerman, 1996; Spain & Conrad, 1997; Kunkel et al., 2018; Bertier et al., 2023; Cecchetti et al., in press b). With burial (mesogenesis), sediments were exposed to an increase in temperature and pressure, and a change in pore fluid chemistry. These processes resulted in further compaction of the sediments and the precipitation of quartz, dolomite, and anhydrite cements (Purvis & Okkerman, 1996; Bertier et al., 2023). The mesogenesis lasted from the Late Triassic till the Early-Mid Cretaceous and from Paleogene up to present-day (Chapter 3 of this thesis). During the Late Cretaceous–

Paleogene inversion, sediments of the Main Buntsandstein Subgroup were exhumated to near-surface conditions, and dissolution of the dolomite and anhydrite took place (Bath et al., 1987; Purvis & Okkerman, 1996; Spain & Conrad, 1997; Mijnlieff, 2020). The process of dissolution enhanced the creation of secondary porosity.

5.3 Data & Methods

Data from two wells were used in this study. Well NLW-GT-01 is located in proximity to the southern margin of the West Netherlands Basin, where the Buntsandstein is encountered at depths of ~ 4 km, whilst well VAL-01 is located closer to the basin axis where the Main Buntsandstein sediments are present at ~ 3 km Fig. 5.1c).

The characterization of fractures and the sedimentological analysis are performed on slabbed and full core. Following the core inspection, image, and wireline logs are used to extrapolate the fracture and sedimentology analysis from cored to uncored intervals and assess potential controls on the fracture density distribution. A more detailed explanation of the methodology and the theory is given below.

5.3.1 Core analysis

5.3.1.1 Sedimentological analysis

The core samples are analyzed in terms of grain size distributions, lithologies, and sedimentary structures. Grain size is determined with a grain-size chart under a hand lens according to Wentworth (1922). Sedimentary structures, bioturbated sections, and changes in lithology are systematically captured throughout the cored interval. The sediments are then subdivided in lithofacies types based on their macroscopic characteristics mentioned above. The lithofacies types are then grouped into lithofacies associations, which represent assemblages of spatially and genetically related lithofacies deposited in a particular depositional environment.

5.3.1.2 Fracture analysis

The core is analyzed at mm to cm scale to capture fracture characteristics and heterogeneities. The depth of each structural discontinuity is measured at the center of the core slab. The sense of movement, the mineralization, and the smoothness of the discontinuity plane are marked and the orientation, length, aperture, and offset are measured. The true fracture orientation is obtained by identifying the fracture interpreted in the core in the image log, as the cores could not be reoriented. If the bedding is tilted, the original fracture position is retrieved by back-tilting the fractures relative to the bedding orientation.

Natural fractures are classified in terms of extensional fractures (Mode I) and shear fractures (Mode II/III) (Figure 5.4) (Fossen, 2010; Lorenz & Cooper, 2020). A Mode I fracture is called a joint when it is barren (not cemented) and a vein when filled with cement. Fractures where opposing fracture walls move in opposite directions parallel to the fracture plane are called Mode II shear fractures (Fossen, 2010; Lorenz & Cooper, 2020). They display offset and have the tendency to develop as pairs of conjugated sets, which can be used to determine the orientation of the three-principle stress (Fossen, 2010). Furthermore, stylolites are identified as another type of discontinuity. A stylolite forms in response to pressure-solution and it is not a fracture (Heald, 1955; Martin Baron, 2007). This process can create an anastomosed surface consisting of rough lines displaying teeth-like peaks. These peaks are formed due to the difference in solubility of minerals (Bruna, 2019) associated with the type of sediment in which the stylolite forms. Stylolites form perpendicular to the maximal principle stress (Martin Baron, 2007).

Drilling-induced fractures were encountered. However, it was often not possible based on the collected observations, to differentiate between natural open fractures (joints) and drilling-induced fractures based only on their appearance. Therefore, an orientation-based filter was employed to identify the drilling-induced fractures. This filter was based on the orientation of the drilling-induced petal fractures that were interpreted with confidence in the core. Petal fractures are curved fractures that begin on the edge of the core and curve parallel to the core length, potentially becoming a centreline fracture. These are created as result of drilling activities. More detailed examples of petal fractures and, more in general, of the orientation-based filter is given in the result section.

The relative chronology of the identified structural features is then assessed to determine the relative time of fracturing in relation to the different tectonic events. The stress station associated to a set of fractures was assessed following the Andersonian theory of faulting (Anderson, 1951). The relative chronology is determined by investigating the cross-cutting relationships of observed discontinuities (abutment terminations), which provide information about the history and relationship between fracture groups (Peacock et al.,2016).

5.3.2 Well log analysis

5.3.2.2 Image logs fracture classification

Image logs are used to identify individual fractures on the borehole wall, thus extending the fracture interpretation to the uncored intervals. The image logs are analyzed in WellCAD to locate fracture and bedding surfaces.

For the well VAL-01, the AST (Acoustic Scanning Tool) was used. The AST records the changes in acoustic impedance in the sediments. High impedance indicates high-density or non-porous media, and low impedance porous and low-density formations. Discontinuities are characterised by low impedance sinusoidal waves in AST images (Lai et al., 2018). The AST has a resolution of 1 cm, thus fractures with apertures smaller than 1 cm will not be detected.

For the well NLW-GT-01, the FMI (Formation Microresistivity Imaging) was available and used to identify fractures based on their resistivity response. FMI has a resolution of 50 μm. Usually, when a fracture is closed (e.g. cemented) it tends to be resistive, whereas, when the fracture is open, it tends to be less resistive. In the FMI, fractures are classified as high-resistive (likely to be open) and low-resistive (likely to be close). In the AST, a classification based on the acoustic impedance response could not be made, as most of the fracture types identified in the core could not be directly matched with the fractures in the AST.

5.3.2.3 Fracture distribution

Once the fractures were interpreted in the image logs, a fracture density curve was computed. The fracture density is the number of fractures per unit length (Makel, 2007; Lorenz & Cooper, 2020). In this work, the fracture density is calculated over a 1 m interval. A correction was applied to the fracture density as the probability of encountering fractures parallel to the orientation of the well is much lower than fractures forming normal to the orientation of the well. Therefore, a correction coefficient equal to (1/costheta) was employed (Tartarotti et al., 1998). Based on the fracture density, the core or image log can be subdivided into units, and the fracture stratigraphy then be discussed (Laubach et al., 2009).

To understand potential controls behind the fracture distribution, the fracture density was compared against the gamma ray log curve, density log, and Young's modulus. The logs are compared by assessing changes in the mean value over depth and the fluctuation in the parameters. The fluctuations are then quantified by calculating the derivative of the parameter over an interval of 20 cm based on the minimum resolution of the wireline logs. Young's modulus (E) is calculated based on the V_p, the V_s, and the density logs (ρ) according to the following equation (Hunfeld et al., 2021):

$$E = 2G(1 - v) \quad (1)$$

Where v is the Poisson's ratio calculated using the formula :

$$v = \frac{V_p^2 - 2V_s^2}{2(V_p^2 - V_s^2)} \quad (2)$$

And G is the Shear modulus, calculated using:

$$G = \rho V_s^2. \quad (3)$$

5.4 Results

5.4.1 Sedimentology of the Main Buntsandstein

The core of NLW-GT-01 is largely composed by fine to medium-grained grey sandstones. Cross-stratification and cross-lamination (ripples) are the most dominant sedimentary structures in sandstones (Fig. 5.2 a). These sandstones can usually contain sub-rounded clay pebbles. Sandstone API values range between 50 and 125 and are characterized by blocky shapes on the gamma ray log. The relatively high upper limit of the sandstone API range is related to the frequent occurrence of clay pebbles that enhance the gamma radiation content.

Sandstone intervals can be locally intercalated with silt/claystone units. These fine-grained units range from 1 cm to 25 cm in thickness and can be laminated or homogeneous (Fig. 5.2a). These units have higher gamma radiation values that can reach up to 160-170 API.

The core of VAL-01 is characterized by an alternation of sandstone and heterolithic units. The sandstones are mostly fine-grained and can be cross- to horizontally-stratified. These are characterized by gamma ray values lower than 80-90 API. The heterolithic layers can reach thicknesses up to 10-15 m. They are formed by an alternation of sand, silt and claystone at mm to cm scale. The sediments are mostly red, and often show mud cracks and dewatering structures. On the gamma ray, the heterolithic sediments are characterized by gamma ray usually larger than 100 API.

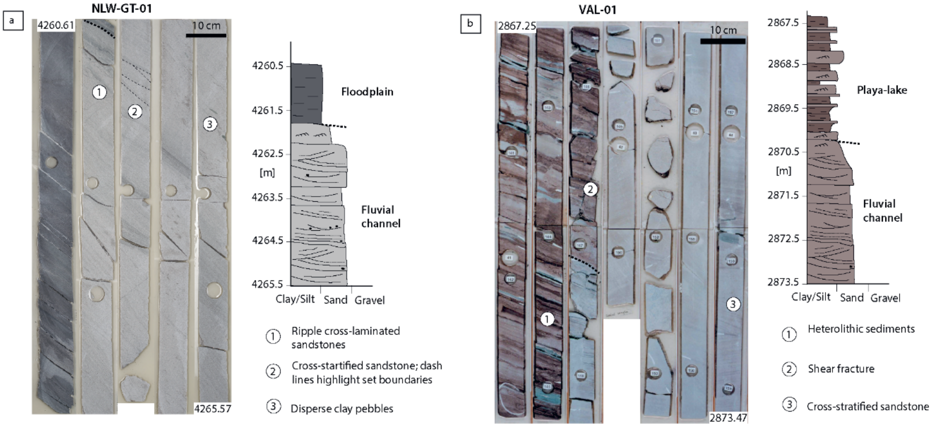

Figure 5.2: a) sedimentology of NLW-GT-01. b) sedimentology of VAL-01.

In well NLW-GT-01, the presence of cross-stratified and cross-laminated bearing ripples sandstones suggest deposition via rivers. Given the high N/G and abundancy of cross-stratified sandstones, these rivers are likely similar to the ephemeral rivers described in Chapter 3 of this thesisThe presence of clay clasts and the low preservation rates of claystone indicate floodplain incision and reworking activity. In well VAL-01, the higher preservation of fine-grained sediments suggests a more distal area where rivers were likely less active. The presence of red colors and frequent mud-cracks in the claystone indicate that sediments were more frequently exposed to subaerial conditions compared to the sediments in NLW-GT-01. Therefore, considering the observed sedimentary structures in VAL-01 and the more distal position from the southern part of the basin where sediments were likely to be sourced, the depositional environment in VAL-01 is interpreted as an arid alluvial floodplain to playa-lake likely related to the playa-lake deposits observed in the northern part of the Roer Valley Graben (Fig. 3.11 in Chapter 3 of this thesis)

5.4.2 Fracture types in the Main Buntsandstein

5.4.2.1 Veins

Veins with either quartz or clay fill have been identified with apertures ranging from 1 mm to 2 cm (Fig. 5.3a). These are usually subperpendicular to the beddings. The exact composition of the clay filled fractures could not be assessed from core only. On the core of wells NLW-01 and VAL-01, 65 veins have been interpreted (Table 5.1). On the FMI of well NLW-GT-01, the clay cemented fractures show a medium resistive response, and the quartz cemented as low resistive.

5.4.2.2 Shear Fractures

Shear fractures are identified on the core by the visible offset they create on the bedding or on pebbles (Fig. 5.3b). These fractures can bear offsets ranging from 1 mm to 15 cm. They usually have rough fracture planes and are concentrated in the coarse-grained sections of the core. A total of 39 shear fractures have been identified in the available core samples (Table 5.1). On the FMI, the resistivity response changes, but they can sometimes be recognized when the offset is visible.

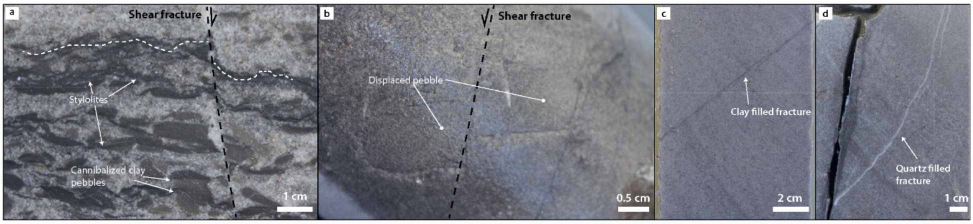

Figure 5.3: Main types of fractures encountered in the main Buntsandstein. A) A series of stylolites cross-cut by a subperpendicular shear fracture with normal offset (NLW-GT-01, 4253-4254 m). b) Shear fracture displaying a clast. The shear fracture shows a normal offset (NLW-GT-01, 4259-4260 m). c) Example of a fracture filled by clay subperpendicular to the bedding offset (NLW-GT-01, 4259-4260 m). d) Quartz vein subperpendicular to the bedding (NLW-GT-01, 4264-4265 m).

5.4.2.3 Stylolites

Stylolites are characterized by irregular surfaces, with usually undulating profiles that evolved around insoluble grains (Fig. 5.3a). Stylolites are commonly found in coarse-grained core sections and around clay pebbles. A total of 18 stylolites have been identified and interpreted (Table 5.1). The stylolites appear as low resistive features, distinctly lighter than the matrix resistivity. However, they are often not interpreted on the image logs as they are below the data resolution.

5.4.2.4 Open fractures: natural joints and drilling-induced fractures

A total of 119 open fractures have been interpreted in the core samples from wells NLW-GT-01 and VAL-01 (Table 5.1). In well NLW-GT-01, nine petal fractures have been interpreted with confidence and oriented (Fig. 5.4a and e). Another type of induced feature is a desiccation crack (Fig. 5.4b). These are very thin cracks (less than 1 mm) that are created primarily on mud-rich intervals due to the shrinking of the mudstone. However, due to their small scale, they could not be identified and oriented on the FMI log thus they could not be used for the orientation-based classification.

The rest of the interpreted open fractures in the core present characteristics common for both natural and drilling-induced fractures. Most of these fractures are planar, not bedding parallel, with smooth or rough fracture planes and are open. No distinctive characteristics have been interpreted that allowed to separate with confidence natural from drilling-induced fractures in the core. In the FMI, natural joints and drilling-induced fractures were also not distinguishable based on their response as they show both low and high resistivity. Therefore, a classification was made developing a filter based on the orientation.

Table 5.1: Table representing the fracture types interpreted in wells NLW-GT-01 and VAL-01. The open fractures include both joint and drilling-induced fractures, which classification was based on their orientation.

Fracture Type	**NLW-GT-01**	**VAL-01**
Mode I - vein	19	45
Mode II - shear fracture	7	32
Stylolite	8	10
Open fracture (joints and drilling-induced)	49	70
Total	**83**	**157**

The 9 petal drilling-induced fractures in well NLW-GT-01 formed the base for the orientation-based classification. Petal fractures have a dip angle higher than 80° and a strike between 118° and 137°(Fig. 5.4e). Their orientation was compared to the orientation of all the other natural fractures interpreted. The interpreted natural fractures in NLW-GT-01 have almost the same orientation as the petal drilling-induced fractures. However, when comparing the dip angle, a distinct difference can be observed. The natural fractures have dip angles between 50-90° while the drilling-induced fractures are limited to a range of 80-90° and the drilling-induced fractures have strikes ranging from 118-137° whereas the natural fractures range from 105-158° (Fig. 5.4d).

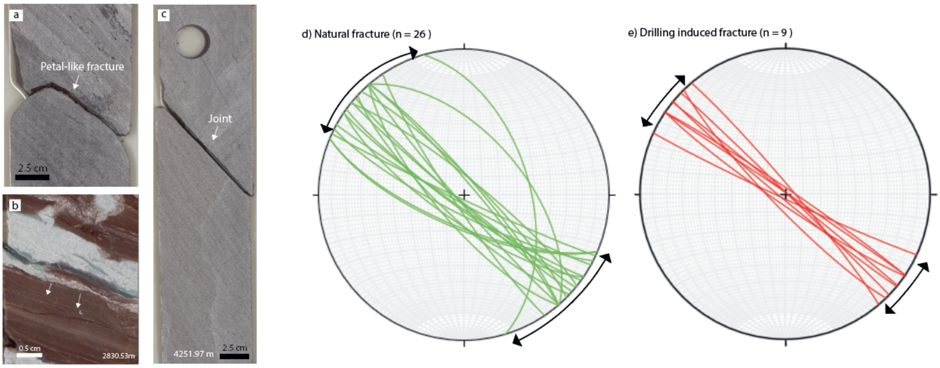

Figure 5.4: a) Petal drilling-induced fracture (NLW-GT-01, 4253.55 m). This type of drilling-induced fracture has formed the basis for the orientation-based classification. b) desiccation elements (VAL-01, 2830.53 m). c) Example of an open fracture that could not be classified based on its appearance (NLW-GT-01, 4251.97 m). d) Orientation of natural fractures from NLW-GT-01. These fractures include joints. e) Orientation of the 9 petal drilling-induced fractures interpreted in the core of NLW-GT-01.

Taking the difference in orientation into account, the open fractures in NLW-GT-01 and VAL-01 are classified as drilling-induced fractures when they are in the range of the orientations of the drilling-induced fractures. The fractures with a dip angle higher than 80° and a strike between 118° and 137° are classified as drilling-induced. The fractures that fall outside these orientations are classified as joints. This filter was used to interpret fractures in the image logs and subsequently calculate the fracture density curves for each well. The uncertainties related to the employment of this method is discussed in 5.1.

5.4.3 Fracture genetic relationship and associated stress regimes

5.4.3.1 NLW-GT-01

The development history of the fractures found in the core of NLW-GT-01 is assessed by interpreting the fracture abutment relations, which serve to understand the genetic and mechanical relationships between different fracture types. Five types of discontinuities are observed with abutment relations over the 30 m of cores. These are: bedding parallel stylolites, quartz and clay-cemented Mode I fractures, Mode II fractures and a tectonic stylolite (Fig. 5.5a and b)

The bedding parallel stylolites are the first discontinuities that are created. These are created by a vertical maximum stress orientation (Fig. 5.5c). The quartz-cemented Mode I fractures are striking NNW-SSE at a 90° angle to the bedding parallel stylolites (Fig. 5.5c) . These could be formed under the same vertical maximum stress (Anderson, 1951; Martin Baron, 2007). Additionally, they indicate a horizontal minimum stress in the NE-SW orientation. The quartz cemented fractures, which are also NNW-SSE oriented, could be one side of a conjugate set, where the shearing component of the fracture on the slab could have been missed (Fig. 5.5b). The other side of the conjugate set is expected to be oriented NNW-SSE dipping in the opposite direction, parallel to the borehole orientation of 075/040. However, the other side of a potential conjugate set is not seen on the core. These types of fractures likely form in a normal stress regime with vertical maximum stress (Fig. 5.5c; Anderson, 1951).

Two other quartz-cemented fractures can be seen with an aperture between 0.5 to 1.5 cm (Fig. 5b). On the slab, the movement of the fractures could not be determined, due to the broken nature of the core on the polymer slab. On the same section, one clay filled fracture is present (Fig. 5.5b). This clay filled fracture terminates against the quartz cemented fracture, indicating that it formed after the quartz cemented fracture (Fig. 5.5b).

The second phase is characterized by the shear fractures at 90° angle to the bedding (Fig. 5.5a and d). These fractures are oriented with 90° angle to the bedding, which is 30° higher than the angle of the expected conjugate fractures in the previously mentioned normal regime (Fig. 5.5d). However, the orientation of the maximum stress could not be determined based on the nature of the collected data.

The last phase is the regime in which a tectonic stylolite forms NNW-SSE oriented and at a 90°angle to the bedding planes (Fig. 5.5e). The tectonic stylolite formed last as it overprints one of the shear fractures and two of the quartz cemented mode I fractures and one shear fracture terminate against the stylolite (Fig. 5.5e). The stylolite plane is very angular and irregular and is not likely to be created by slip on a fracture plane. However, the bottom part of the stylolite plane is more planar and smoother. The bedding parallel stylolites have been displaced over 10 cm by this tectonic stylolite. This displacement could not have been caused by the dissolution of the stylolite only. A hypothesis is that before the tectonic stylolite was created, the bedding parallel stylolites were displaced by a shear fracture. The tectonic stylolite could have been created at the location of the shear fracture, as it might have been open, allowing flow and dissolution, creating a preferential location for the stylolite to form.

The displacement of the bedding can be partly created by the shear of the fracture and partly by the cannibalistic behavior of a stylolite. The stylolite is formed at 90° to the maximum stress direction. This would indicate maximum horizontal stress and where reverse shear fractures may also have been formed.

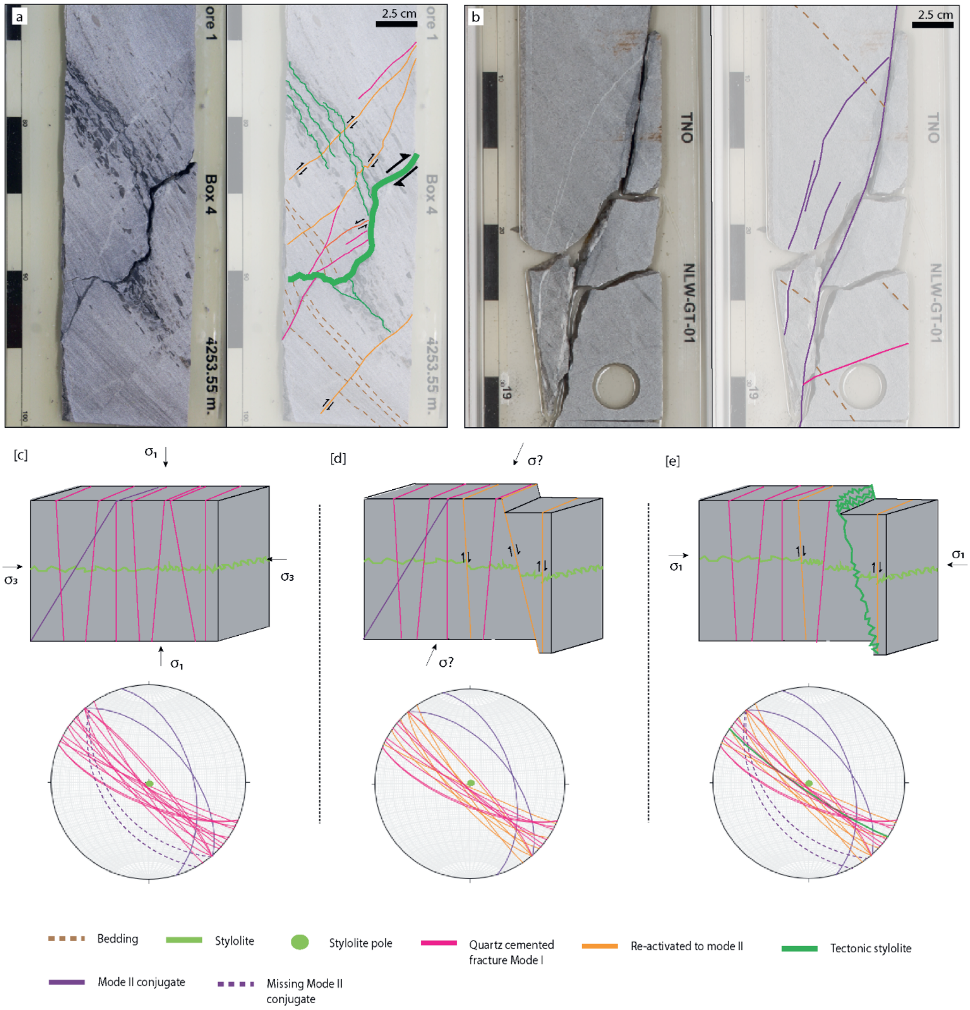

Figure 5.5: a) Relative chronology assessment by abutment relations (NLW-GT-01, 4253.55 m). Arrows indicate the movement of blocks displaced by shear fracture b) Relative chronology assessment by abutment relations (NLW-GT-01, 4266.78-4267.08 m). c), d) and e) three phases of fracturing on schematic block diagrams with stereoplots of all the available backtilted and oriented fractures over the core of NLW-GT-01.

5.4.3.2 VAL-01

There are no intervals on core VAL-01 where the abutment relations between different fracture types could be interpreted. The analysis of fracture genetic relationships is, therefore based solely on the orientation of fracture sets.

On the core, three groups of fracture orientations are recognized (Fig. 5.6b): i) a E-W striking set at an angle of 60-70°; ii) a NW-SE striking set at an angle of 30-40°; iii) a NW-SE striking set at an angle of 50-70°. These sets can also be recognized in the borehole images. iv) a NW-SE set of fractures dipping at an angle of 90° visible in the borehole image.

The fracture sets could have been formed by a combination of a normal regime and reverse regime; both cases are represented in a set of schematic block diagrams (Fig. 5.6a). The order of the stress regimes is not known based on the attitude analysis.

Several bedding parallel stylolites are present in the core. These form perpendicular to the maximum stress direction, which in this case would be vertical, indicating a normal regime. This regime would fit the 90° dipping veins and the mode II fractures at 50-70° in a NW-SE direction. The mode II fractures 50-70° could form one side of a conjugate set; the other side of the conjugate set is expected to be oriented striking parallel but in the opposite direction, which is parallel to the orientation of the well, enhancing the possibility that it goes undetected.

Lastly, the mode II conjugate can be formed as one side of a conjugate set in a reverse regime. The other side of the conjugate pair is expected to be oriented 30° dipping in the opposite direction, which is sub-parallel to the orientation of the borehole.

The fractures in A are dipping south at an angle of 60° striking E-W. They are not striking parallel to the set B, C and D. They could be formed as one side of a conjugate set in a normal regime. The opposite side of the conjugate is not observed on the image log, likely because it could be as the expected orientation is the sub-parallel direction of the borehole.

It is also possible that the fractures ranging from A to B and within the spread of C are formed in a polymodal pattern, where three or more sets of fault planes have formed and slipped simultaneously (Healy et al., 2015). This could explain the spread in strike orientation.

5.4.4 Classification of fractures on the image logs

Over the core interval of NLW-GT-01, 34 natural fractures, 49 open fractures and 9 drilling-induced fractures are identified and matched with the FMI. However, in the image log over the core interval, 99 additional discontinuities were recognized, which are not found on the core. All the fractures which are not observed in the core have to be drilling-induced fractures. This means that at least 68% of the fractures found in the image log over the core interval are drilling induced in NLW-GT-01.

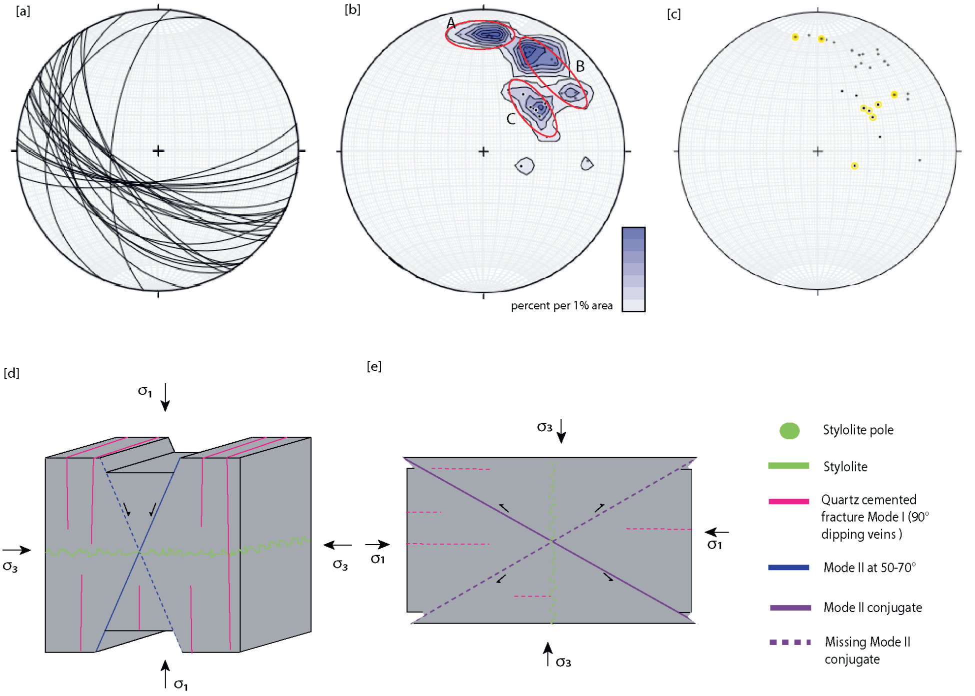

Figure 5.6: a) Stereoplot displaying plane projection of all the backtilted fractures from the core in VAL-01. b) Stereoplot with the clustering poles associated to the fractures displayed in (a). c) The poles for the fractures that showed offsets are colored in yellow. d) and e) schematic block diagram with stress regime representative for the fractures encountered in the core.

Over the core of VAL-01, 157 fractures have been identified. On the image log of VAL-01, only 30 of those discontinuities have been identified, of which 24 are matched to natural fractures and 6 to drilling-induced fractures over the core interval. The absence of the remainder of the interpreted fractures in the core in the AST is likely related to poor resolution of the image log.

Considering that 68% of the fractures over the core interval on the image log of NLW-GT-01 and 20% on VAL-01 are drilling-induced, It is expected that part of the fractures present outside the core interval are also drilling-induced.

On the image log of NLW-GT-01 and VAL-01, all the interpretable discontinuities for the Volpriehausen and Detfurth Formations have been manually picked. Over the image log in NLW-GT-01, 749 discontinuities have been identified, and 1126 bedding. On the image log of VAL-01, 58 discontinuities and 162 bedding planes have been manually picked.

Two types of drilling-induced fractures are recognized based on their appearance in the borehole image logs: petal fractures and borehole breakouts. Petal fractures show an en-echelon pattern and rather constant orientation (Fig. 5.7b). These types of fractures are not distinguishable in the AST of VAL-01. The borehole breakouts represent the failure of the borehole (Fig. 5.7a). These are an indication of less competent lithologies and serve to retrieve the horizontal present-day stress.

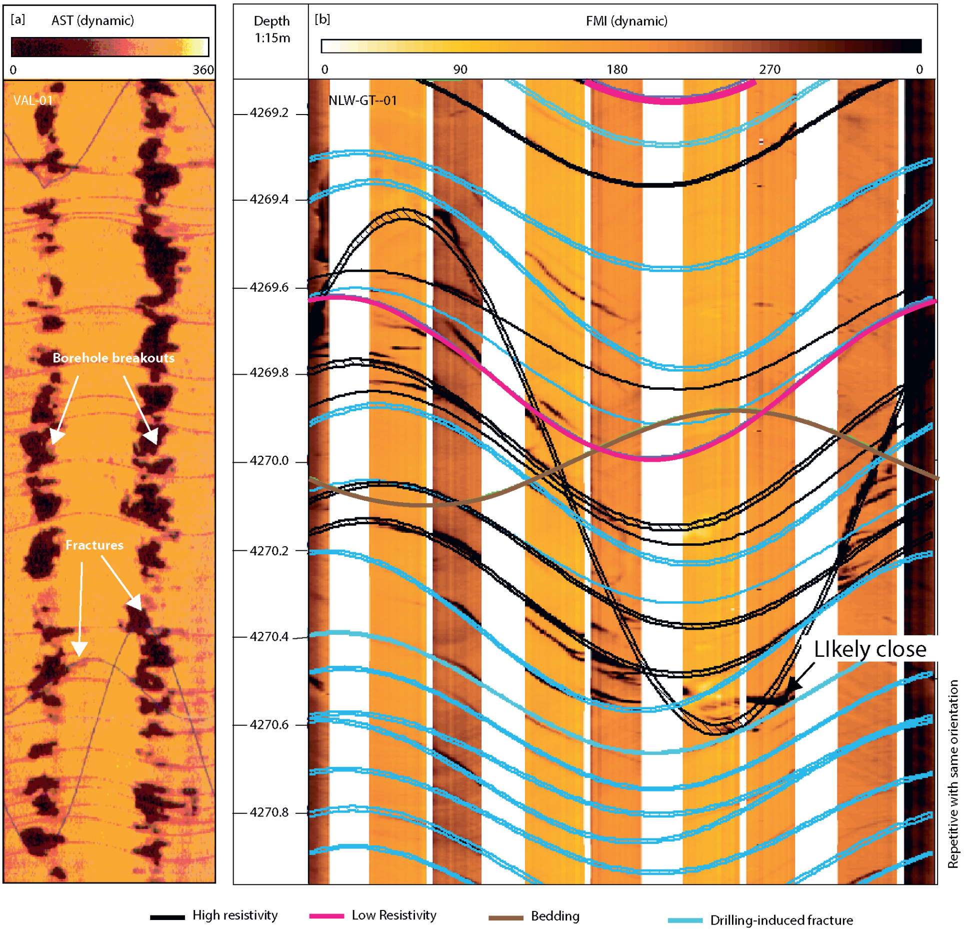

Figure 5.7: Borehole image fracture classification. a) Example of borehole breakouts and natural fractures in the AST in VAL-01. b) Attempt of fracture classification in the FMI in NLW-GT-01. Drilling-induced fractures are classified based on the filter developed to classify drilling-induced fractures in the core. An attempt has been made to differentiate joints from other potentially close natural fractures. However, the results are very uncertain.

However, a classification of fracture types in the image log cannot be established with confidence based only on their appearance and response. For example, in the FMI, the drilling-induced fractures appear as both resistive and non-resistive. Therefore, the fractures outside the core interval were classified based on the filter developed from the orientation of the drilling-induced fractures found on the core. This method serves to obtain a representative density of natural fractures outside the core interval on the image log. The objective is to find an appropriate balance between filtering out the drilling-induced fractures and preserving the natural fractures. After filtering, a total of 227 discontinuities are interpreted as natural fractures over the image log in NLW-GT-01 and 50 in VAL-01. In NLW-01-GT, the natural fractures were classified based on their resistivity response. After applying the filter, 20 low resistive fractures, and 148 highly resistive fractures were interpreted.

5.4.5 Fracture Distribution in the Triassic sandstones

In NLW-GT-01, the abundancy of gamma ray values below 100 API indicates the prevalence of sandy lithologies (Fig. 5.8). The intervals where gamma ray values are larger than 140-150 API (e.g. at ~4290 m) are formed by very fine sand to claystones. Almost all the fractures are situated in intervals dominated by frequent gamma ray fluctuations up to 100 API/m (Fig. 5.8). Based on core observations, the intervals where gamma ray fluctuations occur are formed by sandstone beds alternating with sandstones beds that are enriched in clay pebbles. The gamma ray value fluctuation is tested by the derivative of the log, resulting in a value of over 75 API/m attributed to clay layers.

In VAL-01, there are two sandy intervals between 2845 and 2870 m, and between 2888 and 2940 characterized by gamma ray values lower than 100-110 API (Fig. 5.9). Within these intervals, gamma ray fluctuations are present in correspondence with finer-grained lithologies as observed in the core (e.g. 2910 m in Fig. 5.9). The intervals between 2830 and 2850 m, and 2870 and 2888 m are instead characterized by gamma-ray fluctuations larger than 100 API/m. These fluctuations are caused by heterolithic sediments. The finer grained intervals, characterized with the highest gamma ray values (> 100 API) and largest gamma ray fluctuations (> 45 API), correspond to the intervals with the highest fracture densities (Fig. 5.9). The fracture density is instead lower in the intervals dominated by sandstones, thus gamma ray values largely below 100 API (e.g., 2850-2870 in Fig. 5.9).

A similar correlation can be observed between lithologies and density in both NLW-GT-01 and VAL-01 (Fig. 5.8 and 5.9). In NLW-GT-01, The sandstone intervals tend to have a density lower than 2.70 gr/cm^3, while the density in the claystone intervals is usually higher than 2.70 gr/cm^3. Moreover, the intervals where gamma-ray fluctuations are observed also show a sharp contrast in density (e.g. at ~ 4230 m in Fig. 5.8). Overall, the intervals where fracture density is higher than 5/m appear to have a density higher than 2.7 gr/cm^3. However, intervals where sediment density is higher than 2.7 gr/cm^3 can also bear relatively low fracture density (e.g. at ~4330 m in Fig. 5.8). In VAL-01, the sandy intervals are characterized by density values lower than 2.65 gr/cm^3, while the heterolithic intervals are characterized by values usually larger than 2.65 gr/cm^3. In this context, the intervals with density values larger than 2.65 gr/cm^3 coincide with high gamma ray intervals and high fracture densities.

A correlation between lithology and Young's Modulus is less obvious. In NLW-GT-01, the Young's Modulus along the studied interval ranges from 50 to 85 GPa, but is not visually coupled to lithological changes. A similar pattern is observed when correlating fracture density with the Young's Modulus. Generally, intervals with high fracture density (>5/m) correspond to high fluctuations (> 20 GPa/m) in Young's Modulus. However, these fluctuations are also found in intervals where fracture density is relatively low (< 2-3/m). Thus, a direct correlation between fracture density and Young's Modulus seems absent. The Young's Modulus in VAL-01 ranges from ~ 100 to 190 GPa. the Young's modulus and high fracture density do not show a direct correlation in terms of absolute values. The intervals with fracture densities higher than 5/m show a Young's modulus ranging between 100-180 GPa. At 2920 m, fluctuations larger than 30-40 GPA in Young's modulus correlate with fracture densities larger than 4/m.

However, fractures are almost absent below 2930 m although the Young's modulus curve shows fluctuations

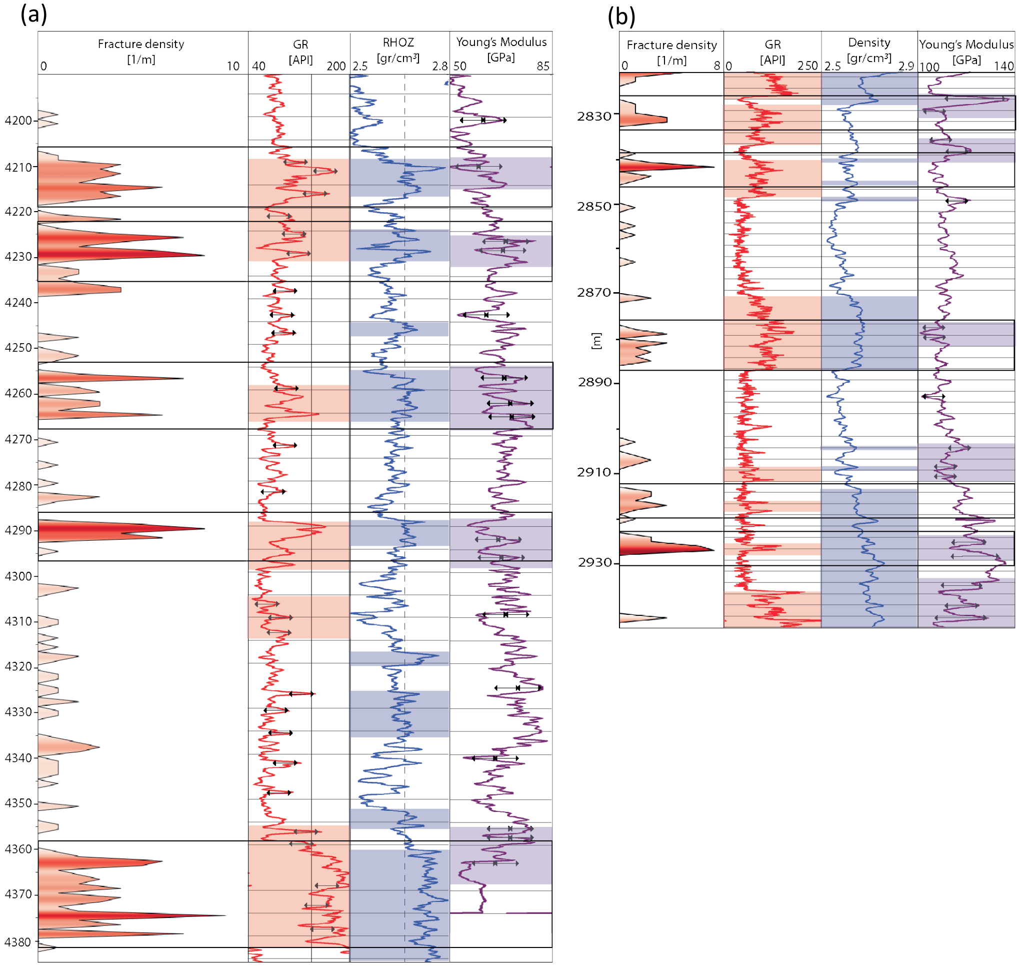

Figure 5.8: Distribution of fractures over the Main Buntsandstein Subgroup in NLW-GT-01 (a) and VAL-01 (b) compared with the gamma ray, density and Young's Modulus. The highest fracture densities are highlighted by black boxes. On the wireline log tracks, colored bands have been used to highlight the intervals where fluctuations were seen. a) NLW-GT-01: Arrows indicate fluctuations of at least 75 API/m for the gamma ray and 10 GPa/m for the Young's modulus. b) VAL-01: Arrows indicate fluctuations of at least 150 API/m for the gamma ray and 30 GPa/m for the Young's modulus.

5.5 Discussion

5.5.1 Uncertainties in fracture classification

The uncertainty in fracture classification is assessed by plotting the distribution of fracture orientations as interpreted from the core based on their characteristics and geometries; two distributions are plotted: one for the 51 natural fractures and one for the 9 petal drilling-induced fractures (Fig. 5.9). Overall, natural fractures have a wider range in orientation when compared to drilling-induced fractures. This suggests that fractures are likely to be natural when they have a dip angle lower than 77° and a strike lower than 113° and higher than 145°. These orientations are based on the application of a filter that uses the lowest probability values from the normal distribution fitted on the drilling-induced dip angles and strikes (Fig. 5.9).

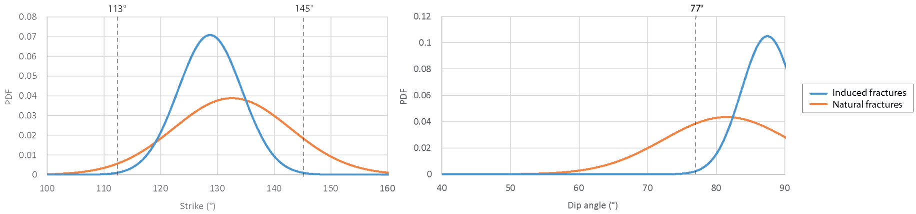

Figure 5.9: Probability density functions (PDF) for backtilted fracture orientations of the core in NLW-GT-01. See Fig. 5.4 for stereoplots.

The application of this filter affects the calculation of the fracture density distribution curves (Fig. 5.10). A total of 899 discontinuities have been manually identified outside the core interval in the FMI of well NLW-GT-01, and these are divided into high and low resistive fractures. When the filter is applied to these discontinuities, the resulting number of discontinuities reduces to 177. However, when comparing the results of manual and filter-based interpretations, the depth sections with high fracture densities remain the same (Fig. 5.10). Therefore, the application of the orientation-based filter results in an underestimation of the number of natural fractures, but the clusters of fractures remain present.

The number of natural fractures interpreted from non-cored intervals is significantly lower than the number of natural fractures interpreted by Kourta and Jocker (2018) for the same well. This discrepancy is related to the presence of drilling-induced fractures, which were possibly mistaken as natural fractures during the FMI interpretation. Boersma et al. (2021) interpreted 58 fractures from the FMI log in well NLW-GT-01. This lower number is likely related to the conservative method they chose in deciding to interpret only the fractures seen in the cores or that show a full sinusoid on the FMI log. The method adopted in this study provides a less biased alternative to the method used by Boersma et al. (2011) given that fractures are not interpreted based on their appearance on the FMI, but are interpreted based on their orientation. However, our method strongly depends on the assumption that the fracture orientations interpreted in the core are representative of all the fracture sets present in the sedimentary units. Furthermore, when natural fractures are similarly orientated to drilling-induced fractures, our method loses efficacy as it likely underestimates the numer of natural fractures (see Fig. 5.9). Further research should be conducted to develop a more efficient filter potentially subdividing natural fracture type orientations or through the help of machine learning algorithms.

5.5.2 Fracture drivers

The fracture analysis in NLW-GT-01 indicated that fractures formed during at least three tectonic regimes: a normal regime, a transition, and a reverse stress regime. The fracture patterns in VAL-01 and NLW-GT-01 show the same dominant NW-SE dip direction. The main fracture orientation coincides with the average NW-SE fault orientation, as shown by Worum et al. (2005). This could indicate that the fractures are more likely associated with larger-scale tectonic events.

The normal stress regime with a vertical maximum stress is defined based on the interpretation of bedding parallel stylolites in the core of wells NLW-GT-01 and VAL-01. The Mode I fractures oriented at 90° to the bedding support the sigma 1 stress regime normal to the bedding parallel stylolites and one side of a possible conjugate pair. Some of these fractures did not show an offset in the core. This offset could have gone undetected on the 3 cm polymer slab. The normal regime can be related to the burial of the rock succession during the extensional phase of the WNB during the Mesozoic, either in the Early, Mid, or Late Kimmerian Phase (Van Wijhe, 1987; Wong et al., 2007).

In NLW-GT-01, analysis of thin sections revealed a large presence of grain dissolution features enhanced by the presence of clay clasts (Maniar, 2019). Stylolites in clastic sediments are poorly investigated, compared to stylolites in carbonate sediments. Thus, there is a chance that not all the stylolites have been identified, and the thin clay layers observed along the core may be in fact locus for pressure dissolution. A detailed thin section analysis is needed to clarify these issues.

The Mode II fractures that formed perpendicular to the bedding do not fit an Andersonian stress orientation(Anderson, 1951). The shear fractures are formed at approximately 90° to the stylolite, which means that they are not at a compatible angle to be part of the conjugate set from the normal regime. The origin of the shearing event is not clear. The fractures could have formed as Mode I fractures during the normal regime and have sheared later when the stress orientation shifted. They could have formed due to a local stress anomaly, or they could have formed during a time when the bedding was tilted.

The reverse regime is defined by the tectonic stylolite at a 90° angle to the bedding. On the core, only one of these stylolites was found. However, the identified clay-filled veins could also be interpreted as small-scale stylolites and not veins. This hypothesis could be validated by looking at the change in permeability normal to the stylolite plane on thin sections and by the pressure-solution behavior. No Mode I or conjugate fractures have been identified fitting this regime. The conjugate set formed during the normal regime could have been reactivated during this phase. The reverse regime can be related to the inversion of the WNB during the Late Mesozoic and Cenozoic. The conjugate fractures created in the normal regime could be reactivated in the reverse regime. This reactivation also happened on a larger scale on the faults (Van Wijhe, 1987; Wong et al., 2007).

5.5.3 Controls on fracture distribution in the Buntsandstein Subgroup

By comparing the fracture densities in NLW-GT-01 and VAL-01 in the core, average fracture densities of 1.6 and 2.0, respectively, are observed. The difference in fracture density can be linked to the different lithologies in the two wells as result of different positions in the depositional system. Geluk (2005) indicates that the Main Buntsandstein sediments are more sand-prone in the southwestern region of the WNB, where the well NLW-GT-01 is located. This is a result of the proximal position to the active fluvial system. On the other hand, well VAL-01 is located towards the northwest, more distant from the active fluvial system. Overall, the Main Buntsandstein Subgroup in VAL-01 is characterized by a succession of predominantly playa-lake siltstones and claystones with subordinate sandstones. The more frequent alternation of clay and sandstone in the distal northwestern part could explain the average higher fracture density.

It is observed that fracture spacing is proportional to layer thickness, whereby the layer boundary forms a mechanical boundary due to sharp grain size contrasts (Bai and Pollard 2000; Bai et al., 2000; Olson, 2004). The distance between imposed fractures confined to a layer is subjected to tension. With increasing strain, the fractures become spaced so closely that no more fractures can form, even with increasing strain. The additional strain is accommodated by further opening of existing fractures. This minimum fracture spacing is called fracture saturation (Bai and Pollard, 2000; Bai et al., 2000). Only 4 out of the 45 fractures in VAL-01 are seen to be confined within a bed. The assessment of the fractures compared to the bedding is difficult on a 3.5 cm slab, so this could not be tested.

In wells NLW-GT-01 and VAL-01, the fracture stratigraphy and the mechanical stratigraphy seem to coincide only partially. The correlation between fracture density and sediment density and Young's modulus cannot always be explained. We have observed how intervals with densities above 2.65 g/m^3 can result in both a high or a low fracture density (Fig. 5.8 and 9). The same behavior is observed for the Young's modulus, although this is expected because Young's modulus is calculated as a direct product of the density. The lack of correlation could be potentially explained by the diagenetic alteration of the sediments during burial. With burial, formation water is subjected to an increase in temperature and pressure that can trigger physical and chemical processes that may alter the primary sediment properties, such as density and consequently the geomechanical behavior (Worden and Burley, 2003).

5.5.4 Fracture effect on permeability

5.5.4.1 Joints

Joints are expected to have the highest impact on fracture permeability, as they are likely to have the biggest aperture. However, the identification of joints from core and image logs is prone to uncertainties. Boersma et al. (2021) identified the joints based on the continuity of the sinusoidal form on the image log in combination with the resistivity response. In this work, no correlation between the different fracture types and image log response has been seen, neither in resistivity nor in sinusoidal continuity.

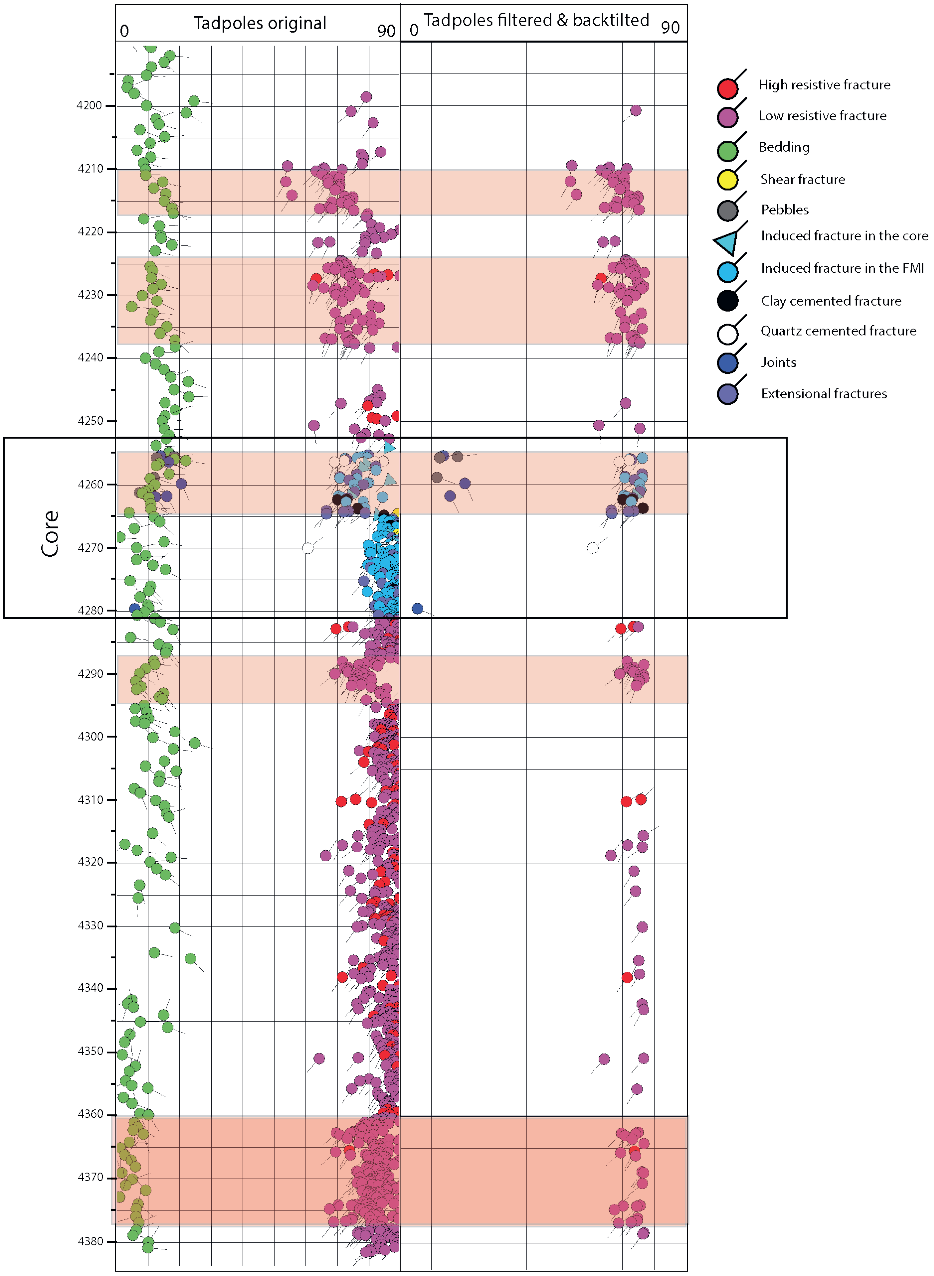

Figure 5.10 (previous page): An overview of the fracture types and density identified in well NLW-GT-01. The first column shows all the interpreted fractures. The second column shows the interpreted fracture after the application of the orientation-based filter.

The uncertainty in the classification of joints is subject to the uncertainty associated with the interpretation of the natural fractures and of the drilling-induced fractures. Based just on the appearance in the core, joints could not be distinguished from drilling-induced fractures. The correct interpretation relies on the orientation of the drilling-induced fractures. In this work, we have used a conservative approach, as the filter is based on the extreme values of a normal distribution fitted to the orientations of the high-confidence drilling-induced fractures. Therefore, the number of joints is likely to have been underestimated compared to the real number of joints that may enhance permeability in the Main Buntsandstein Subgroup.

On the other hand, the VAL-01 the NLW-GT-01 wells were both drilled close to faults. In general, fracture density is expected to decrease away from faults (Nelson, 2001). The fracture density, and consequently the density of joints in these wells, could be overestimating the number of fractures due to the position of the well close to a fault. The proximity to faults should be considered when assessing the fracture density across a basin.

5.5.4.2 Stylolites

On the cores of both NLW-GT-01 and VAL-01, several stylolites have been identified. For a stylolite to form and grow, fluid circulation is required (Bruna, 2019; Martin Baron, 2007). Thus, the presence of the stylolite is indirect proof of past permeability of the formation. Therefore, it is likely that all stylolites were once conduits of formation water flow, which were later transformed into permanent or temporary baffles to flow groundwater, hydrocarbon, or CO2 brine (Bruna, 2019).

Depending on the maturity of a stylolite, the stylolite can remain a conduit of flow. When the stylolite has reached its maximum roughening stage, the available pore space in the matrix is likely to be filled by the product of dissolution, and stylolites become inactive. The observation of the stylolites under the microscope could help define the maturity of the stylolites.

5.6 Conclusion

This study re-evaluates the fracture data of wells NLW-GT-01 and VAL-01. Core data, wireline, and borehole images are analyzed to characterize fracture types and distribution in two wells located in different sectors of West Netherlands Basin, and to investigate the geological parameters influencing the development of natural fractures in the Main Buntsandstein Subgroup.

The analysis of core samples revealed the presence of five types of discontinuities: i) veins, quartz or clay-filled fractures, forming sub-perpendicular to the bedding; ii) joints, open fractures that have not a characteristic appearance nor orientation to the bedding; iii) shear fractures, displacing the bedding either with a normal or reverse offset; iv) stylolites, that evolve around insoluble grains and usually from parallel to the bedding; v) drilling-induced fractures, that have a rather consistent orientation and are not natural. These discontinuities have a dominant NW-SE strike orientation.

The drilling-induced fractures and the borehole breakouts indicate an in-situ NE-SW oriented minimum stress and a NW-SE maximum stress. The joints, veins, and the tectonic stylolite are oriented perpendicular to the minimum stress direction, thus, are likely to be open at present.

The genesis of fractures is interpreted to be largely driven by large-scale tectonic events. The veins, joints, conjugate fractures, and stylolites are interpreted to have formed in a normal stress regime, which coincides with the extensional tectonics that dominated the West Netherlands Basin during the Mesozoic. The inversion of the basin in the Late Mesozoic was likely responsible for the formation of tectonic stylolites and a potential inversion of the previously formed conjugate fracture sets.

The natural fractures appear to be concentrated more in heterolithic intervals, where sandstones alternate with silt- and claystones. Overall, VAL-01 has a higher average fracture density compared to NLW-GT-01. This can be explained by the different locations of the wells in the basin. VAL-01 is located in a more distal environment, where finer sediments were mostly deposited, occasionally alternating with coarser sandstones. In contrast, well NLW-GT-01 is located in a more proximal area with respect to the fluvial depositional system, where mostly sandstones were deposited. These variations in lithology control the fracture stratigraphy. The absence of a direct correlation between fracture and mechanical stratigraphy may be related to diagenesis, thus altering the primary properties of sediment.

Chapter 6: Geothermal potential of the Main Buntsandstein Subgroup in the Roer Valley Graben

6.1 Introduction

Sandstones from the Main Buntsandstein Subgroup represent a promising geothermal play in the subsurface of the Netherlands (Mijnlieff, 2020). However, their geothermal potential in the southern part of the Netherlands specifically in the Roer Valley Graben, remain uncertain. This uncertainty is a consequence of poorly understood geological processes that affect the quality of the sandstone reservoir, such as variability in porosity and permeability, which are critical for efficient heat extraction. Understanding these processes and how they affect the quality of the sandstone reservoirs is essential for assessing the viability of geothermal energy production in this region.

In the geothermal industry, quantifying the potential of sedimentary reservoirs is a standard approach for evaluating resources. Two key parameters commonly used are the heat initially in place (HIIP) and geothermal power (GP). HIIP provides an estimate of the total recoverable heat from the reservoir, while GP estimates how much energy can be continuously extracted from the system, often tied to a specified flow rate. Together, these parameters offer a first-order estimate of the resource's capacity for energy production, which serve to guiding development strategies and investment decisions.

The estimation of the heat initially in place was first introduced by researchers at the United States Geological Survey (USGS), who employed average values of temperature and thickness from different geothermal reservoirs in combination with a probability distribution function to estimate the volumetric generation capacity of geothermal resources (Brook et al., 1979). However, in a more recent study, Gar and Combs (2010) revised the USGS volumetric heat initially in place calculation, eliminating ambiguities associated with temperatures and reservoir efficiency, thus providing a more precise estimation of HIIP.

The geothermal potential of the Main Buntsandstein play in the Roer Valley Graben, southern Netherlands, is assessed. This is done by analytically calculating the heat initially in place (HIIP) and geothermal power (GP) for the Main Buntsandstein sedimentary units at well scale. These calculations were possible by integrating the results obtained within the previous chapters of this thesis, such as the total thickness of the sandstone units, while data for temperature, porosity and permeability of the units were calculated from available logs or taken from legacy data. No dynamic simulations are performed. The results of this chapter serve to quantify some of the outcomes of this thesis in a way that may be helpful for the geothermal industry. Once the HIIP and GP are addressed, three case studies are presented where the geological uncertainties are assessed and discussed. These three case studies have been chosen as representative for the main types of Main Buntsandstein plays in the study area.

6.2 Data and Methods

The geothermal potential (GP) of the Main Buntsandstein Subgroup is assessed for 23 wells in the Roer Valley Graben, southeastern Netherlands (Table 6.2). The well selection is based on data availability. A total 23 wells out of the 33 wells that penetrate the Main Buntsandstein Subgroup in the Roer Valley Graben are equipped with the required logs, which are density, neutron or sonic logs, to compute porosity and permeability.

The heat initially in place is estimated by using the following equation according to Garg and Combs (2015):

$$HIP = A\Delta x(T_r - T_i)(\rho_f C_f \phi + \rho_r C_r (1 - \phi)) \quad (1)$$

where ρ_r rock density (kg/m^3), C_r rock heat capacity (J/(kgK)), ρ_f fluid density (kg/m^3), C_f fluid heat capacity (J/(kgK)), and T_r and T_i are the reservoir initial and injection temperature (K), respectively, A is the cross-sectional area (m^2) of the reservoir volume with h thickness and w width.

The geothermal power is calculated following the equation proposed by Zaal et al., 2021:

$$\Delta H_{fe} = \rho_f C_f (T_r - T_i) Q \Delta t \quad (2)$$

where ρ_f fluid density (kg/m^3), C_f fluid heat capacity (J/(kgK)) and T_r and T_i are the reservoir initial and injection temperature (K), respectively, Q volume flow rate (m^3/s) and Δt the time period. Dynamic modeling has not been performed. Moreover, the aim of this study is not to assess the power production over time (Watthours), thus, we have removed the Δt from equation 2 to calculate the power in Watts.

The volume flow rate is calculated using Darcy's law for radial flow:

$$\mathrm{Q_r} = \frac{2\pi k(\Delta P)}{\ln\left(\frac{r1}{r2}\right)} * \frac{1}{\mu} * H \quad (3)$$

Where k is the permeability (m^2), ΔP the pressure difference (MPa) between the pressure at the inner radius (r1) and the pressure at the outer radius (r2), μ the viscosity (Pa*s) and H is the reservoir thickness (m^2). The inner radius (r1) is the wellbore radius and the outer radius is the outer radius is the distance from the wellbore to the edge of the reservoir, which in this case is assumed to be 500 m, half of the reservoir width, which is assumed to be 1000 m in alignment with channel belt width reconstruction (see Chapter 2 of this thesis).

These equations are solved analytically for each well. The reservoir zone width and length are assumed to be 1000 m. The heat capacity and density for the sediments and the fluid, the injection temperature, and hydrostatic gradient have been taken from literature studies tailored to our case study for sandstone reservoirs at depths below 1500 m (Table 6.1). Furthermore, a maximum pressure of 1.3 the undisturbed pressure at the top of the reservoir is used for the calculations. This is based current regulations by Staatstoezicht op de Mijnen in the Netherlands (SodM, 2019). The other parameters are calculated from the available well data. An overview of the main parameters used in the analytical calculations is given below.

6.2.1 Reservoir dimensions

The reservoir zone is intended as the volume of sediments from which geothermal heat can be produced. For simplicity, we have assumed an average width and length of 1000 m, which is in line with the river channel belt dimension of ~1-1.5 km estimated for the Main Buntsandstein Subgroup sedimentary system (see Chapter 2 of this thesis). The thickness of the reservoir zone is estimated based on a cut-off on the effective porosity. In this work, only the sediments that have an effective porosity higher than 8 % are considered to contribute to heat production as it is assumed that no water will be produced from sediments with lower porosity.

Table 6.1: Set of standard parameters used for the calculation of HIIP and GP.

Parameter	Unit (SI)	Value
Reservoir width/length	m	1000
Rock density	kg/m^3	2690
Rock heat	J/(kgK)	1000
Fluid density	kg/m^3	997
Injection Temperature	K	35
Fluid heat cap	J/(kgK)	4181
Hydrostatic gradient	Mpa/m	0.0105
Viscosity	Pa*s	0.00028
Wellbore radius	m	0.0762
Injection Temperature	°C	35

6.2.2 Temperature

The initial temperature of the reservoir zone was defined by employing the geothermal gradient determined in the work of IF Technology (2012). In their work, they use corrected borehole temperature data (BHT) from 22 wells, determining a geothermal gradient of:

$$T = 4.8859 + 0.0369 * Z \qquad (4)$$

Where Z represents the depth in m. This gradient is valid within a depth range of 1153 to 3241 m TVD and suggests that temperatures in the subsurface of the Roer Valley Graben are higher than the average Dutch subsurface temperatures in accordance with previous studies (Luijendijk et al., 2010). Well STH-01 does not fit this temperature gradient. The corrected bottomhole measurements in STH-01 are lower than those of other wells in the same depth range (IF Technology, 2012). However, for the purpose of this regional study, we used the same gradient everywhere, keeping the STH-01 deviation in mind when discussing uncertainties. The temperatures are then arithmetically averaged for the sediments composing the reservoir zone.

6.2.3 Petrophysics

6.2.3.1 Porosity

Total porosity (ϕ_{total}) is calculated from density through the following formula:

$$\phi_{total} = \frac{\rho_{ma} - \rho_{log}}{\rho_{ma} - \rho_{mf}}$$

Then the total porosity was corrected for clay content to calculate the effective porosity ($\phi_{effective}$):

$$\phi_{effective} = \phi_{total} - V_{clay} * \frac{\rho_{ma}-\rho_{cl}}{\rho_{ma}-\rho_{mf}} \qquad (5)$$

Where the parameters represent: (ρ_{ma}) matrix density (2.69 g/cm^3),(ρ_{mf}) mud filtrate density (1.05 g/cm^3),(ρ_{cl}) clay density (2.73 g/cm^3), (ρ_{log}) bulk density log (g/cm^3) and (V_{cl}) volume of clay. The density of matrix and clay was taken from core measurements by averaging all the available grain density measurements for sand and clay-size sediments. The volume of clay was estimated from gamma ray according to:

$$V_{clay} = \frac{GR_{log} - GR_{min}}{GR_{max} - GR_{min}} \tag{6}$$

Where GR_{log} represents the gamma ray values from wireline logs, and GR_{min} and GR_{max} the minimum and maximum gamma ray values for the Main Buntsandstein in the Roer Valley Graben. For the wells that are not equipped with density log, the effective porosity is calculated using neutron and sonic logs (courtesy of Aardyn). The porosity was then arithmetically averaged in each well.

6.2.3.2 Permeability

Permeability was computed from porosity using a porosity-permeability relationship constructed using plug measurements at ambient conditions. When plotting the porosity and permeability core measurements for only the Main Buntsandstein sediments with effective porosity higher than 8% in the Roer Valley Graben, a positive linear correlation (R^2=0.66) can be observed performing an ordinary least squares (OLS) regression (Fig. 6.1). Thus, permeability was estimated using the equation derived from the regression.

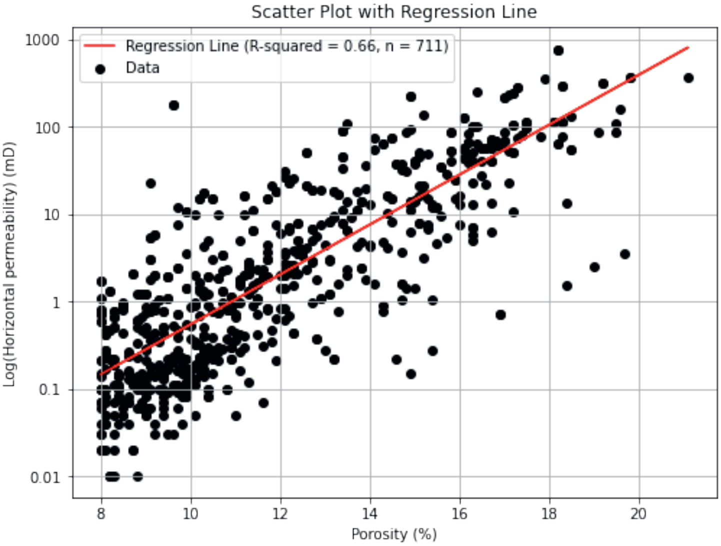

Figure 6.1: Permeability porosity cross-plot for Main Buntsandstein sediments with effective porosity higher than 8% in the Roer Valley Graben area. Data from www.nlog.nl.

The resulting porosity-permeability relationship is the following:

$$K = 10^{(0.28 * \emptyset_{effective} - 3.13)}$$

Once permeability logs were calculated for each well, permeability was then converted into stressed brine-permeability following Juhasz (1986). This was done in order to have a better representation of the permeability in reservoir systems in the subsurface and to avoid the usually optimistic values derived from core routing analysis. The formula used for the conversion is the following:

If $K_{air} > 660mD$ then $$K_{brine} = K_{air}\left(\frac{\phi_{effective}}{\phi_{total}}\right)^3$$

If $160\ mD < K_{air} < 660mD$ then $$K_{brine} = 0.28K_{air}^{1.194}\left(\frac{\phi_{effective}}{\phi_{total}}\right)^{3.045}$$

If $K_{air} < 160mD$ then $$K_{brine} = AK_{air}^{B}\left(\frac{\phi_{effective}}{\phi_{total}}\right)^{C}$$

Where A = 4.14 $\sigma^{-0.39}$, B = 0.8 $\sigma^{0.058}$ and C = 4.14 $\sigma^{0.058}$. To calculate A, B and C, the net confining stress in psi is calculated following Nelson (1981).

Once stressed brine permeability was calculated, the permeability dataset was cleaned applying the Z-score method to identify and remove outliers. The Z-score method is a statistical technique that measures how many standard deviations a data point is from the mean of the dataset, helping to identify extreme values for removal. In this work data points exceeding of at least three times the standard deviation were excluded. This ensures the dataset is more representative of typical values by filtering out data points that are significantly different from the mean. Additionally, the permeability values were capped at 1000 mD to maintain a realistic range for the dataset, given the observed range of core permeability values. At this point, the arithmetic average of the permeability was computed for the reservoir zone. From now on, the computed stressed brine permeability will be referred to as permeability.

6.3 Heat initially in place and geothermal power for the Main Buntsandstein sediments in the Roer Valley Graben

The heat intially in Place (HIIP) averages at 18 PJ for the Main Buntsandstein Subgroup sediments in the wells analyzed in the Roer Valley Graben. The largest value of HIIP (39 PJ) is found in well BKZ-01 that is located close to the southern margin of the Roer Valley Graben where the top of the Main Buntsandstein is encountered at a depth of 2400 m TVD (Fig. 6.2a). The lowest value of HIIP (2.6 PJ) occurs in well KWK-01 that is located close to the basin axis at depths of approximately 2500 m.

The geothermal power (GP) has an average of 2.5 MW, with the highest value found in well STH-01 (13.9 MW) located in the southern platform and the lowest value in SPG-01-S2 (0.01 MW) located close to the Roer Valley Graben axis (Fig. 6.2b). The GP calculation accounts for the flow rate thus it is related to the permeability of the sediments. On the other hand, the HIIP only accounts for porosity. Furthermore, the equations are differently sensitive to the rest of the parameters. This is manifested in some of the wells that show among the highest values of HIIP (e.g. WWK-01) and the lowest values of GP (Table 6.2).

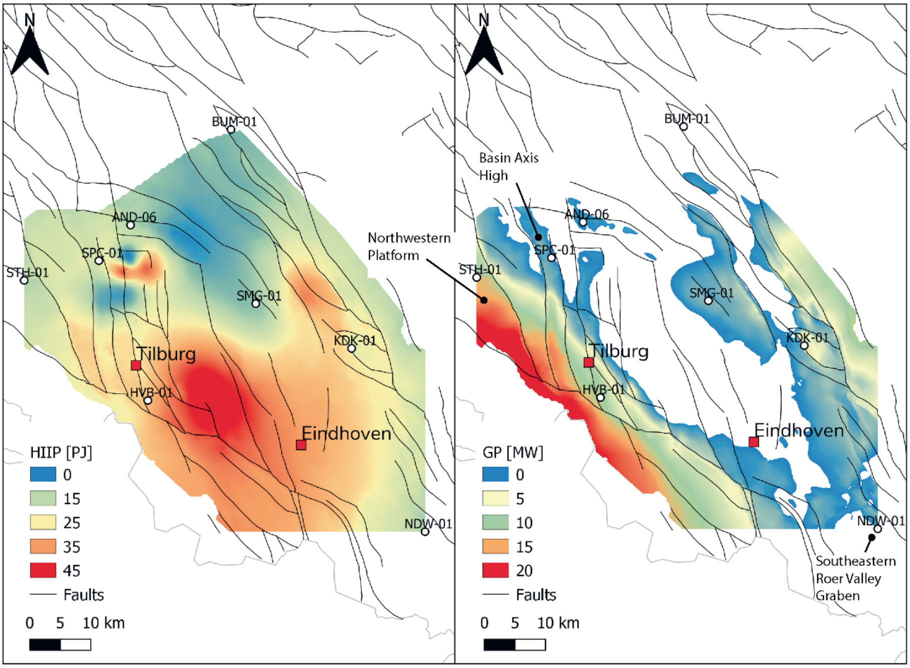

Figure 6.2: Heat initially in place (a) and geothermal power (b) for the Main Buntsandstein in the Roer Valley Graben area. The areas left blank either fall outside the study area or the interpolation method yields values that are unrealistically low or even below 0 (e.g. central part of the basin). This is related to the absence of well data in these areas.

A sensitivity analysis has been conducted to better understand the impact of various input parameters on the heat initially in place and geothermal potential. The data presented in Table 6.2 has been standardized using z-scores to normalize the different scales. Normalizing the different scales allows meaningful comparisons between the different variables. Next, a correlation matrix has been employed to quantify the linear relationships between the variables.

The HIIP is positively correlated with thickness for the given dataset, displaying a Pearson coefficient of 0.86. The highest values of HIIP (higher than 3 PJ) are found in wells that have a thickness above 130 m, combined with an average temperature above 93 °C (e.g. HVB-01 and BKZ-01). However, some of these wells (e.g. WWK-01) are located in the central part of the Roer Valley Graben, where the Buntsandstein is buried below 2.5-3 km and exhibits low average permeability (e.g., 1.8 mD in WWK-01). In fact, these wells exhibit relatively low values of GP (e.g. 62 MW for WWN-02-S4).
The GP is strongly positively correlated with flow rate, thus permeability. The highest GP values are found in the wells where permeability values are larger than 130 mD. These wells are mostly located along the southern margin of the Roer Valley Graben. A strong correlation exists with porosity as well, although porosity is not taken into account in the calculation of the GP. This is a consequence of the positive correlation that exists between permeability and porosity (Fig. 6.1a).

Table 6.2: Parameters and results of the heat initially in place (HIIP) and geothermal power (GP). HIIP and GP highest values are displayed by darker red colors.

Well	Top_res_depth (m)	Thickness (m)	Temperature (°C)	Porosity	Permeability (m2)	Radial_Flow_Rate	HIIP (PJ)	GP (MW)
AND-06	2434	36.8	97.0	0.11	6.2E-15	0.04	6.5	0.08
BKZ-01	2407	214.9	97.7	0.13	3.5E-14	1.15	38.8	3.93
BRAK-01	2431	78.0	93.5	0.1	1.0E-15	0.01	13.0	0.04
BUM-01	1367	111.7	58.5	0.12	1.5E-14	0.15	7.5	0.30
HBV-01	2010	172.1	81.5	0.19	2.1E-13	4.72	23.8	13.42
HSW-01-S1	2577	125.6	102.7	0.13	4.6E-14	0.97	24.5	3.47
HVB-01	2299	176.7	93.3	0.14	1.3E-13	3.42	29.8	11.14
KDK-01	1982	167.8	80.8	0.15	8.6E-14	1.85	22.4	5.21
KWK-01	2416	14.8	95.9	0.12	5.0E-15	0.01	2.6	0.04
NDW-01	2030	96.0	82.7	0.13	2.6E-15	0.03	13.2	0.10
SMG-01	3067	45.8	120.7	0.14	5.9E-14	0.54	11.4	2.27
SPC-01	2391	117.0	95.7	0.13	1.4E-14	0.26	20.5	0.87
SPG-01-S2	2991	27.7	116.7	0.1	2.9E-16	0.00	6.4	0.01
STH-01	1708	129.0	70.0	0.23	4.0E-13	5.67	13.7	13.85
VRK-01	1751	96.2	67.5	0.12	6.6E-15	0.07	9.0	0.17
WAA-01	2751	36.8	107.4	0.1	1.7E-15	0.01	7.6	0.04
WAA-01-S1	2751	99.2	109.2	0.1	7.1E-15	0.12	20.9	0.48
WWK-01	2921	156.0	115.2	0.11	1.9E-15	0.05	35.7	0.22
WWN-01-S2	2798	90.2	110.0	0.1033	1.6E-15	0.03	19.2	0.10
WWN-03	2885	43.3	112.7	0.1	9.2E-16	0.01	9.6	0.03
WWS-01-S1	2842	84.3	112.2	0.1	3.1E-16	0.00	18.5	0.02
WWS-02	2746	129.7	108.3	0.11	2.5E-14	0.57	27.1	2.17
WWN-02-S4	2997	131.9	118.0	0.11	1.6E-15	0.04	31.2	0.17

6.4 Case studies

Based on the HIIP and GP calculations, and more in general, the results of this thesis, three case studies have been further evaluated. Each case study is representative of a certain type of geothermal play in the Roer Valley Graben. For each case, the HIIP and GP values and associated uncertainties are assessed based on the geological knowledge of the area developed within this thesis. The case studies are the following: i) Northwestern Platform (Fig. 6.2), where well STH-01 displays the highest permeability values observed for the Main Buntsandstein across the Roer Valley Graben; ii) Basin Axis High (e.g., SPC-01 well in Fig. 6.2), where the shallower burial during the Jurassic has led to the preservation of primary reservoir properties (Chapter 4 of this thesis); iii) Southeastern Roer Valley Graben (Fig. 6.2) where the presence of aeolian sediments in combination with dissolution processes have resulted in high optical porosities as displayed in NDW-01 well (Chapter 3 and 4 of this thesis). The Northwestern Platform case was selected based on the quality of the play, as indicated by the available data. The other two cases were identified as promising, based on the geological knowledge developed throughout this thesis.

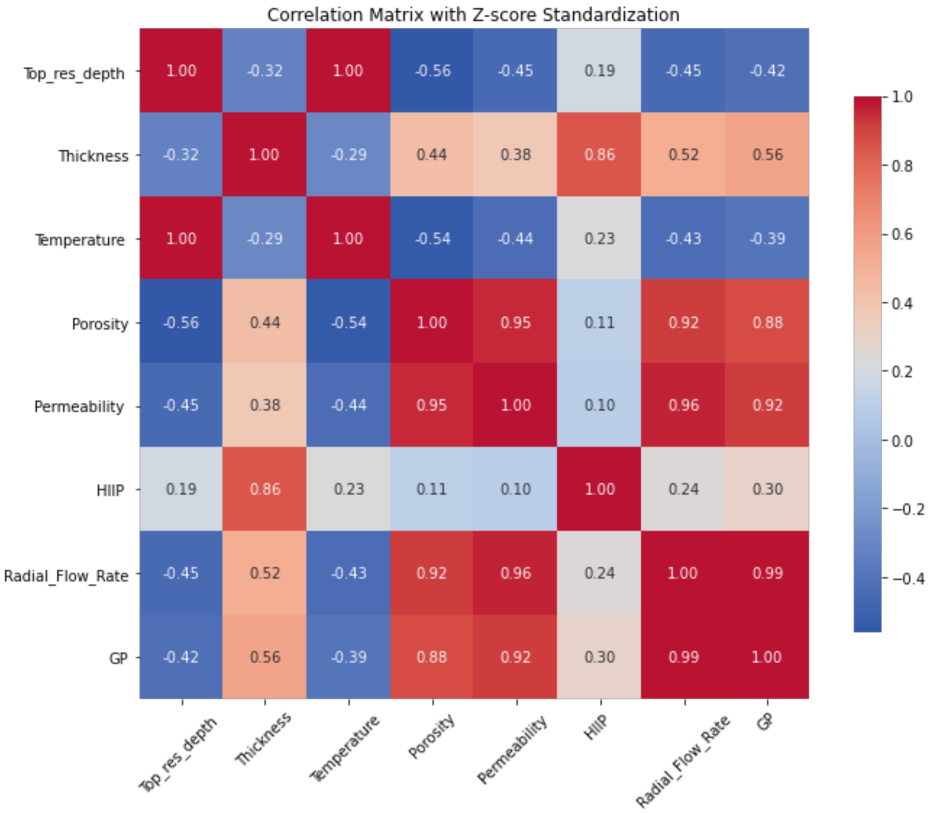
Correlation Matrix with Z-score Standardization

	Top_res_depth	Thickness	Temperature	Porosity	Permeability	HIIP	Radial_Flow_Rate	GP
Top_res_depth	1.00	-0.32	1.00	-0.56	-0.45	0.19	-0.45	-0.42
Thickness	-0.32	1.00	-0.29	0.44	0.38	0.86	0.52	0.56
Temperature	1.00	-0.29	1.00	-0.54	-0.44	0.23	-0.43	-0.39
Porosity	-0.56	0.44	-0.54	1.00	0.95	0.11	0.92	0.88
Permeability	-0.45	0.38	-0.44	0.95	1.00	0.10	0.96	0.92
HIIP	0.19	0.86	0.23	0.11	0.10	1.00	0.24	0.30
Radial_Flow_Rate	-0.45	0.52	-0.43	0.92	0.96	0.24	1.00	0.99
GP	-0.42	0.56	-0.39	0.88	0.92	0.30	0.99	1.00

Figure 6.3: Correlation matrix for the heat initially in place (HIIP) and geothermal potential (GP) calculations. The matrix displays the Pearson correlation coefficients between the variables that have been standardized prior to the regression analysis. Note the strong positive correlation between HIIP and thickness, and GP and permeability.

6.3.1 Northwestern Platform

This area is located in the northwest part of the Roer Valley Graben, in a platform area where the top of the Buntsandstein is located at relatively shallow depths (~1700 m) and locally subcrops below the base Chalk Group unconformity. The well is located on the edge of the Buntsandstein fluvial system, in an area characterized by lower subsidence compared to the surrounding blocks (see Chapters 2 and 3 of this thesis).

The Main Buntsandstein Subgroup has a total thickness of ~180 m in well STH-01, which is located within this platform structure (Fig. 6.3). This thickness seems to be rather constant in the block where the well is drilled and increases to over 200 m in the adjacent blocks (see Fig. 6.10 in Chapter 2). In well STH-01, the net thickness of sedimentary units with an effective porosity greater than 8% is around 130 m. This relatively low thickness, compared to other wells in the Roer Valley Graben, contributes to the resulting low HIIP of approximately 13 PJ in STH-01. The net thickness in the block is uncertain, though a significant variation in the net thickness is not expected given the similar lithologies indicated by the uniformity in reflector configuration across the block (Chapter 2). The net thickness is expected to increase in the blocks directly adjacent to the STH-01 block; the block where the STH-01 is drilled was a structural high during the Early Triassic, thus the thickness of the sandstones may be larger in the adjacent blocks where fluvial sedimentation was likely more dominant (see Chapter 3 of this thesis). Furthermore, the block to the north of STH-01 likely experienced higher subsidence rates from the Jurassic onward, while the block to the south likely underwent a similar diagenetic history to STH-01. Consequently, the porosity in the southern block adjacent to STH-01 is expected to be comparable to that of the STH-01 block.

The Geothermal Potential in STH-01 well is the highest across the Roer Valley Graben. This is likely driven by the high values of permeability that reach values of 992 mD when considering only sediments with higher porosity than 8%. The favourable permeability values are attributed to the reduced diagenesis that the Main Buntsandstein sediments experienced in well STH-01 compared to other wells in the Roer Valley Graben (e.g., KWK-01, see Chapter 4 of this thesis). Given the similarities in sediment composition and sedimentary facies to other adjacent wells, the less intense diagenesis experienced by the sediments in STH-01 is likely a different burial history. The minor burial phases experienced during the Triassic and Jurassic periods resulted in lower compaction and cementation rates, which may have helped the preservation of primary reservoir properties overall.

An alternative explanation for the enhanced porosity and permeability could be the dissolution of existing cement, creating secondary porosity. In the block adjacent to STH-01, the Main Buntsandstein sediments subcrop the base of the Chalk Group. As discussed in Chapter 2, the presence of the base Chalk Group unconformity suggests that these sediments were exposed to surface conditions before the deposition of the Chalk Group in the Late Jurassic to Early Cretaceous. This exposure may have allowed acidic meteoric water to infiltrate, leading to cement dissolution and improved reservoir properties. Unfortunately, the lack of thin section data from the Buntsandstein in STH-01 prevents further investigation of this hypothesis.

Well STH-01 does not record the presence of hydrocarbons in the Main Buntsandstein Subgroup in the STH-01 block. Thus, the pressure in the reservoir is likely to be hydrostatic. Although the temperature in STH-01 well employed in this work may overestimate the real temperature field in the area, the adequate thickness, porosity and permeability in STH-01 and the likelihood of encountering favourable conditions in the blocks adjacent to the south where the Triassic sediments subcrop at the base Chalk Group unconformity, make this platform area attractive for geothermal energy production.

6.3.2 Basin Axis High

This case study is located close to the basin axis, in a block where the well SPC-01 encounters the top of the Main Buntsandstein at ~2390 m TVD. This block is located within the Buntsandstein fluvial system where the Main Buntsandstein Subgroup has a total thickness of 130 m. When accounting for sediments with a porosity higher than 8%, the thickness reduces to 117 m. No seismic data across the block where SPC-01 well is drilled have been interpreted, so the thickness variation across the block could not be assessed. However, the Buntsandstein thickens in the wells located to the north (i.e., WWN-01-S2), so we expect the thickness of the layers to remain constant or likely increase to the north.

The Main Buntsandstein Subgroup in SPC-01 exhibits an HIIP and GP of ~20.5 PJ and 0.8 MW, respectively. The lower value of GP compared to the sediments in STH-01 is to be attributed to the overall lower average permeability in SPC-01. Permeability ranges between 0.0044 and 887 mD, with the upper boundary determined using a cut-off of 1000 mD. Without this cut-off, the permeability log shows values as high as 2 Darcy. However, core data from the Detfurth Formation indicate air permeabilities reaching only 350 mD. Unfortunately, the data points showing permeability up to 2 Darcy are not from cored sections, preventing verification of these values. Therefore, we opted for a conservative approach by applying the 1000 mD cut-off.

However, we do not rule out the possibility of encountering values up to 1 D in well SPC-01. The analysis of new thin sections has revealed that sediments are much less compacted and cemented compared to the wells nearby (e.g., KWK-01). The better reservoir properties in SPC-01 compared to adjacent wells where the Main Buntsandstein Subgroup sediments are encountered at similar depths and with similar sedimentary facies, are related to the different burial histories the sediments in SPC-01 wells experienced. The petrographic analysis conducted in Chapter 4 of this thesis suggests that permeability may be higher than reported by available plug measurements. For this reason, we believe that blocks that experience a comparable burial history as the SPC-01 block may be favourable for geothermal operations given the appropriate reservoir thickness and favourable porosity and permeability. However, the well SPC-01 reported gas in the Main Buntsandstein. Hydrocarbonshows occur in other blocks near to SPC-01 (e.g. WWN-01-S2). It is important to understand the implications hydrocarbons can have on reservoirs related to brine composition and reservoir pressure before geothermal activities should commence.

6.3.3 Southeastern Roer Valley Graben

The well NDW-01 is located on the southeast part of the Roer Valley Graben, where the top of the Main Buntsandstein is found at 2030 m TVD. This well is located in an area where sediments were deposited by both fluvial and aeolian processes. This produced better sorted and more rounded sedimentary grains than elsewhere in the Roer Valley Graben. This is the only well with appropriate logs and core data in the southeastern part of the Dutch Roer Valley Graben. Furthermore, the presence of aeolian facies and very well-sorted sediments in NDW-01 does not make the sediments here comparable to any other wells in the Roer Valley Graben where core data are available. In terms of sedimentary facies, this well is similar to the wells located on the Belgian side of the Roer Valley Graben (e.g., KB201). However, the Buntsandstein in those wells is located below 800 m, which is much shallower than the depth in NDW-01.

The Main Buntsandstein Subgroup in NDW-01 has a gross thickness of ~220 m in NDW-01. This thickness seems to increase when moving away from the well, reaching locally even 250 m (see Chapter 2 of this thesis). Nonetheless, the net thickness of the Main Buntsandstein in NDW-01 is only ~ 96 m. This is related to the overall poor porosity of the sediments, especially in the Hardegsen and Volpriehausen Formations. The Detfurth Formation has overall better porosity, reaching up to 20%, as confirmed by core data.

The Main Buntsandstein Subgroup sediments display an average permeability of 2.6 mD when considering only sediments with higher porosity than 8%. The permeability ranges from 0.003 mD to 49 mD. The presence of data points with low permeability (<0.1 mD) but relatively high porosities (> 8%) are related to the presence of secondary pores enhanced by dissolution that are not necessarily connected to each other and thus do not contribute to increasing the overall permeability of the pore network.

The petrographic analysis has revealed the presence of sediments that are barely cemented and show a dense network of pores that appear to be well connected to each other. These characteristics are found in the well-sorted aeolian sandstones. Unfortunately, aeolian sediments are poorly sampled compared to the cemented, low permeable fluvial sandstones. This results into the relatively low value of GP for NDW-01 (Table 6.2). Furthermore, the porosity log in this well is calculated based on neutron log data given the absence of density log. This makes the porosity and consequently the permeability values more uncertain considering that the absence of reliable plug measurements does not allow an adequate benchmark of the results. In this context, we believe that further sampling and measurements of the “good” reservoir intervals in NDW-01 may provide further insights especially into the properties of the aeolian sandstones.

6.5 Discussion and Conclusions

The assessment of geothermal potential for the Main Buntsandstein Subgroup in the Roer Valley Graben reveals significant variability in both heat initially in place (HIIP) and geothermal power (GP). This variation is largely influenced by geological parameters such as reservoir net thickness, porosity, permeability, and temperature of the sedimentary units. These findings provide a detailed look at the Main Buntsandstein's geothermal viability, offering new insights into the area's geothermal resource distribution.

The highest HIIP values are concentrated in areas with net reservoir thicknesses exceeding 130 m and temperatures above 90°C, primarily near the southern margin of the graben. In wells such as BKZ-01, the favourable thickness leads to substantial HIIP values, consistent with earlier geothermal assessments for the region, such as IF Technology (2012) and data from ThermoGIS (www.ThermoGIS.nl). However, these studies combine multiple Triassic reservoir layers, whereas this analysis focuses exclusively on the Main Buntsandstein, yielding a more targeted understanding of the formation’s potential. Interestingly, although the HIIP is a key indicator of stored thermal energy, it does not align with GP, which depends more critically on permeability.

Permeability emerges as the most significant factor for geothermal power generation. The wells in the northwestern platform (e.g., STH-01) exhibit high GP values (up to 13.8 MW), which correlates with permeability values as high as 992 mD. This capacity would be suitable for large scale district heating and greenhouse applications (Khodayar and Bjornsson, 2024). This suggests that areas with lower subsidence, such as the northwestern platform, are suitable for geothermal exploitation, as the primary reservoir properties are well preserved. In contrast, wells located near the basin axis, such as SPC-01, show lower GP values despite moderate HIIP. This discrepancy can be attributed to the poor permeability caused by deeper burial, thus greater compaction, and cementation. These findings reflect broader geothermal research, where deeper reservoirs often suffer from reduced porosity and permeability due to diagenetic alterations (e.g., Dillinger et al., 2016). Therefore, while deeper formations may store significant thermal energy, their reduced permeability significantly hampers the ability to extract that energy efficiently.

The case study of the southeastern RVG, particularly well NDW-01, presents a stand-alone scenario where localized geological factors, such as aeolian facies and secondary porosity creation from dissolution processes, may have enhanced reservoir potential despite overall poor porosity and permeability elsewhere in the region. This suggests that even in areas traditionally considered less favourable for geothermal extraction, localized sedimentological processes can create high-quality reservoirs. This underlines the importance of detailed geological assessments when evaluating geothermal viability across heterogeneous formations.

An additional factor that could enhance geothermal potential in parts of the RVG is the presence of natural fracture networks within the Main Buntsandstein Subgroup. In regions such as the central and northern parts of the graben, where heterolithic sediments are prevalent, fracture permeability may play a key role in augmenting overall reservoir performance. Open fractures can significantly increase the effective permeability, allowing for greater fluid flow and heat extraction. Studies such as Boersma et al., (2021) emphasize the importance of integrating fracture network analysis into geothermal models, as fractures could help overcome the limitations posed by matrix permeability alone. This study does not directly account for fracture permeability as the plug measurements used mostly report matrix permeability only. Further exploration and characterization of natural fractures are necessary to fully understand their contribution to the geothermal system, particularly in areas where matrix permeability is low but natural fractures may be occurring.

Despite the valuable insights provided by this study, several uncertainties persist, particularly regarding the accuracy of permeability estimates. The limited availability of plug measurements, especially in wells like NDW-01, could underrepresent the real permeability structure of the reservoir. Future studies should focus on acquiring more representative data, possibly through resampling or drilling new wells in data-scarce areas such as the southeastern axial zone and northwestern platform. Furthermore, the presence of hydrocarbons in some wells (e.g., SPC-01) introduces additional complexity, as the interaction between hydrocarbons and reservoir pressure could affect brine composition and extraction rates. This aspect needs careful consideration before geothermal operations are conducted.

In conclusion, while this study provides a robust assessment of geothermal potential for the Main Buntsandstein Subgroup in the Roer Valley Graben, further investigation is required to address uncertainties related to permeability, fracture networks, and the presence of hydrocarbons. These factors, if better understood, could unlock additional geothermal resources in the Main Buntsandstein Subgroup across the Roer Valley Graben.

Chapter 7: Synthesis

This dissertation investigates different geological heterogeneities of the Main Buntsandstein Subgroup in the subsurface in the southern Netherlands and evaluates their impact on the geothermal potential of the studied sedimentary units. The study employed an integrated, multiscale geological approach, utilizing subsurface data such as reflection seismic data, well logs, and core data. The results of this study show that the Main Buntsandstein sediments are largely present across the southern Netherlands where have been initially deposited through different fluvial processes with minor aeolian influence. The interplay between different depositional processes results in different reservoir architectures with sedimentary heterogeneities at different scales. After deposition, the sediments were strongly affected by extensional and compressional tectonic regimes. The fault movements associated with these tectonic regimes affected the distribution of the sediments after deposition, limiting their entire preservation only to the grabens and significantly reducing their thickness on the structural highs. The different burial histories that affected the sediments across the Roer Valley Graben triggered a series of diagenetic processes that modified initial sedimentary properties, such as porosity and permeability. Moreover, a complex fracture network emerged under these tectonic regimes, with fracture distribution closely tied to the sediment properties. By integrating all the findings, this study attempts to provide a quantitative estimate of the geothermal potential at the well scale and highlights areas of interest for future geothermal exploration. A more detailed synthesis is provided below, addressing the hypotheses outlined in the introduction of this thesis and discussing future outlooks for this field of research.

7.1 Tectonics, basin geometry, and sediment distribution

The results developed in **Chapter 2** of this thesis have shown the Main Buntsandstein Subgroup sediments in the southeastern part of the Netherlands have been deposited during early stages of rifting, as indicated by the presence of ~NW-SE syn-sedimentary normal faults producing depocenters for sedimentation on their hanging walls. This rift developed contemporaneously with the Permo-Triassic rifting stage affecting the North Sea area (Fossen et al., 2021), and produced a half-graben like with most of the growing syn-sedimentary faults located on the southern margin of the Roer Valley Graben supporting what previously hypothesized (e.g., Geluk, 2005).

Our basin geometry reconstruction based on 2D palinspastic analysis and the study of the reflector characteristics have shown that the central and southern parts of the Roer Valley Graben were likely preferred sandstone depocenters. In these areas, the average high continuity (5-7 km) and low amplitude suggest a great lateral extent of the same sedimentation conditions and rather homogeneous sandy lithologies (Veeken and Van Moerkerken, 2013; Zeng, 2018). This is further supported by the average high N/G values in the wells in these regions of the Roer Valley Graben. In the northern edge of the study area, an increase in reflector amplitudes exemplifies the frequent lithological contrasts between sandstones and claystones observed in the available wells. This suggests that these wells are in a more marginal area close to the southern edge of the Central Netherlands swell, where mostly fine particles were delivered (Geluk and Röhling, 1997). While the study of the seismic reflectors provides qualitative insights about the lithological variations through the basin, the employment of multi-attribute classification methods (e.g., AVO, acoustic impedance) and neural network pattern recognition could provide more quantitative insights into vertical and lateral lithological boundaries as well as sediment properties (Xu et al., 2022). The 3D seismic surveys present on the western part of the Roer Valley Graben and across the West

Netherlands Basin, and the reprocessed and newly acquired 2D seismic data in the central and southeastern part of the Roer Valley Graben may provide appropriate quality, thus valuable case studies.

Our palinspastic restoration reveals that the Main Buntsandstein sediments have been extensively impacted by subsequent extensional and compressional tectonic events (Vercouter and Haute, 1993; NITG, 2004; Deckers et al., 2023). These tectonic processes led to the compartmentalization of the sedimentary sequences through faulting, localized erosion, and the development of unconformities such as the base Chalk Group unconformity. Moreover, the study demonstrates that during the Jurassic to Early Cretaceous periods, regional extensional tectonics caused the Main Buntsandstein sediments in the central Roer Valley Graben to be buried to depths of up to 3.5 km (Ziegler, 1992; Geluk et al., 2007). In contrast, in some areas along the flanks of the graben - referred to as platform areas - shallower burial depths of 2 to 2.5 km were experienced. These platform areas are identified as potential zones for geothermal exploration, given the increased likelihood of encountering favourable reservoir properties due to the relatively shallow burial. While this study has highlighted a few of these promising areas, further refinement is necessary. Our burial history reconstruction is quite simplistic and not fully coupled to 1D backstripping data at well scale. Furthermore, we have assumed quite homogeneous sediment properties for the Triassic units. However, this thesis has shown how property can change quite significantly across the Roer Valley Graben, especially as result of post-depositional processes. A 2D/3D reconstruction adequately calibrated to 1D backstripping data and well lithologies could significantly enhance the identification zones that experienced shallower burial histories.

7.2 Depositional processes, stratigraphy, and reservoir architecture

In **Chapter 3**, a comprehensive sedimentological and stratigraphical analysis was conducted on a subsurface dataset composed of well log and core data from the Main Buntsandstein Subgroup in the Roer Valley Graben. Our results show that the deposition is dominated by different fluvial processes, with minor aeolian reworking. The river plan from style evolved from being more highly mobile and ephemeral in the Volpriehausen and Detfurth Formations to being more perennial in the Hardegsen. We believe that such a change in sedimentary facies association across the Buntsandstein stratigraphy is related to a decrease of aridity in time and a decrease in tectonic activity upwards in the Buntsandstein stratigraphy, as observed in adjacent Triassic basins (Ames and Farfan, 1996; Bourquin et al., 2007). The increase in paleosol development and vegetation, and a decrease in vertical amalgamation upwards in the stratigraphy support this hypothesis. Despite the presence of many common depositional features between our model and the models already available in the literature, the change in fluvial style across the Buntsandstein stratigraphy had not been documented before. This is a fundamental aspect as the different depositional processes resulted in the development of different types of reservoir architectures with their own set of heterogeneities.

Our paleogeographic reconstruction based on subsurface data from the Roer Valley Graben indicates that the sediments were sourced from at least two distinct sources: a proximal source, the London-Brabant Massif, and more distant sources such as the Armorican and Rhenish Massifs. These findings align partially with previous Early Triassic paleogeographic reconstructions, both at the regional scale of the study area (e.g., Geluk, 2005; IF Technology,

2012) and within the broader context of the Germanic Basin (Bourquin et al., 2009; McKie and Williams, 2009). However, there is still considerable room for refinement in our understanding of the paleogeographic framework and the roles of these sedimentary sources. The lateral extent of well-sorted, quartz-rich aeolian sediments remains ambiguous based solely on the available data. This uncertainty is particularly important because aeolian sediments exhibit superior reservoir properties, making them a prime target for geothermal exploration. A better understanding of the sedimentary sources and their associated drainage systems could be key to predicting where these valuable aeolian deposits might be encountered. Currently, aeolian sediments are identified only in the southeastern part of the Roer Valley Graben, where the sediments are predominantly interpreted to have been sourced from the distal Armorican Massif. Conducting a detail analysis on rock fragments from the Main Buntsandstein sediments and a benchmark again potential source composition similar to what proposed by Ravida et al. (2022) may provide further insights into the distribution of specific sedimentary facies, thereby improving the ability to locate areas with high reservoir potential.

The different depositional processes resulted in the development of three main types of reservoir architecture with their own set of heterogeneities. Amalgamated and compensational stacked sandstones are the most dominant across the study area but also the most heterogeneous, with primary porosity and permeability largely altered by later diagenesis. On the other hand, marginal isolated sandstones show apparent preserved relationship between primary reservoir properties and depositional facies. These type of facies are proven to form prolific reservoirs in the North Sea area (e.g., the Triassic Skagerrak Formation across the Forties-Montrose High). The connectivity of these sandstone bodies largely depends on the lateral extent of the playa-lake deposits that may act as fluid flow barriers. This remains an open question that could not be fully resolved given the sampling of this facies only in one well. The acquisition of a 3D survey covering the area where these isolated sandstones have been encountered could provide further insights into the extent of this sedimentary facies. However, given the relatively shallow depths and low temperatures, this area does not represent an attractive target for deep geothermal operations.

7.3 Diagenesis and its effect on reservoir quality

Chapter 4 examines the diagenesis of the Main Buntsandstein sediments and its influence on reservoir properties. A comprehensive petrographic analysis was performed, including point-counting on both legacy and newly collected thin sections from various wells in the Roer Valley Graben at depths ranging from 1500 to 2500 meters. The study identifies four main diagenetic stages in the Buntsandstein sediments: (i) eogenesis, (ii) 1st mesogenesis, (iii) telogenesis, and (iv) 2nd mesogenesis. Each stage corresponds to specific tectonic regimes experienced by the Roer Valley Graben.

The sandstones of the Main Buntsandstein are predominantly cemented by illite, quartz, and dolomite. One of the earliest cementation phases includes tangential illite grain coatings, which can preserve porosity by limiting quartz cementation, as observed in other arid environments (Beyer et al., 2014; Busch et al., 2022). However, early illite cementation can also lead to increased grain compaction, reducing the intergranular volume. When illite forms a radial meshwork, it can further restrict pore throats, negatively impacting permeability.

Dolomite cementation occurs in various forms throughout eogenesis and both mesogenetic stages, while quartz cementation is more common during the two mesogenetic phases. In fine-grained sandstones, quartz and dolomite cements help preserve porosity by stabilizing the grain framework and reducing compaction. In contrast, in coarser sandstones, these cements tend to reduce porosity. While no strong statistical correlation was found between the amount of quartz and dolomite cements and the overall porosity or permeability of the sandstones, integrating a larger set of samples could allow for further exploration of potential statistical relationships and provide a more robust test of these concepts. However, it is crucial to ensure that the additional samples come from sediments with similar properties, such as grain size, sedimentary structures, and burial depth, to maintain consistency and reliability in the analysis.

Dissolution, a significant process during telogenesis due to exhumation, has contributed to the formation of secondary porosity. In some samples from the southeastern part of the Roer Valley Graben, secondary porosity accounts for up to 65% of the total optical porosity. Mijnlieff (2020) suggests that dissolution may enhance permeability in areas where the Main Buntsandstein is truncated beneath the base Chalk Group unconformity. While we recognize that dissolution could play a role in improving permeability, we found no clear evidence on our dataset that this process alone would create reservoir properties conducive to economically viable production rates.

Our findings suggest that reservoir quality is better preserved along the flanks of the Roer Valley Graben, where the sandstones have experienced shallower burial depths during the Mesozoic. This shallower burial likely contributed to the preservation of primary reservoir properties such as porosity and permeability, which are critical for geothermal potential. The concept of encountering better reservoir quality preservation at reduced burial depths could also be extended to adjacent basins such as the West Netherlands Basin, offering new opportunities for exploration.

7.4 Fractures: distribution and controls

Chapter 5 aims to characterize fractures in the Main Buntsandstein sediments in the West Netherlands Basin, which represents the northwest continuation of the Roer Valley Graben. The analysis compares rock core inspection, wireline and image logs interpretations to document the drivers and characteristics of natural fracture distribution and investigate the fracture and mechanical stratigraphy to place these along the geodynamics history of the basin. The analysis of core samples revealed the presence of five types of discontinuities, including natural and drilling-induced fractures. An orientation-based filter was employed to attempt a distinction between natural and drilling-induced fractures in the core and in the wireline logs given the high degree of uncertainty when trying to classify the fractures just based on their appearance. The employment of this orientation-based classification effect may affect the fracture classification. However, when comparing the manual fracture interpretation with the orientation-based interpretation, the fracture densities over the interpreted sections display the same trend. The natural fractures appear to be concentrated more in heterolithic intervals when compared the fracture density curves against the sedimentary facies. Overall, VAL-01 has a higher average fracture density compared to NLW-GT-01. This can be explained by the different locations of the wells in the basin. VAL-01 well is drilled in a more distal part of the basin, where finer sediments were mostly deposited, occasionally alternating with coarser sandstones. In contrast, well NLW-GT-01 is located in a more proximal area with respect to the fluvial depositional system, where fluvial sandstones were largely deposited. These variations in lithology control the fracture stratigraphy. The absence of a direct correlation between fracture and geomechanical properties may be related to diagenesis, which altered the initial sediment properties and, thus, geomechanical behaviour (Worden and Burley, 2003).

The fractures are interpreted to be formed during at least three tectonic regimes, which partially coincide with the extensional and compressional regimes the West Netherlands Basin experienced from the Triassic till the present. The drilling-induced fractures and the borehole breakouts indicate an in-situ NE-SW oriented minimum stress and a NW-SE maximum stress. The joints, veins, and the tectonic stylolite are oriented perpendicular to the minimum stress direction and, thus, are likely to be open considering the current stress regime retrieved from the drilling-induced fracture orientation. These fractures could then potentially contribute to increasing the permeability of the sediments and enhance heat recovery as described by previous studies (Boersma et al., 2021). Unfortunately, production data for the analysed wells are unavailable, leaving the direct contribution of fractures to permeability an educated hypothesis. Nonetheless, the identified fracture network presents a promising foundation for future reservoir engineering. Extending the existing fracture network through techniques such as water injection could further enhance reservoir permeability. Engineered Geothermal Systems (EGS) are gaining interest for this purpose, as they provide access to deeper, higher-temperature reservoirs, increasing heat production potential. Within this context, Sage Geosystems may provide a considerable option. Sage Geosystem approach harvests the heat in the reservoir utilizing the fracture as a balloon that open when they are filled with fluid and close when the fluid is pumped out (Khodayar and Bjornsson, 2024). If the fracture network is extensive, this could represent an alternative that does not require intense fluid injection to create new fractures. However, the application of EGS in sedimentary reservoirs, such as those found in the Netherlands, remains relatively underdeveloped. While EGS technologies show considerable promise, there are still significant technical and economic challenges that need to be addressed. Consequently, conventional doublet systems in reservoirs with sufficient matrix permeability currently present the most viable solution for the rapid development of geothermal energy.

7.5 Geothermal potential

In **Chapter 6** the geothermal potential of the Main Buntsandstein Subgroup in the Roer Valley Graben is assessed by calculating the heat initially in place (HIIP) and geothermal power (GP) and then discussed against the geological knowledge developed within this thesis. The highest HIIP values are found in areas where reservoir thickness exceeds 130 m and temperatures are above 90°C. These areas are largely located along the southern margin of the Roer Valley Graben. This is consistent with general trends from previous geothermal assessments in the region for the entire Triassic stratigraphy (e.g., IF Technology, 2012;).

Permeability largely drives geothermal power generation. The wells in the northwestern platform (e.g., STH-01) exhibit high GP values (up to 6.28 MW), which correlates with permeability values as high as 992 mD. This suggests that areas with reduced diagenesis and lower subsidence, such as the northwestern platform, are more suitable for geothermal exploitation, as the primary reservoir properties are well preserved. In contrast, wells located near the basin axis, such as SPC-01, show lower GP values despite moderate HIIP. This discrepancy can be attributed to the poor permeability caused by deeper burial, greater compaction, and cementation. Nonetheless, we suggest that some blocks in the deeper part of the basin may have preserved appropriate reservoir properties if maximum burial during the Mesozoic was shallower than 2-2.5 km. Moreover, we identify the southeastern area of the Roer Valley Graben as a promising sector, where the presence of aeolian facies in combination with dissolution and creation of secondary porosity, may have enhanced reservoir potential despite overall poor porosity and permeability elsewhere in the region. In this context, our work emerges as new as the geothermal potential of the Main Buntsandstein Subgroup only was assessed here for the first time. However, the calculations remain quite simplistic and would benefit from a more rigorous modelling approach, incorporating sensitivity analyses of key reservoir parameters and heterogeneities to improve the reliability of the results such as presented by Crooijmans et al. (2016).

7.6 Final Remarks

This study provides a detailed investigation of the geological aspects of the Main Buntsandstein Subgroup sediments in the southern Netherlands, offering a solid foundation for future research and application. The findings can serve as a baseline for both future targeted academic studies and practical efforts within the geothermal industry, which should leverage these results to unlock the potential of the rather underdeveloped geothermal Triassic play. The observed heterogeneities, driven by depositional and post-depositional processes, introduce significant uncertainties to the Triassic Main Buntsandstein geothermal play. This thesis suggests that the southeastern part of the Roer Valley Graben and its flanks, particularly the southern one, represent the most promising areas for geothermal energy exploration and development. However, these areas also suffer from limited well data, increasing uncertainty in reservoir assessments. To address this, drilling an exploration well on the southern flank would be highly beneficial. Such a well could be used to acquire core material for detailed sedimentological and petrophysical analysis, significantly reducing uncertainties regarding reservoir properties, which are currently inferred only from well logs. To optimize costs, a vertical exploration well could be designed for future re-use, allowing it to be sidetracked as an injector or producer. This approach would streamline development and cut drilling expenses. Additionally, conducting a detailed attribute analysis in the southern Netherlands, particularly in areas with available 3D seismic data or where 2D seismic lines are of sufficient quality, would provide valuable insights into sediment properties, further improving geothermal exploration efforts in the region.

Author Contributions

The chapters were authored by the people listed below. Author contributions are listed via the Contributor Role Taxonomy (CRediT) after Brand et al. (2015). Funding for all chapters was aquired by A.W. Martinius and H.A. Abels.

Chapter 2: Structural controls on the Triassic Main Buntsandstein sediment distribution in the Roer Valley Graben, the Netherlands

E. Cecchetti: Conceptualisation, Investigation, Methodology, Data Curation, Writing Original Draft, Formal Analysis, Visualization, Software
A.W. Martinius: Conceptualisation, Investigation, Review and Editing, Supervision
H.A. Abels: Conceptualisation, Investigation, Review and Editing, Supervision
A. Bender: Investigation, Review and Editing, Supervision, Data Curation, Software
P.O. Bruna: Conceptualisation, Methodology, Investigation, Review and Editing, Software

Chapter 2 is based upon: Cecchetti, E., Martinius, A. W., Bruna, P. O., Bender, A., Abels, H. A., 2024. Structural controls on the Triassic Main Buntsandstein sediment distribution in the Roer Valley Graben, the Netherlands. *Netherlands Journal of Geosciences*, *103*, e23.

Chapter 3: Sedimentology, stratigraphy and reservoir architecture of the Lower Triassic Main Buntsandstein in the Roer Valley Graben, the Netherlands
E. Cecchetti: Conceptualisation, Investigation, Methodology, Data Curation, Writing Original Draft, Formal Analysis, Visualization
A.W. Martinius: Conceptualisation, Investigation, Methodology, Review and Editing, Supervision
H.A. Abels: Conceptualisation, Investigation, Methodology, Review and Editing, Supervision
M.E. Donselaar: Conceptualisation, Investigation, Review and Editing
M. Felder: Conceptualisation, Investigation, Review and Editing

Chapter 3 has been submitted to the Journal of Marine and Petroleum Geology

Chapter 4: Diagenetic controls on sandstone properties of the Main Buntsandstein Subgroup in the Roer Valley Graben, the Netherlands
E. Cecchetti: Conceptualisation, Investigation, Methodology, Data Curation, Writing Original Draft, Formal Analysis, Visualization
A.W. Martinius: Conceptualisation, Investigation, Methodology, Review and Editing, Supervision
H.A. Abels: Conceptualisation, Investigation, Methodology, Review and Editing, Supervision
M. Felder: Conceptualisation, Investigation, Methodology, Review and Editing

Chapter 5: Fracture characterization and development in the Main Buntsandstein Subgroup in the West Netherlands Basin
E. Cecchetti: Conceptualisation, Investigation, Methodology, Data Curation, Writing Original Draft, Formal Analysis, Visualization, Software
A.W. Martinius: Review and Editing, Supervision

H.A. Abels: Conceptualisation, Investigation, Methodology, Review and Editing, Supervision
F. Tutuarima: Conceptualisation, Investigation, Methodology, Data Curation, Writing Original Draft, Formal Analysis, Visualization, Software
G. Bertotti: Review and Editing, Supervision
P.O. Bruna: Conceptualisation, Methodology, Investigation, Review and Editing, Software, Supervision

Chapter 6: Geothermal potential of the Main Buntsandstein Subgroup in the Roer Valley Graben
E. Cecchetti: Conceptualisation, Investigation, Methodology, Data Curation, Writing Original Draft, Formal Analysis, Visualization
A.W. Maritnius: Conceptualisation, Review and Editing, Supervision
H.A. Abels: Conceptualisation, Methodology, Review and Editing, Supervision
A. Daniilidis: Conceptualisation, Investigation, Methodology, Review and Editing, Supervision

References

Aehnelt, M., Hilse, U., Pudlo, D., Heide, K. and Gaupp, R., 2021. On the origin of bleaching phenomena in red bed sediments of Triassic Buntsandstein deposits in Central Germany. Geochemistry, 81(2), p.125736.

Ames, R. and Farfan, P.F., 1996. The environments of deposition of the Triassic Main Buntsandstein Formation in the P and Q quadrants, offshore the Netherlands. In: Geology of Gas and Oil under the Netherlands: Selection of papers presented at the 1983 International Conference of the American Association of Petroleum Geologists, held in The Hague (pp. 167-178). Springer Netherlands.

Anderson, E.M., 1951. Dynamics of faulting and dyke formation with application to Britain. Hafner Publishing Company, pp.206.

Atlas Geoscience, 1998. AST image analysis and structure interpretation of Well VAL-01.

Audley-Charles, M.G., 1970. Triassic palaeogeography of the British Isles. Quarterly Journal of the Geological Society, 126(1-4), pp.49-74.

Augustsson, C., Aehnelt, M., Voigt, T., Kunkel, C., Meyer, M. and Schellhorn, F., 2019. Quartz and zircon decoupling in sandstone: Petrography and quartz cathodoluminescence of the Early Triassic continental Buntsandstein Group in Germany. Sedimentology, 66(7), pp.2874-2893.

Bachmann, G.H. and Müller, M., 1991. The Molasse Basin, Germany: evolution of a classic petroliferous foreland basin. In: Generation, accumulation, and production of Europe's hydrocarbons: Special publication of the European Association of Petroleum Geoscientists (pp.263-276).

Bachmann, G.H., Geluk, M.C., Doornenbal, J.C. and Stevenson, A.G., 2010. Chapter 9, Triassic. In: Doornenbal, H. and Stevenson, A. (eds) Petroleum Geological Atlas of The Southern Permian Basin Area, pp.148-173. EAGE Publications B.V., Houten.

Bai, T., Pollard, D.D. and Gao, H., 2000. Explanation for fracture spacing in layered materials. Nature, 403(6771), pp.753-756.

Bai, T. and Pollard, D.D., 2000. Fracture spacing in layered rocks: a new explanation based on the stress transition. Journal of Structural Geology, 22(1), pp.43-57.

Baron, M. and Parnell, J., 2007. Relationships between stylolites and cementation in sandstone reservoirs: Examples from the North Sea, UK and East Greenland. Sedimentary Geology, 194(1-2), pp.17-35.

Békési, E., Struijk, M., Bonté, D., Veldkamp, H., Limberger, J., Fokker, P.A., Vrijlandt, M. and Van Wees, J.D., 2020. An updated geothermal model of the Dutch subsurface based on inversion of temperature data. Geothermics, 88.

Bello, A.M., Al-Ramadan, K., Babalola, L.O., Alqubalee, A. and Amao, A.O., 2023. Impact of grain-coating illite in preventing quartz cementation: Example from permo-carboniferous sandstone, Central Saudi Arabia. Marine and Petroleum Geology, 149, p.106073.

Beyer, D., Kunkel, C., Aehnelt, M., Pudlo, D., Voigt, T., Nover, G. and Gaupp, R., 2014. Influence of depositional environment and diagenesis on petrophysical properties of clastic sediments (Buntsandstein of the Thuringian Syncline, Central Germany). Zeitschrift der deutschen Gesellschaft für Geowissenschaften, 165(3), pp.345-365.

Bertier, P., Swennen, R., Kemps, R., Laenen, B. and Dreesen, R., 2022. Reservoir characteristics and diagenesis of the Buntsandstein sandstones in the Campine Basin (NE Belgium). Geologica Belgica.

Bjørlykke, K. and Egeberg, P.K., 1993. Quartz cementation in sedimentary basins. AAPG Bulletin, 77(9), pp.1538-1548.

Boersma, Q.D., Bruna, P.O., De Hoop, S., Vinci, F., Tehrani, A.M. and Bertotti, G., 2021. The impact of natural fractures on heat extraction from tight Triassic sandstones in the West Netherlands Basin: a case study combining well, seismic and numerical data. Netherlands Journal of Geosciences, 100, p.e6.

Bourquin, S., Guillocheau, F. and Péron, S., 2009. Braided rivers within an arid alluvial plain (example from the Lower Triassic, western German Basin): recognition criteria and expression of stratigraphic cycles. Sedimentology, 56(7), pp.2235-2264.

Bonté, D., Van Wees, J.D. and Verweij, J.M., 2012. Subsurface temperature of the onshore Netherlands: new temperature dataset and modelling. Netherlands Journal of Geosciences, 91(4), pp.491-515.

Bourquin, S., Peron, S. and Durand, M., 2006. Lower Triassic sequence stratigraphy of the western part of the Germanic Basin (west of Black Forest): fluvial system evolution through time and space. Sedimentary Geology, 186(3-4), pp.187-211.

Bourquin, S., Durand, M., Diez, J.B., Broutin, J. and Fluteau, F., 2007. The Permian-Triassic boundary and Early Triassic sedimentation in Western European basins: an overview. Journal of Iberian Geology, 33(2), pp.221-236.

Bourquin, S., Guillocheau, F. and Péron, S., 2009. Braided rivers within an arid alluvial plain (example from the Lower Triassic, western German Basin): recognition criteria and expression of stratigraphic cycles. Sedimentology, 56(7), pp.2235-2264.

Bourquin, S., Bercovici, A., López-Gómez, J., Diez, J.B., Broutin, J., Ronchi, A., Durand, M., Arché, A., Linol, B. and Amour, F., 2011. The Permian–Triassic transition and the onset of Mesozoic sedimentation at the northwestern peri-Tethyan domain scale: palaeogeographic maps and geodynamic implications. Palaeogeography, Palaeoclimatology, Palaeoecology, 299(1-2), pp.265-280.

Bridge, J.S. and Tye, R.S., 2000. Interpreting the dimensions of ancient fluvial channel bars, channels, and channel belts from wireline-logs and cores. AAPG Bulletin, 84(8), pp.1205-1228.

Bridge, J.S., 2006. Fluvial facies models: recent developments.

Bradley, R.W. and Venditti, J.G., 2017. Reevaluating dune scaling relations. Earth-Science Reviews, 165, pp.356-376.

Bryant, M., Falk, P. and Paola, C., 1995. Experimental study of avulsion frequency and rate of deposition. Geology, 23(4), pp.365-368.

Bruna, P.O., 2019. Are stylolites fluid-flow efficient features? Journal of Structural Geology, 125(1), pp.270-277. doi: https://doi.org/10.1016/j.jsg.2018.05.018

Buatois, L.A. and Mángano, M.G., 1998. Trace fossil analysis of lacustrine facies and basins. Palaeogeography, Palaeoclimatology, Palaeoecology, 140(1-4), pp.367-382.

Busch, B., Hilgers, C. and Adelmann, D., 2020. Reservoir quality controls on Rotliegend fluvio-aeolian wells in Germany and the Netherlands, Southern Permian Basin–Impact of grain coatings and cements. Marine and Petroleum Geology, 112, p.104075.

Busch, B., Adelmann, D., Herrmann, R. and Hilgers, C., 2022. Controls on compactional behavior and reservoir quality in a Triassic Buntsandstein reservoir, Upper Rhine Graben, SW Germany. Marine and Petroleum Geology, 136, p.105437.

Cain, S.A. and Mountney, N.P., 2009. Spatial and temporal evolution of a terminal fluvial fan system: the Permian Organ Rock Formation, South-east Utah, USA. Sedimentology, 56(6), pp.1774-1800.

Casado, A.I., Alonso-Zarza, A.M. and La Iglesia, Á., 2014. Morphology and origin of dolomite in paleosols and lacustrine sequences. Examples from the Miocene of the Madrid Basin. Sedimentary Geology, 312, pp.50-62.
Carter, R., Cade, C. and Amiri Garoussi, K., 1990. Sedimentology and reservoir quality of the middle and upper Bunter Formations, Cores 1-7 Waalwijk-2. EXT 58541.

Cecchetti, E., Martinius, A., Bruna, P.O., Bender, A., Abels, H., 2024. Structural controls on the Main Buntsandstein sediment distribution in the Roer Valley Graben, the Netherlands. Submitted to: Netherlands Journal of Geoscience.

Cecchetti, E., Martinius, A., Donselaar, M., Felder, M., Abels, H., in press. Sedimentology, stratigraphy, and reservoir architecture of the Lower Triassic Main Buntsandstein in the Roer Valley Graben, the Netherlands. Submitted to: Journal of Marine and Petroleum Geology.

Chapelle, F.H., 1993. Ground-water Microbiology and Geochemistry. John Wiley & Sons, New York, 448 pp.

Chatterjee, S., & Mukherjee, S., 2023. Review on drilling-induced fractures in drill cores. Marine and Petroleum Geology, 151 (106089), 270-277. DOI: https://doi.org/10.1016/j.marpetgeo.2022.106089.

Clemmensen, L.B., 1998. Desert sand plain and sabkha deposits from the Bunter Sandstone Formation (Lower Triassic) at the northern margin of the German Basin. Geologische Rundschau, 74(3), pp.519-536.

Colombera, L. and Mountney, N.P., 2021. Influence of fluvial crevasse-splay deposits on sandbody connectivity: Lessons from geological analogues and stochastic modelling. Marine and Petroleum Geology, 128, p.105060.

Coronel, M.D., Isla, M.F., Veiga, G.D., Mountney, N.P. and Colombera, L., 2020. Anatomy and facies distribution of terminal lobes in ephemeral fluvial successions: Jurassic Tordillo Formation, Neuquén Basin, Argentina. Sedimentology, 67(5), pp.2596-2624.

Crostella, A. and Backhouse, J., 2000. Geology and petroleum exploration of the central and southern Perth Basin, Western Australia (Report No. 57, pp. 1-85). Perth, WA: Geological Survey of Western Australia.

De Jager, J., M. A. Doyle, P. J. Grantham, and J. E. Mabillard, 1996. Hydrocarbon habitat of the West Netherlands Basin. In Geology of Gas and Oil under the Netherlands: Selection of papers presented at the 1983 International Conference of the American Association of Petroleum Geologists, held in The Hague, pp. 191-209. Springer Netherlands.

De Jager, J., 2003. Inverted basins in the Netherlands, similarities and differences. Netherlands Journal of Geosciences, 82(4), 339-349.

Deckers, J., Rombaut, B., Van Noten, K., and Vanneste, K., 2021. Influence of inherited structural domains and their particular strain distributions on the Roer Valley Graben evolution from inversion to extension. Solid Earth, 12(2), 345-361.

Deckers, J., Rombaut, B., Broothaers, M., Dirix, K. and Debacker, T., 2023. New 787 3D fault model for eastern Flanders (Belgium) providing insights on the major deformation phases in the region since the late Paleozoic. Journal of Structural Geology, 166, p.104779.

De Lucia, M., Bauer, S., Beyer, C., Kühn, M., Nowak, T., Pudlo, D., Reitenbach, V., Stadler, S., 2012. Modelling CO2-induced fluid–rock interactions in the Altensalzwedel gas reservoir. Part I: from experimental data to a reference geochemical model. Environmental Earth Sciences, 67, 563–572.

DiPippo, R., 2012. Geothermal power plants: Principles, applications, case studies, and environmental impact. Butterworth-Heinemann.

Donselaar, M.E., Cuevas Gozalo, M.C., van Toorenenburg, K.A. and Wallinga, J., 2022. Spatio-temporal reconstruction of avulsion history at the terminus of a modern dryland river system. Earth Surface Processes and Landforms, 47(5), pp.1212-1228.

Duin, E.J.T., Doornenbal, J.C., Rijkers, R.H., Verbeek, J.W., and Wong, T.E., 2006. Subsurface structure of the Netherlands-results of recent onshore and offshore mapping. Netherlands Journal of Geosciences, 85(4), p.245.

Felder, M. and Fernandez, S., 2018. Core hot shot NLW-GT-01. The Hague: PanTerra Geoconsultants B.V., 7 pp.

Field, J., 2001. Channel avulsion on alluvial fans in southern Arizona. Geomorphology, 37(1-2), pp.93-104.

Fielding, C.R., 2006. Upper flow regime sheets, lenses, and scour fills: extending the range of architectural elements for fluvial sediment bodies. Sedimentary Geology, 190(1-4), pp.227-240.

Fisher, J.A., Nichols, G.J. and Waltham, D.A., 2007. Unconfined flow deposits in distal sectors of fluvial distributary systems: examples from the Miocene Luna and Huesca Systems, northern Spain. Sedimentary Geology, 195(1-2), pp.55-73.

Fisher, J.A., Krapf, C.B., Lang, S.C., Nichols, G.J. and Payenberg, T.H., 2008. Sedimentology and architecture of the Douglas Creek terminal splay, Lake Eyre, central Australia. Sedimentology, 55(6), pp.1915-1930.

Folk, R.L. and Ward, W.C., 1957. Brazos River bar (Texas): A study in the significance of grain size parameters. Journal of Sedimentary Research, 27(1), pp.3-26.

Folk, R.L., 1980. Petrology of Sedimentary Rocks. Hemphill Publishing Company.

Fossen, H., 2010. Structural Geology. Cambridge University Press.

Fossen, H., Ksienzyk, A.K., Rotevatn, A., Bauck, M.S. and Wemmer, K., 2021. From widespread faulting to localized rifting: Evidence from K-Ar fault gouge dates from the Norwegian North Sea rift shoulder. Basin Research, 33(3), 1934-1953.

Gaupp, R., Matter, A., Platt, J., Ramseyer, K., and Walzebuck, J., 1993. Diagenesis and fluid evolution of deeply buried Permian (Rotliegende) gas reservoirs, northwest Germany. AAPG Bulletin, 77(7), pp.1111-1128.

Gawthorpe, R.L. and Leeder, M.R., 2000. Tectono-sedimentary evolution of active extensional basins. Basin Research, 12(3-4), 195-218.

Geel, C.R. and Donselaar, M.E., 2007. Reservoir modelling of heterolithic tidal deposits: Sensitivity analysis of an object-based stochastic model. Netherlands Journal of Geosciences-Geologie en Mijnbouw, 86(4), p.403.

Geluk, M.C., Duin, E.T., Dusar, M., Rijkers, R.H.B., Van den Berg, M.W. and Van Rooijen, P., 1994. Stratigraphy and tectonics of the Roer Valley Graben. Geologie en Mijnbouw, 73, p.129.

Geluk, M., Plomp, A., van Doorn, T., 1996. Development of the Permo-Triassic succession in the basin fringe area, southern Netherlands. In: H. E. Rondeel, D. A. J. Batjes, & W. H. Nieuwenhuijs (Eds.), Geology of Gas and Oil under the Netherlands: Selection of papers presented at the 1983 international conference of the American association of petroleum geologists, held in the Hague (pp. 57–78). Dordrecht: Springer Netherlands. DOI: 10.1007/978-94-009-0121-6-7

Geluk, M.C. and Röhling, H.G., 1997. High-resolution sequence stratigraphy of the Lower Triassic 'Buntsandstein' in the Netherlands and northwestern Germany. Geologie en Mijnbouw, 76, 227-246.

Geluk, M.C., 1998. Palaeogeographic and structural development of the Triassic in the Netherlands—new insights. Epicontinental Triassic, 1, pp.545-570.

Geluk, M.C., 2005. Stratigraphy and tectonics of Permo-Triassic basins in the Netherlands and surrounding areas. PhD Thesis, Utrecht University, Utrecht, 171 pp. ISBN: 90-393-3911-2.

Gibling, M.R., 2006. Width and thickness of fluvial channel bodies and valley fills in the geological record: A literature compilation and classification. Journal of Sedimentary Research, 76(5), pp.731-770.

Glennie, K.W., Mudd, G.C. and Nagtegaal, P.J.C., 1978. Depositional environment and diagenesis of Permian Rotliegendes sandstones in Leman Bank and Sole Pit areas of the UK southern North Sea. Journal of the Geological Society, 135(1), pp.25-34.

Gómez-Gras, D. and Alonso-Zarza, A.M., 2003. Reworked calcretes: their significance in the reconstruction of alluvial sequences (Permian and Triassic, Minorca, Balearic Islands, Spain). Sedimentary Geology, 158(3-4), pp.299-319.

Goswami, R., Seeberger, F.C. and Bosman, G., 2018. Enhanced gas recovery of an ageing field utilizing N2 displacement: De Wijk Field, The Netherlands. Geological Society, London, Special Publications, 469(1), pp.237-251.

Green, P. F., Moore, M. E., 1992a. Thermal history reconstruction in four onshore Netherlands wells using apatite fission track analysis and vitrinite reflectance. Geotrack Report #393.

Green, P. F., Moore, M. E., 1992b. Thermal history reconstruction in two onshore Netherlands wells using apatite fission track analysis and vitrinite reflectance. Geotrack Report #407.

Hamm, V. and Lopez, S., 2012. Impact of fluvial sedimentary heterogeneities on heat transfer at a geothermal doublet scale. Stanford Geothermal Workshop, 18 pp.

Hartkamp-Bakker, C.A. and Donselaar, M.E., 1992. Permeability patterns in point bar deposits: Tertiary Loranca Basin, central Spain. The Geological Modelling of Hydrocarbon Reservoirs and Outcrop Analogues, pp.157-168.

Hartmann, D. J., Beaumont, E. A., & Foster, N. H., 1999. Predicting reservoir system quality and performance. Exploring for Oil and Gas Traps: AAPG Treatise of Petroleum Geology, Handbook of Petroleum Geology, 9-1.

Hassan, M.A., Church, M., Lisle, T.E., Brardinoni, F., Benda, L. and Grant, G.E., 2005. Sediment transport and channel morphology of small, forested streams. Journal of the American Water Resources Association, 41(4), pp.853-876.

Heald, M.T., 1955. Stylolites in sandstones. The Journal of Geology, 63(2), pp.101-114.

Healy, D., Blenkinsop, T.G., Timms, N.E., Meredith, P.G., Mitchell, T.M. and Cooke, M.L., 2015. Polymodal faulting: Time for a new angle on shear failure. Journal of Structural Geology, 80, pp.57-71.

Henares, S., Caracciolo, L., Cultrone, G., Fernández, J., & Viseras, C., 2014. The role of diagenesis and depositional facies on pore system evolution in a Triassic outcrop analogue (SE Spain). Marine and Petroleum Geology, 51, pp.136-151.

Henares, S., Arribas, J., Cultrone, G., Viseras, C., 2016. Muddy and dolomitic rip-up clasts in Triassic fluvial sandstones: Origin and impact on potential reservoir properties (Argana Basin, Morocco). Sedimentology, 339, 218–233.

Henares, S., Donselaar, M.E. and Caracciolo, L., 2020. Depositional controls on sediment properties in dryland rivers: Influence on near-surface diagenesis. Earth-Science Reviews, 208, p.103297.

Herbert, C.M. and Alexander, J., 2018. Bottomset architecture formed in the troughs of dunes and unit bars. Journal of Sedimentary Research, 88(4), pp.522-553.

Herngreen, G.F.W. and Wong, T.E., 2007. Cretaceous. In: T.E. Wong, D.A.J. Batjes, and J. De Jager, eds., Geology of the Netherlands (Amsterdam, Royal Netherlands

Hjuler, M.L., Olivarius, M., Boldreel, L.O., Kristensen, L., Laier, T., Mathiesen, A., Nielsen, C.M. & Nielsen, L.H., 2019. Multidisciplinary approach to assess geothermal potential, Tønder area, North German Basin. Geothermics, 78, pp.211-223.

Hunfeld, L.B., Foeken, J.P.T. & Van Kempen, B.M.M., 2021. Geomechanical parameters derived from compressional and shear sonic logs for main geothermal targets in The Netherlands. TNO, Utrecht.

IF Technology, 2012. Geothermal energy Noord-Brabant: Geological study of Triassic reservoirs in the province of Noord-Brabant. Summary report 3/60125/NB.

IRENA, 2017. Renewable Energy in District Heating and Cooling: A Sector Roadmap for REmap. International Renewable Energy Agency, Abu Dhabi. Available at: https://www.irena.org/remap

Khoshbakht, F., Azizzadeh, M., Memarian, H., Nourozi, G.H. & Moallemi, S.A., 2012. Comparison of electrical image log with core in a fractured carbonate reservoir. Journal of Petroleum Science and Engineering, 86, pp.289-296.

Kilhams, B., Kukla, P.A., Mazur, S., McKie, T., Mijnlieff, H.F., van Ojik, K. & Rosendaal, E., 2018. Mesozoic resource potential in the Southern Permian Basin area: The geological key to exploiting remaining hydrocarbons whilst unlocking geothermal potential. Geological Society, London, Special Publications, 469(1), pp.1-18.

Kombrink, H., Doornenbal, J.C., Duin, E.J.T., Den Dulk, M., Van Gessel, S.F., Ten Veen, J.H. & Witmans, N., 2012. New insights into the geological structure of the Netherlands: Results of a detailed mapping project. Netherlands Journal of Geosciences, 91(4), pp.419-446.

Kortekaas, M., Böker, U., Van Der Kooij, C. & Jaarsma, B., 2018. Lower Triassic reservoir development in the northern Dutch offshore. Geological Society, London, Special Publications, 469(1), pp.149-168.

Köppen, A. & Carter, A., 2000. Constraints on provenance of the central European Triassic using detrital zircon fission track data. Palaeogeography, Palaeoclimatology, Palaeoecology, 161(1-2), pp.193-204.

Kourta, M. & Jocker, J., 2018. Fracture analysis on basis of FMI and sonic scanner. Schlumberger SIS Data Services, 12pp.

Kramers, L., Van Wees, J.D., Pluymaekers, M.P.D., Kronimus, A. & Boxem, T., 2012. Direct heat resource assessment and subsurface information systems for geothermal reservoirs: The Dutch perspective. Netherlands Journal of Geosciences, 91(4), pp.637-649.

Kunkel, C., Aehnelt, M., Pudlo, D., Kukowski, N., Totsche, K.U. & Gaupp, R., 2018. Subsurface reservoir heterogeneities of Lower Triassic clastic sediments in central Germany. Marine and Petroleum Geology, 97, pp.209-222.

Lai, J., Wang, G., Wang, S., Cao, J., Li, M., Pang, X., Qin, Z., 2018. A review on the applications of image logs in structural analysis and sedimentary characterization. Marine and Petroleum Geology, 95, pp.139-166. https://doi.org/10.1016/j.marpetgeo.2018.04.020

Larue, D.K. & Hovadik, J.M., 2006. Connectivity of channelized reservoirs: A modelling approach. Petroleum Geoscience, 12, pp.291-308.

Laubach, S.E., Olson, J.E. & Gross, M.R., 2009. Mechanical and fracture stratigraphy. AAPG Bulletin, 93(11), pp.1413-1426.

Leclair, S.F. & Bridge, J.S., 2001. Quantitative interpretation of sedimentary structures formed by river dunes. Journal of Sedimentary Research, 71(5), pp.713-716.

Liewig, N. & Clauer, N., 2000. K-Ar dating of varied microtextural illite in Permian gas reservoirs, northern Germany. Clay Miner., 35, pp.271-281. https://doi.org/10.1180/000985500546648.

Limaye, A.B., 2020. How do braided rivers grow channel belts? Journal of Geophysical Research: Earth Surface, 125(8), p.e2020JF005570.

Lingrey, S. & Vidal-Royo, O., 2016. Evaluating a 2-D Structural Restoration: Validating Section Balance. AAPG Annual Convention and Exhibition, Calgary, Alberta, Canada.

Linol, B., Bercovici, A., Bourquin, S., Diez, J.B., López-Gómez, J., Broutin, J., Durand, M. & Villanueva-Amadoz, U., 2009. Late Permian to Middle Triassic correlations and palaeogeographical reconstructions in south-western European basins: New sedimentological data from Minorca (Balearic Islands, Spain). Sedimentary Geology, 220(1-2), pp.77-94.

Lorenz, J.C. & Cooper, S.P., 2017. Atlas of natural and induced fractures in core. John Wiley & Sons.

Lorenz, J.C. & Cooper, S., 2020. Applied concepts in fractured reservoirs. John Wiley and Sons Ltd.

Mahmood, B., Khoshnaw, F., Abdalqadir, M. & Rezaei Gomari, S., 2023. Natural fracture characterization and in situ stress orientation analysis using fullbore formation micro imager (FMI): A case study on the X oil field, Kurdistan region, Iraq. Arabian Journal of Geosciences, 16(2). https://doi.org/10.1007/s12517-023-11178-7

Lundegard, P., 1992. Sandstone porosity loss-A "big picture" view of the importance of compaction. Journal of Sediment. Petrol., 62(2), pp.250-260.

Mackey, S.D. & Bridge, J.S., 1995. Three-dimensional model of alluvial stratigraphy: Theory and applications. Journal of Sedimentary Research, 65(1b), pp.7-31.

Mader, D., 1982. Aeolian sands in continental red beds of the Middle Buntsandstein (Lower Triassic) at the western margin of the German Basin. Sedimentary Geology, 31(3-4), pp.191-230.

Mader, D. & Yardley, M.J., 1985. Migration, modification, and merging in aeolian systems and the significance of the depositional mechanisms in Permian and Triassic dune sands of Europe and North America. Sedimentary Geology, 43(1-4), pp.85-218.

Mäkel, G.H., 2007. The modelling of fractured reservoirs: Constraints and potential for fracture network geometry and hydraulics analysis. Geological Society, London, Special Publications, 292(1), pp.375-403.

Maniar, Z., 2019. Reservoir quality analysis of the Triassic sandstones in the Nederweert and Naaldwijk areas: A post-mortem study. (Unpublished master's thesis). Delft University of Technology, Delft.

McKie, T. & Williams, B., 2009. Triassic palaeogeography and fluvial dispersal across the northwest European Basins. Geological Journal, 44(6), pp.711-741.

McKie, T., 2011. Architecture and behavior of dryland fluvial reservoirs, Triassic Skagerrak Formation, central North Sea. In: From River To Rock Record: The Preservation of Fluvial Sediments and Their Subsequent Interpretation. SEPM Special Publication No. 97, pp.189–214.

McKinley, J.M., Atkinson, P.M., Lloyd, C.D., Ruffell, A.H. & Worden, R.H., 2011. How porosity and permeability vary spatially with grain size, sorting, cement volume, and mineral dissolution in fluvial Triassic sandstones: The value of geostatistics and local regression. Journal of Sedimentary Research, 81(12), pp.844-858.

Miall, A.D., 1977. A review of the braided-river depositional environment. Earth-Science Reviews, 13(1), pp.1-62.

Miall, A.D., 1981. Facies Models for Alluvial Fans and Braided Rivers. In: Sedimentary Geology, 5.

Milliken, K.L., 2003. Late diagenesis and mass transfer in sandstone shale sequences. In: MacKenzie (ed) Treatise on Geochemistry. Elsevier, Amsterdam, vol. 7, pp.159–190.

Ministry of Economic Affairs and Climate Policy (MEA), 2023. Natural resources and geothermal energy in the Netherlands, 2023. Annual review. Ministry of Economic Affairs and Climate Policy, The Hague.

Mijnlieff, H.F., 2020. Introduction to the geothermal play and reservoir geology of the Netherlands. Netherlands Journal of Geosciences, 99, e2. https://doi.org/10.1017/njg.2020.2

Morad, S., Al-Ramadan, K., Ketzer, J.M. & De Ros, L.F., 2010. The impact of diagenesis on the heterogeneity of sandstone reservoirs: A review of the role of depositional facies and sequence stratigraphy. AAPG Bulletin, 94(8), pp.1267-1309.

Molenaar, N. & Felder, M., 2019. Origin and distribution of dolomite in Permian Rotliegend siliciclastic sandstones (Dutch Southern Permian Basin). Journal of Sedimentary Research, 89(10), pp.1055-1073.

Monsees, A.C., Busch, B., Schöner, N. & Hilgers, C., 2020. Rock typing of diagenetically induced heterogeneities: A case study from a deeply-buried clastic Rotliegend reservoir of the Northern German Basin. Marine and Petroleum Geology, 113, p.104163.

Morad, S., Al-Ramadan, K., Ketzer, J.M. & De Ros, L.F., 2010. The impact of diagenesis on the heterogeneity of sandstone reservoirs: A review of the role of depositional facies and sequence stratigraphy. AAPG Bulletin, 94(8), pp.1267-1309.

Mountney, N.P. & Thompson, D.B., 2002. Stratigraphic evolution and preservation of aeolian dune and damp/wet interdune strata: An example from the Triassic Helsby Sandstone Formation, Cheshire Basin, UK. Sedimentology, 49(4), pp.805-833.

Nelskamp, S. & Verweij, J.M., 2012. Using basin modelling for geothermal energy exploration in the Netherlands: An example from the West Netherlands Basin and Roer Valley Graben. TNO-060-UT-2012-00245, 113pp.

Nelson, R.A., 2001. Geologic analysis of naturally fractured reservoirs. 2nd ed. Elsevier.

Nichols, G.J. & Fisher, J.A., 2007. Processes, facies and architecture of fluvial distributary system deposits. Sedimentary Geology, 195(1-2), pp.75-90.

Nichols, G., 2009. Sedimentology and Stratigraphy. John Wiley and Sons.

NITG, 2004. Geological Atlas of the Subsurface of the Netherlands – Onshore. Netherlands Institute of Applied Geoscience TNO (Utrecht), 104pp.

North, C.P. & Taylor, K.S., 1996. Ephemeral-fluvial deposits: Integrated outcrop and simulation studies reveal complexity. AAPG Bulletin, 80(6), pp.811-830.

Olivarius, M., Weibel, R., Friis, H., Boldreel, L.O., Keulen, N. & Thomsen, T.B., 2017. Provenance of the Lower Triassic Bunter Sandstone Formation: Implications for distribution and architecture of aeolian vs. fluvial reservoirs in the North German Basin. Basin Research, 29, pp.113-130.

Palermo, D., Aigner, T., Geluk, M., Poeppelreiter, M. & Pipping, K., 2008. Reservoir potential of a lacustrine mixed carbonate/siliciclastic gas reservoir: The Lower Triassic Rogenstein in the Netherlands. Journal of Petroleum Geology, 31(1), pp.35-45.

Here are the references you provided, now formatted correctly in Harvard style:

Paxton, S.T., Szabo, J.O., Ajdukiewicz, J.M. and Klimentidis, R.E., 2002. Construction of an intergranular volume compaction curve for evaluating and predicting compaction and porosity loss in rigid-grain sandstone reservoirs. *AAPG (American Association of Petroleum Geologists) Bulletin*, 86(12), pp.2047–2067.

Parkash, B., Awasthi, A.K. and Gohain, K., 1983. Lithofacies of the Markanda terminal fan, Kurukshetra district, Haryana, India. In: Collinson, J.D. and Lewin, J. (eds.), *Modern and Ancient Fluvial Systems*. International Association of Sedimentologists Special Publication, 6, pp.337–344.

Peacock, D.C.P., Nixon, C.W., Rotevatn, A., Sanderson, D.J. and Zuluaga, L.F., 2016. Glossary of fault and other fracture networks. *Journal of Structural Geology*, 92, pp.12–29.

Péron, S., Bourquin, S., Fluteau, F. and Guillocheau, F., 2005. Paleoenvironment reconstructions and climate simulations of the Early Triassic: Impact of the water and sediment supply on the preservation of fluvial systems. *Geodinamica Acta*, 18(6), pp.431–446.

Pettijohn, F.J., 1975. *Sedimentary rocks* (3rd ed.). New York: Harper & Row.

Pharaoh, T.C., Dusar, M., Geluk, M., Kockel, F., Krawczyk, C.M., Krzywiec, P., Scheck-Wenderoth, M., Thybo, H., Vejbaek, O. and Van Wees, J.D., 2010. Tectonic evolution. In: *Petroleum Geological Atlas of the Southern Permian Basin Area*, pp.25–57.

Pimentel, N.L., Wright, V.P. and Azevedo, T.M., 1996. Distinguishing early groundwater alteration effects from pedogenesis in ancient alluvial basins: Examples from the Palaeogene of southern Portugal. *Sedimentary Geology*, 105(1-2), pp.1–10.

Postma, G., 2014. Generic autogenic behaviour in fluvial systems: Lessons from experimental studies. In: *From Depositional Systems to Sedimentary Successions on the Norwegian Continental Margin*, pp.1–18.

Purvis, K. and Okkerman, J.A., 1996. Inversion of reservoir quality by early diagenesis: An example from the Triassic Buntsandstein, offshore the Netherlands. In: *Geology of Gas and Oil under the Netherlands: Selection of Papers Presented at the 1983 International Conference of the American Association of Petroleum Geologists*, pp.179–189. Springer Netherlands.

Ringrose, P.S., Martinius, A.W. and Alvestad, J., 2008. Multiscale geological reservoir modelling in practice. *Geological Society, London, Special Publications*, 309(1), pp.123–134.

Rogers, D.A. and Astin, T.R., 1991. Ephemeral lakes, mudpellet dunes and wind-blown sand and silt: Reinterpretations of Devonian lacustrine cycles in north Scotland. In: Anadon, P., Cabrera, L. and Kelts, K. (eds.), *Lacustrine Facies Analysis*, International Association of Sedimentologists Special Publication, 13, pp.199–222.

Sambrook Smith, G.H., Ashworth, P.J., Best, J.L., Woodward, J. and Simpson, C.J., 2006. The sedimentology and alluvial architecture of the sandy braided South Saskatchewan River, Canada. *Sedimentology*, 53(2), pp.413–434.

Sanner, B., Ria, K., Land, A., Mutka, K., Papillon, P., Stryi-Hipp, G. and Weiss, W., 2011. Common vision for the renewable heating & cooling sector in Europe. Office of the European Union, 2011.

SCAN, 2019. Geological evaluation for the seismic acquisition programme for SCAN areas D (Zeeland and Zuid Hollandse Eilanden) and E (West-Brabant). *EBN*, October 2019.

Scheck, M. and Bayer, U., 1999. Evolution of the Northeast German Basin—inferences from a 3D structural model and subsidence analysis. *Tectonophysics*, 313(1-2), pp.145–169.

Schmid, S., Worden, R.H. and Fisher, Q.J., 2006. Sedimentary facies and the context of dolocrete in the Lower Triassic Sherwood Sandstone group: Corrib Field west of Ireland. *Sedimentary Geology*, 187(3-4), pp.205–227.

Schmidt, C., Busch, B. and Hilgers, C., 2020. Lateral variations of detrital, authigenic and petrophysical properties in an outcrop analog of the fluvial Plattensandstein, Lower Triassic, S-Germany. *Zeitschrift der Deutschen Gesellschaft für Geowissenschaften*, 172, pp.541–564.

Schöner, R. and Gaupp, R., 2005. Contrasting red bed diagenesis: The southern and northern margin of the Central European Basin. *International Journal of Earth Sciences*, 94, pp.897–916.

Spain, D. and Conrad, C., 1997. Quantitative analysis of top-seal capacity: Offshore Netherlands, southern North Sea. *Geologie en Mijnbouw*, 76, pp.217–2226.

Spötl, C. and Wright, V.P., 2003. Groundwater dolocretes from the Upper Triassic of the Paris Basin, France: A case study of an arid, continental diagenetic facies. In: *Sandstone Diagenesis: Recent and Ancient*, pp.303–320.

Steel, R.J. and Thompson, D.B., 1983. Structures and textures in Triassic braided stream conglomerates (‘Bunter’ pebble beds) in the Sherwood Sandstone Group, North Staffordshire, England. *Sedimentology*, 30(3), pp.341–367.

Szurlies, M., 2004. Magnetostratigraphy: The key to a global correlation of the classic Germanic Trias-case study Volpriehausen Formation (Middle Buntsandstein), Central Germany. *Earth and Planetary Science Letters*, 227(3-4), pp.395–410.

Suppe, J., 1985. *Principles of Structural Geology*. Englewood Cliffs (New Jersey): Prentice-Hall.

Tartarotti, P., Ayadi, M., Pezard, P.A., Laverne, C. and De Larouziere, F.D., 1998. Multi-scalar structure at DSDP/ODP Site 504, Costa Rica Rift, II: Fracturing and alteration. An integrated study from core, downhole measurements and borehole wall images. *Geological Society, London, Special Publications*, 136(1), pp.391–412.

Toonen, W.H., Kleinhans, M.G. and Cohen, K.M., 2012. Sedimentary architecture of abandoned channel fills. *Earth Surface Processes and Landforms*, 37(4), pp.459–472.

Tooth, S., 2005. Splay formation along the lower reaches of ephemeral rivers on the Northern Plains of arid central Australia. *Journal of Sedimentary Research*, 75(4), pp.636–649.

Ulmer-Scholle, D.S., Scholle, P.A., Schieber, J. and Raine, R.J., 2014. *A Color Guide to the Petrography of Sandstones, Siltstones, Shales and Associated Rocks* (Vol. 109). Tulsa, OK, USA: American Association of Petroleum Geologists.

Van Adrichem Boogaert, H.A. and Kouwe, W.F.P., 1993–1997. Stratigraphic nomenclature of the Netherlands, revision and update by RGD and NOGEPA. *Mededelingen Rijks Geologische Dienst*, 50.

Van Balen, R., van Bergen, F., de Leeuw, C., Pagnier, H., Simmelink, H., van Wees, J., Verweij, J., 2000. Modelling the hydrocarbon generation and migration in the West Netherlands Basin, the Netherlands. *Netherlands Journal of Geosciences*, 79(e1), pp.29–44. DOI: 10.1017/S0016774600021557

Van der Zwan, C.J. and Spaar, P., 1992. Lower to Middle Triassic sequence stratigraphy and climatology of the Netherlands, a model. *Palaeogeography, Palaeoclimatology, Palaeoecology*, 91(3–4), pp.277–290.

Van Lochem, H., Ter Borgh, M. and Mijnlieff, H., 2019. Geological Evaluation for the Seismic Acquisition Programme for SCAN Areas F (Oost-Brabant and Noord-Limburg) and G (Zuid-Limburg). *SCAN Programme*, 2019, pp.11.

Van Wijhe, D.V., 1987. Structural evolution of inverted basins in the Dutch offshore. *Tectonophysics*, 137(1–4), pp.171–219.

Vercouter, C. and Van den Haute, P., 1993. Post-Palaeozoic cooling and uplift of the Brabant massif as revealed by apatite fission-track analysis. *Geological Magazine*, 130(5), pp.639–646.

Veeken, P.P. and Van Moerkerken, B., 2013. *Seismic Stratigraphy and Depositional Facies Models*. EAGE Publications.

Verweij, J.M., 1993. *Hydrocarbon Migration Systems Analysis*. Elsevier.

Vinci, F., 2018. Core analysis NLW-GT-01 (5 p.). Leiderdorp: PanTerra.

Voigt, T., 2017. Die Ablagerungssysteme des Unteren und Mittleren Buntsandsteins in Thüringen. *Geowissenschaftliche Mitteilungen Thüringen*, 14, pp.39–95.

Walker, T.R., 1979. Red color in dune sands. In: McKee, E.D. (ed.), *A Study of Global Sand Seas*. U.S. Government Printing Office, Washington, D.C., pp.61–81.

Weber, K.J., 1982. Influence of common sedimentary structures on fluid flow in reservoir models. *Journal of Petroleum Technology*, 34(3), pp.665–672.

Wennberg, O.P., Casini, G., Jonoud, S. and Peacock, D.C., 2016. The characteristics of open fractures in carbonate reservoirs and their impact on fluid flow: A discussion. *Petroleum Geoscience*, 22(1), pp.91–104.

Wentworth, C.K., 1922. A scale of grade and class terms for clastic sediments. *The Journal of Geology*, 30(5), pp.377–392.

Willems, C.J., Vondrak, A., Mijnlieff, H.F., Donselaar, M.E. and Van Kempen, B.M., 2020. Geology of the Upper Jurassic to Lower Cretaceous geothermal reservoirs in the West Netherlands Basin–An overview. *Netherlands Journal of Geosciences*, 99, p.e1.

Williams, G.D., Powell, C.M. and Cooper, M.A., 1989. Geometry and kinematics of inversion tectonics. *Geological Society, London, Special Publications*, 44(1), pp.3–15.

Winstanley, A.M., 1993. A review of the Triassic play in the Roer Valley Graben, SE onshore Netherlands. *Geological Society, London, Petroleum Geology Conference Series*, 4(1), pp.595–607.

Wong, T.E., Batjes, D.A.J. and Jager, J., 2007. *Geology of the Netherlands*. Royal Netherlands Academy of Arts and Sciences.

Worden, R.H. and Burley, S.D., 2003. Sandstone diagenesis: The evolution of sand to stone. In: *Sandstone Diagenesis: Recent and Ancient*, pp.1–44.

Worum, G., Michon, L., van Balen, R.T., Van Wees, J.D., Cloetingh, S. and Pagnier, H., 2005. Pre-Neogene controls on present-day fault activity in the West Netherlands Basin and Roer Valley Rift System (southern Netherlands): Role of variations in fault orientation in a uniform low-stress regime. *Quaternary Science Reviews*, 24(3–4), pp.473–488.

Xu, G. and Haq, B.U., 2022. Seismic facies analysis: Past, present and future. *Earth-Science Reviews*, 224, p.103876.

Yagishita, K., 1997. Paleocurrent and fabric analyses of fluvial conglomerates of the Paleogene Noda Group, northeast Japan. *Sedimentary Geology*, 109(1–2), pp.53–71.

Zeng, H., 2018. What is seismic sedimentology? A tutorial. *Interpretation*, 6(2), pp.11–12.

Zhang, G., Buatois, L.A., Mángano, M.G. and Aceñolaza, F.G., 1998. Sedimentary facies and environmental ichnology of a Permian playa-lake complex in western Argentina. *Palaeogeography, Palaeoclimatology, Palaeoecology*, 138(1–4), pp.221–243.

Ziegler, P.A., 1992. European Cenozoic rift system. In: Ziegler, P.A. (ed.), *Geodynamics of Rifting, Volume I. Case History Studies on Rifts: Europe and Asia*. *Tectonophysics*, 208, pp.91–111.

Ziegler, P.A., Schumacher, M.E., Dèzes, P., Van Wees, J.D. and Cloetingh, S.A.P.L., 2004. Post-Variscan evolution of the lithosphere in the Rhine Graben area: Constraints from subsidence modelling. *Geological Society, London, Special Publications*, 223(1), pp.289–317.

Zijerveld, L., Stephenson, R., Cloetingh, S.A.P.L., Duin, E. and Van den Berg, M.W., 1992. Subsidence analysis and modelling of the Roer Valley Graben SE Netherlands. *Tectonophysics*, 208(1–3), pp.159–171.

Curriculum Vitae

Emilio Cecchetti, *born in Firenze (Italy) on the 17-04-1993*

Education

2012-2016	BSc in Earth Science, Unversità degli Studi di Firenze
2017-2019	MSc in Geology and Geophysics, Utrecht University
2020-2025	PhD in Geoscience, Delft University of Technology

Working Experience

2024-present	Goescientist at Sproule ERCE

List of Publications

Journal Publications

Cecchetti, E., Martinius, A. W., Donselaar, M. E., Felder, M., Abels, H. A, Sedimentology, Stratigraphy and Reservoir Architecture of the Lower Triassic Main Buntsandstein in the Roer Valley Graben, the Netherlands. Submitted to Marine and Petroleum Geology.

Cecchetti, E.,Martinius, A. W., Bruna, P. O., Bender, A., & Abels, H. A. (2024). Structural controls on the Triassic Main Buntsandstein sediment distribution in the Roer Valley Graben, the Netherlands. *Netherlands Journal of Geosciences*, *103*, e23.

Conference Proceedings

Cecchetti, E., Martinius, A.W., Felder, M., Abels, H. A, 2023. Diagenetic controls on dryland clastic reservoirs from the Buntsandstein Subgroup in the Netherlands. 84th EAGE Annual Conference & Exhibition, Wien (Austria).

Tutuarima, F., **Cecchetti, E**., Abels, H. A., Bertotti, G., Bruna, P.O., 2023. Main controls on natural fracture distribution in the Lower Triassic sandstones of the West Netherlands Basin. 84th EAGE Annual Conference & Exhibition, Wien (Austria).

Cecchetti, E., Martinius, A. W., Felder, M., Abels, H. A, 2023. Reservoir Heterogeneities in the Buntsandstein Subgroup: Investigating the Role of Sedimentary Facies. 12th International Conference on Fluvial Sedimentology, Riva Del Garda (Italy).

Acknowledgments

Looking back on my journey as a PhD candidate, there are many people I need to acknowledge and to whom I am deeply grateful.

First of all, I want to thank my supervisors, Allard and Hemmo.

Allard, even though you were often physically in another country, you were always there to support and motivate me. You taught me to be pragmatic and reminded me to zoom out whenever I felt overwhelmed or lost in progress. Thank you for the valuable lessons on sedimentology you shared in the field, and for helping me understand how these concepts are relevant and essential for geoenergy applications. I greatly appreciated our conversations about science and society, and the contrasting perspectives of working in industry versus academia.

Hemmo, thank you for providing me with the confidence and motivation to move forward. Starting a PhD shortly before a major pandemic outbreak was not easy, but you were there to talk and to provide essential knowledge and resources when needed. I really appreciated the knowledge you passed on to me through core views and fieldwork, as well as our scientific discussions in the office. Furthermore, your trust in me with responsibilities such as being your teaching assistant truly elevated my experience and made me feel accomplished.

I want to thank Pierre Olivier Bruna for being an awesome colleague, collaborator, and supervisor. It has been a pleasure and truly inspiring to work with you and to observe your approach to structural geology.

Tim, thank you for being such a great colleague, always ready to help and discuss science and life in general. What a great time we had in the field, truly memorable. Camping in the desert surrounded by pristine fluvial system outcrops is something that simply cannot be described.

Andrea, we go way back, and knowing you were joining the section felt like a good old friend moving to the neighborhood. I really enjoyed our fieldwork in Montana and the Pyrenees, our discussions about science, and all the great time outside of work.

Akeel, thank you for being a great friend, colleague, and fieldwork partner. What an adventure in Lourinhã, digging trenches, sampling stunning outcrops, and even playing detective after our gears were stolen. Unforgettable!

This PhD was supported by industry partners Aardyn (now Gaia) and PanTerra Geoconsultants. From Aardyn, I am deeply grateful to Annelies Bender for supporting my study all the way through, sharing insights about the geothermal industry in the Netherlands, and passing on extremely valuable knowledge of the Triassic. From PanTerra Geoconsultants, I want to thank Marita Felder, who even after leaving the company, remained committed to helping me with sedimentology and diagenesis.

I would also like to thank Rick Donselaar for sharing his knowledge of the Triassic and sedimentology more broadly, and Alexandros Daniilidis for helping me translate my results into concepts applicable to the geothermal industry.

I would like to thank the people at TNO and NAM for providing resources that were extremely valuable for this study. In particular, I am grateful to André Slupik at TNO for always being available to grant me access whenever I needed to view some Triassic cores.

I want to thank the people from Applied Geology for being such pleasant colleagues, supervisors, and office mates. Thanks to Giovanni, Jan Kees, Joep, Remi, Parvin, Guillaume, Sebastian, Aulia, Santosh, Boris, Jasper Hupkes, Jasper Maars, Martha, and Eli. I cannot forget Quinten, Stephan, and Youwei. I'd also like to thank all the PhDs from other sections with whom I shared an office and spent quality time at TUD: Alle, David, Hamed, Milad, Mahmoud, Entela, Billie, Eddie, Aydin, Fardad, and Jingming. Thanks to whoever had the brilliant idea to place a ping-pong table at the faculty, and thanks to Milad for being the greatest opponent.

I want to thank the students I had the pleasure of supervising during their MSc theses, whose work contributed to enhancing the quality of this book. Deema, Ewoud, and Frederieke, you are all exceptionally talented scientists, and I wish you the very best in your future endeavors.

I also want to thank my new colleagues from Sproule ERCE, who over the past year have helped me develop my professional path and have taught me much about the geothermal industry and professional ethics.

Finally, I want to thank all my friends. Mentioning all of you and the reasons I'm grateful would take the time of another PhD. I'll simply say: thank you for being the fantastic people you are!

Mamma e Babbo, non ci sono parole per descrivere quanto vi sono grato per tutte le opportunità che mi avete dato e il supporto durante questi anni. Vi voglio bene.

Lastly, to you Cris, you have supported me and “tolerated” me every single day throughout this journey, thank you. Through all the highs and lows, you were always there to motivate and uplift me. Sei unica.

Samenvatting

Zandstenen uit de Trias Hoofd-Bontzandsteen Subgroep vormen een veelbelovende diepe geothermische doelformatie in de ondergrond van Nederland. Deze zandstenen zijn wijdverspreid en bereiken lokaal temperaturen tot 140–150 °C op dieptes van circa 4 tot 5 km. De Hoofd-Bontzandsteen Subgroep betreft een zandrijk interval, maar de reservoirkwaliteit van deze zandstenen staat bekend als heterogeen als gevolg van de wisselwerking tussen afzettings- en diagenetische processen. Recente boorcampagnes op dieptes groter dan 4 km hebben in meerdere gebieden de lage reservoirkwaliteit bevestigd. Desondanks zijn succesvolle geothermische projecten gerealiseerd in de Hoofd-Bondtzandsteen Subgroep in Zuid-Nederland op kleinere dieptes van 2 tot 3 km, waar temperaturen van 70 tot 90 °C kunnen voldoen aan de lokale warmtevraag voor glastuinbouw en stadsverwarming.

Om verdere geothermische exploratie te vergemakkelijken, is het belangrijk om de geologische omstandigheden die de reservoirkwaliteit beïnvloeden te begrijpen en gebieden met gunstige ondergrondse condities te identificeren. De Hoofd-Bontzandsteen afzettingen zijn op regionale schaal uitgebreid bestudeerd in Nederland. De factoren die de reservoirkwaliteit bepalen zijn echter nog beperkt begrepen inZuid-Nederland, met name in het zuidoostelijke deel waarvan weinig gegevens beschikbaar zijn.
Ditproefschrift heeft als doel het geologisch inzicht in de afzettingen van deHoofd-Bontzandsteen te vergroten door middel van een geïntegreerde geologische studie op basis van een uitgebreide koolwaterstofdataset en nieuw verkregen gegevens uit geothermische exploratie in het zuidoosten van Nederland. De studie karakteriseert de structurele, sedimentologische en diagenetische heterogeniteiten van de Hoofd-Bontzandsteen Subgroep en evalueert hun invloed op porositeit, permeabiliteit en uiteindelijk het geothermisch potentieel.

Het eerste deel van dit proefschrift (Hoofdstuk 2) onderzoekt de structurele evolutie van de Roerdalslenk en de verspreiding van de Hoofd-Bontzandsteenafzettingen aan de hand van een gedetailleerde interpretatie van seismische en boorgegevens. Een 2D palinspastische reconstructie is uitgevoerd om de begravingsgeschiedenis en de bekkengeometrie tijdens het Vroeg tot Midden-Trias te evalueren. De analyse toont aan dat het centrale en zuidelijke deel van de Roerdalslenk actieve afzettingsgebieden waren in deze periode, terwijl het noordelijke deel meer marginale zone, waar voornamelijk fijnkorrelige sedimenten zijn afgezet. Na afzetting werden de sedimenten aanzienlijk beïnvloed door breukvorming, met begravingsdieptes tot 4–5 km in het centrale gedeelte van de slenk, terwijl de flanken minder diep zijn begraven (2–3 km), wat deze gebieden veelbelovend maakt voor toekomstig geothermische onderzoek, vanwege de grotere kans op het behoud van primaire reservoireigenschappen.

In Hoofdstuk 3 worden de sedimentologie en lithostratigrafie van de Hoofd-Bontzandsteen Subgroep onderzocht aan de hand van een ondergrondse dataset van boorkernen, gamma-logmetingen en slijpplaatjes. De studie identificeert zes lithofaciesassociaties die zijn afgezet door verschillende fluviatiele processen met beperkte eolische herwerking. Over het algemeen worden de verschillende afzettingsprocessen gekoppeld aan tektonische en klimaatsveranderingen, wat heeft geleid tot de ontwikkeling van drie onderscheiden types reservoirarchitectuur, elk met hun eigen set heterogeniteiten op verschillende ruimtelijke schalen. Op schaal van het studiegebied kunnen de heterolitische sedimenten, afgezet tijdens uitbreidingen van playa-meeromgevingen, de verticale connectiviteit van zandsteenlagen belemmeren vanwege hun kilometers lange continuïteit. Binnen de zandsteenlagen zijn gecementeerde zones of kleipluggen de meest voorkomende barrières voor vloeistofstroming. Bovendien behouden de meeste zandsteentypes geen primaire relatie met reservoirkwaliteit als gevolg van post-depositionele diagenetische processen.

De diagenetische processen die porositeit en permeabiliteit beïnvloeden in de Hoofd-Bontzandsteen Subgroep zijn geanalyseerd aan de hand van gedetailleerde petrografische studies van bestaande en nieuwe slijpplaatjes (Hoofdstuk 4). De resultaten tonen aan dat illiet, kwarts en dolomiet de dominante cementen zijn in deze zandstenen, waarbij de invloed op de reservoirkwaliteit varieert afhankelijk de sedimentaire facies. In gebieden zoals de flanken van de Roerdalslenk, waar de maximale begraving tijdens het Trias en Vroeg tot Midden-Jura grotendeels ondieper was dan 2 km, dragen largere graden van compactie en cementatie bij aan het behoud van van primaire reservoireigenschappen.

Een structurele studie werd uitgevoerd om de verspreiding en kenmerken van natuurlijke breuken te analyseren, en om de mechanische stratigrafie van de Hoofd-Bontzandsteen Subgroepte onderzoeken (Hoofdstuk 5). Hiervoor is gebruik gemaakt van een dataset uit het West-Nederland Bekken, aangezien in de Roerdalslenk niet de benodigde gegevens beschikbaar zijn. De resultaten tonen aan dat natuurlijke breuken gunstig georiënteerd zijn ten opzichte van de huidige in-situ spanningsvelden, wat de kans vergroot dat deze breuken open zijn. De breukdichtheid blijkt hoger te zijn in de heterolitische sedimentaire successies, wat duid op een verband met het afzettingsmilieu en de stratigrafie van de Main Buntsandstein Subgroep.

De geologische inzichten uit deze studies zijn vervolgens toegepast om het geothermisch potentieel van de Hoofd-Bontzandsteen Subgroepin de Roerdalslenk te evalueren (Hoofdstuk 6). Porositeit en permeabiliteit zijn beoordeeld, en berekeningen van de initiële warmteinventaris (HIIP) en geothermisch vermogen (GP) zijn uitgevoerd op individuele putten. Een gevoeligheidsanalyse heeft de dikte van het reservoir en de permeabiliteit geïdentificeerd als de belangrijkste parameters die deze berekeningen beïnvloeden.. De resultaten worden geïnterpreteerd binnen de bredere geologische kennis die tijdens dit proefschrift is ontwikkeld, en drie casusstudies die overeenkomen met drie types potentiële geothermische systemen, worden gepresenteerd en besproken.

Een afsluitende synthese wordt gepresenteerd in Hoofdstuk 7, waarin de belangrijkste bevindingen van deze scriptie worden samengevat en wordt besproken hoe deze resultaten in de toekomst kunnen worden gebruikt om onzekerheden te verkleinen en risico’s te beperken bij geothermische exploratie binnen de Hoofd-Bontzandsteen Subgroep in Zuid-Nederland. Om aan de toenemende warmtevraag en de eisen van de energietransitie te voldoen is een versnelde ontwikkeling van de geothermiesector noodzakelijk. De Hoofd-Bontzandsteen Subgroep heeft het potentieel om te fungeren als een veelbelovend reservoir, met name in regio’s zoals het noordwesten van de Roerdalslenk, waar de geologische condities wijzen op gunstigere reservoirkwaliteiten. Toekomstige exploratie en productie in deze gebieden kunnen een cruciale rol spelen in het realiseren van de duurzame energiedoelstellingen van Nederland.